

Morphodynamic mechanisms in steep channels: from local processes to large-scale evolution

THÈSE N° 6065 (2014)

PRÉSENTÉE LE 10 OCTOBRE 2014

À LA FACULTÉ DE L'ENVIRONNEMENT NATUREL, ARCHITECTURAL ET CONSTRUIT
LABORATOIRE D'HYDRAULIQUE ENVIRONNEMENTALE
PROGRAMME DOCTORAL EN MÉCANIQUE

ÉCOLE POLYTECHNIQUE FÉDÉRALE DE LAUSANNE

POUR L'OBTENTION DU GRADE DE DOCTEUR ÈS SCIENCES

PAR

François METTRA

acceptée sur proposition du jury:

Dr M. Farhat, président du jury
Prof. C. Ancey, directeur de thèse
Dr G. De Cesare, rapporteur
Dr Ph. Frey, rapporteur
Prof. P. Molnar, rapporteur



ÉCOLE POLYTECHNIQUE
FÉDÉRALE DE LAUSANNE

Suisse
2014

Acknowledgements

I would like to take the opportunity to thank all the people who have contributed in some way to this study, particularly, Prof. Christophe Ancey who initiated and supervised this thesis. I thank the MICS (Mobile Information and Communication Systems) for the funding. I would also like to offer my sincere thanks to all the members of my jury, Prof. Christophe Ancey, Prof. Peter Molnar, Dr. Giovanni De Cesare and Dr. Philippe Frey, for their recommendations to improve this manuscript, and the president of the jury Dr. Mohamed Farhat, for his report on the thesis examination.

My thanks also go to Joris Heyman, for his friendship, his support and the time he awarded to me, his advice and his help were really useful and appreciated.

I also thank all the members of the LHE who were always ready to help me, Bob for the technical work, Barbara for her valuable assistance, Nicolas, Gael, Belinda, Kasper and Blaise for the advice and the good atmosphere in the lab. Special thanks go to Hongbo Ma for the work he did at LHE and for the invitation in China. I also thank Giacomo and Pascal for their work on the Armfield flume experiment.

I particularly thank Joris Heyman (again!), Belinda Bates, Nico Baetz, Colin Ferster, Koen Blanckaert, Marcin Mirski and Julien Sandevor for revising parts of my thesis.

Then, I would like to thank all my students, my friends, and my family for their patience, their support, their encouragement and also for the good time spent with them during these years at EPFL.

Abstract

The purpose of this thesis is to experimentally explore the origins of the strong fluctuations in bedload transport rates in steep channels. The thesis shows that idealized flume experiments are a valuable approach to observing specific river processes and developing simple concepts of channel evolution. A discussion of the results is presented with the aim to improve hazard mitigation by increasing the understanding of complex natural bedload transport events.

Innovative measurement techniques were developed for the production of an accurate data set of bed morphological measurements and bedload fluxes of a steep morphodynamic channel system. Simultaneously, bedload transport rates were measured by a new method using accelerometers and bed elevation was computed using camera recordings, in an 8-cm-wide and 2.5-m-long flume. The study was limited to well-sorted gravel and constant external conditions during the main measurement campaign. The response of the system to these different external conditions was tested by a precise control of the experimental parameters including varying the flume inclination, the sediment feeding and the water discharge.

This precise data allowed the characterization of the bedload transport rate fluctuations and the antidunes present in the channel. The intermittency of bedload transport increases with increasing channel steepness and decreasing transport conditions, i.e. low sediment supply and low water discharge. The importance of the antidune shape, height and celerity on channel evolution and bedload transport intermittency was inferred. Particularly, bedload transport pulses correspond to theoretical bedload transport computed from antidune translation equations. Specifically, the occurrence of avalanches on the steepest antidunes is suggested by observations. Moreover, a simple avalanche model confirms the presence of important granular interactions in steep channels at small scales.

Analyzing the global morphological evolution, it was found that steep channels behave like metastable systems. The bed profile fluctuates around a stationary state by successive aggradation and degradation events of variable intensity and duration. Aggradation periods are slow and directly dependent on the sediment supply rate, whereas degradation periods are abrupt morphological changes, i.e. a break in the bed stability. These hysteretic effects (analog to metastability), such as long aggradation periods, short and intense degradation periods, and large fluctuations in the bed profile, are increased with increasing channel steepness and decreasing transport conditions. The stationary state is represented by the time- and space-averaged channel slope, whereas the profile state is represented by the instantaneous space-averaged channel slope. The latter ranges from the angle of repose to the critical angle of stability, similarly to grain pile systems. This analogy suggests that other processes than direct water flow entrainment have significant impacts on bedload transport at large scales in steep channels.

A mechanism of channel evolution for a steep stream subject to low transport conditions is proposed. This mechanism shows the interactions between spatial-scales, from local instabilities, i.e. antidunes, to the hysteresis at the channel scale. In a channel close to its global critical state, the propagation of instabilities is easily triggered, relaxing the system to a more stable state (close to

its angle of repose). These relaxation events, which explain the periods of high bedload transport rates, might be present in steep streams at all spatial scales from grain-scale to reach-scale. Finally, the mechanism is in agreement with large-scale flume data and natural stream measurements.

Keywords : bedload transport, river morphodynamics, steep slope, antidunes, hysteresis, metastability, granular avalanches, laboratory experiments, accelerometers, imaging techniques

Résumé

L'objectif principal de cette étude est de déterminer expérimentalement les causes possibles des grandes variations observées dans le charriage de sédiments des rivières de montagne. Ce travail réalisé sur des modèles fortement idéalisés montre l'intérêt des expériences en laboratoire pour comprendre certains processus spécifiques et développer des concepts simples expliquant les changements morphologiques. En particulier, les résultats présentés améliorent la compréhension des événements impliquant un fort charriage lors de faibles crues.

De nouvelles techniques de mesure permettent d'obtenir des données précises sur la topographie du lit et le charriage dans un canal à forte pente de 8 cm de large et 2,5 m de long. Simultanément, le charriage est mesuré à l'aide d'accéléromètres et les fluctuations du lit par analyse d'images. Les graviers utilisés possèdent une distribution granulométrique étroite, afin de limiter la complexité de l'étude. La campagne de mesure principale est réalisée sous conditions stables pour permettre le développement du régime stationnaire. La réponse du modèle face aux différents paramètres expérimentaux, qui sont l'angle du canal, l'apport amont de sédiments et le débit liquide, est étudiée.

La qualité des données obtenues permet de caractériser les fluctuations du charriage et les antidunes observées. Les résultats montrent que l'intermittence du charriage augmente avec une hausse de la pente du lit et une baisse de l'apport de sédiments et du débit liquide (baisse des conditions favorisant le charriage). L'influence de la forme, de la hauteur et de la vitesse de migration des antidunes sur la variabilité du transport sédimentaire est mise en évidence. En particulier, les pics de charriages observés peuvent être estimés à partir d'équations tenant compte de la translation des antidunes. De plus, les observations suggèrent que des phénomènes avalancheux sont possibles sur les antidunes les plus raides. Le modèle d'avalanche développé confirme la présence de tels comportements granulaires à petites échelles.

L'analyse des données morphologiques du lit montre que les canaux à forte pente se comportent comme des systèmes métastables. En effet, le profil longitudinal du lit fluctue autour d'un état stationnaire dû à l'occurrence successive de périodes d'exhaussement et de dégradation. L'intensité et la durée de ces dernières sont variables. L'exhaussement est lent et dépend de l'apport de sédiments amont, tandis que la dégradation est un changement brusque du lit, suite à une perte de stabilité. Cette état de stabilité du profil est évalué par sa pente. Par analogie aux systèmes granulaires, les angles de repos et critique définissent l'amplitude maximale des fluctuations de la pente. L'intensité de ces effets hystérétiques (analogues au concept de métastabilité), caractérisée par cette amplitude, augmente avec une hausse de la pente du canal et une baisse des conditions favorables au charriage. Ces résultats suggèrent qu'une rivière à forte pente se comporte comme un système granulaire également à grandes échelles.

Un mécanisme d'évolution d'une rivière à forte pente soumise à des conditions de transport faibles est ainsi proposé. Les interactions entre les processus à petites échelles, la migration d'antidunes, et à grandes échelles, la métastabilité du lit, sont démontrée. En effet, quand le profil du lit approche l'angle critique, la propagation des antidunes est favorisée, conduisant à un nouvel état plus stable. Ces relaxations dans les canaux à forte pente sont très probablement présentes à toutes

les échelles spatiales (d'une particule à un tronçon de rivière). Des observations, effectuées à plus grandes échelles dans un canal de 17 m de long et en rivière de montagne suggèrent que ce mécanisme s'applique à de nombreuses rivières de montagne.

Mots-clés : charriage, morphodynamique des rivières, forte pente, antidunes, hystérésis, métastabilité, avalanches granulaires, expériences en laboratoire, accéléromètres, traitement d'images

Contents

Abstract	v
Résumé	vii
List of figures	xii
List of tables	xviii
Nomenclature	xxi
1 Introduction	1
1.1 Steep streams issues	1
1.2 Objectives and experimental approach	3
1.3 Contributions and outline	6
2 State of the art	7
2.1 River morphodynamics	7
2.1.1 River equilibrium	8
2.1.1.1 Equilibrium in physics	8
2.1.1.2 Equilibrium and time scale	8
2.1.1.3 Hydraulic geometry theories	9
2.1.1.4 Stationary equilibrium	10
2.1.2 Bedload transport rate	10
2.1.2.1 Definition	10
2.1.2.2 Threshold of motion and fluid force: an ideal case	11
2.1.2.3 Particle entrainment	12
2.1.3 Bedload transport prediction	13
2.1.3.1 Empirical formulations	13
2.1.3.2 Deterministic equations	13
2.1.3.3 Einstein bedload function	14
2.1.3.4 Recking bedload formula	14
2.2 Measurements, processes and their variability	14
2.2.1 Measurements in steep channels	15
2.2.1.1 In-situ investigations	15
2.2.1.2 Laboratory experiments	16
2.2.2 Bedload transport variability	17
2.2.2.1 Hydrograph characteristics	18
2.2.2.2 Sediment supply	18
2.2.2.3 Collective motion	19
2.2.3 Bedform formation and migration	19
2.2.3.1 Bedforms in steep streams	19
2.2.3.2 Flow over bedforms	22

2.2.3.3	Bedform migration and channel evolution	22
2.3	Stream equilibrium? Recent concepts and hypotheses	23
2.3.1	Stochastic theories	24
2.3.2	Granular concepts	24
2.3.3	Equilibrium in geomorphology	25
2.3.3.1	Equilibrium and stability in steep streams?	25
2.3.3.2	Metastability and self-organized system	26
2.3.4	Summary	27
3	Experimental facilities and methods	29
3.1	General experimental objectives and contributions	29
3.1.1	Experimental variables and measurements	30
3.1.2	Sediment feeding	31
3.1.3	Development of new bedload measurement techniques	31
3.1.3.1	Sediment discrete weighing	31
3.1.3.2	Microphone	31
3.1.3.3	Particle counting system with accelerometer	32
3.1.3.4	Particle counting using camera recordings	33
3.2	2D-flume	36
3.2.1	Experimental setup	36
3.2.2	Measurements	38
3.2.3	Experimental campaign	41
3.3	Armfield flume	42
3.3.1	Experimental setup	44
3.3.2	Measurements	45
3.3.3	Summary of experiments	46
4	Bedload transport analysis in steep channels	47
4.1	Data characteristics	47
4.1.1	Preliminary analyses	47
4.1.1.1	Data summary	47
4.1.1.2	Situation of the data in bedload studies	48
4.1.1.3	Bedload transport equations	50
4.1.2	Data statistics and consistency	51
4.1.2.1	Stationarity	51
4.1.2.2	System size and time scale	52
4.1.2.3	Validation of the experimental methods to solve the problematic . .	54
4.2	Bedload transport fluctuations	57
4.2.1	Quantification of the variability	57
4.2.1.1	Mean bedload transport rate and coefficient of variation	57
4.2.1.2	Bedload transport rate and waiting time pdfs	58
4.2.1.3	Bedload transport rate power spectrum	58
4.2.2	Effects of experimental parameters	61
4.2.2.1	Shields stress	61
4.2.2.2	Flume inclination	62
4.2.2.3	Sediment supply - input discharge	62
4.3	Discussion	63
4.3.1	Comparison with Armfield flume data	63
4.3.1.1	Lateral variability	64
4.3.2	Conclusion on bedload transport fluctuations	65

5	Bed stability at reach scale	69
5.1	Channel bed hysteresis	69
5.1.1	Global channel slope fluctuations	69
5.1.1.1	Bed slope determination	69
5.1.1.2	Fluctuation behaviour	70
5.1.2	Hysteresis and metastability	71
5.1.2.1	Analogy with the grain pile case	71
5.1.2.2	The slope range: an indicator of the hysteretic behaviours	72
5.1.3	Comparison with hydrodynamics variables	73
5.1.3.1	Flow acceleration	74
5.1.3.2	Shields stress	74
5.1.3.3	Discussion	75
5.2	Effects of the experimental parameters	76
5.2.1	Averaged channel steepness	76
5.2.2	Sediment supply	77
5.2.3	Shields stress	79
5.2.4	Discussion	80
5.3	Hysteresis in mountain streams	80
5.3.1	Comparison with other data	80
5.3.1.1	Armfield flume	80
5.3.1.2	The Navisence River case	81
5.3.2	Conclusion	84
6	Bedforms and meso-scale instabilities	87
6.1	Bedforms in steep channels	87
6.1.1	Antidunes, grain clusters and microforms	87
6.1.1.1	2D-flume observations	87
6.1.1.2	Other data	88
6.1.1.3	Bed elevation processing and quantification	88
6.1.2	Antidune characteristics	90
6.1.2.1	Antidune geometry	90
6.1.2.2	Migration celerity	91
6.1.2.3	Hysteresis in flow over antidunes	93
6.1.3	Local slope analysis	94
6.1.3.1	Method of computation	94
6.1.3.2	The grain pile problem and experiments	94
6.1.3.3	Local instabilities	95
6.2	Effects of the parameters	95
6.2.1	Channel parameters	95
6.2.1.1	Flume inclination	95
6.2.1.2	Sediment characteristics	98
6.2.2	External conditions	98
6.2.2.1	Sediment supply	98
6.2.2.2	Shields stress	99
6.2.3	Discussion	100
6.2.3.1	Comparison with existing antidune studies	100
6.2.3.2	Bedload intermittency and antidune migration	100
6.3	Some quantifications of local processes	101
6.3.1	Bedload transport rate from bedform migration	102
6.3.1.1	Equation for bedload transport rate due to antidune translation	102
6.3.1.2	Local bedload transport rate	103
6.3.2	Bedload transport rate from grain slides	104

6.3.2.1	Avalanche/slide observations	104
6.3.2.2	Avalanche model	105
6.3.2.3	Local avalanches	105
6.3.2.4	System relaxation	107
6.3.3	Summary	108
6.4	Conclusion: antidunes and channel evolution	109
7	Conclusion	111
A	Shear stress correction	117
B	Accelerometer constructor characteristics	119
C	Complementary experiments	123
C.1	Tests on fixed bed	123
C.1.1	Set-up and runs	123
C.1.2	Shields stress relation	123
C.2	Flow observations over a fixed wavy bed	123
C.3	Grain pile experiments	126
C.3.1	Conical dry grain pile	126
C.3.2	Submerged grain pile in a 8-cm-wide gap	126
D	Navisence River site	129
D.1	Navisence River watershed	129
D.2	Geophone measurements	129
E	Power spectrum of bedload transport rates	133
F	Spatio-temporal plots of bed elevation	137
G	Global channel slope fluctuations	145
	Curriculum Vitae	157

List of Figures

1.1	Scheme defining the stream system considered in this thesis with qs the studied bedload transport variable, Q_l the water discharge and qs_{in} the bedload transport parameter imposed on the system.	2
1.2	Large sediment deposits in Brig, Wallis, Switzerland, September 1993.. . . .	3
1.3	River evolution between the end of the winter (a) and the beginning of the summer (b) in 2011.	4
1.4	The Navisence River, Wallis in August 2013, after an exceptional bedload event. . .	4
2.1	Lane's diagram from Brierley & Fryirs [2005], illustrating the relation between the work used for sediment transport and the stream power (equation 2.2). If the equilibrium is not verified, a bed erosion or deposition occurs.	10
2.2	Shields' diagram from Buffington [1999]. The observed adimensional threshold for particle entrainment, i.e. the critical Shields stress S_{hc} , is represented as a function of the critical Reynolds number Re_c	12
2.3	Bedform diagram from Mazumder [2003] showing the existence domains of the main types of bedforms observed in rivers as functions of the mean flow velocity U and the mean grain diameter d_{50} (USPB = upper-stage plane bed and LSPB = lower-stage plane bed). Note the presence of antidunes in steep slope flows, i.e. at large Froude number Fr	20
3.1	Schemes of the accelerometer measurement system devised for this study. One of them was used for the 2D-flume experiment and six of them for the Armfield flume experiment to measure bedload transport rates at the outlet of the flumes (figure 3.2).	33
3.2	(a) Picture of an accelerometer measurement system placed at the outlet of the 2D-flume (with water flowing from left) used for bedload measurements. The accelerometer recording the particle impacts is fixed on the backward face of the plate and is protected by a metallic box. (b) The 6 accelerometer measurement systems placed along the width of the Armfield flume outlet (without water flow, downstream direction is from right to left).	34
3.3	Zoom on an accelerometer signal showing lag time and energy threshold from the calibration optimisation performed on a validation test (2D-flume), to detect the exact arrival time of each particle at the outlet.	34
3.4	Accelerometer signal and processing leading to the number of particle passing the flume outlet through time (and their arrival time), after signal filtering and peak detection. Sample of a validation test of one minute in the 2D-flume.	35
3.5	Two hour long segment of a luminosity time series computed from a camera recording, at a frame rate of 60 Hz, on a narrow window of the 2D-flume (1 cm). Downward spikes correspond to particles passing through the window and global increases and decreases to deposition and erosion respectively.	36
3.6	View of the 2D-flume with the lighting panels along the whole flume length permitting a good contrast on camera shots, flow is from left to right.	37

3.7	Scheme of the 2D-flume installation. This side view corresponds to the view recorded by the two cameras to measure bed and water elevation (figure 3.10).	38
3.8	Granulometric cumulative distribution of the gravel diameters (in the 2D-flume experiments). The mean diameter d_{50} is 6.25 mm.	39
3.9	Comparison between inlet and outlet measured bedload transport rates for run <i>5deg3v</i> , the weighing data are also shown. The error bars stand for the maximum error (accelerometer signal error + errors of the calibration data) of the time series that are used in the study (section 3.1.3.3).	40
3.10	Side view (downstream half-part of 2D-flume, around one meter) of the bed and water level captured by one of the two cameras recording the bed evolution at a sampling frequency of 1 s. Due to the powerful back lighting, an exposure time of 0.2 s permits to detect all the bed particles that did not move during this 0.2 s. All the moving ones are not seen on the images.	41
3.11	Shields stress versus water discharge: tests on fixed bed. The different lines represent the relation at different flume inclinations: 2° , 2.3° , 3° , 3.2° , 4° , 5° and 6° , from bottom to top. These tests allow defining of the initial conditions S_{hini} of the main measurement campaign.	43
3.12	Armfield flume. (b) Note the six accelerometers for the recording of bedload transport rates at the top of the image and the construction bag to retrieve and weigh the accumulated sediments.	44
3.13	Granulometric cumulative distribution of the diameter of the gravel used in the Armfield flume, and comparison with the 2D-flume. The different horizontal lines show d_{90} , d_{50} and d_{30} .	45
3.14	Experimental conditions imposed at the inlet of the Armfield flume during the flood experiment.	46
4.1	Measured S_h for the different runs (red dots: main set of runs at constant S_h , black circles: all runs) and S_{hini} (black squares) as a function of Θ . The dashed lines delimit the partial transport regime defined by equations 2.11 and 4.1.	50
4.2	(a) Theoretical values given by the Einstein [1950] bedload function and experimental data. (b) Bedload transport rate qs_E deduced from the Einstein [1950] function against the measurements.	51
4.3	(a) Values computed from the Recking [2010] equations 2.9 and 2.10 side by side with experimental data. (b) Comparison between the bedload transport rate qs_R from equation 2.9 and experimental values.	52
4.4	Time series of the accumulated sediments over run <i>3.2deg6v</i> , the straight line represents the constant feeding, the red curve the continuous outlet measurements and the red dots the outlet discrete measured weight.	53
4.5	Power spectrum of measured outlet solid discharge from run <i>4deg3v</i> . The saturation time scale T of the system is estimated around 10000 s ($1/f = 10^{-4}$) and the intermediate time scale T' at 200 s ($1/f = 5 \cdot 10^{-3}$).	54
4.6	Variation of the saturation time-scale T . (a) Dependence on the feeding rate qs_{in} . (b) Zoom on the dependence on qs_{in} for the main measurement campaign at constant S_h . (c) Dependence on the averaged channel slope α for different qs_{in} (low to high rates from top to bottom). (d) Dependence on the number of particles recorded at the flume outlet.	55
4.7	Pdfs of waiting time (time between the arrival of two consecutive moving particles) at five different locations along the channel. Data from the accelerometer signal for the two flume ends and from the three cameras for the three locations in the channel.	56
4.8	Pdfs of waiting time at flume inclinations 3.2° (a) and 5° (b) for three different sediment feeding conditions.	57

4.9	Time series of the outlet bedload transport rate for $4deg3v$ and the corresponding averaged rates for different time scales.	58
4.10	Coefficient of variation Cv of bedload transport rates, computed at several time scales (section 2.2.2) for different runs. (a) Comparison with the inlet measurements. (b) Effects of qs_{in} . (c) and (d) Effects of α for low and high qs_{in} respectively.	59
4.11	Probability density function (pdf) of bedload transport rates for run $4deg3v$	59
4.12	Pdf of the waiting times for $4deg3v$ and comparison with an exponential distribution.	60
4.13	Pdfs of bedload transport rates. (a) Comparison with different S_h . (b) Comparison with different α at low qs_{in} . (c) Comparison with different α at high qs_{in} . (d) Comparison with different qs_{in}	61
4.14	Evolution of Cv as a function of the flume inclination for three different solid input discharges.	63
4.15	Evolution of bedload transport variability, Cv , as a function of the mean solid discharge for all the tested conditions in log-log scales. Note the decreasing power law trend with increasing qs_m	64
4.16	Time series of qs in the Armfield flume with an inclination of 2° and $Q_l = 10$ l/s (run $arm2deg$); red lines show the averaged value qs_m and the domain defined by $qs_m \pm s(qs)$ (values computed from the stationary regime).	65
4.17	Cumulative bedload transport rates measured at the Armfield outlet (same run as figure 4.16), the colors stand for the 6 accelerometers and the black curve for the total bedload transport.	65
4.18	Cv of Armfield bedload transport rates (same run as figure 4.16) as a function of the time-scale and comparison with 2D-flume data (red dots), the colors stand for the 6 accelerometers and the black curve for the total bedload transport.	66
5.1	Examples of instantaneous bed profiles deduced from camera shots for run $4deg3v$, the linear regression is used to compute the averaged bed profile and determine the global channel slope Θ . (a) $\Theta = 4.03^\circ$ at 4 hours. (b) $\Theta = 3.59^\circ$ at 5 hours. (c) $\Theta = 4.07^\circ$ at 12 hours. (d) $\Theta = 3.14^\circ$ at 15 hours.	70
5.2	Time evolution of the global space-averaged channel slope Θ computed every second for run $4deg3v$: initial slope is 4° , solid input discharge is 0.19 g/s and mean channel slope is 3.7°	71
5.3	Comparison between Θ and qs for the first 22 hours of the time series of run $4deg3v$. (a) Time series of Θ . (b) Time series of qs	72
5.4	Time evolution of Θ for four runs, $4deg6v$, $4deg15v$, $2deg6v$ and $2deg15v$. Note that for the highest solid input rate, a six-hour-long run is sufficient to reach the stationary state and record the autogenic fluctuations.	73
5.5	Comparison between time series of variables Θ , Θ_w and S_h (averaged over a 40 cm window situated just upstream of the flume outlet) and qs sampled at one minute for run $2deg3v$. The vertical dashed lines show the main bedload transport peaks.	74
5.6	Comparison between time series of variables Θ , Θ_w and S_h (averaged over a 40 cm window situated just upstream of the flume outlet) and qs sampled at one minute for run $4deg3v$. The vertical dashed lines show the main bedload transport peaks.	75
5.7	Time evolution of Θ for 2 experiments with initial slopes of 2° ($2deg3v$) and 4° ($4deg3v$), low solid input discharge of ~ 0.20 g/s for both runs.	78
5.8	(a) $R = \Theta_c - \Theta_r$ as a function of Θ_m for several qs_{in} . (b) Θ_m as a function of qs_{in} for different flume angles.	78
5.9	(a) Θ_c (above) and Θ_r (below) as a function of Θ_m for several qs_{in} , same legend as the legend in figure 5.8(a). (b) R as a function of Θ_c and Θ_r , the lines represent the linear regressions.	79

5.10	Time series of Θ : effects of Shields stress on the fluctuations in Θ . (a) Comparison between runs with same qs_{in} and Θ_{ini} and different S_h . (b) Comparison between runs with strong difference in qs_{in} and S_h	79
5.11	R as a function of S_h for all 2D-flume runs.	80
5.12	Fluctuations of Θ for runs <i>arm2deg</i> (left) and <i>arm1.4deg</i> (right).	81
5.13	Channel (black) and water (blue) slope fluctuations for the experiment of 35 consecutive floods (flume angle 1.7°). The solid line and the dashed line are computed from the linear regression and the height difference of the longitudinal profiles respectively.	82
5.14	Navisence data. Plot of the water discharge Q_l and the sediment transport rate qs for eight days at the end of May 2012. The hydrogram shows quasi-daily small floods (from snow and glacier melt) of similar magnitudes. The sampling rate is one minute.	83
5.15	Navisence data. Plot of the water discharge Q_l and the sediment transport rate qs for 12 days at the end of June 2012 during a period of high flow rate with daily peaks. The sampling rate is one minute.	83
5.16	(a) Scatter of S_h as a function of qs for all 2D-flume runs. (b) Relation between R and Cv (same data).	85
6.1	Spatio-temporal plots of bed elevation for run <i>2deg3v</i> ((a) duration of 24 hours) and run <i>2deg15v</i> ((b) duration of 6 hours). The distance is measured from the inlet in the downstream direction.	88
6.2	Bed elevation profile, its trend at scale 2.5 cm and the computed extrema (triangles) at a given time showing the processing steps for the detection of bedforms.	89
6.3	Scheme of an asymmetric antidune. Several characteristics are defined. The dashed line represents the instantaneous space-averaged profile of the channel, corresponding to Θ	90
6.4	Pdfs of antidune heights for runs at flume inclinations 2° (a) and 4° (b).	90
6.5	Extract of the time series of Θ for experiment <i>4deg3v</i> with temporal localizations of the antidune heights superior to 1.6 cm (red circles), the black dashed line represents Θ_m	91
6.6	λ as a function of $H = (H_{up} + H_{down})/2$ for run <i>2deg15v</i> ; the black, red and green dots represent the bin averaged values for $\lambda = f(H)$, $\lambda_{up} = f(H_{up})$ and $\lambda_{down} = f(H_{down})$ respectively.	92
6.7	H_{down} as function of H_{up} for runs <i>4deg3v</i> (a), <i>4deg15v</i> (b), <i>2deg3v</i> (c) and <i>2deg15v</i> (d). Dots are bin averaged values and dashed lines represents $H_{up} = H_{down}$	92
6.8	Antidune celerity c as a function of antidune height for flume angle 2° (a) and 4° (b).	93
6.9	Hysteresis in the relation h as a function of Q_l , measurements taken over a fixed wavy bed (appendix C.2), flume inclination is 2°	94
6.10	Pdfs of local slope for scales 2 cm, 6 cm and 10 cm with gaussian fitting for runs <i>2deg3v</i> (b) and <i>4deg3v</i> ((a) and (d)). (c) Comparison of pdfs at scale 2 cm for 2° (run <i>2deg3v</i>) and 4° (run <i>4deg3v</i>).	96
6.11	Pdfs of the local slope at scale 2 cm for $qs_{in} = 0.2$ g/s (a) and $qs_{in} = 1$ g/s (b) for flume inclinations 2° and 4°	99
6.12	Comparison between low and high transport conditions at 4° (respectively runs <i>4deg3v</i> and <i>4deg48v</i>). (a) Pdfs of bedform heights. (b) Antidune celerity as a function of bedform height.	99
6.13	Antidune domain defined by the two equations 2.15 and 2.14 (section 2.2.3.1) with the situation of the present data.	100
6.14	Spatio-temporal plot of bed elevation of run <i>2deg3v</i> with corresponding outlet bedload transport rates integrated over 1 minute on the right.	101
6.15	Scheme of antidune migrating at celerity c , at time t in blue and at time $t + \Delta T$ in red, A is the cross-sectional area of the scour.	103
6.16	Picture showing an antidune in the 2D-flume.	103

6.17	(a) plots of $qs_{loc,m}$ and qs_{loc}^* as a function of qs_{in} for flume angle 2° and 4° . (b) Maximum of the outlet bedload rate at the characteristic temporal scale of the highest bedforms (25 s). (c) Pdfs of $qs_{loc}/\overline{qs_{out}}$	104
6.18	Sequence of successive images (sampling time = 1 s) showing a slide event (run <i>4deg3v</i> during the sharp failure at time 13 hours). Particularly note the antidune height and the position of the through before and after the event. Flow is left to right.	105
6.19	Sketch of forces acting on a volume of grains potentially moving as an avalanche. . .	106
6.20	Plot showing θ_c as a function of h for $h_{av} = 2d_{50} = 1.25$ cm (line) and $h_{av} = 3d_{50} = 1.875$ cm (dashed line).	107
6.21	Plots showing θ_c as a function of h_{av} for $h = 0.08$ m (case of flume angle 4° , left) and $h = 0.029$ m (case of flume angle 2° , right).	108
6.22	Plot showing $\Theta_{c,system}$ as a function of h for $h_{av} = 2d_{50} = 1.25$ cm (line) and $h_{av} = 3d_{50} = 1.875$ cm (dashed line).	109
6.23	Diagram summarizing local bedform behaviours linked with intermittency observed in bedload transport rates.	110
A.1	S_h as a function of Θ_m for the main set of runs (at constant S_h) in the 2D-flume (table 3.2), comparison with the different correction methods. h and Rh represent the assumption of an infinite width and the assumption of walls with the same roughness as the bed, respectively.	118
B.1	Main features of the accelerometer evaluation board used in the accelerometer measurement system.	120
B.2	Maximum characteristics of operation of the accelerometer evaluation board used in the accelerometer measurement system.	120
B.3	Main technical characteristics of the accelerometer evaluation board used in the accelerometer measurement system.	121
C.1	Shields stress S_h versus water discharge Q_l : experimental measurements (crosses) and linear fitting, for different flume angle α . Black squares represent S_{hini} and red dots the campaign runs.	124
C.2	Linear regression of the coefficients of the linear regression of the relations between S_h and Q_l for different α (figure C.1).	124
C.3	View of the channel for flow observations over a wavy bed.	125
C.4	Side views of the flow over an artificial antidune, flow from left to right.	125
C.5	Picture of the conical grain pile experiment.	127
C.6	Picture of the grain pile experiment in a 8-cm-wide gap under water.	127
D.1	The Navisence River. (a) Map from Travaglini & Bardou [2012]. (b) The Navisence River just upstream the Zinal measurement station.	130
D.2	Zinal measurement station on the Navisence.	131
E.1	Power spectrum of bedload transport rates: run <i>2deg3v</i>	134
E.2	Power spectrum of bedload transport rates: run <i>2deg15v</i>	134
E.3	Power spectrum of bedload transport rates: run <i>5deg3v</i>	135
E.4	Power spectrum of bedload transport rates: run <i>5deg15v</i>	135
E.5	Power spectrum of bedload transport rates: run <i>3.2deg45v</i>	136
E.6	Power spectrum of bedload transport rates: run <i>5deg45v</i>	136
F.1	Spatio-temporal plots of bed elevation: run <i>4deg3v</i>	138
F.2	Spatio-temporal plots of bed elevation: run <i>4deg6v</i>	138
F.3	Spatio-temporal plots of bed elevation: run <i>4deg15v</i>	139
F.4	Spatio-temporal plots of bed elevation: run <i>3.2deg3v</i>	139

F.5	Spatio-temporal plots of bed elevation: run <i>3.2deg6v</i>	140
F.6	Spatio-temporal plots of bed elevation: run <i>3.2deg15v</i>	140
F.7	Spatio-temporal plots of bed elevation: run <i>2deg3v</i>	141
F.8	Spatio-temporal plots of bed elevation: run <i>2deg6v</i>	141
F.9	Spatio-temporal plots of bed elevation: run <i>2deg15v</i>	142
F.10	Spatio-temporal plots of bed elevation: run <i>3.2deg45v</i>	142
F.11	Spatio-temporal plots of bed elevation: same experimental parameters as for run <i>2deg6v</i> with sediment feeding stopped after approximately 14 hours. The system should relax towards a new stationary equilibrium, however, as no feeding rate are set, degradation will continue indefinitely. Thus, the system could not reach an equilibrium.	143
G.1	Θ for run <i>3.2deg15v</i> (red dashed line) and <i>4deg15v</i> (black line).	146
G.2	Θ for run <i>3.2deg10v</i> (red dashed line) and <i>4deg10v</i> (black line).	146
G.3	Θ for run <i>3.2deg6v</i> (red dashed line) and <i>4deg6v</i> (black line).	147
G.4	Θ for run <i>2deg3v</i> (blue dot line), <i>3.2deg3v</i> (red dashed line) and <i>4deg3v</i> (black line).	147

List of Tables

3.1	Properties of the 2D-flume sediments: density ρ_s , apparent density ρ_{app} , ϕ =porosity and a =aspect ratio= ratio of larger to minor particle axes.	38
3.2	Experimental runs and corresponding parameters for the data set with constant Shields stress: flume angle α , mean solid discharge qs , water discharge Q_l , initial Shields stress S_{hini} , run duration t_{exp} , water depth h , Froude number $Fr = U/\sqrt{gh}$ with U the mean velocity, Reynolds number $Re = d_{50}\sqrt{S_h(\rho_s - \rho)gd_{50}/\rho}/\nu$ with ν the kinematic viscosity, and flume width to water depth ratio W/h	42
3.3	Experimental runs and corresponding parameters for the complementary runs at stronger Shields stress.	43
3.4	Properties of the Armfield flume sediments.	45
3.5	Parameters of runs at constant Shields stress conducted on the Armfield flume. . . .	46
4.1	Experimental measurements and bulk parameters: Cv the coefficient of variation of the solid discharge qs , Θ_w the global free surface slope, τ_b the corrected bed shear stress and S_h the corrected Shields stress.	49
4.2	Experimental parameters of the two long Armfield runs.	64
5.1	Parameters linked with metastability: the time- and space-averaged channel slope Θ_m , the minimum and maximum space-averaged channel slopes Θ_r and Θ_c and the slope range R	76
C.1	Characteristic angles computed from the grain pile experiment in a 8-cm-wide gap under water: the critical avalanche angle Γ_c of the profile, the critical avalanche angle γ_c at scale 2 cm and the angle of repose Γ_r of the profile.	126

Nomenclature

α	flume angle (°)
β	bedform shape factor (-)
η_0	Einstein's lift force fluctuation parameter (-)
Γ_c	critical angle of stability of the grain pile profile (°)
γ_c	local critical angle of the grain pile profile (°)
Γ_r	angle of repose of the grain pile profile (°)
Γ	angle of the grain pile profile (°)
λ	wavelength (m)
λ_{down}	downstream half-wavelength of a given antidune (m)
λ_{up}	upstream half-wavelength of a given antidune (m)
ν	kinematic viscosity (m ² /s)
Φ	adimensional bedload transport rate (-)
ϕ	porosity (-)
Ψ	Einstein's non-dimensional fluid stress (-)
ρ_{app}	apparent sediment density (kg/m ³)
ρ	water density (kg/m ³)
ρ_s	sediment density (kg/m ³)
τ_{bc}	critical bed shear stress (kg·m ⁻¹ ·s ⁻²)
τ_b	bed shear stress (kg·m ⁻¹ ·s ⁻²)
$\Theta_{c,system}$	critical avalanche angle for the relaxation of the whole channel (°)
Θ_c	critical angle of stability of the channel bed (°)
Θ_r	angle of repose of the channel bed (°)
Θ	space-averaged bed channel slope (°)
Θ_m	time- and space-averaged bed channel slope (°)
Θ_w	water surface slope (°)
Θ_0	critical angle of stability of the profile for no flow = Γ_c (°)
θ_0	critical angle of stability for no flow = γ_c (°)
a	sediment aspect ratio (-)
c	antidune celerity (mm/s)

Cv	coefficient of variation of the bedload transport rate (-)
d_{16}	grain diameter at which 16% of the sediment is finer than (m)
d_{30}	grain diameter at which 30% of the sediment is finer than (m)
d_{50}	mean sediment diameter (m)
d_5	grain diameter at which 5% of the sediment is finer than (m)
d_{84}	grain diameter at which 84% of the sediment is finer than (m)
d_{90}	grain diameter at which 90% of the sediment is finer than (m)
d_{95}	grain diameter at which 95% of the sediment is finer than (m)
f	frequency (s^{-1})
F_f	solid friction force (N)
F_p	pressure force (N)
F_W	apparent weight (N)
F_τ	shear fluid force (N)
F_a	antidune mobility number (-)
Fr	Froude number (-)
g	acceleration due to gravity ($m \cdot s^{-2}$)
H	antidune height (m)
h	water depth (m)
H_m	mean antidune height (m)
h_{av}	avalanche depth (m)
H_{down}	downstream crest height of a given antidune (m)
H_{max}	maximum antidune height for a given run (m)
h_m	mean water depth (m)
H_{th}	antidune height threshold delimiting aggrading and degrading antidune (m)
H_{up}	upstream crest height of a given antidune (m)
k	wave number (-)
L	system size (m)
m_{av}	mass of entrained grains during a slide (kg)
P_m	channel wetted perimeter (m)
Q_l	water discharge (l/s)
Q_s	volumetric bedload transport rate (m^3/s)
qs	bedload transport rate (g/s)
$qs_{in,cum}$	cumulative bedload transport rate at the flume inlet (g/s)
qs_{in}	input solid discharge (g/s)
$qs_{loc,m}$	local bedload transport rate for an averaged antidune from the translation equation (g/s)
qs_{loc}^*	local bedload transport rate for the highest antidune from the translation equation (g/s)

qs_m	mean bedload transport rate (g/s)
$qs_{out,cum}$	cumulative bedload transport rate at the flume outlet (g/s)
qs_{th}	theoretical bedload transport rate from antidune translation equation (g/s)
R	slope range = $\Theta_c - \Theta_r$ (°)
R_h	channel hydraulic radius (m)
Re	Reynolds number (-)
Re_c	critical Reynolds number (-)
S	channel cross-sectional area (m ²)
s	standard deviation of bedload transport rate (g/s)
S_h	Shields stress (-)
S_{hc}	critical Shields stress (-)
S_{hini}	initial experimental Shields stress (-)
T	saturation time scale of a geomorphic system (s)
t	a given time scale (s)
t_{exp}	run duration (s)
U	mean velocity (m/s)
W	channel width (m)

Chapter 1

Introduction

In mountainous areas, the slope of stream channels is much higher than in lowland regions. Rivers are classified according to slope, where mountain stream refers to river with slopes superior to 0.8° [Weichert, 2006]. Here, a channel is considered as a steep mountain stream for slopes higher than around 3° . Streams of this type are often enclosed in narrow valleys and display complex morphodynamics in term of watershed geology, morphology, hydrology and weathering at different spatial and temporal scales.

This thesis seeks to improve the understanding of steep-stream morphodynamics, i.e. the relations between the channel topography and the external fluxes — mainly water discharge and sediment sources, taking into account the transport of sediment, from small to large scales. Indeed, sediment transport is the mediator between the external fluxes imposed by the hydrological and geological conditions and the river morphology. Thus, the interplay between external variables such as flow discharge and sediment sources, and the channel morphology leads to a range of different behaviours and possible evolution. For instance, positive or negative feedbacks between bedload transport rates, morphology changes and flow characteristics are expected; however, simple and general mechanisms explaining the evolution and the possible different states of the system — a given stream reach subjected to external forces (figure 1.1) — might emerge.

It is important to recall that transport of sediment in steep streams occurs mainly by saltation, sliding and rolling on the stream bed due to the relatively large sediment size. In contrast to suspended load, which is the main transport regime in lowland rivers, this type of transport is named bedload transport. Only this type of transport will be studied in this work.

1.1 Steep streams issues

After more than a century of research on bedload transport and channel evolution, the problem is far from being solved. Many aspects are still unclear at different temporal and spatial scales, including:

- the relation between bedload transport rates and external fluxes;
- the characterization of the intermittency and variability of bedload transport rate;
- the formation and the role of bedforms.

The lack of understanding has been attributed to several possible causes:

- the difficulty of conducting long and accurate field measurements;
- the complexity and the particularity of each stream and watershed;
- the omission of taking into account processes that play a role in certain circumstances.

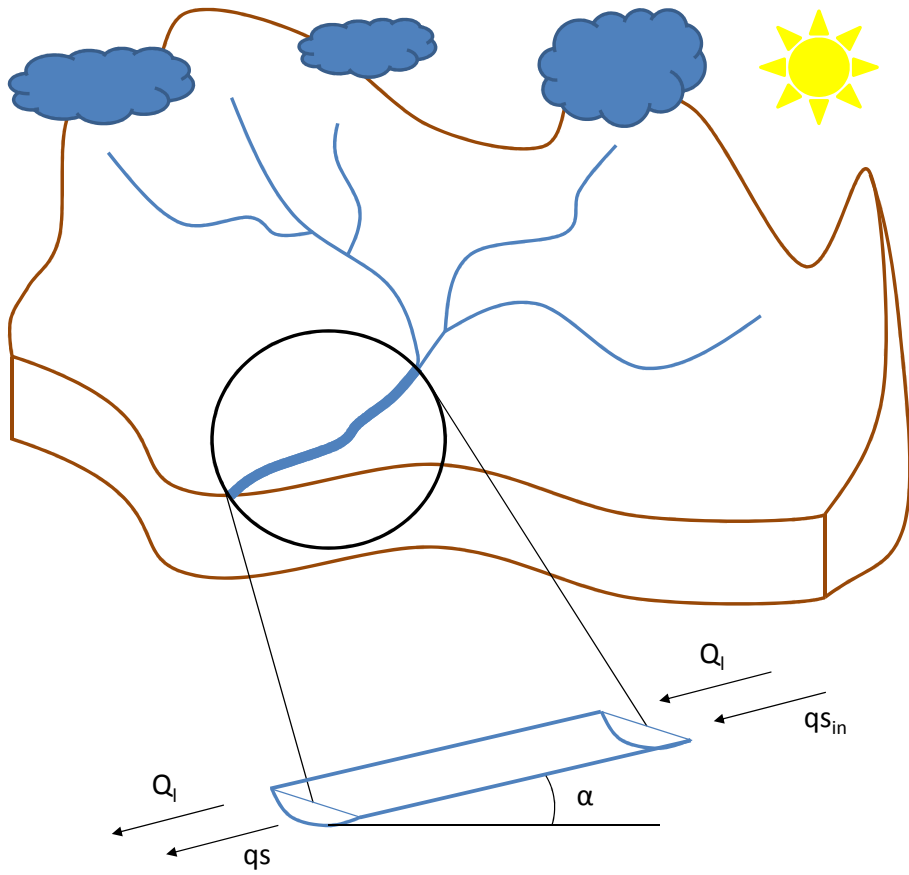


Figure 1.1: Scheme defining the stream system considered in this thesis with q_s the studied bedload transport variable, Q_l the water discharge and $q_{s_{in}}$ the bedload transport parameter imposed on the system.



Figure 1.2: Large sediment deposits in Brig, Wallis, Switzerland, September 1993..

The morphodynamics of steep channels, in particular for high roughness and low transport conditions, is poorly understood. In many cases, bedload transport rate estimates are different from measurements by a few orders of magnitude.

There are two different applications of stream morphodynamics research, the first one being hazard mitigation. Flood waves can be only modelled if the channel characteristics and its evolution during the flood are known. This requires a thorough understanding of sediment transport, deposition and erosion at different scales. For instance strong local erosion can lead to river bank failures, whereas strong deposition at a certain location can increase the water level and worsen the consequences of a given flood. Even small-scale features like migrating antidunes can lead to unpredictable behaviour if not taken into account. For instance, the flood in September, 1993 in Brig, Wallis, Switzerland left large deposits of sediments in the town's streets. This was probably caused by increased overflow due to large volumes of sediment deposited along the stream channel [LHG, 1994; Badoux & Rickenmann, 2008] (figure 1.2).

Second, the long term evolution of a stream is interesting in many ways, particularly in civil engineering and hydraulic structure operations. New buildings should be planned away from flood risk areas and possible future river paths for the next few decades. Similarly, if the stream is modified for some reason, like dredging, structure construction or dam removal, it is essential to assess the response of the stream to these new conditions. For instance pictures taken at the field measurement station on the Navisence River, Wallis show significant changes to the main channel path. For example, the straight narrow channel became more sinuous at the end of the winter with strong changes to the position of the deposits with only small to moderate floods (figure 1.3). More recently, in August 2013 at the same site, a strong but not exceptional flood event leads to exceptional deposit and erosion patterns (figure 1.4).

1.2 Objectives and experimental approach

In this thesis, I seek to bring new hypothesis and findings to solve the following global problematic: “What are the origins of the particular bedload transport fluctuations observed in mountainous rivers?” (section 2.2.2). Here, the terme “fluctuations” refers to the variation of the rate of bedload



Figure 1.3: River evolution between the end of the winter (a) and the beginning of the summer (b) in 2011.



(a) Aerial view, note for instance the position of (b) Large deposit on the right bank and strong erosion on the the bridge and the felled trees. Photo: E. Bardou. left bank, to be compared with figure 1.3. Photo: C. Ancey

Figure 1.4: The Navisence River, Wallis in August 2013, after an exceptional bedload event.

transport for constant external parameters. More precisely the specific question “Which simple morphodynamics mechanisms could explain these fluctuations?” will be answered. There are probably general physical concepts that govern the evolution of a wide range of river types. The different objectives to clarify this problematic are summarized in the following paragraphs.

First, the main idea is to study the bedload transport fluctuations in the case of steep channels. These fluctuations will be quantified in respect to several external parameters whose the effects will be observed independently. Some causes could then be hypothesized. The resulting observations and analysis in a wide range of spatial and temporal scales are essential.

Second, I identify and classify several morphodynamics mechanisms. These mechanisms correspond to the succession of simple processes occurring in the stream system that may explain the creation or destruction of morphological features or the observation of specific bedload transport behaviours.

Third, it is interesting to quantify the relative importance of the different identified mechanisms to eventually infer the main causes explaining bedload transport fluctuations. This point might be dependent on the external parameters and the spatial and temporal scales. To perform this analysis, several approaches will be used, like bedform migration theories, avalanche models and granular flow concepts.

To achieve the previous points, I aim to produce an accurate data set of bedload transport rates and bed elevations at high spatial and temporal resolution. The acquisition of bedload and elevation data have to be simultaneous over a long time interval — compared to the evolution time scale of the system — with a high sampling frequency. These two characteristic time may differ depending on the external parameters.

These specific data were obtained by developing an idealized experiment, the necessary measurement systems and a methodology for systematic testing. The term “idealized experiment” indicates a prototype experiment displaying the typical morphodynamics processes without the specificity of a particular stream or river-reach. This implies the definition of the complete specifications and technical requirements for the experiment relative to the objectives detailed above and to the technical feasibility. These experimental objectives are detailed in section 3.1.

The approach is therefore to design and use experimental facilities to precisely study bedload transport processes in a less complex setting than in real rivers. The process and variability of bedload transport itself are sufficiently complex to be studied separately. The idealized approach is also essential to produce accurate measurements from new techniques developed during this work. The experimental restrictions are:

- steep channel without suspended load transport;
- low flow conditions;
- well-sorted but natural sediments;
- straight channel.

In addition, only external fluxes at the channel inlet were considered — no erosion, modification or supply of the channel banks are discussed. From this study, a better understanding of the morphodynamics of steep channels is expected, permitting to answer to the key question of the strong unpredictability observed in the evolution of steep streams. An understanding of the mechanisms and processes explaining the observed behaviours should arise from these laboratory experiments.

1.3 Contributions and outline

In this work, two efficient experimental facilities have been designed to produce high quality measurements related to bedload transport and channel evolution. The sampling frequency and the resolution of the data are very high compared to common studies. Besides observing the processes in detail, new concepts in steep channel evolution are proposed explaining features that are commonly reported in the literature. The main contributions of this study can be summarized as follows:

- high sampling frequency bedload measurements were conducted in laboratory at low cost: in particular, a new technique recording the arrival time of each transported particle was developed;
- a greater understanding of how bedload transport is subject to strong fluctuations in a wide range of spatial and temporal scales, was reached;
- the channel steepness and the sediment supply are crucial parameters in bedload transport and channel evolution;
- in certain cases steep channels can be interpreted as metastable systems, i.e. systems where a succession of slow accumulations and fast releases of sediments is observed (2.3.3.2);
- the characteristics and migration of bedforms play an essential role in channel evolution by accumulating and releasing sediment.

Note that most of the results presented in this study are based on a small and narrow flume experiment in which an extensive measurement campaign was conducted. A complementary experiment using a larger scale flume was designed to compare and validate some of the results. Also data from a mountain river, the Navisence River (appendix D), illustrate the morphodynamic concepts developed in this thesis.

Chapter 2 details the state of the art of bedload transport rate and channel bed topography characteristics. Special attention is paid to define notions of stability and equilibrium, which are essential when studying stream bed evolution. The common hypothesis answering the problematic and new lines of research are given. The experimental designs and methods are presented in chapter 3. In particular, I highlight the experimental choices relative to the objectives of the study and the measurement techniques that I developed for this study. Three chapters of results then follow. First, in chapter 4 bedload transport data are analyzed underlining the high variability and the poor predictability of bedload equations. These analysis led to several hypotheses that were developed to explain the observed behaviours. Second, evidence of hysteretic behaviours in steep channel is presented in chapter 5 using the collected data. This new concept in the field of river morphodynamics seems to explain why such strong fluctuations are observed. Third, in chapter 6 a topographical analysis at micro- to meso-scale is conducted. New mechanisms of channel evolution from the smallest scales to reach-scale are deduced and used to validate the analogy with metastability. Finally, chapter 7 summarizes the important conclusions and outlook for the understanding of steep river evolution.

Chapter 2

State of the art

This chapter reviews the state of the art in river morphodynamics, underlying accepted knowledge, the lack of understanding of certain points, recent advances and new concepts to solve issues related to steep channel evolution. Research in bedload transport and fluvial morphology has been extensive during the last century. Thus, a synthesis of the undertaken work is an essential step to introduce future research approaches and some hypothesis that I will attempt to verify and develop in this study.

This review is divided in three parts. First, general concepts, definitions and transport formulations in river morphodynamics are presented, such as river equilibrium and bedload transport. This synthesizes the current view on river evolution and processes through time and space. For instance, the equilibrium of a river is inseparable from the time- and spatial-scale of observation.

Second, specific measurement techniques, observations and findings about morphological and transport processes are reported. The current description of bedload transport rate variability and their possible causes are summarized. Then, bedform observed in steep streams are presented. The corresponding findings about their formation and migration are reviewed through specific studies. Indeed, there is a lack of global approach trying to relate morphological evolution and bedload transport fluctuations. Moreover, not enough extensive data are available to verify the general hypothesis of river equilibrium, especially in steep mountain streams. This emphasizes the need to conduct more idealized experiments to eventually see the emergence of global behaviours, in the sense that they are verified in a wide range of experimental or natural situations.

Finally, hypothesis aiming a global description of river evolution and based on recent concepts and new theory improvements are made. Moreover, this approach should take into account the local description of bedload transport fluctuations and morphological processes. Several local mechanisms and concepts of river evolution, from local to system scale, are presented to be tested with the collected data of this study. Some of them could appear simultaneously, showing the complexity to understand river morphodynamics. This also implies the need to quantify the relative importance of each mechanism.

2.1 River morphodynamics

First, I define the basic notions of stability and equilibrium that come from physics. This is necessary because the terms *stability* and *equilibrium* and their subsequent qualifying terms have been used with different definitions and contexts in geomorphology literature [Thorn & Welford, 1994]. These terms have generally a different meaning than original physics definitions. Then, concepts of equilibrium in river evolution are reviewed, defining the terms used in this study compared to the physics description. Many principles of evolution have been proposed, supposing that rivers

tend to an equilibrium state. In the last section of this chapter, I will discuss on the validity of this equilibrium hypothesis that has not been demonstrated.

Second, findings related to bedload transport, i.e. the mediator between environmental actions and the river evolution, are summarized. The question of the incipient motion and the entrainment of particles is discussed.

Third, an overview of the predictive bedload transport equations proposed in the literature is given. Particularly, the problems of predicting bedload transport is discussed. Many of these common formulations are based on the principle of channel stability, with a water discharge value corresponding to a unique bedload transport rate. As this assumption is not clearly proven, we should wonder if these formulations reflect the river processes correctly.

2.1.1 River equilibrium

2.1.1.1 Equilibrium in physics

In physics and thermodynamics, the concept of equilibrium is precisely defined, whereas in fluvial hydraulics the notion of equilibrium is rather approximate. For instance, in the review of Church [2006], a river is identified in equilibrium if there is no significant global aggradation or degradation of the bed. In physics, a body is at equilibrium if and only if the acting external forces are balanced, meaning that the body is at rest (static equilibrium) or moving at constant velocity (dynamic equilibrium). The equilibrium can be qualified as stable, unstable, neutral or metastable, depending on the consequences of a small perturbation in the force balance [Thorn & Welford, 1994]. The system, subject to the perturbation, may respond by a negative feedback (stable), positive feedback (unstable) or no feedback (neutral) reactions. The metastable equilibrium is a more general case where the system is stable or unstable according to the magnitude of the perturbation. When the perturbation is small, the feedback is negative, bringing back the system to its initial state, whereas for a sufficient perturbation, the feedback becomes positive and the system evolves towards another more stable equilibrium.

The concepts presented in the following are relatively far from these definitions. However, hypothesis proposed in this study get closer to these physical descriptions as it will be discussed in section 2.3.

2.1.1.2 Equilibrium and time scale

Starting with a general description of a river, its typical longitudinal profile shows a concave shape with high slope in the upper profile close to the source. From the top reach, the slope decreases rapidly, the grains are finer [Parker, 1991] and the water discharge increases [Singh, 2003]. The coarser bed particles are in the mountain part of the river, particularly in steep reaches. Finer sediments are found in alluvial plains and deltas. This typical longitudinal profile of a river is the result of long-term erosion and geologic changes which are often supposed to lead to an equilibrium at our time-scale of observation. The changes of these parameters — channel slope, grain size and water discharge — might adjust to an equilibrium state as explained in the following.

First, it is necessary to define the considered time-scale. At the geologic and climatic period time scale, the river is certainly not in equilibrium due to tectonic movements, global erosion of mountain ranges or changes in climate [Nanson *et al.*, 2008]. Moreover, at the time scale of a meteorological event, like a flood, in many cases, morphologic changes are visible, particularly for an exceptional event [Singh, 2003]. However, between these short-term adjustments and long-term evolution trends, i.e. at the current climate period scale, a stable equilibrium might be observed [Leopold & Maddock, 1953; Molnar & Ramirez, 1998]. The range of spatial and temporal influence

of several environmental factors are discussed for instance by Montgomery & Buffington [1998]. Finally, note the importance to well-defined the time-scale of observation to assess the equilibrium, in the case of a natural mountainous stream, several tens years.

2.1.1.3 Hydraulic geometry theories

At this intermediate scale (defined above), the intensity and probability of events — flood, bedload transport event or debris flow — are well defined and dependent on the climatic and geologic characteristics. Mean variables, like the water discharge, and geomorphic features could be known and are fairly constant at this scale. Thus, rivers are most of the time considered in stable equilibrium, meaning no significant changes are expected in their geometry. Indeed, geometric scaling laws (“hydraulic geometry”) are found [Leopold, 1953]. They state that an equilibrium between the channel form, sediment transport and water fluxes exists. They give relations between the water discharge Q_l , the mean flow velocity U , the channel width W and depth h and the sediment transport rate q_s as follows:

$$W = a_1 Q_l^{b_1}, h = a_2 Q_l^{b_2}, U = a_3 Q_l^{b_3} \text{ and } q_s = a_4 Q_l^{b_4}, \quad (2.1)$$

with the constant numbers $a_1, a_2, a_3, a_4, b_1, b_2, b_3$ and b_4 . For instance, in a given reach, under certain typical flow and geometry conditions, a particular grain size is expected. These laws are used in fluvial engineering for planning, design and river management. The basic hypothesis leading to these laws is that the river tends to a stable equilibrium.

Geomorphologists used different ways to adapt the concept of equilibrium to more potentially testable concepts [Thorn & Welford, 1994]. Several principles were proposed based on extremal hypotheses — efficiency, optimality, maximization and minimization — of different quantities, such as energy, energy dissipation, stream power, entropy and friction [Singh, 2003]. In terms of energy and physical quantities, the equilibrium concept was initially expressed by the classic Lane’s law [Lane, 1955]. It states that the work used for sediment transport is equal to the available stream power, i.e.

$$q_s d_{50} \propto Q_l \Theta, \quad (2.2)$$

with q_s the bedload transport rate (defined in 2.1.2.1), d_{50} the mean particle diameter, Q_l the water discharge and Θ the mean channel slope. It means that for given grain size, sediment transport rate and water discharge, the channel slope is adjusted to a fixed value to achieve a state of no global aggradation and degradation. This equilibrium was then illustrated as the well-know Lane’s diagram (figure 2.1).

Flume experiments, under steady conditions with uniform sediments, generally show that the channel is in a static equilibrium. After a certain experiment duration, the channel slope stabilized to a fixed value for given experimental conditions [Recking, 2006]. However, for a large grain size distribution, periodic fluctuations in bedload transport rates are observed [Recking, 2006]. This is due to successive accumulations and releases of sediments [Recking, 2006; Recking *et al.*, 2009b] which then lead to fluctuations in bed topography and channel slope. The system can still be qualified in stationary equilibrium at temporal scales larger than the fluctuation time scale. However, if morphological fluctuations of that sort exist at different time-scales, can we still qualify the channel in equilibrium ?

The deviation from the classic concept of equilibrium (Lane’s diagram) was quantified by an efficiency term. This efficiency concept was proposed by Bagnold [1966]. For instance, the equilibrium is not verified for instance by changing the fraction of fine sediments in experiments using a bi-modal grain size distribution [Iseya & Ikeda, 1987]. This can be explained by a change in transport efficiency. Also the channel slope was found to decrease with increasing efficiency [Ikeda & Iseya,

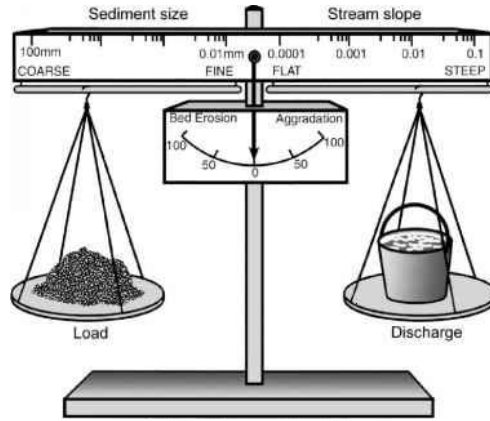


Figure 2.1: Lane's diagram from Brierley & Fryirs [2005], illustrating the relation between the work used for sediment transport and the stream power (equation 2.2). If the equilibrium is not verified, a bed erosion or deposition occurs.

1988]. Thus the equilibrium concept might not be reliable in the case of steep streams where a large and variable grain size distribution is observed. As it will be discussed in this thesis, even with a narrow grain size distribution, the concept of equilibrium is questionable.

2.1.1.4 Stationary equilibrium

Since Lane [1955], the concept of equilibrium was revisited. For instance, Nanson & Huang [2008] incorporate a new adjustable term in the relationship, the channel width to water depth ratio. This allows some fluctuations around a *stationary* equilibrium [Nanson & Huang, 2008]. The instantaneous system state can be different than the stationary state. In fact it is constantly the case, and negative feedbacks, at more or less long-term, tend to bring back the system to its stationary state. For steep mountain streams, the “more or less long-term” has a great importance. Feedbacks might be complex and present at different spatial- and time-scales. Indeed, a succession of positive and negative feedbacks are possible, but at a relatively large temporal scale the global feedback should be negative as the river do not aggrade or degrade continuously. Again, this underlines the effect of the considered time-scale discussed previously.

Next, bedload transport is presented as the variable regulating morphological changes through erosion and deposition and leading to these fluctuations around the stationary state. Also, bedload transport can be seen as the response of a specific channel morphology to external conditions. Due to these complexe interactions in river, I wonder the validity of the equilibrium concept which should be verified taking into account the time-scale.

2.1.2 Bedload transport rate

2.1.2.1 Definition

The term bedload transport represents the solid material in motion at the surface of the river bed. The transport by the fluid occurs by rolling, saltation and sliding. This is the part of the sediment load that really interacts with the bed in contrast to the suspended load. Usually the bedload transport rate is defined physically as a quantity linked to the load of sediments such as the weight, the number or the volume of particles passing through a cross-section of the channel flow per unit of time (for instance see [Allen, 1984]). Other approaches are also used like the number of particles in a reference window or the particle concentration. Several empirical studies

present a multitude of ways to study bedload transport (sections 2.2.1.1 and 2.2.1.2) leading to new approaches to estimate bedload transport rates.

There are different theoretical, experimental and in-situ approaches to determine the bedload discharge. In field investigations, the choice of techniques and computational methods are limited. The nature of field data are generally different from formulations given by theories. The problem is to know if the different approaches are equivalent or how there are linked together [Ancy, 2010]. These questions must be answered to compare theoretical, numerical, experimental and field data. For instance what are the relations between Lagrangian and Eulerian points of view [Ancy, 2010]? Also, the time series recorded at a given location and its statistics might be seen as representative of the spatial fluctuations. However, Heyman *et al.* [2013] shows from precise flume experiments and theoretical work that this assumption might not be valid. Thus, particular attention must be paid when comparing different studies, and particularly with regard to the fluctuations and the statistics.

In the following section, classical concepts about the incipient motion of bedload particles and the link between bedload transport rates and fluid forces are reported. Bedload transport formulation are based on expressions of the fluid force acting on the river bed.

2.1.2.2 Threshold of motion and fluid force: an ideal case

Shields [1936] defined a dimensionless number, called the Shields stress S_h , to represent the relative intensity of the fluid stress acting on a granular bed. S_h is expressed as the ratio of the fluid force on a particle to the weight of this particle,

$$S_h = \frac{\tau_b}{g(\rho_s - \rho)d_{50}} = \frac{\rho h \sin \Theta}{(\rho_s - \rho)d_{50}}, \quad (2.3)$$

with $\tau_b = \rho g h \sin \Theta$ the bed shear stress, d_{50} the mean grain diameter, ρ_s and ρ the grain and water density respectively, Θ the channel slope, and h the water depth. In the bedload transport community, S_h is considered as the major criteria to determine the potential energy of the flow for the entrainment and transport of bedload particles. For instance, S_h is used in many bedload transport equations and allows to situate data relative to other studies, both laboratory experiments and field work. Other studies define a motion threshold on other quantities, such as the stream power [Petit *et al.*, 2005; Ferguson, 2005; Parker *et al.*, 2011], the mean flow velocity or the mean flow discharge [Turowski *et al.*, 2011].

The critical Shields stress S_{hc} is defined as the threshold of incipient particle motion. Many curves, representing S_{hc} as a function of the particle Reynolds number and known as the Shields diagram, have been deduced from experimental study, assuming the validity of the threshold concept based on the work of Shields [1936]. However, some points have not been clarified as some uncertainty and incoherences arise from Shields' work [Buffington, 1999]. The Shields' curve, supported by several data sets, is shown in figure 2.2. Different interpolation have obtained and different ways were used to infer a critical threshold, such as extrapolated transport rates to zero [Shields, 1936] or visual observations of motion [Kramer, 1932]. This reflects the difficulty of observing an unique non-dimensional threshold.

A method of deriving S_{hc} , developed by Recking [2008], might be a more suitable approach than many other work in defining an arbitrary threshold. In this case, the threshold is deduced from the observed behaviour changes in the friction law — occurring when significant bedload transport starts. Although all of these critical stress estimates are not representative of a real threshold of motion, they set a reference stress value for the beginning of significant morphodynamic changes in rivers. However, a special attention must be paid for steep channels as several studies pinpoint the

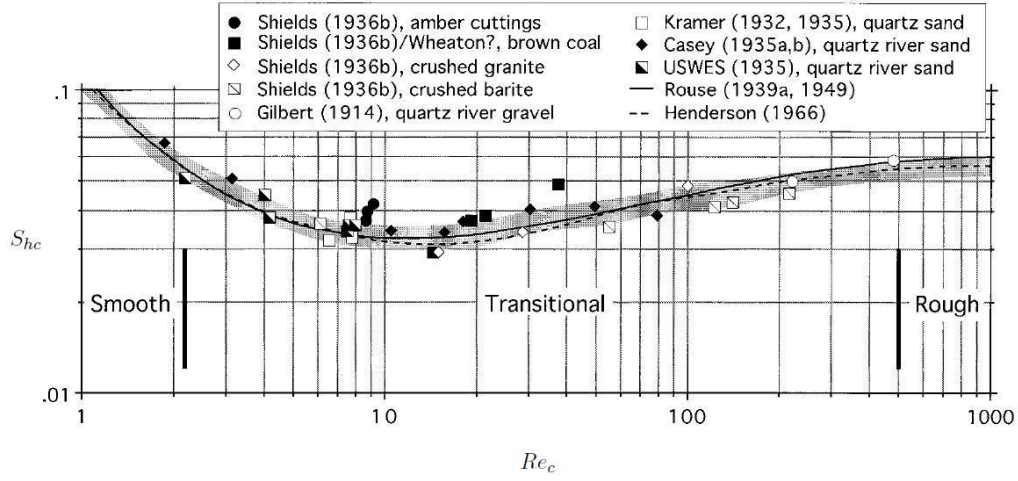


Figure 2.2: Shields' diagram from Buffington [1999]. The observed adimensional threshold for particle entrainment, i.e. the critical Shields stress S_{hc} , is represented as a function of the critical Reynolds number Re_c .

dependence of S_{hc} on the slope [Recking, 2008] (section 2.1.3.4). Even when studying an isolated particle, its entrainment is not clearly related with measurable flow variables as presented in the following.

2.1.2.3 Particle entrainment

In order to understand the reasons behind the imprecise global threshold approach, many efforts have been made to study local processes leading to particle entrainment. Drake *et al.* [1988] found by observations in a gravel-bed river that particles are entrained by rollover or liftoff depending on their size and their surrounding environment. Indeed, certain grain size classes have a higher entrainment rate on finer than coarser areas. Paintal [1971] already hypothesized that the entrainment of grains is due to randomness in turbulence, particle neighborhood, bed packing and surrounding moving particles. The simultaneous measurements of bedload transport and fluid turbulence of Paiement-Paradis *et al.* [2011] show the important role of fluid acceleration and deceleration, inducing pressure fluctuations, on particle motion in a gravel-bed river. The acceleration could be a more interesting variable to determine particle entrainment than shear stresses or normal stresses, at least in certain circumstances [Paiement-Paradis *et al.*, 2011].

Great efforts have been undertaken to find correlations between numerous variables and particle entrainment. Transient forces from local pressure fluctuations have been computed by Smart & Habersack [2007] or particle-scale pressure gradients have been deduced by Schmeeckle *et al.* [2007]. Valyrakis *et al.* [2010] proved that not only the force intensity but also the duration of the force peak is crucial for the entrainment of a single particle. Although many approaches for particle entrainment have been validated in specific configurations, no standard entrainment mechanism have been generalized. Moreover, the relation between local velocities and pressure fluctuations is complex. Schmeeckle *et al.* [2007] show that only low correlations exist between instantaneous lift forces and flow velocities.

Finally, a stochastic approach might help to handle this problem of threshold by defining a probability of entrainment in function of the flow variables. This approach starts as early as 1950 with the work of Einstein, and with recent advances, due to improvement of laboratory experiments

(section 2.3.1). In the next section, only few bedload formulations are presented as they are based on the threshold concept and do not really work in predicting bedload transport rates.

2.1.3 Bedload transport prediction

Bedload equations deduced for lowland rivers generally show low agreement with mountain streams due to the specific morphologies and the wide grain size distribution. Even most common bedload equations developed for mountain streams overestimate bedload transport rates for low to intermediate intensity floods, i.e. frequently occurring floods. Although data still show large scatter, these equations are more efficient for high to exceptional intensity events. This is the case for many steep mountain streams, such as the study site of D'Agostino & Lenzi [1999] in Eastern Italy. Note that a plethora of bedload transport equations exists and their use has to be cautious. The formulations are generally the result of an empirical approach using the concept of entrainment threshold (deterministic or probabilistic). Also some empirical formula have been fitted to experimental or in-situ data leading in some cases to good physical interpretations of the empirical coefficients.

2.1.3.1 Empirical formulations

Many bedload transport data are well described by power laws. More precisely, Paintal [1971] found two power laws of the Shields stress S_h to fit his flume data, one for very low bedload transport rates and one for higher rates. The intersection between the two curves is at $S_h = 0.05$. This shows that bedload transport behaviour is different at very low transport conditions, close to the critical Shields stress S_{hc} , than at moderate to high transport rates.

In the field, it is also shown that regressions of bedload data by a power law are efficient. Barry [2004] proposed a simple regression of the water discharge using a large bedload data set. Considering the characteristics of several sites, their work also suggests that the power law exponent is related to the transport capacity of the channel and the coefficient to the drainage area.

2.1.3.2 Deterministic equations

Many equations have the following form, which is based on the shear stress concept — excess of shear stress $S_h - S_{hc}$,

$$\Phi = A_c S_h^a (S_h - S_{hc})^b, \quad (2.4)$$

with Φ the adimensional bedload transport rate defined by Einstein [1950],

$$\Phi = \frac{qs}{W\rho g} \left(\frac{\rho}{\rho_s - \rho} \right)^{0.5} \left(\frac{1}{gd_{50}^3} \right)^{0.5}. \quad (2.5)$$

W represents the channel width. a , b and A_c are theoretical constants. However, many different values have been found by different authors and also depending of the river type.

Probably the most well-known equation is the Meyer-Peter & Muller [1948] formula which is nowadays still widely used for bedload transport estimates:

$$\Phi = 8(S_h - 0.047)^{3/2}. \quad (2.6)$$

Several improvements have been proposed based on this formulation, for specific conditions. The width of the grain size distribution is taken into account in Smart [1984] formula. The Rickenmann [1991] equation was developed for high bedload transport rates in steep streams. Other formulations are based on the ratio S_h/S_{hc} for instance, or others take into account the sub-surface grain size or the full surface grain size distribution [Wilcock & Crowe, 2003]. Two classic bedload transport

formulations which might work with my data are presented in the following, one is probabilistic and the other is developed for high transport as well as low transport conditions. They are tested with my data in section 4.1.1.3.

2.1.3.3 Einstein bedload function

The Einstein bedload function is the first probabilistic formulation of bedload transport and is still the base for recent stochastic approaches. Einstein [1950] defined another non-dimensional variable relative to fluid stress acting on the bed,

$$\Psi = \frac{\rho_s - \rho}{\rho} \frac{d_{50}}{h \sin \Theta_w} = \frac{(\rho_s - \rho)gd_{50}}{\tau_b}. \quad (2.7)$$

The following stochastic relation was determined:

$$1 - \sqrt{\pi} \int_{-B\Psi-1/\eta_0}^{B\Psi-1/\eta_0} \exp -t^2 dt = \frac{A\Phi}{1 - A\Phi}, \quad (2.8)$$

with $\eta_0 = 0.5$ a parameter accounting for fluctuations in lift forces close to the gravel bed and A and B two universal constants taking values of 27 and 0.156 respectively.

2.1.3.4 Recking bedload formula

Recking [2010] tried to bridge the gap for low transport rates. He derived two equations for low and high transport regimes respectively. The Recking [2010] bedload formula is composed of two expressions, one for the partially mobile grains regime and one for the fully mobile grains regime,

$$\Phi = 15.6(S_h - S_{hc})^2 \text{ if } S_h < 0.65\Theta^{0.41} \quad (2.9)$$

$$\Phi = 14S_h^{2.45} \text{ if } S_h > 0.65\Theta^{0.41} \quad (2.10)$$

where S_{hc} is defined by:

$$S_{hc} = 0.15 \tan(\Theta)^{0.275}. \quad (2.11)$$

This equation shows the influence of Θ on the value of S_{hc} and comes from a friction analysis of more than 2000 flume and field data points [Recking *et al.*, 2008].

2.2 Measurements, processes and their variability

To better understand the origins of the hypothesis and formulations presented in the previous section, it is necessary to display the classical measurement techniques used in river morphodynamics and the results of the main measurement campaigns. The emergence of new innovative measurement approaches, especially in lab experiments, give the possibility to test and improve classical assumptions. As the fluctuations in bedload transport rates have been reported through a wide range of time-scales, the duration and the resolution of the data is of essential importance. Here, after presenting measurement methods, I synthesize several descriptions of these fluctuations. Although several explanations have been suggested to explain bedload transport fluctuations, no global concepts have been proposed for steep streams. Finally, in this section, I detail knowledge of river bedforms which is seen as one of the main causes leading to bedload transport fluctuations. Moreover, bedform migration intuitively may interact more or less directly with the global evolution of the river. This last point, i.e. interactions between morphologies at different spatial-scales, has to be emphasized in this section and will be developed further in this thesis.

2.2.1 Measurements in steep channels

Field observations are essential in the sense that they should be the representation of the natural world. They are, neglecting measurement uncertainty, what the scientific community wants to understand, model and predict. On the other hand, laboratory work is useful to investigate a given issue or decompose a complex problematic into simpler processes with the help of precise data. In parallel, theoretical studies develop certain aspects that can be analyzed using measurements. Altogether, the different types of data allow the verification of predictions and numerical simulations.

In this section, the measurement techniques to study of channel morphodynamics are introduced. An overview of classical measurement techniques is presented, underlining the difficulty of collecting data, especially in steep channels. Due to the challenging issue to accurately measure bedload transport rates, many methods have been tested and no standard techniques exist. Then, the interest of laboratory measurement is emphasized. Finally, new approaches and concerns in morphodynamic measurements are briefly discussed.

2.2.1.1 In-situ investigations

Most of the classical measurement methods used in lowland rivers are not transferable to steep streams studies. Here, techniques applicable in mountain rivers are summarized and new alternative approaches are presented.

Classical techniques

Bed topographies in subcritical flows, like ripples, dunes and large sinuositities (section 2.2.3) are relatively well-studied. These bedforms are present in many easily accessible lowland rivers. Also in this case, bathymetric surveys and laboratory measurements are much more readily performed than in the supercritical case. Deep water relative to grain size and bedform height, in large- and gentle-slope rivers, generally permits intrusive measurements without perturbing the flow and bedload transport.

Topographic measurements are possible using acoustic transducers that detect the change of medium. If the apparatus is at the free surface, the interface between a bed particle and the flowing water is captured, and this allows accurate measurements [Carling *et al.*, 2000; Parsons *et al.*, 2005; Abraham *et al.*, 2011]. Also recording images from the top (using a helium balloon for instance, McElroy & Mohrig [2009]), showed the possibility of obtaining topographic data from luminosity patterns on the images. However, in mountain streams, the same techniques cannot be deployed due to the harsh environment, important free surface effects, and small relative depth. The measurements have to be made manually or by airborne photogrammetry during low flow periods. These techniques are expensive and one-time, and not able to accurately study the evolution. Solutions to fill this measurement gap are still sought, which are more accessible via conducting laboratory experiments (section 2.2.1.2).

In mountain streams, classical standardized methods for measuring bedload transport rates have been tested — Helley-Smith sampler [Helley & Smith, 1971] or Birkbeck pit bedload samplers [Reid *et al.*, 1980]. For instance, Hassan & Church [2001] showed, using pit trap data, the presence of a partial transport regime in a cobble-gravel stream dominated by snow-melt events. In Lenzi *et al.* [1999], bedload transport characteristics in a small catchment are presented from continuously monitored data. A large installation has been built using grids and collecting basins to separately measure the water discharge, and the fine and coarse sediments. Birkbeck-type pit bedload samplers also allow continuous and high-frequency bedload measurements but are limited by the size of the sampler. Garcia *et al.* [2000] show that this system works well in a Mediterranean mountain gravel-bed stream with longitudinal slope of 1° . However, these methods do not permit to record

long time series at high resolution. Indeed, Bunte & Abt [2005], using bedload traps and Helley-Smith samplers, underline the necessity to collect bedload transport data for a relatively long time, especially at low transport rate conditions.

Video recording is a very interesting technique, as it is a direct observation of moving particles. Particularly, the improvement in image processing allows accurate measurements. Although experiments using a camera are challenging to carry out in the field, Drake *et al.* [1988] used one to quantify particle motion in a gravel bed stream. Although this approach is not suitable for long measurements, it was efficient to describe and quantify the different types of bedload motion. Nowadays imaging techniques are well developed in laboratory experiments as described in section 2.2.1.2.

Indirect bedload technics

Many methods have been tested in the investigation of bedload transport processes, some permitting to deduce bedload transport rates indirectly. Particularly, techniques to follow particles have been developed, from active tracers [Mikos & Spazzapan, 2006] to Passive Integrated Transponders [Lamarre *et al.*, 2005; Liebault *et al.*, 2012] and magnetic particles [Bunte, 2010]. The corresponding studies give particle behaviours, like trajectories, displacements and rest periods. However, high-resolution bedload transport rates cannot be measured because of the limited number of tracers used. Although local mechanisms of particle erosion can be deduced, these methods do not inform about global evolution mechanisms.

Another interesting technique is detailed as it is used on the Navisence River site and it permits continuous measurements at high temporal resolution. The energy transmitted to the bed by the impacts of moving stones was demonstrated to be an interesting indirect variable in estimating bedload transport rates. This energy is measured, for instance, by geophones — basically sensors recording vibrations — via metallic plates set into the channel bed [Turowski *et al.*, 2011]. Correlations between the mean energy generated by bedload transport and geophone signals are then established. The response of geophones depends on multiple factors like grain size, grain speed, grain shape and their impact angle. Moreover, at highly concentrated bedload transport, a damping effect is present due to the increasing bedload layer depth. Thus, many particles may not impact directly the sensors. However, the total energy received by the bed gives continuous information of the sediment transport in the field. For instance, the start and end of bedload transport and its standard deviation can be deduced from the analysis of this type of data [Turowski & Rickenmann, 2011; Turowski *et al.*, 2011]. Although this type of data is of great interest, only a few monitoring stations exist as their construction is expensive. More work is needed to obtain more accurate instrument calibration, for instance, by conducting laboratory flume tests of these sensors.

Finally, other approaches can be cited, using recordings of sound of particle collisions by hydrophones [Belleudy *et al.*, 2010] or ambient seismic noise Burtin *et al.* [2008]; Hsu *et al.* [2011]; Tsai *et al.* [2012] to measure bedload transport rates. However, successful high-resolution calibrations have not yet been carried out for these techniques and might depend on temporal changing conditions and characteristics of each site. That is why laboratory techniques are still promising to study accurately and continuously bedload processes at lower cost.

2.2.1.2 Laboratory experiments

As in-situ measurements are difficult to conduct, in particular for long duration and high accuracy investigations, laboratory experiments provide essential alternative and complementary approaches for studying morphodynamic processes. Although such experimental setups are an idealization of the natural phenomena, scientists are able to control and measure processes separately,

leading to a more complete understanding of the phenomenon. The main objective of new techniques development is the production of extensive data from easy-to-use and low-cost installations.

Controlled and idealized situations

In the laboratory, parameters are well controlled in order to study bedload transport under chosen conditions. Parameter adjustments are possible for grain size, channel divagation, bed slope, flow conditions and sediment supply. For instance, the case of steady flow can be studied before interpreting a hydrograph. It is essential to understand the simplest conditions, even if they do not appear in nature. These ideal cases are also very useful for the validation of numerical models in simple situations, as opposed to applying them directly to situations where accurate measurements do not exist.

Laboratory experiments in wide flumes under controlled conditions also give the opportunity to verify the efficiency of classic bedload measurement techniques and to test new methods. Weighing pans are still widely used for measuring the exact quantity of sediments leaving the flumes. Coupled with an automatic sampling device, long time series at high sampling frequencies are obtained [Singh *et al.*, 2009].

Accurate measurement techniques

Camera recordings and image processing techniques are now widely used in laboratories to study sediment transport and, more generally, fluid mechanics issues. These techniques give high temporal and spatial resolution of data. Particle Tracking Velocimetry (PTV) allows the computation of the trajectory of each particle using detection and tracking algorithms. With this increasing measurement accuracy, the statistics of the variables are well known. Roseberry *et al.* [2012] detected particle trajectories from a plan view in subcritical regime. Ancey *et al.* [2006] used a steep and narrow flume with a movable bed of glass beads to track particles with an automatic routine from side-view camera recordings. It was found that the probability density function of moving particles follows the negative binomial distribution in a given window. PTV experiments show very impressive accuracy but are limited by the time length of measurements and sometimes by the fastidious work necessary to accurately reconstruct the trajectories. To overcome this problem, Frey *et al.* [2003] developed a method recording images at the outlet of a flume and simultaneously processing the bedload transport rate and the grain size distribution.

Finally, no standard laboratory and field measurement techniques exist. Also no low-cost, continuous and accurate methods are available, even for simple laboratory experiments. Aiming to obtain this accuracy with simpler technology, I developed a technique based on the record of particle impact, similarly than the geophone sensors (section 2.2.1.1) but, here, it was possible to count every movable particle (section 3.1.3).

Also no continuous and systematic elevation observations of steep channels are available. However, this information is essential in explaining the fluctuations observed in bedload transport (section 2.2.2). This lack of morphological data is also solved by the experimental installations designed in this work.

2.2.2 Bedload transport variability

In many studies related to sediment transport, bedload transport rate qs shows wide fluctuations in time and space. It is admitted that, with an higher water discharge Q_l , a higher qs is expected. However, the correlation between Q_l and qs is weak [Garcia *et al.*, 2000]. This relation depends on numerous parameters and on the watershed characteristics [Recking, 2010].

The coefficient of variation Cv is a simple parameter to quantify the variability of a time series. Cv for bedload transport is defined as

$$Cv = qs_m/s, \quad (2.12)$$

with qs_m the mean bedload transport rate and s the standard deviation of qs . Note that Cv is greatly dependent on the time scale, in other words on the sampling time [Fienberg *et al.*, 2010].

Mountain streams, during periods of low sediment transport, show the largest bedload fluctuations [Ancey *et al.*, 2006]. This variability of bedload transport was observed in laboratory flumes in steady conditions [Ancey *et al.*, 2008]. Several factors to explain these fluctuations have been suggested, such as sediment sorting, bedform migration, sediment availability, turbulence intermittency and granular interactions. Depending on the watershed and the studied river, these causes might have different importance. Also, there are certainly feedbacks between these causes, such as sorting creating bedforms, bedforms implying turbulent eddies or a failure in the granular bed leading to an increase of available sediment. As it will be presented in the following section, several authors reported the existence of collective motion events. Local mechanisms were described, which might explain large fluctuations in bedload transport rates.

Finally, note that much of the data were collected, particularly in the field, under non-stationary and non-uniform flow conditions. This may be one of the reasons of the large observed scatter in bedload data. The influence of these non-steady conditions are also briefly discussed thereafter. The important observations and results on bedforms will be more developed in the next section. As in my experiments, well-sorted sediments are used, the case of sediment sorting is not presented here. We may refer to [Brayshaw, 1985], Iseya & Ikeda [1987], Drake *et al.* [1988], Gomez [1991], Powell [1998], Radice *et al.* [2009] and Recking *et al.* [2009b] who discuss about the great dependence of the grain size distribution on particle motion and bedload transport rates.

2.2.2.1 Hydrograph characteristics

The temporal and spatial variability of qs is present for a given river even during a single flood event. In particular, Hassan & Church [2001] observed seasonal hysteresis of bedload transport, in a watershed dominated by snow melt events, with higher qs in spring than at the end of the summer (for the same water discharge Q_l). During a single flood, hysteresis have also been observed both in the field [D'Agostino & Lenzi, 1999] or in laboratory experiments [Lee *et al.*, 2004]. In certain cases, qs is higher during the rising limb than the falling one [D'Agostino & Lenzi, 1999; Mao, 2012] which is explained by higher turbulence intensity in the rising stage [Nezu & Onitsuka, 2001]. Contrary, Lee *et al.* [2004] observed that bedload transport was larger during the falling stage as the maximum size of bedforms occurs after the peak flow [Griffiths & Sutherland, 1977]. However, Martin & Jerolmack [2013] argue that the hysteresis between bedform evolution and Q_l depends on the time scale of the bedform response relative to the flood characteristics. Recently, it was shown that, for a given system, various hydrograph duration and intensity change the magnitude and the sense of the hysteresis [Heyman *et al.*, 2013].

2.2.2.2 Sediment supply

In bedload transport equations, the quantity of sediment available for transport is generally not accounted for. However, this parameter has a huge influence especially when the transport capacity of the stream, i.e. the available stream power for transport, is larger than the sediment availability [Montgomery & Buffington, 1997]. Rock avalanches, hill slope instabilities, debris flows and general watershed weathering play an essential role on the sediment availability for bedload transport. In addition, in mountain areas, it has been observed that for the same Q_l , qs is higher at the beginning of the high flow season than at the end of the summer [Hassan & Church, 2001]. This might due to a large quantity of available loose sediments after thawing.

In experimental studies, a significant influence of sediment supply, on bedform growth and fluctuations in qs was reported. Kleinhans [2005] shows two interesting points. First, in recirculation flumes — outlet solid discharge is directly re-injected at the inlet — the dune height is smaller than in feed flumes — imposed solid discharge at the inlet. Second, the dune irregularity is less important in recirculation flume because of the formation of a coarse layer. With limited sediment availability, for instance in the case of an armor layer, qs and the bedform characteristics are strongly dependent on the inlet sediment rate and its fluctuations [Kleinhans *et al.*, 2002].

2.2.2.3 Collective motion

Drake *et al.* [1988] demonstrated that more than two thirds of the bedload transport occur during a certain type of turbulence event called sweep-transport events, although these events are only present 9% of the time. On their gravel bed study reach, they observed that locally many particles are entrained together during a short time. Several other reasons have been proposed to explain these collective motion events, such as the reduction of the critical angle of stability for grains sheared by a fluid [Loiseleux *et al.*, 2005], the presence of turbulent eddies that can dislodge several particles quasi-simultaneously [Papanicolaou *et al.*, 2002], the shock by a moving particle or also the migration of bedforms where locally the entrainment rate is higher. All of these causes induce correlations either in the turbulent flow [Drake *et al.*, 1988; Dinehart, 1999], in moving particles [Ancey, 2010; Heyman *et al.*, 2013] or in bed topography [Singh *et al.*, 2009].

These approaches have been proposed to explain some characteristics of bedload transport fluctuations. However, no physical general description at several spatial- and time-scale have been found. In the next section, state of the art in stream morphology is synthesized as the starting point to understand stream evolution from local scales to global scales.

2.2.3 Bedform formation and migration

Depending on the flow regime, the grain size distribution of the bed and sediment transport intensity, different morphological patterns possibly appear at the bed surface of mountain streams. In a review of the extensive stability and morphodynamics analyses, Mazumder [2003] presents seven bedform states, ripples, lower stage plane beds, pebble clusters, bedload sheets, dunes, upper stage plane beds and antidunes. Their height varies from plane bed to steep steps. Their longitudinal extension range is wide from small particle clusters to long bars and riffles — with a spatial scale of several times the channel width. Their presence depends on external parameters which change over time in natural environment. Thus, these morphological features constantly evolve in the channel [Mazumder, 2003]. Moreover, even for a given set of parameters, most of time they are in a dynamic state as they induce interactions with the flow and moving sediments — except when they are frozen in a given state due to the decrease of the flow strength.

As they regulate the response of the stream to different environmental conditions, the bedform shape and their migration might have important impacts on the global evolution of the stream. First, the different morphological features present in steep channel are described. Second, their migration and their implication in channel evolution processes are introduced. Besides, the lack of mechanisms of describing steep-channel evolution is underlined.

2.2.3.1 Bedforms in steep streams

The Froude number $Fr = U/\sqrt{gh}$, the dimensionless ratio of the flow characteristic velocity to the gravitational wave velocity, allows to characterize the flow regime. For $Fr > 1$, the flow, often named *steep* flow, is supercritical with information travelling downstream on the free surface, whereas for $Fr < 1$ the flow is subcritical with information propagating upstream. In steep channels and in steep sections of mountain rivers, the flow is frequently supercritical or around critical, i.e.

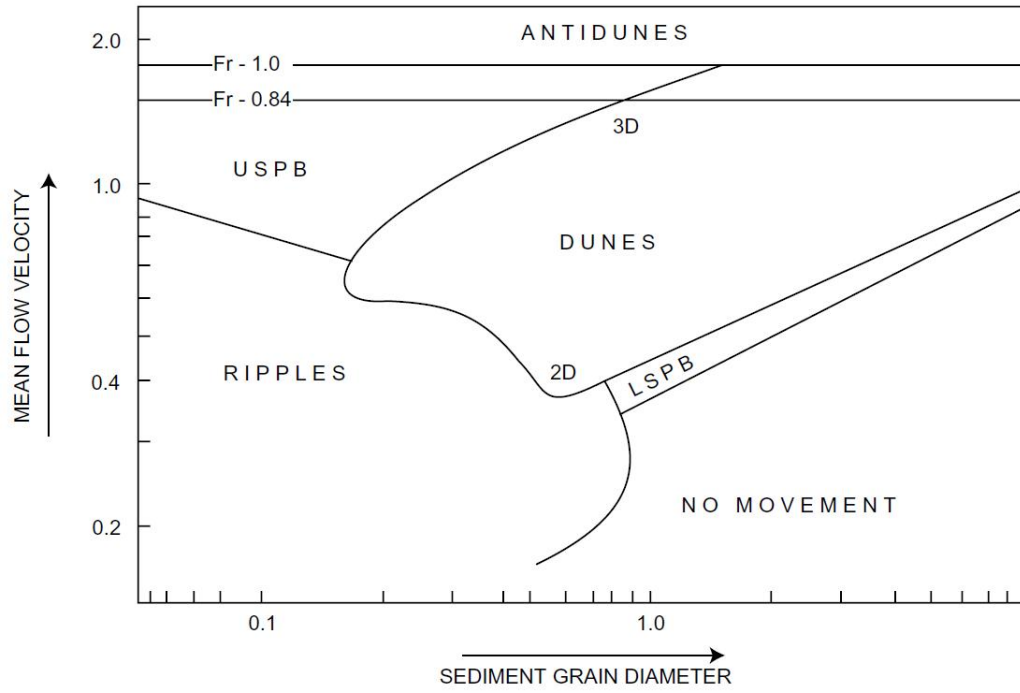


Figure 2.3: Bedform diagram from Mazumder [2003] showing the existence domains of the main types of bedforms observed in rivers as functions of the mean flow velocity U and the mean grain diameter d_{50} (USPB = upper-stage plane bed and LSPB = lower-stage plane bed). Note the presence of antidunes in steep slope flows, i.e. at large Froude number Fr .

with a Froude number $Fr \geq 1$. The flow shows stationary waves and temporary hydraulic jumps that modify the local erosion creating bed patterns nearly in phase with the flow surface [Kennedy, 1969; Alexander, 2008]. Two common bedform types are observed in this type of configurations, antidunes and cyclic steps — including step-pool morphologies — that can appear together or not [Alexander, 2008].

Microforms and isolated morphologies

Although not all bedforms in gravel bed channels have a well defined shapes, they can have large effects on energy dissipation and stability (section 2.3.3.1). This can be simply illustrated by the large energy dissipation due to a big boulder with a characteristic size of the same order of magnitude as the water depth [Yager *et al.*, 2007; Ghilardi & Schleiss, 2012]. Also all types of microforms, pebble clusters and reticulate structures can dissipate large amount of energy. Generally these microforms are well-developed in partial bedload transport conditions, i.e. for $S_h \leq 2$ [Church *et al.*, 1998; Strom *et al.*, 2004] and are linked with strong fluctuations in bedload transport rates.

Step-pool morphologies

Step-pool sequences appear mainly in steep, narrow mountain streams with mean slopes ranging from 2° to 17° [Weichert, 2006]. Church & Zimmermann [2007] proposed the jammed state hypothesis to define the conditions of step formation based on three characteristics of the stream: the jamming ratio, the relative Shields stress and the bed sediment concentration. These steps temporarily stabilize the stream bed for many frequent events, and are rearranged only during large hydrological events [Turowski *et al.*, 2009; Molnar *et al.*, 2010]. Just after a large magnitude event, sediment transport occurs for lower flood intensity than before due a less rough channel bed. Indeed, the stream need a few of competent floods to rebuilt its stable steps [Turowski *et al.*, 2009]. This emphasizes the influence of local morphologies on the stability of the entire stream profile. It seems that there is a kind of threshold overrun leading to important stream changes. In this work, I will partly focus on this concept of threshold in different other situations — antidune case, thresholds on other variables and with well-sorted sediments.

Antidunes

In contrast to the downstream migration of the dunes and ripples in low-land rivers, antidunes can propagate in the upstream direction — historical definition of Gilbert [1914]. Erosion, and deposition, occur on the lee side, and the stoss side, of the antidune respectively. This is due to a slight acceleration or deceleration of the flow as described in section 2.2.3.2. Nowadays, it is commonly admitted to define the term antidune for any bedforms that are in phase with the free surface [Recking *et al.*, 2009a]. Effectively, some experimental and theoretical works show that antidunes also possibly migrate downstream or are stationary [Kennedy, 1969; Nunez-Gonzalez & Martin-Vide, 2011].

Most of the time, antidunes appear only in supercritical flows ($Fr > 1$), although apparently they could sometimes form for a froude number slightly lower than one in particular conditions [Mazumder, 2003; Nunez-Gonzalez & Martin-Vide, 2011]. In natural streams, the presence of constantly supercritical flow is rare as underlined by Grant [1997]. Thus, antidunes are only present in specifically steep reaches [Recking *et al.*, 2009a].

Antidunes are relatively poorly studied. Although they are not rare, their observation is difficult in the field. Generally, antidunes appear for a relatively short time or in harsh conditions, either during very high flows on intermediate slope or during moderate flow on steep slope streams, usually during the rising or falling stage of a flood event. However, several antidune studies were conducted in flumes [Kennedy, 1963; Alexander, 2008; Recking *et al.*, 2009a; Nunez-Gonzalez & Martin-Vide,

2011]. Several equations relating antidune geometry to flow characteristics can be cited, such as the following one from Kennedy [1961]:

$$\lambda = \sqrt{2\pi}U^2/g. \quad (2.13)$$

Also the domain of antidune existence was analytically determined by the two following equations [Kennedy, 1961; Reynolds, 1965; Parker, 1975], for the upper and the lower limits respectively:

$$Fr^2 = \frac{\tanh kh}{kh} \text{ and} \quad (2.14)$$

$$Fr^2 = \frac{1}{\tanh kh \cdot kh}, \quad (2.15)$$

with $k = H \frac{2\pi}{\lambda}$ the wave number and Fr the Froude number.

2.2.3.2 Flow over bedforms

The turbulence over dunes in fluvial conditions has been extensively investigated. The results show a separation of the flow on the lee side of the dunes [Nelson *et al.*, 1993], implying a zone of large energy dissipation. This induces the deposition of all of the particle on dune lee side. On the contrary, in a supercritical flow the water level is quasi in phase with the bed level. There is only a light contraction in the trough of the antidune associated with acceleration flow on the lee side and deceleration flow on the stoss side. No flow separations have been observed in the case of non-breaking antidunes [Nunez-Gonzalez & Martin-Vide, 2011]. Thus, it is often assumed that antidune bed and plane bed have approximately the same bed resistance [Engelund & Fredsoe, 1982].

In some cases, a cyclic behaviour of antidune growth and obliteration (breaking antidunes, [Alexander *et al.*, 2001]) is observed. The antidune grows until a critical condition, depending on Fr and leading to the appearance of a hydraulic jump, is reached. The hydraulic jump changes the flow field, which implies changes of the locations of particle erosion and the local sediment transport rates. This leads to the obliteration of the antidune. However, a hysteresis in the flow keeps the hydraulic jump presence until the antidune is seriously obliterated, i.e. for a critical condition different than in the antidune growth regime [Deigaard, 2006]. The cycle restarts when the hydraulic jump finally disappears. Thus, in this case of breaking antidunes, strong changes in flow field, energy dissipation and sediment transport are observed through time and space. This is certainly a mechanism that partly explain bedload transport rate fluctuations and might have consequences at larger scale than the antidune scale. In the next paragraph, the important effects of these bedform migration is exposed.

2.2.3.3 Bedform migration and channel evolution

In the case of grain clusters and microforms, no migrations were observed. These kinds of bedform are created and destroyed by particles deposition and erosion, creating zones of preferential deposition or erosion — collective motion. In the case of step-pool morphologies, the destruction of a step (by a strong flood) lead to the propagation of an upstream-migrating degrading wave, similarly to certain type of antidunes (mechanisms developed in chapter 6). On the contrary, sediments accumulates upstream of a stable step during lower competent flow, especially if the step is recent. Finally antidunes can propagate downstream or upstream, or are stationary depending on the flow and channel bed characteristics.

Antidune migration direction

In supercritical flows, it is known that the information in the flow only migrates downstream. However, the propagation of information on the bed surface can be in both downstream and upstream directions as the processes are driven by erosion and deposition patterns. In most cases,

antidunes and cyclic steps, are observed to migrate upstream [Parker & Izumi, 2000; Recking *et al.*, 2009a]. In a few cases, antidunes can also migrate downstream [Carling & Shvidchenko, 2002; Nunez-Gonzalez & Martin-Vide, 2011].

Nunez-Gonzalez & Martin-Vide [2011] developed a theory to predict the antidune migration state that is downstream or upstream migrating, or stationary, as a function of the wave number k and the Froude number Fr . The corresponding dimensionless number, the antidune mobility number F_a , writes

$$F_a = kFr \text{ with } k = H \frac{2\pi}{\lambda} \text{ and } H \text{ the antidune height.} \quad (2.16)$$

The migration is upstream for $F_a < 1$ and downstream for $F_a > 1$. At the transition $F_a = 1$, antidunes are stationary.

Generally, antidunes are quite ephemeral with a period of growing followed by destruction which leads to local fluctuations in bedload transport rates. They usually migrate in train of antidunes which itself migrate downstream due to the global downstream advection of sediment. In my experiments, I only observe upstream migrating antidune, but their shape and height are changing through time. An important research question is if these parameters influence the migration celerity and the capacity of the channel to advect sediment.

2.3 Stream equilibrium? Recent concepts and hypotheses

In the previous sections of this chapter, I underline that no standard threshold of incipient motion of particles can be defined, no proof of strict stream equilibrium exist and no general description of processes explaining bedload transport rate fluctuations have been determined. In my experiments, I will take into account these points, not assuming that the channel bed should strictly tend to an equilibrium and focusing on general behaviours in steep channels — no specific cases. First of all, the physical description of an equilibrium (section 2.1.1.1) and its application in river to develop new hypotheses of evolution is discussed.

In the river case, the physical approach suggests that all the particles at the surface of the river bed are in a metastable equilibrium — physical sense (section 2.1.1.1). Every particle is likely to be dislodged by a more or less strong perturbation and to evolve towards a new equilibrium by settling further downstream in the channel. This new equilibrium is more stable in the sense that the particle elevation is lower (lower potential energy), but it does not mean that the particle might not be easily dislodged again.

At the river reach scale, interpretations are more complex as the system shape changes. However, a first physical description of the river system can be drawn. Through the aggradation and degradation of particles, the system change its *potential energy*. Accumulation of sediment in the system increases its global potential energy as the elevation increases. This energy can be *potentially* released in the future when perturbations allow entrainment of sediment, leading to the transformation of the potential energy into kinetic energy. The latter is then dissipated along the channel by friction. Similar processes were observed in granular systems in which the larger sediment accumulations occur, the easier and stronger sediment releases are expected [Chevoir, 2008]. However, in geomorphological systems, the quantification of energy is complex, and the concepts of physic might not be directly used.

One way to circumvent this issues of energy quantification and threshold definition is to use a probabilistic description of the events that can occur in a river. The advantage is that events can be defined at different spatial-scales. Then, introducing granular concepts in fluvial transport can

aid the understanding of steep stream morphodynamics. Finally, several equilibrium aspects are taken from the broader domain of geomorphology to formulate hypotheses about stream evolution.

2.3.1 Stochastic theories

Lavelle & Mofjeld [1987] argues that the notion of threshold is subjective and unnecessary to understand bedload transport processes and derive bedload equations. The problem have to be hold in a stochastic way using distributed variables for stresses and particle thresholds. Indeed, the high intermittency in the boundary layer due to turbulence can move an isolated grain even for a very low mean Shields stress, as low as one order of magnitude below commonly used critical Shields stress [Neill & Yalin, 1969]. A large body of observations and measurements gives some evidences that motion of grains are random in space and time, especially at low shear stress [Paintal, 1971; Lavelle & Mofjeld, 1987]. These observations prevent from observing a defined and objective threshold. This also underlines the importance of the frequency and the duration of measurements to draw correct interpretations.

The first stochastic formulation for bedload transport was made by Einstein [1950] (section 4.1.1.3 for equations). Later, many stochastic formulations have been proposed [Hamamori & Laboratorium, 1962; Carey & Hubbell, n.d.]. The stochastic approach has been reinvestigated recently to specifically describe the bedload variability in steep channels [Ancey *et al.*, 2008; Lajeunesse *et al.*, 2010; Turowski, 2010; Ancey, 2010; Furbish *et al.*, 2012; Heyman *et al.*, 2013]. Ancey *et al.* [2008] model the different particle fluxes within a fixed window using stochastic variables parameterized by erosion, deposition, emigration and correlation (called collective motion parameter) parameters. The results of this model, using the stochastic Exner equation (mass conservation, [Exner, 1925]), are in agreement with experiments conducted in a 1D flume with glass beads [Bohm *et al.*, 2004]. It was showed that the variance of the bedload transport rate is larger than the mean, i.e. that extreme events are relatively frequent [Ancey, 2010; Heyman *et al.*, 2013].

2.3.2 Granular concepts

Here, the discussion is limited to granular solids where the grains are stationarity between each other (when no external forces act on the media) and the stresses are distributed through force chains in the media. Mainly studies aimed to observed and understand granular flow, i.e. the interactions between grains when subjected to external forces and the behaviour consequences on the media. Recent findings highlight the important presence of grain-grain interactions in stream bed more than it was thought. In classical fluvial transport, bedload transport occurs mainly by erosion of individual particles by the flow. From granular concepts, for instance, shocks by moving particles could erode particles from the bed granular media or changes in force direction and intensity in the media could lead to destabilization and failure. Granular behaviours are inherent to bedload transport, especially for steep streams where the effects of gravity on sediment became stronger.

This new approach studying bedload transport as a granular phenomenon was recently introduced [Frey & Church, 2011]. Equilibrium in granular systems has been extensively studied and might help our understanding in river evolution as discussed in the following sections. River system might show morphodynamics behaviours similar than geomorphologic systems, like grain pile or landscape evolution.

Armoring and bed dilatation and contraction are granular behaviours related to sorting [Marquis & Roy, 2012]. An armor layer, i.e. a coarse grain layer at the surface of the bed, prevents particle erosion while the flow intensity is not sufficient to entrain the coarser particles. However, when the armor layer starts to be eroded, a sudden degradation of the bed is generally seen leading to an abrupt increase of bedload transport. Marquis & Roy [2012] show that some areas of a gravel bed

are subject to successive contractions and dilations. When the bed is in a contracted state, the particle erosion is more difficult due to the tight packing. Contrary, in a dilated bed area, single particle entrainment is easier due to the looser grain arrangement. The work of Marquis & Roy [2012] also suggest that contraction is the result of the entrainment of the fine sediment part in the bed (winnowing) and dilation is the infiltration of the fine sediment part in the granular matrix.

Finally, several physical analogy between fluvial and granular behaviours are reported. Bouchaud *et al.* [1994] found that the bedforms on the profile of the grain pile migrate uphill, similarly to upstream migrating antidunes (at a velocity proportional to the density of rolling grain). Thus, the analogy between the steep channel and the grain pile might improve our understanding of mountain river morphodynamics. Along the grain pile profile, there is always few locations where grains are close to their mechanical stability. While Γ_c , the critical angle of stability of the pile, is not reached and no strong perturbations are imposed, these local instabilities cannot propagate to destabilized the whole pile. Similarly, antidune lee side might be see as potential locations of instabilities. Also in step-pool streams, the steps are steep local instabilities (up to 60° , [Milzow *et al.*, 2006]) that are reorganized during high floods, destabilizing the whole channel [Milzow *et al.*, 2006].

2.3.3 Equilibrium in geomorphology

In geomorphology, sediment transport is the mediator between environmental conditions and the landscape as it is in the river case. In physics, concepts have an exact mathematical expression, which allows strict definitions. In geomorphology, concepts are often qualitative which explains the numerous proposed principles and the difference senses given to the common linguistic terms [Thorn & Welford, 1994]. Equilibrium concepts must be precisely tackled with respect to data to avoid confusions between studies.

At the human time scale, many geomorphic systems are considered to be in equilibrium from qualitative observations (section 2.1.1). This might be intriguing because of the strongly perturbed environment of geomorphologic system. However, the hypothesis of equilibrium seems correct when no trend are detected. Jerolmack [2011] argues that in these geomorphologic systems, the fluctuations in external forces might be too short to cause changes at the system scale. This suggests that the perturbed environment of the system could induce its stability from internal behaviours that buffer external perturbations. The question of equilibrium depends then on the time- and spatial-scales of the studied system as well as the intensity and the time-scale of the external forces.

2.3.3.1 Equilibrium and stability in steep streams?

First, in the river case, the physical definitions (2.1.1.1) suggests that all of the particles at the surface of the river bed are in a metastable equilibrium. Every particle is likely to be dislodged by a more or less strong perturbation and to evolve towards a new equilibrium by settling further downstream in the channel. This new equilibrium is more stable in the sense that the particle elevation is lower (lower potential energy), but it does not mean that the particle might not be easily dislodge again.

Second, at the river reach scale, interpretations are more complex as the system shape changes. However, a first physical description of the river system can be drawn. Through the aggradation and degradation of particles, the system change its *potential energy*. Accumulation of sediment in a river system increases its global potential energy as the elevation increases. This energy can be *potentially* released in the future when perturbations allow entrainment of sediment, leading to the transformation of the potential energy into kinetic energy. The latter is then dissipated along the channel by friction. Similar processes were observed in granular systems in which the larger sediment accumulations occur, the easier and stronger sediment release is expected [Chevoir, 2008].

However, in geomorphology, the quantification of energy is complex, and the concepts of physics could not be used directly.

In step-pool streams, it has been observed that large reorganizations of the steps occur during exceptional events, such as more than 40-years return period events [Whittaker, 1987; Lenzi, 2001; Turowski *et al.*, 2009; Molnar *et al.*, 2010]. During these events, the channel stability is broken by the destruction of one or several steps. These depositional steps exist due to jammed boulders that are rearranged to stabilize the channel [Church & Zimmermann, 2007]. After step reformation, the channel bed accumulates sediments and readjusts its slope. This stock of sediments can be considered as available potential energy that will be released during the next exceptional event. Thus, here there is certainly no static equilibrium, but a stationary equilibrium state is still expected at large time scale. Step-pool systems might be qualified as metastable systems in the sense of accumulation/failure cycles (next section).

In a flume investigation, Church *et al.* [1998] concluded that for a given flow, moving particles rearrange themselves in a more stable configuration by creating reticulate structures. The appearance of these bedforms reduces sediment transport by orders of magnitude [Brayshaw, 1985; Church *et al.*, 1998; Hassan & Church, 2000]. Given the long time of this stabilization process, it suggests that the river stability state is the result of recent hydrological history instead of a single flood.

These examples confirm that at the scale of the human life, steep streams are not in equilibrium as they show a dependence on the history of recent environmental conditions. Thus, for short-term prediction, streams should not be considered in equilibrium. At larger time-scales, a stationary equilibrium might be found and the extremal boundaries of the system variability should be determined in terms of fluxes and morphologies.

2.3.3.2 Metastability and self-organized system

As previously discussed, the static equilibrium is generally not verified in river system, but the channel state oscillate more or less around a mean stationary state. A geomorphic system can be identified as a *metastable* system, by analogy with physics (first order transition, [Bouchaud *et al.*, 1995]) when a hysteresis is observed at the scale of the system. Other terms are used for the same behaviour, such as stick-slip cycles [Jerolmack, 2011] or bistability [Jaeger *et al.*, 1990]. This is one type of fluctuations around a mean morphologic state. Indeed, most of transport processes in geomorphology are near-threshold which often leads to hysteretic behaviours, such as sediment accumulation and failure [Jerolmack, 2011]. This signifies that the current state of the system has a finite life time and can, spontaneously or under specific perturbations, relaxes to a more stable state.

Bouchaud *et al.* [1995] show that grain piles are subject to metastability, i.e. to a hysteresis of the macroscopic dynamics of the pile profile. They show the existence of the critical angle of stability Γ_c which is different from the angle of repose Γ_r . If the grain pile reaches Γ_c , an infinitesimal perturbation leads to a complete relaxation — the slope decreasing to Γ_r . If the global slope is between Γ_r and Γ_c , the relaxation can only be partial. The evolution of the system is controlled by the density of rolling grains, i.e. an external force, that perturb the system. At the limit of no external perturbations, the system is frozen in a metastable state, whereas for very large density of rolling particles, the relaxation can be almost complete at all time, meaning that $\Gamma_r = \Gamma_c$ (no hysteresis). This shows the significance of external forces intensity, and the interest of low external perturbations leading to strong intermittency.

In many geomorphologic systems, the global structure seems to be stable and organized, whereas at smaller scales processes are chaotic [Jerolmack, 2011]. Thus, theories based on self-organization have been proposed suggesting that a global coordination at the system scale arises from local interactions even if the system is randomly perturbed. However, non-self organizing behaviours are also observed depending on the observed scales and specific circumstances [Phillips, 1995].

In certain cases (for instance with rice pile, [Frette *et al.*, 1996; Denisov *et al.*, 2012]), the dynamics of the pile can show signs of Self-Organized Criticality (SOC). SOC systems have a fixed point as an attractor, i.e. the system behaviour tends towards the scale-invariance characteristic at large scale. The high spatial micro-roughness of the profile, which is in relation to Γ_c of the concerned grains, might be a condition to obtain SOC behaviour [Denisov *et al.*, 2012]. The dynamics of granular system is sensitive to details of the grains like the shape [Carrigy, 1970]. Rounded particles with small surface roughness gain rapidly high velocity when dislodge from the bed. Thus, they regularly impact the bed with high energy. This prevents strong fluctuations of the profile of the grain pile ($\Gamma_r \approx \Gamma_c$). Moreover, the friction between grains plays a great role in grain arrangement (profile roughness) and dynamics.

All these behaviours observed in geomorphology and in granular physics might be expressed in channel morphodynamics. Also details, like sediment characteristics, should be well chosen depending on the purpose of the experiments.

2.3.4 Summary

Many bedload transport formulations need a defined threshold characterizing the beginning of motion. However, it was found that equations based on threshold generally poorly describe bedload transport rates. In many cases, simple power law functions seem to display a better representation. Moreover, the equation complexity do not improve the prediction accuracy. For instance, recently Recking [2010] and Recking [2013] proposed simple and reliable equations that require minimal knowledge of site conditions for the estimation of bedload transport rates. This is explained by the inaccuracy of the threshold concept, as seen in section 2.1.2.2. In addition, Recking *et al.* [2012] demonstrated that bedload transport predictions were improved by taking into account the time scale of the observations.

In this review, I also show that certain bedforms, like antidunes or cyclic steps, including step-pool sequences, could be considered as instabilities. They could lead to global changes on a longitudinal profile when their migration or destruction are initiated — as described in chapter 6. These bedforms could respond more or less actively towards different configurations depending on the state of the profile, and the flow and sediment transport conditions. This paradigm reconsiders channel stability and equilibrium. This finding also emphasized the interest to precisely investigate the different channel states, their possible evolution and the possible analogies with granular dynamics — see chapter 5.

On the basis of the concept of equilibrium, many authors have considered that most rivers are stable in the sense that the channel geometry do not significantly change. However, no extensive data are available to verify this general hypothesis. New data are necessary to investigate this equilibrium issue, particularly in steep channels. Moreover, many authors try to conduct their experiments at “equilibrium” as it is commonly assumed. The relative difficult to find this equilibrium in flume experiments may wonder about its real existence. Thus, the aim of the following chapters is to quantify and understand the fluctuations around this possible fictive equilibrium state.

In addition, many investigations on the morphology evolution in steep channels, mechanisms and concepts interpreting bedload transport variability are still necessary. New continuous and accurate measurement techniques have to be developed to produce simultaneously time series of bed elevation, water level and bedload transport rates. The experimental design and work of this thesis are summarized in the next chapter in an effort to resolve this issue.

Chapter 3

Experimental facilities and methods

This chapter presents the two experimental facilities designed and used to study steep channel morphodynamics. The choices made in terms of conception and measurement techniques to reach the defined objectives (section 1.2) are underlined. As it was discussed in the previous chapter, to answer the problematic, specific facilities has to be invented. The prototype experiments should permit to conduct long runs — relative to the response time of the system. An idealized case was chosen to possibly generalize the findings, not taking into account the specific details of a particular configuration. Moreover, as a resolution of several orders of magnitude is needed, the new automatized measurement systems had to be developed. Throughout the chapter, the experimental procedures are described and measurement incertitudes are discussed in each paragraph related to the concerning measurement technique.

3.1 General experimental objectives and contributions

This experimental study is motivated by the necessity of investigating behaviours and processes in morphodynamics of mountain-like streams. The four following points were taken into account in the design of the experimental facilities. First, to reduce the number of phenomena involved, the experiments were idealized compared to a natural stream. Second, design constraints were determined by the choice of using particularly low-cost and accurate measurement techniques, permitting the collection of large volumes of precise data. Third, efforts have been made in obtaining a precise control on the experimental parameters — the flume angle α , the water discharge Ql and the sediment feeding. Finally, long experimental runs up to several days, were conducted, reaching the stationary state and capturing the largest fluctuations in bedload transport rates and bed elevation. As in this work, the interest is focused on bedload transport processes from the grain-size scale up to the stream reach scale, the experimental setup is a prototype of a small stream reach with relatively homogeneous topography and flow conditions.

Two experimental facilities were designed for the observation of the 2-dimensional and 3-dimensional bedload transport phenomenon over an erodible bed. In the 2-dimensional flume, 2D-flume in the following, accurate measurements were possible leading to the precise description of the processes and their evolution. A 3-dimensional and larger scale experiment, called the Armfield flume in the following, was needed to compare, extend and generalize the findings of the small scale investigation. A narrow grain size distribution was chosen for the two setups to limit the effects of segregation and sorting and to independently study the process of bedload transport. As it will be detailed in the following, this choice of sediment size also simplifies the measurements.

Another important point is the high control wished on the experimental parameters. Here, at first, the water discharge is fixed constant for each run. Different flume angles can be investigated by tilting the flume. Finally, great efforts have been done to have a high accuracy on the solid

discharge imposed at the inlet of the flumes. In particular, it was verified that the variability of bedload transport rates at the inlet was much more smaller than at the outlet (section 2.2.2 and figure 4.10). Indeed, it is important to study the collected data knowing precisely the external conditions that are acting on the system, especially for a such small flume (2D-flume).

Most of the results presented in this study are based on the 2D-flume experiment in which an extensive campaign was conducted. Complementary experiments in the Armfield flume were used to compare the results. Also measurements from a monitoring station in a mountain river, the Navisence River (field site described in appendix D), in addition to the Armfield data, illustrate the concepts examined in the 2D-flume. The objectives concerning the measured variables and the sediment feeding are now detailed.

3.1.1 Experimental variables and measurements

To fully understand which interactions happen between the flow and the steep mobile bed, bedload transport rates, bed elevation and characteristics of the fluid flow must all be known. As seen in section 2.2.1, many methods exist to estimate bedload transport rates. The temporal resolution, i.e. the sampling time, and the accuracy, i.e. errors, of the measurements have great effects on the behaviours and the statistics inferred.

The bedload transport rate, usually defined as the weight of sediment flowing through a cross section during a certain amount of time, depends on the integration time. Theoretically, the sampling time could be chosen, depending on the purpose of the study and given the correlation time of the concerned variable. However, the correlation time of a given variable is dependent on the channel configuration and the experimental parameters. This leads to a more delicate comparison between different studies. More generally, it seems hazardous to compare the statistics of time series that were measured with different sampling times, conditions and accuracies without knowing the complete statistics of the variable driving the process. In order to understand and analyze the processes of bedload transport, scientists would prefer to deal with a measurable variable that does not depend on the sampling time.

The number of moving particles in a window — or in a volume — at a given time, or the exact time of an event occurrence (erosion/deposition of a particle or particle flowing through a cross section of the water flow) seem to be more appropriate variables for the analysis of the processes involved in bedload transport. Following this remark, techniques were developed and installations designed to measure the exact time of particles leaving the flume. The resulting bedload transport data, which was acquired continuously during my experiments, has a wide temporal resolution (up to 6 orders of magnitude).

Measurements of bed elevation and its fluctuations are necessary in order to deduce essential behaviours, parameters and variables such as bedform migration, bedform characteristics, roughness, local and global slope and erosion/deposition estimates. Depending on the experimental installation, the techniques used are different with a different resolution and accuracy. They are described in the two respective sections, 3.2.2 and 3.3.2, for the 2D-flume and the Armfield flume. In both experimental facilities the experiments were not stopped and restarted in order to keep the precision of the time series and not to disturb the stochastic process in play. As discussed in chapter 6, steep morphologies are present which induce important changes if a stop and restart occurs. Because the water flow is the main driving phenomenon, it is necessary to investigate its properties. The water elevation was measured in the same manner as the bed elevation.

3.1.2 Sediment feeding

Similar to sediment availability in real mountain streams [Recking, 2012], the solid discharge imposed at the inlet has a strong influence on the processes. For this reason, this sediment flux was taken as one of the main external parameter studied here. As the objective was to observe the influence of a given external condition, sediment recirculation was not appropriate in this case (section 2.2.2.2). Moreover, studies focusing on the influence of the feeding solid rate are not common even though it plays a great role in the response of the channel system.

In natural streams, the sediment comes from bank erosion, active tributaries and rock slides directly reaching the stream. In my experiments, a feeding rate is imposed at the inlet of the flume. As in certain conditions, collective motion initiated by particle-particle interactions plays an important role [Heyman *et al.*, 2013], the difference from natural supply can be significant, particularly when erosion takes place in the stream bed. However, the objective is the study of the channel response to a given imposed condition, considering that certain natural stream reaches are similar to feed systems at small temporal and spatial scales [Recking *et al.*, 2009b].

First, a constant input solid discharge was chosen. This rate should be easily and accurately changed. A constant rate permits the study of a simpler case, the isolation of certain processes and the recording of the autogenic fluctuations of the system (Jerolmack & Paola [2010] and section 4.1.2.2). Eventually the input rate will be varied in order to study the effects of periodic external conditions. The feeding systems are described in detail in sections 3.2.1 and 3.3.1 for the 2D-flume and the Armfield flume respectively.

3.1.3 Development of new bedload measurement techniques

Different methods were used, tested and developed to measure the bedload transport rate qs . As it is simpler, in most flume studies qs is measured at the outlet of the flume. In addition to classical sediment weighing, an accurate system to record the arrival time of each particle passing the flume outlet was developed. For selected experiments on the 2D-flume, an image processing technique was performed to obtain the time series of qs at several locations along the flume. This last technique allows us the validation of the experimental settings and to infer spatial behaviour.

3.1.3.1 Sediment discrete weighing

The most classic way to measure qs in experimental facilities is by direct weighing. This data, collected in the two installations for each run, is essential in order to verify the mass balance and to calibrate and validate the other techniques described below.

The error made on the cumulative mass is very small, and estimated to be between 0.1% and 0.3% depending on the run. The dominant error is the lost particles when manipulating the gravel pan and drying the gravel before weighing. A fixed error is then made at each weighing and was estimated at 30 particles \simeq 12 g. This estimation was deduced from the weighing of all the particles that were left in the reservoir and around the installation after the first measurement campaign. The global error depends on the number of weighing during the run and on the total transport. It seems that the longest runs with moderate to high bedload transport rates show the smallest error. Given these small error values, the weight measurements are considered as the reference value.

3.1.3.2 Microphone

A low-cost standard microphone was used with the aim of developing an accurate technique to measure qs . This acoustic device was able to capture the sound of gravel hitting a metallic plate at the outlet of the flume. The plate, placed perpendicular to the water flow, receives one sole impact

from each particle as it falls out of the flume (similarly to the accelerometer plate, see below). A processing method was developed for the computation of qs from the sound recording without much errors. This initial testing shows that it was a valuable technique for determining an solid discharge — recording of the arrival time of each particle leaving the flume — but it was too sensitive to environmental noise. In the following subsection, the technique was improved using accelerometers, which are more suitable for the recording of the plate vibrations and less sensitive to surrounding noise.

3.1.3.3 Particle counting system with accelerometer

An efficient and low-cost technique, based on the recording of gravel impacts, was designed to produce high-resolution bedload transport data. The idea consists of measuring the impact energy of the gravel when it falls out of the flume. A metallic grid, placed vertically at the end of the flume, produces characteristic vibrations at each particle impact. A MEMS accelerometer, fixed on a support plate, itself mechanically connected the grid (figures 3.1 and 3.2), was used to record these vibrations. The measured signal shows very sharp peaks when recorded at high frequency rates — more than 10 000 Hz. The measurements were made with a National Instrument acquisition board at a sampling rate of 20 000 Hz. The MEMS used, 3-axis evaluation boards, are from Freescale (reference number KIT3376MMA7361LC, appendix B) and protected in a specific metallic box. They are not expensive and permit accurate detection of shocks. To avoid artifactual vibrations, the accelerometer measurement systems, including the support plate, the grid and the accelerometer, were mechanically insulated from the experimental installation using caoutchouc sheet. The exact position of the system at the flume outlet was carefully adjusted to be sure that each particle hits only one time the grid.

To obtain outlet particle arrival time from the accelerometer signal, a processing method in two steps was developed. First, the signal is filtered using the Fourier transform to reduce the noise and remove components that come from other processes (e.g., gravity, water impact, anomalous shocks). The best signal to noise ratio was found with a filter keeping two frequency bands (3900-4220 Hz and 4240-7700 Hz).

Second, a peak detection method was necessary. As the measured signal represents the plate vibrations, it is composed of several oscillations with decreasing intensity through time at each impact. A threshold, combined with a lag time accounting for the damping of these oscillations, was adjusted (figure 3.3). Errors are mostly due to small impacts that were below the threshold for detection and by impacts that occur during the damping of a previous peak, depending on the lag time. The first error is not an important problem because most of the smallest impacts are due to the smallest particles that do not account much in the solid discharge. The second is more problematic because, for instance, it changes the statistical characteristics of the interval time between particles leaving the flume.

Validation tests were carried out in the 2D-flume to confirm the correctness of the technique. This validation was made from several short tests where the particles were retrieved and counted at the end of the flume. In order to conduct enough tests, the counting was automatically performed by processing images of the retrieved particles. The best lag time, with respect to the total number of particles, was found to be around 40 ms. In figure 3.4, the raw signal, the filtered signal and the resulting number of particles detected are presented from validation tests. These tests were done at relatively high bedload transport rates to be sure that almost no particles are missed. At that stage, the mean error on the number of particles was 2%.

Looking for better resolution at small time scales, a smaller lag time and higher threshold were chosen by conducting a calibration. Thus only a few small particles were missed and the mass

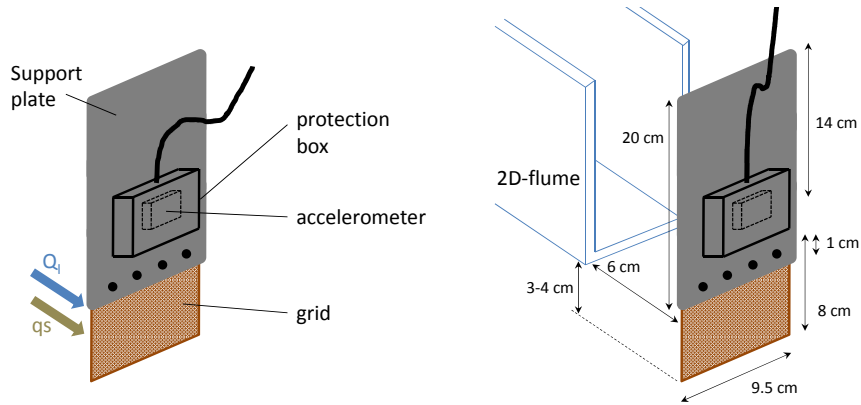


Figure 3.1: Schemes of the accelerometer measurement system devised for this study. One of them was used for the 2D-flume experiment and six of them for the Armfield flume experiment to measure bedload transport rates at the outlet of the flumes (figure 3.2).

balance was respected. This optimisation of the calibration was performed for each run as some experimental features can slightly change between runs. Indeed, water flowing noise and gravel impact intensity, recorded by the accelerometer, varied with the flume inclination and the water discharge. Also, eventually, the sensor position could have been adjusted.

This technique permits high resolution measurements of the bedload transport rates; however this kind of low-cost electronic MEMS do not give a very accurate and constance response. It can show little signs of drift for instance, in particular in the longest experiments. Thus it shows a certain uncertainty that was quantified. In this case, a small drift should not have large effects as the important point is to extract the signal peaks.

The incertitude was estimated on the resulting instantaneous bedload transport rates by the comparison with the weighing measurements. For all these measurements, the error stands between 0.5% and 5%, with an error below 2% for most of them. In fact, the error is higher at the beginning of the run, especially for long run, and drops rapidly around 1% or below. This remark was expected as the signal was calibrated to respect the mass balance, i.e. using the cumulative weighing measurement of the run. Note that it is not an issue as the results of this study are from the stationary part of the time series (section 4.1.2.1), i.e. starting few hours after the beginning of the run, where the error is much lower. The error from the weighing measurement have to be added. For instance, the maximum error is represented as error bars for a 2D-flume run in figure 3.9.

3.1.3.4 Particle counting using camera recordings

As it is of great interest to measure q_s at different locations along the flume, a purpose-built imaging technique in the 2D-flume case was developed. The statistical behaviour of bedload transport could be biased by the boundary conditions at the end of the flume where measurements are usually undertaken. Moreover, these kind of high-resolution measurements at a middle section of a flume are relatively rare.

The principle of the technique is to take narrow images at a high frequency and compute the global luminosity of them. The resulting luminosity time series shows the local minimum values when a particle passes through the narrow window of observation. Typically the image width corresponds



Figure 3.2: (a) Picture of an accelerometer measurement system placed at the outlet of the 2D-flume (with water flowing from left) used for bedload measurements. The accelerometer recording the particle impacts is fixed on the backward face of the plate and is protected by a metallic box. (b) The 6 accelerometer measurement systems placed along the width of the Armfield flume outlet (without water flow, downstream direction is from right to left).

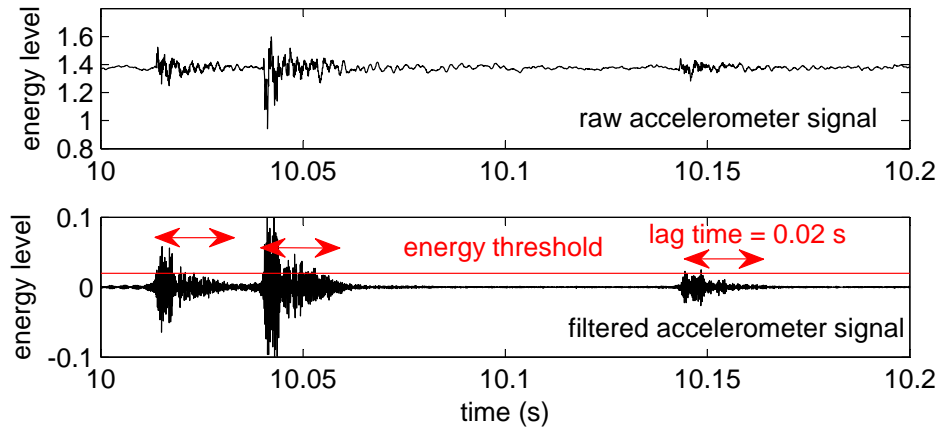


Figure 3.3: Zoom on an accelerometer signal showing lag time and energy threshold from the calibration optimisation performed on a validation test (2D-flume), to detect the exact arrival time of each particle at the outlet.

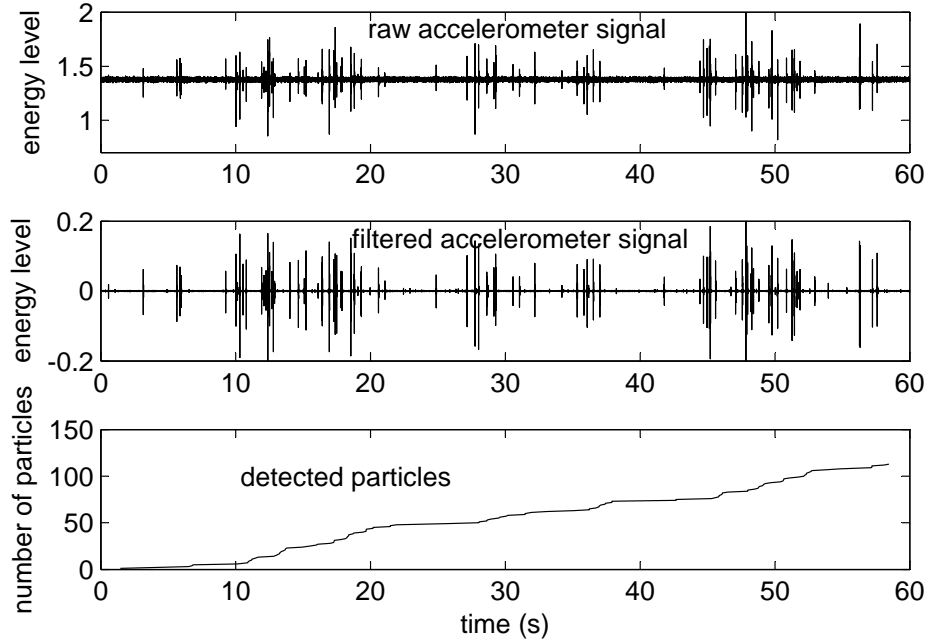


Figure 3.4: Accelerometer signal and processing leading to the number of particle passing the flume outlet through time (and their arrival time), after signal filtering and peak detection. Sample of a validation test of one minute in the 2D-flume.

to the order of magnitude of the medium grain size d_{50} . Using a processing method to detect these local minimum values, qs was computed at a particular section of the flume.

The recordings were made with three Basler cameras (A311f camera), mounted on a rail one meter away from the flume. They can be placed at any point along the flume. The acquisition frequency was set at 60 images per second over several hours. The image height is 80 pixels to account for the fluctuations in bed and water surface elevations. The image width of 12 pixels corresponds to 1 cm. In this configuration, it takes a few images for a grain to traverse the observation window.

Basic image processing consists of transforming the raw image into a binary image to reduce the effects of luminosity changes during the run. The water free surface on these images shows very strong fluctuations. As this implies large fluctuations in the global luminosity of the images, it is necessary to detect and suppress the free surface. The global luminosity, i.e. the sum of white pixels, is computed for each image. A time series of luminosity at a high temporal resolution is then obtained.

The time series of image luminosity shows sharp local minima and also some steps. An extract is plotted in figure 3.5. These minima correspond to particles passing through the observation window, whereas the steps are the signature of erosion/deposition events. The decrease or the increase of luminosity represents the erosion or the deposition of particles respectively. The detection of these two event types are not based on an absolute value of the luminosity. Several thresholds are calibrated from images and applied to filtered time series. Different filters are used to separately detect the sharp minima and the erosion/deposition steps. The procedure detects grains in saltation as well as the rolling or sliding ones, and also particles that are partially hidden behind others.

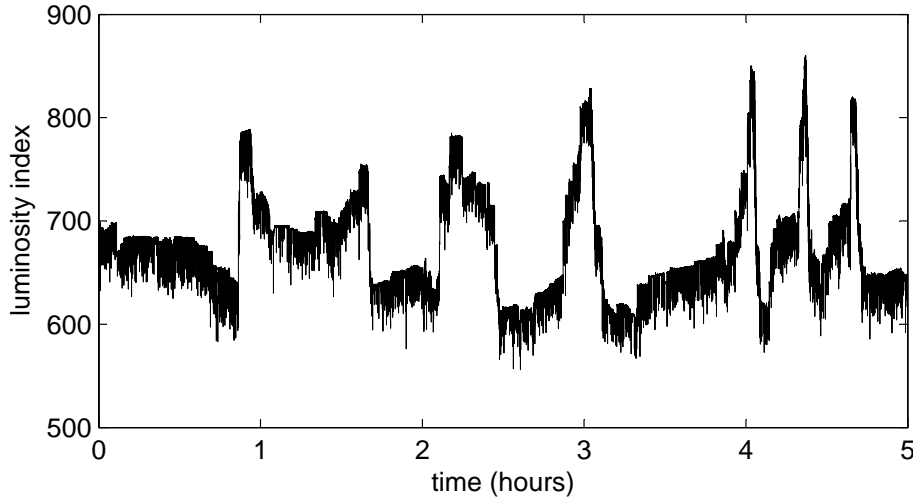


Figure 3.5: Two hour long segment of a luminosity time series computed from a camera recording, at a frame rate of 60 Hz, on a narrow window of the 2D-flume (1 cm). Downward spikes correspond to particles passing through the window and global increases and decreases to deposition and erosion respectively.

More precisely, a filter computes a local moving maximum of the time series at the scale 0.5 s — computed in the same manner as the moving average — which removes all of the local minimum values due to the passing grains. This resulting time series gives the luminosity steps that correspond to the local entrainment and deposition of particles. When subtracting this filtered time series from the initial one, a time series with spikes corresponding to the passing grains is obtained. Then, a simple spike detection technique computes the passing time of each particle. Thus it results in a series of passing times similar to the accelerometer data. This simple technique used here permits an easier and more accurate detection of the spikes and steps than techniques based on fourier transform filters or moving averaging.

3.2 2D-flume

The main data were collected on the 2D-flume. The large quantity of accurate data were helpful in improving the understanding of steep channel evolution. As the name suggests, the installation was designed for the study of a 2-dimensional configuration. This was needed to obtain high-resolution data in space and time of the water and bed elevations and bedload discharges. The installation gives relatively easy and automatic observations for a long measurement campaign. The small size of the flume also permits to reach quite rapidly a stationary state which is necessary for the use of statistic tools. All the techniques are quite sophisticated compared to the limited cost of the installation. A view of the installation is given in figure 3.6.

3.2.1 Experimental setup

The main part of the installation is a simple hydraulic closed circuit (only water recirculation) composed of a constant-head pump allowing a maximum water discharge capacity of 5000 l/h. The pump is submersible and placed in a reservoir at the outlet of the flume. A 8-cm-wide and 2.5-m-long prototype flume was designed to provide the right conditions for accurate and high-resolution measurements of qs and bed fluctuations in a super-critical regime. The flume was made with transparent plastic walls constructed using Makrolon® in order to observe the bed topography and

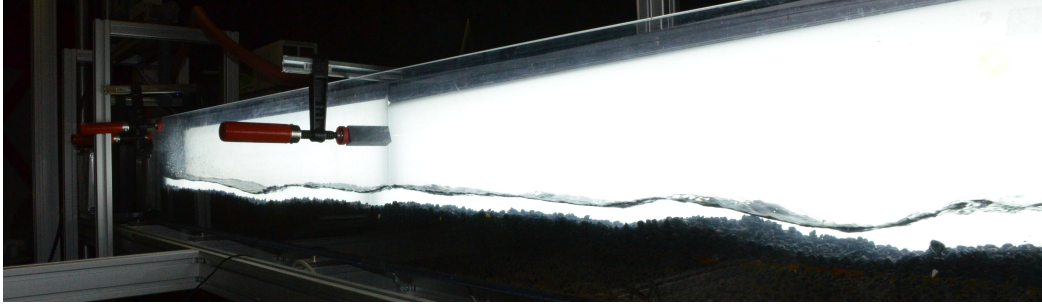


Figure 3.6: View of the 2D-flume with the lighting panels along the whole flume length permitting a good contrast on camera shots, flow is from left to right.

the water free surface from the side walls. A system of pipes, taps with a by-pass and a flowmeter give the possibility to control the water discharge delivered at the inlet of the flume. Figure 3.2.1 shows the general technical scheme of the experiment.

To avoid strong singular conditions — hydraulic jump and anomalous erosion — at the upstream end of the gravel bed, a porous box was placed in the upper part of the flume. This box, which has the same height as the mean bed depth, shows the same roughness on its surface and the same porosity as the gravel used in the flume. Moreover, a honeycomb structure linearizes the input water flow. Given the high roughness and the low submergence, the rough turbulent flow is fully developed very close to the flume inlet. Following these last remarks, the upstream boundary does not have influence on bedload processes occurring along the whole flume.

Feeding system

A specific feeding system was designed to fulfill the characteristics needed. The aim was to be able to accurately fix a constant rate for several days. The possibility of setting a very low input sediment transport rate was also a specific requirement. A conveyor belt, powered by a small engine, regulates the particle flow from a pipe which makes the connection to a reservoir. Playing with the speed of the conveyor belt and the gear arrangement, the input particle rates can be adjusted between 0.5 and 40 particles per second. One particle detection system using an accelerometer, described in section 3.1.3.3, was placed at the outlet of the feeding system to control its regularity and obtain the exact value of the sediment feeding rate.

Sediment characteristics

The sediment particle size and the flume width were chosen to obtain a 2-dimensional evolution of the bed elevation. A fairly low flume-width to water-depth ratio $W/h < 6$ was needed (table 3.2). A relatively large flume-width to particle-diameter ratio $W/d_{50} \simeq 13$ respecting the condition of non-jamming was also observed to limit the wall effects on grain arrangement [Weichert, 2006].

A narrow particle diameter distribution was chosen in order to suppress the influence of the sorting process. The measured corresponding diameter distribution is presented in figure 3.8. Following the classification of Folk & Ward [1957], who defines the inclusive standard deviation as $\sigma_i = \frac{d_{84}+d_{16}}{4} + \frac{d_{95}+d_5}{6.6}$, the sediments can be qualified as very well-sorted for $\sigma_i < 0.35d_{50}$. In my case, the sediments are very well sorted as $\sigma_i = 0.56$ mm is inferior to $0.35d_{50} = 2.2$ mm.

Natural gravel was intentionally used in order to keep the natural strong variability in grain shapes. This choice also permits experiments with a flume angle corresponding closely to real

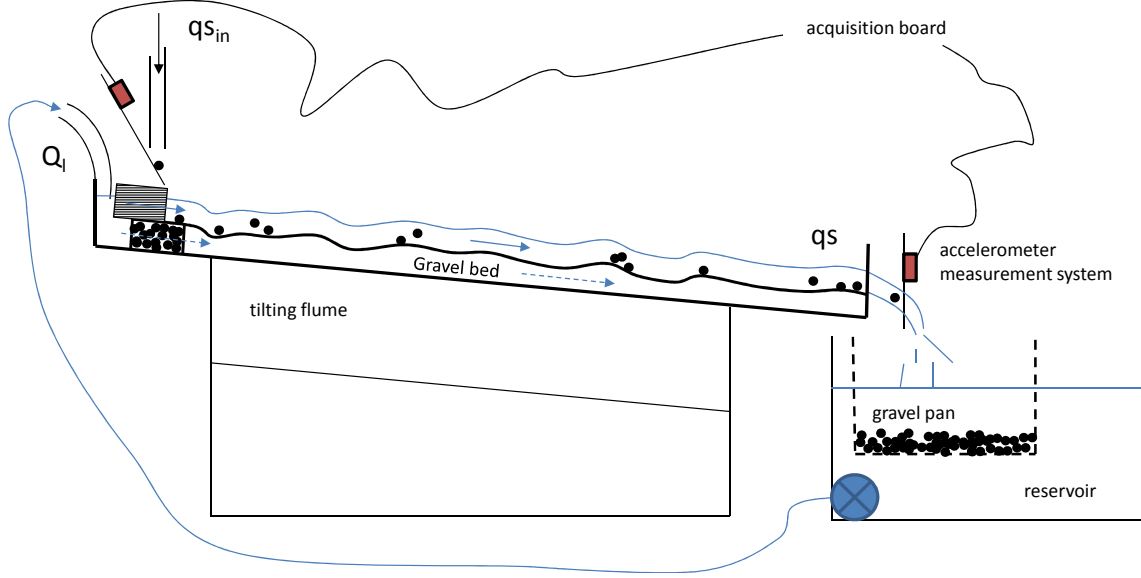


Figure 3.7: Scheme of the 2D-flume installation. This side view corresponds to the view recorded by the two cameras to measure bed and water elevation (figure 3.10).

mountainous streams. Indeed, the grain arrangement and the angle of repose of a grain pile, thus also the stability of a grain bed sheared by water, is highly dependent on the grain shape and the surface characteristics [Carrigy, 1970]. Thus, instead of using artificial spherical beads for instance — which could greatly simplify the measurements — natural gravel was preferred. This choice should also reveal important natural behaviours (section 2.3.3.2).

Finally the mean bed height of 8 cm — fixed as initial condition — leaves enough space for the development of hyporheic flows and bed morphologies. The water depth and the amplitude of the morphologies are at maximum around 3 cm. Some characteristic values of the sediments are summarized in table 3.1.

Table 3.1: Properties of the 2D-flume sediments: density ρ_s , apparent density ρ_{app} , ϕ =porosity and a =aspect ratio= ratio of larger to minor particle axes.

d_{30} (mm)	d_{50} (mm)	d_{90} (mm)	ρ_s (kg/m ³)	ρ_{app} (kg/m ³)	ϕ	a
6	6.25	6.8	2690	1570	0.42	1.5

3.2.2 Measurements

Bedload transport measurements

In all experiments conducted in the 2D-flume, the flume inlet and outlet solid discharges were continuously recorded. Also the gravel was retrieved at the outlet in a pan during each run, then dried and weighed with a digital scale. An example of a measured time series is presented in figure 3.9 where a comparison between the input and outlet bedload transport rates, along with the occasionally weighed sediment measurements, are shown. This figure confirms the viability of the

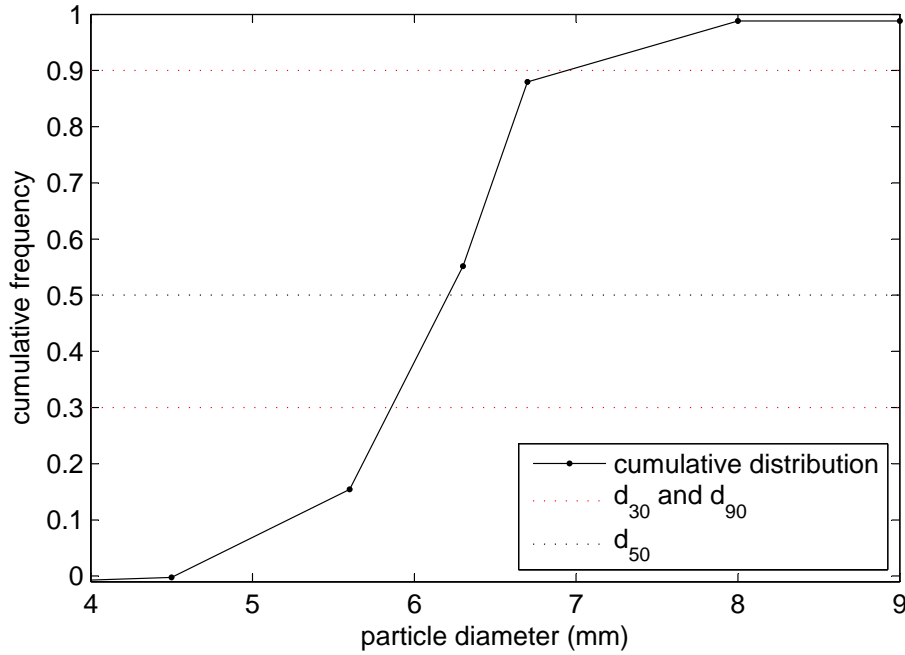


Figure 3.8: Granulometric cumulative distribution of the gravel diameters (in the 2D-flume experiments). The mean diameter d_{50} is 6.25 mm.

measurement techniques used. The imaging technique to count particles at several cross-sections of the flume was used only for few runs as described in section 3.2.3.

Bed and water elevation measurements

An image processing technique was developed to obtain time series of bed and water level elevations. Due to the 2-dimensional flow and bed evolution, a side view of the flume using two side-by-side cameras (Basler avA1000-120kc) records all of the morphodynamic features. Each camera covers a flume window of approximately one-meter-long at a sampling frequency of one image per second.

A back light technique gives an optimum contrast on the images. Two LED panels produce a diffuse and homogeneous light along the whole flume in the opposite side of the camera (figure 3.6). This technique avoids spurious reflections on the transparent walls and is insensitive to scratches and dirtiness on the walls due to the use of natural gravel. These lights, combined with carefully chosen camera settings, produce high quality images for processing.

For the detection of the bed elevation, the moving particles were removed on the images by setting a long exposure time of 0.2 s. An example image is shown in figure 3.10. At an exposure time of 0.1 s, the moving particles would show a blur trail of their trajectory on the images. Supposing that the moving particles reach quasi-instantaneously their typical velocity, at an exposure time of 0.2 s, it is admitted that only the particles that did not move are captured. As, it was not possible to track moving particles with this set-up, I could not estimate the exact time-scale that distinguishes particles at rest from motion. The resulting elevation resolution is higher than the particle scale as the image pixels correspond to about 1 mm on the prototype experiment.

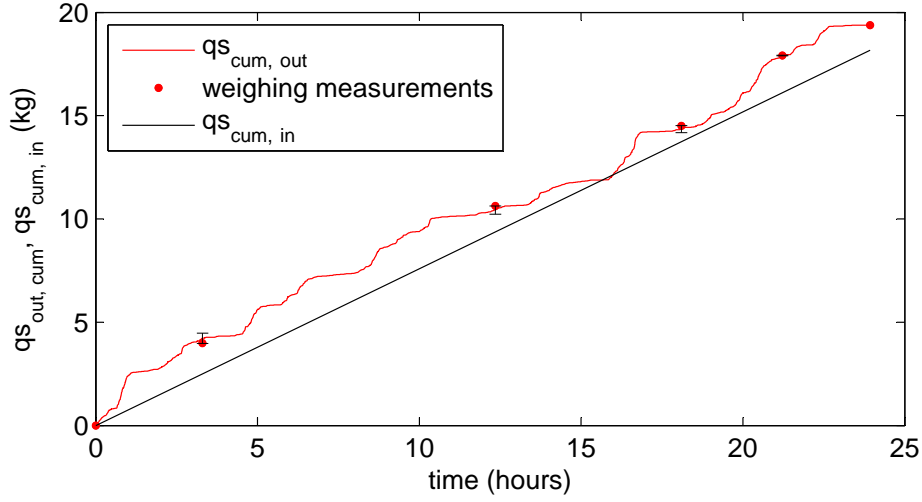


Figure 3.9: Comparison between inlet and outlet measured bedload transport rates for run *5deg3v*, the weighing data are also shown. The error bars stand for the maximum error (accelerometer signal error + errors of the calibration data) of the time series that are used in the study (section 3.1.3.3).

The image processing is decomposed into three steps. First object edges were detected, they correspond to the pixels where the intensity gradient is maximum. Here the Canny [1986] method was used to compute the local maxima of this gradient. In this method, two thresholds are used for a better detection of edges when the local maximum is relatively low. Tuning these thresholds, the water surface and the bed elevation were independently detected. A second step consisted of detecting and removing anomalous values by imposing a threshold on the water depth — when, for instance, a single particle was stuck against the wall. Finally an interpolation of the two levels is made for every millimeter. Note that the water surface is technically averaged over the exposure time.

A calibration of the images has to be performed so that the distortion due to the wide angle lenses may be corrected and the measurements may be transposed at the real scale. Exactly the same experimental settings are kept during the calibration. It consists of taking images with a calibrated sheet deployed in the flume. The calibration was made when the flume was filled with water as the light rays do not have exactly the same incident angle when there is no water in the channel.

As the incertitude of the technical measurements during the calibration and the tests are small with respect to the resolution of the camera, the error is determined by the conversion from one pixel to the corresponding distance on the prototype which is 1 mm. Thus, the error of the bed and water elevation is estimated to be ± 0.5 mm when the bed is perfectly 2-dimensional. Assuming that the errors are uniformly distributed along the bed and water profiles and given that the corresponding slopes are computed by a linear regression (section 5.1.1.1), the errors on the channel slope is very small. It only depends on the adjustment of α which is estimated to be around 0.01° (inclinometer and graduation reading errors). Given the small errors compared to the fluctuations of the variables, they were not represented on the figures.



Figure 3.10: Side view (downstream half-part of 2D-flume, around one meter) of the bed and water level captured by one of the two cameras recording the bed evolution at a sampling frequency of 1 s. Due to the powerful back lighting, an exposure time of 0.2 s permits to detect all the bed particles that did not move during this 0.2 s. All the moving ones are not seen on the images.

3.2.3 Experimental campaign

The objectives of the main set of runs was to conduct experiments at low and constant Shields stress S_h , changing qs_{in} and α for each run. Thus the influence of qs_{in} and α could be studied independently of the flow conditions. This will permit to assess the influence of the mean bedload transport intensity and the mean channel slope on the characteristics of bedload transport rate fluctuations. Second, runs with higher S_h will permit to assess the influence of larger external forces qs_{in} and Q_l .

Tables 3.2 and 3.3 summarize the characteristics and the names of the different runs with constant S_h and higher S_h respectively. The runs are named by the value of α followed by the supply voltage of the feeding system engine. The sign + differentiates the experiment with a larger S_h . For instance, the run *2deg3v* was conducted at a flume angle of 2° with a constant sediment feeding rate corresponding to a supply voltage of 3 v. Few runs, marked with the letter b, were redo to verify the reproducibility — at low (*3.2deg3vb*) and high qs_{in} (*4deg20vb*). Moreover, run *4deg20v* was reproduced changing only the initial bed conditions — different bed compactions. It leads that, after reaching the stationary state, the initial bed conditions do not have further influence on the statistics of the time series. Finally, given the clear trends on the statistics shown by varying the different experimental parameters (chapter 4), the runs were judged reproducible.

For runs with a flume inclination of 5° , the bed elevation was not recorded as the flume-width to water-depth ratio W/h was too high, leading to 3D morphologies. During runs *3.2deg3v+* and *3.2deg6v+*, the bedload imaging technique explained in section 3.1.3.4 was used, additionally to the other measurements. Finally, two runs with no sediment feeding were conducted for flume inclinations 3.2° and 5° . These runs are not stationary as the channel progressively degrades, even after 24 hours, but the comparison with runs with sediment feeding is of great importance (section 4.1.2.3).

Shields stress

The Shields stress S_h is computed from equation 2.3, using bulk and time-averaged variables. The determination of Θ is explained in details in section 5.1.1.1. This expression is valid for an infinitely large channel, i.e. for $h/W \ll 1$. Considering the narrow flume used in this study, S_h has to be corrected for wall effects. When the roughness of the walls and the bed is the same, the water depth h is just replaced by the hydraulic radius $R_h = S/P_m$, with S the cross-sectional area and P_m the wetted perimeter. Here, as the walls are made of smooth transparent material the roughness is much lower than the bed and a specific correction, using common methods, has to be performed. The Vanoni & Brooks [1957] correction method was used. It is presented and compared with other correction methods in appendix A.

Critical and initial Shields stress

For the main set of runs, the objective was to fix S_h just slightly above the threshold of motion. The critical Shields stress S_{hc} is generally difficult to determine visually, particularly in steep channels due to the high intermittency. Thus, short experiments on a flat and fixed bed were conducted to determine the relation between S_h and the water discharge for different α . Further details of the test procedure are given in appendix C. Thus it was possible to determine the experimental parameters Q_l and α to fix the same initial Shields stress S_{hini} for all of the runs of the set.

The figure 3.11 compiles the results of the tests in a diagram S_h versus Q_l . The crosses represent the test data points and red dashed lines represent the corresponding linear fitting. The dashed gray lines show the inferred relation for two angles that were not tested (details in appendix C). S_{hini} is set just above the critical value S_{hc} and is approximately the same for all of the tested α . For the first run, S_{hini} was adjusted visually by tuning Q_l to have a very low bedload transport rate corresponding to an intermittent transport condition. Then, Q_l for the other runs were deduced from the figure 3.11.

Table 3.2: Experimental runs and corresponding parameters for the data set with constant Shields stress: flume angle α , mean solid discharge qs , water discharge Q_l , initial Shields stress S_{hini} , run duration t_{exp} , water depth h , Froude number $Fr = U/\sqrt{gh}$ with U the mean velocity, Reynolds number $Re = d_{50}\sqrt{S_h(\rho_s - \rho)gd_{50}/\rho}/\nu$ with ν the kinematic viscosity, and flume width to water depth ratio W/h .

experiments	α (°)	qs (g/s)	Q_l (l/s)	S_{hini}	t_{exp} (h)	h (m)	Fr	Re	W/h
2deg3v	2.0	0.22	1.29	0.093	24	0.029	1.04	596	2.8
2deg6v	2.0	0.59	1.29	0.093	24	0.028	1.09	633	2.8
2deg10v	2.0	1.14	1.29	0.093	6	0.028	1.10	632	2.9
2deg15v	2.0	1.67	1.29	0.093	6	0.027	1.17	626	3.0
3.2deg3v	3.2	0.21	0.74	0.091	47	0.021	0.97	-	3.8
3.2deg3v(b)	3.2	0.23	0.74	0.091	27	0.021	0.96	637	3.8
3.2deg4v	3.2	0.32	0.74	0.091	48	0.021	0.95	636	3.7
3.2deg5v	3.2	0.45	0.74	0.091	48	0.021	0.99	641	3.8
3.2deg6v	3.2	0.54	0.74	0.091	48	0.019	1.13	617	4.2
3.2deg10v	3.2	1.02	0.74	0.091	6	0.018	1.22	611	4.4
3.2deg15v	3.2	1.53	0.74	0.091	6	0.019	1.16	648	4.3
4deg3v	4.0	0.20	0.57	0.093	48	0.016	1.14	618	5.0
4deg4v	4.0	0.32	0.57	0.093	48	0.015	1.31	605	5.5
4deg5v	4.0	-	0.57	0.093	48	0.014	1.34	598	5.6
4deg6v	4.0	0.55	0.58	0.093	48	0.016	1.19	626	5.2
4deg10v	4.0	0.99	0.57	0.093	6	0.014	1.39	603	5.8
4deg15v	4.0	1.49	0.57	0.093	6	0.014	1.42	599	5.8
5deg3v	5.0	0.20	0.39	0.095	24	0.011	1.45	563	7.6
5deg6v	5.0	0.57	0.39	0.095	24	-	-	-	-
5deg10v	5.0	0.97	0.39	0.095	6	-	-	-	-
5deg15v	5.0	1.47	0.39	0.095	6	-	-	-	-

3.3 Armfield flume

The Armfield flume experiment was especially designed to give data at an intermediate scale between the 2D-flume experiment and a real mountain stream, as the 2D-flume experiment is very idealized. However, it is more difficult to obtain a stationary state than it was on the 2D-flume. On

Table 3.3: Experimental runs and corresponding parameters for the complementary runs at stronger Shields stress.

experiments	α (°)	qs (g/s)	Q_l (l/s)	S_{hini}	t_{exp} (h)	h (m)	Fr	Re	W/h
3.2deg6v+	3.2	0.60	0.97	0.106	24	0.024	1.07	648	3.4
3.2deg3v+	3.2	0.19	0.97	0.106	24	0.027	0.86	685	2.9
3.2deg15v+	3.2	1.62	0.97	0.106	6	0.024	1.05	659	3.3
5deg3v+	5.0	0.12	0.57	0.111	24	0.014	1.38	610	5.7
5deg15v+	5.0	1.62	0.57	0.111	6	0.015	1.19	625	5.2
5deg6v+	5.0	0.53	0.57	0.111	24	0.016	1.17	630	5.1
4deg20v	4.0	2.19	0.78	0.111	6	0.019	1.17	646	4.2
4deg20v(b)	4.0	2.11	0.78	0.111	6	0.019	1.16	664	4.1
4deg36v	4.0	5.74	0.83	0.114	3	0.020	1.18	681	4.0
4deg48v	4.0	9.35	0.83	0.114	3	0.019	1.24	687	4.2
4deg45v	4.0	8.35	0.83	0.114	3	0.019	1.22	675	4.1
3.2deg45v	3.2	7.95	0.83	0.114	3	0.019	1.22	659	4.1
5deg45v	5.0	8.00	0.65	0.119	3	0.017	1.22	682	4.8

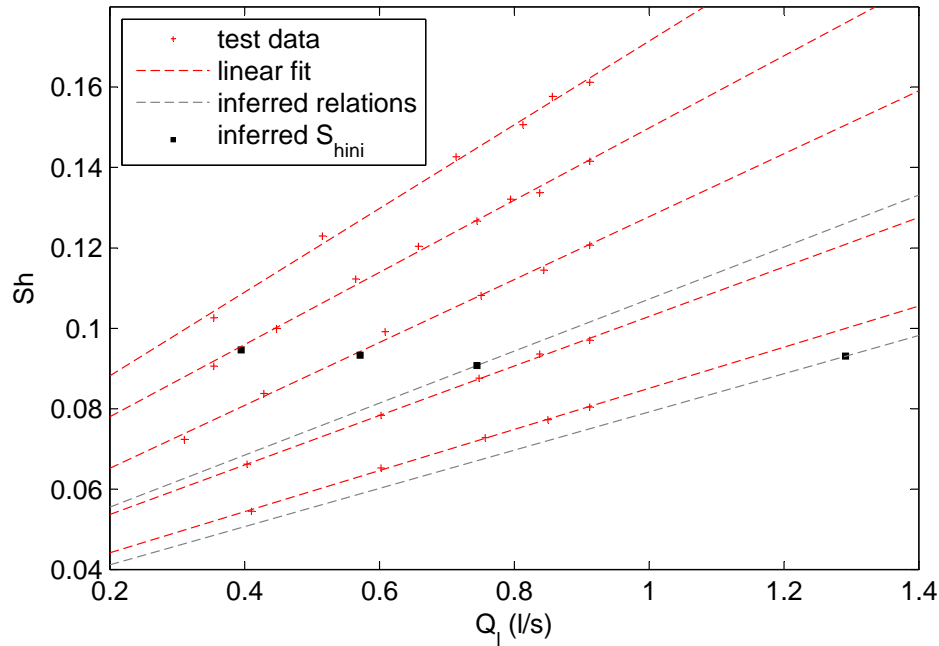
Figure 3.11: Shields stress versus water discharge: tests on fixed bed. The different lines represent the relation at different flume inclinations: 2°, 2.3°, 3°, 3.2°, 4°, 5° and 6°, from bottom to top. These tests allow defining of the initial conditions S_{hini} of the main measurement campaign.



Figure 3.12: Armfield flume. (b) Note the six accelerometers for the recording of bedload transport rates at the top of the image and the construction bag to retrieve and weigh the accumulated sediments.

this installation, the size and the complexity are increased. The size is about one order of magnitude larger than the 2D-flume and it results a 3-dimensional evolution of the channel bed.

A few runs were conducted at constant experimental parameters. Also one experiment, composed of a succession of flood cycles of the same magnitude, is presented illustrating interesting behaviour. Unfortunately, the techniques used in the 2D-flume could only be partly applied to this experiment. Still, bedload transport rates were measured at a high temporal resolution and the parameters were fixed and controlled accurately.

3.3.1 Experimental setup

The Armfield flume is a 17-m-long and 60-cm-wide tilting flume with glass walls allowing visual observations from the side (figure 3.12). The water discharge, from 5 l/s up to 60 l/s is controlled by a pump in a closed-circuit and can be servo-controlled using a NI acquisition board and a frequency variator. The gravel bed is around 30-cm-thick and two porous boxes filled with gravel were placed at each end of the flume to minimize the boundary effects. At the downstream end the water discharge flowing out from the granular bed can be controlled by two valves. Thus, the hyporheic discharge — inter-granular flow in the channel bed — is adjusted depending on the flume angle to obtain homogeneous hyporheic flow conditions along the flume.

Feeding system

The feeding system was composed of two key pieces, an industrial conveyor belt with a constant speed and a gravel hopper which could deliver the gravel at a chosen rate. Specifically, a rotating cylinder with a small bucket, specifically designed for the requirements of my work, empties a constant volume of sediments from the hopper reservoir. The hopper was designed in EPFL-LHE laboratory to fulfill the necessary requirements and can also be servo-controlled during experiments with non-stationary solid input rates. The laboratory is equipped with a hoist, permitting the use of big construction bags with a capacity of 400 kg to retrieve gravel at the flume outlet and refill the gravel hopper (figure 3.12).

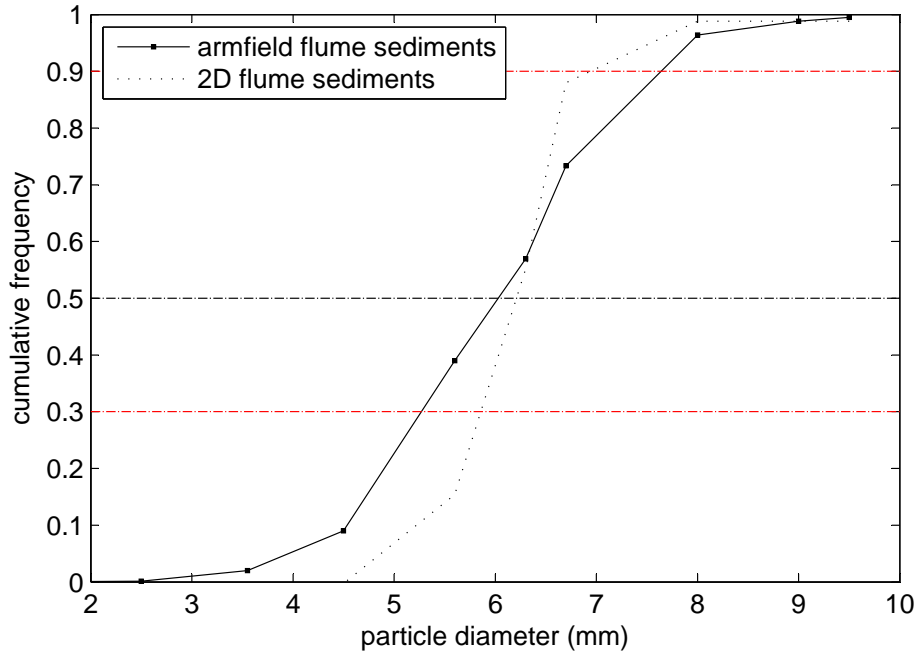


Figure 3.13: Granulometric cumulative distribution of the diameter of the gravel used in the Armfield flume, and comparison with the 2D-flume. The different horizontal lines show d_{90} , d_{50} and d_{30} .

Sediment characteristics

The sediments were chosen to have similar characteristics to the ones used in the 2D-flume. Although also well-sorted, their diameter distribution is a slightly wider, as shown in figure 3.13. The initial bed layer was set around 30 cm as well-developed bed scours can be as deep as 15 cm. Table 3.4 presents a few characteristics of the sediments.

Table 3.4: Properties of the Armfield flume sediments.

d_{30} (mm)	d_{50} (mm)	d_{90} (mm)	ρ_s (kg/m ³)	ρ_{app} (kg/m ³)	ϕ
5.25	6	7.7	2660	1490	0.44

3.3.2 Measurements

Bedload transport measurements

In the Armfield flume, the gravel was collected at the outlet of the flume in large construction bags which were weighed using a scale suspended from a crane. For this installation, the gravel were weighed wet, thus a correction was made. The correction factor was deduced by letting the sediments dry completely and taking several measurements. The maximum error for these measurements is 1%, mainly due to the approximative correction from wet to dry sediment — which is not linear.

To obtain a high temporal resolution for the bedload transport rates, my accelerometer measurement systems were also used (section 3.1.3.3). On this installation, six of them were placed at the outlet of the flume (figure 3.12). It allows the obtaining of better accuracy and variability

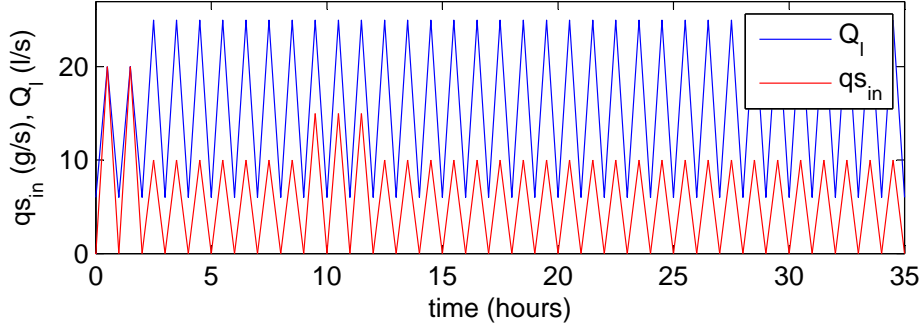


Figure 3.14: Experimental conditions imposed at the inlet of the Armfield flume during the flood experiment.

information on the channel width. The elevation of the plates and their distance from the outlet had to be adjusted in order to capture the impact of every particle and not to disturb the flow. Their position were chosen to avoid particles sticking between plates — which has the result of changing the vibration characteristics of the plates — and impacting two side-by-side plates at the same time. The simultaneous acquisition of the data from the six accelerometers was performed with a National Instrument acquisition board using Matlab.

Bed and water elevation measurements

Compared to the 2D-flume, the complexity of the bed evolution prevents the use of simple camera techniques for monitoring the bed evolution. As a result elevation scans were only occasionally conducted to give an idea of the topographical changes. The scanning is made using eight ultrasonic probes fixed to a motorized cart moving at a constant speed above the flume. Before and after each run the bed elevation was measured, but during the experiment only the water surface elevation could be estimated.

3.3.3 Summary of experiments

Similarly to the 2D-flume experiments, runs with constant parameters were performed. Two long runs were conducted for different flume inclinations and water discharges, keeping the same qs_{in} . These two runs aim to compare some results with the 2D-flume experiment. Also a flood experiment was carried out. It was composed of a series of 35 floods, lasting one hour each. The water discharge and qs_{in} peaks were respectively around 20 l/s and 10 g/s (figure 3.14). This data will give information in unsteady conditions (but periodic) and better comparison with the Navisence data (appendix D). Indeed, during summer time, regular daily flood can be observed at the Navisence measurement station due to daily snow/glacier melt.

Table 3.5: Parameters of runs at constant Shields stress conducted on the Armfield flume.

name	α (°)	t_{exp} (hours)	Q_l (l/s)	S_{hini}	qs_{in} (g/s)
arm1.4deg	1.43	16	10	0.065	0.0185
arm2deg	2	32	7.5	0.08	0.0185

Chapter 4

Bedload transport analysis in steep channels

This chapter is dedicated to the characterization of the bedload transport variability in steep channels. First, for this kind of analysis, the importance of the sampling time is emphasized. Second, the measurements collected from the 2D-flume experiment show strong intermittency. This variability is dependent on the experimental parameters. Finally, it is shown that the present experimental data are not explained by common theories or empirical equations. Several causes are then evoked.

4.1 Data characteristics

In this section, the data are described. Their particularities, the computed variables and the statistical significance are presented. Particularly, the importance of the sampling time, the data stationarity and the relevant system scales are pinpointed.

4.1.1 Preliminary analyses

4.1.1.1 Data summary

The data set is composed of bed profiles with sampling period of 1 s and bedload transport rates with a resolution time scale as low as 0.01 s. However, in the following, when the exact time arrival of each particle is not required, time series of sediment mass accumulation measured with a sampling interval of 1 s are used. The bedload transport rate qs , which is measured at the outlet of the flume, does not give spatial information along the channel. However, it gives an interesting signal, representing the modifications of the inlet signal qs_{in} by the morphodynamics processes occurring in the channel.

The flume angle α ranges from 2° to 5° leading to ranges of 2.02° to 4.66° and 1.7° to 5.17° for the time- and space-averaged channel slope Θ_m and instantaneous space-averaged channel slope Θ respectively. The flow and bed evolution were 2-dimensional for all of the experiments, except at the flume angle 5° . For flume inclinations close to 5° and higher, h becomes too small compared to d_{50} leading to important 3-dimensional effects. Temporary banks and divagation patterns appear especially for a low S_{hini} preventing the recording of bed and water levels. However, for S_h greater than S_{hini} , it was possible to take measurements at these large angles as h was higher. The main experimental parameters and mean measured variables are summarized in table 4.1.

Although the external parameters, i.e. water discharge Q_l and input solid discharge qs_{in} , remains steady, significant fluctuations of the different variables are observed during the runs even after reaching the stationary state. In particular, the variations of the global channel slope Θ are relatively

strong. Chapter 4 is dedicated to this particular point which is essential for the understanding of the morphodynamics of steep channels and their stability.

α is also an important parameter which plays a role in determining the available flow energy, for instance by changing the critical Shields stress S_{hc} (equation 2.11). Indeed, the stress transmission from the flow to the bed, permitting entrainment of particles, is observed to be weaker in steep streams, i.e. for streams with low relative depth, increasing S_{hc} [Recking, 2008; Recking *et al.*, 2009b]. Some signs of this slope effect are probably hidden in my bedload time series.

Fluctuations of Θ induced fluctuations in $S_h(t)$. However, the mean Shields stress S_h keeps a value close to the initially set value S_{hini} . For all the runs starting with the same S_{hini} , S_h does not change significantly for different input sediment rates (table 3.2), whereas a slight increase of Θ at the beginning of the run is observed for runs with high qs_{in} . This slope increase shows the adaptation of the bed to the imposed external conditions, a higher Θ being required to transport the higher sediment feeding rate (keeping the same S_h).

In figure 4.1, S_h of the conducted experiments are shown as a function of Θ_m . The black squares show S_{hini} chosen for the main set of runs — at low S_h . The red dots represent the computed S_h for the corresponding runs. It confirms that S_{hini} has the same value for the four different α tested. The circles represent all experiments including experiments with the highest bedload transport conditions. S_h values are bounded between 0.08 and 0.12, whereas the mean bedload transport rates are spread out over nearly two orders of magnitude — from 0.19 to 9.35 g/s. It is commonly reported that, in steep streams, S_h remains relatively close to S_{hc} [Church *et al.*, 1998]. Strong changes in bedload transport rates are found to be related to very small fluctuations in S_h [Recking *et al.*, 2009b]. This might be one of the reason that bedload transport equations, especially those using an incipient motion threshold, do not work well in the steep slope case (section 4.1.1.3).

4.1.1.2 Situation of the data in bedload studies

In contrast to the literature, my idealized experiments were designed specifically to understand the morphodynamics of steep channels. S_h was then chosen relatively low to observe weak bedload transport conditions. This is verified in figure 4.1 where the partially mobile grains domain is delimited by two slope-dependent equations determined by Recking [2010]. The lower bound corresponds to the critical Shields stress S_{hc} as expressed in equation 2.11. Interestingly, S_{hc} increases for steeper channels. This behaviour could be due to the existence of a complex velocity profile characterizing gravel bed river flows [Ferro & Baiamonte, 1994; Katul *et al.*, 2002; Franca, 2005]. Note, however, that the corresponding flow velocity threshold in my experiments decreases with increasing bed steepness, as commonly reported [Whitehouse & Hardisty, 1988].

The upper bound of the domain, defined by

$$S_{hup} = 0.65 \tan(\Theta)^{0.41}, \quad (4.1)$$

separates the partial transport regime from the high transport regime, where the power exponent in the bedload formula differs [Recking, 2010].

Compared with the Shields diagram (figure 2.2), for observed boundary Reynolds numbers between 550 and 700, the corresponding Shields stresses S_h lie between 0.05 and 0.06 depending on the method that was used to fit the data [Buffington, 1999]. These Reynolds numbers are the lower limit for the rough flow domain where a value of 0.06 for S_{hc} is commonly used. This value of S_{hc} is slightly lower than my observations, probably due to the effects of the slope as mentioned previously and also to the different motion threshold definitions. Recall that Shields' work contains

Table 4.1: Experimental measurements and bulk parameters: Cv the coefficient of variation of the solid discharge qs , Θ_w the global free surface slope, τ_b the corrected bed shear stress and S_h the corrected Shields stress.

name	α ($^\circ$)	qs (g/s)	Cv	Θ_w ($^\circ$)	h (m)	Fr	Re	U (m/s)	τ_b (m ² /s)	S_h
2deg3v	2.0	0.22	2.52	2.02	0.029	1.04	596	0.56	9.1	0.088
2deg6v	2.0	0.59	1.83	2.33	0.028	1.09	633	0.57	10.3	0.099
2deg10v	2.0	1.14	1.42	2.33	0.028	1.10	632	0.58	10.2	0.099
2deg15v	2.0	1.67	1.19	2.41	0.027	1.17	626	0.60	10.0	0.097
3.2deg3v	3.2	0.21	2.84	-	0.021	0.97	-	0.44	-	-
3.2deg3v(b)	3.2	0.23	-	3.02	0.021	0.96	637	0.44	10.4	0.100
3.2deg4v	3.2	0.32	2.33	2.98	0.021	0.95	636	0.44	10.4	0.100
3.2deg5v	3.2	0.45	2.14	3.11	0.021	0.99	641	0.45	10.5	0.101
3.2deg6v	3.2	0.54	2.00	3.16	0.019	1.13	617	0.49	9.8	0.094
3.2deg10v	3.2	1.02	1.45	3.28	0.018	1.22	611	0.51	9.6	0.092
3.2deg15v	3.2	1.53	1.20	3.55	0.019	1.16	648	0.50	10.8	0.104
4deg3v	4.0	0.20	2.97	3.76	0.016	1.14	618	0.45	9.8	0.094
4deg4v	4.0	0.32	2.39	3.96	0.015	1.31	605	0.49	9.4	0.090
4deg5v	4.0	-	-	3.94	0.014	1.34	598	0.50	9.2	0.088
4deg6v	4.0	0.55	2.08	3.96	0.016	1.19	626	0.47	10.0	0.097
4deg10v	4.0	0.99	1.56	4.12	0.014	1.39	603	0.51	9.3	0.090
4deg15v	4.0	1.49	1.31	4.12	0.014	1.42	599	0.52	9.2	0.089
5deg3v	5.0	0.20	3.34	4.71	0.011	1.45	563	0.47	8.1	0.078
5deg6v	5.0	0.57	2.15	-	-	-	-	-	-	-
5deg10v	5.0	0.97	1.67	-	-	-	-	-	-	-
5deg15v	5.0	1.47	1.36	-	-	-	-	-	-	-
3.2deg6v+	3.2	0.60	1.24	2.85	0.024	1.07	648	0.52	10.8	0.104
3.2deg3v+	3.2	0.19	2.69	2.71	0.027	0.86	685	0.44	12.0	0.116
3.2deg15v+	3.2	1.62	1.20	2.90	0.024	1.05	659	0.51	11.1	0.107
5deg3v+	5.0	0.12	4.25	4.18	0.014	1.38	610	0.51	9.5	0.092
5deg15v+	5.0	1.62	1.19	3.97	0.015	1.19	625	0.46	10.0	0.097
5deg6v+	5.0	0.53	2.00	3.97	0.016	1.17	630	0.46	10.1	0.098
4deg20v	4.0	2.19	1.03	3.44	0.019	1.17	646	0.51	10.7	0.103
4deg20v(b)	4.0	2.11	0.99	3.61	0.019	1.16	664	0.51	11.3	0.109
4deg36v	4.0	5.74	0.73	3.69	0.020	1.18	681	0.52	11.9	0.115
4deg48v	4.0	9.35	-	3.89	0.019	1.24	687	0.54	12.1	0.117
4deg45v	4.0	8.35	0.58	3.72	0.019	1.22	675	0.53	11.7	0.113
3.2deg45v	3.2	7.95	0.56	3.55	0.019	1.22	659	0.53	11.1	0.107
5deg45v	5.0	8.00	0.51	4.39	0.017	1.22	682	0.49	11.9	0.115

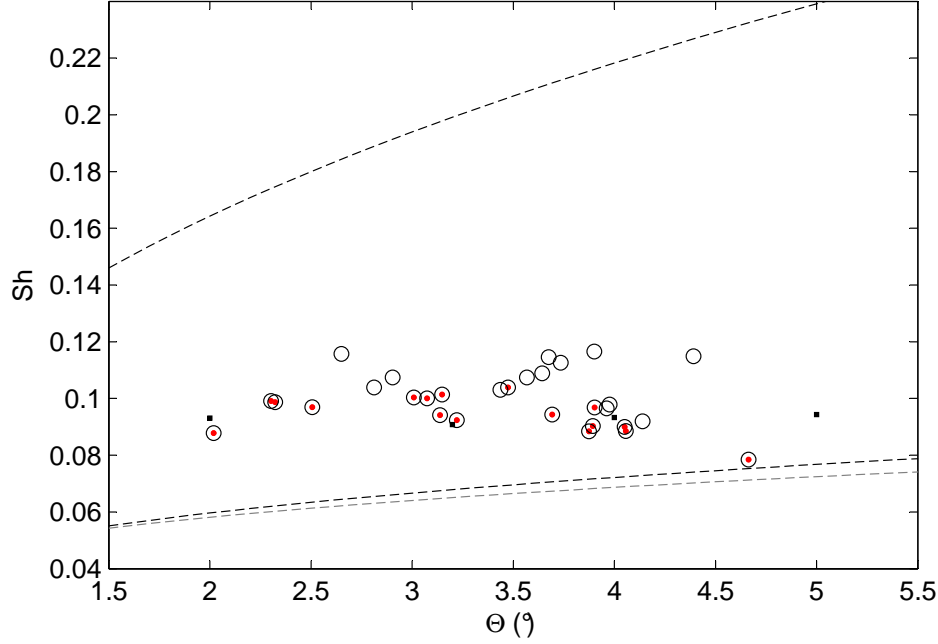


Figure 4.1: Measured S_h for the different runs (red dots: main set of runs at constant S_h , black circles: all runs) and S_{hini} (black squares) as a function of Θ . The dashed lines delimit the partial transport regime defined by equations 2.11 and 4.1.

some imprecision and subjectivity [Buffington, 1999], and that S_{hc} should be only considered as a reference instead of a strict motion threshold. Thus, equation 2.11 seems to be a good alternative for this flow strength reference (section 2.1.2.2).

Note on the sampling time

Several studies already examined the effects of sampling time and they pinpoint that statistics deduced from time series depend on the duration and frequency of the sampling. This is especially the case when studying the stochastic processes of bedload transport. Indeed, to describe the characteristics of the shortest events, such as erosion/deposition of a single grain, a high sampling frequency is necessary.

The determination of scaling laws is also a common topic to generalized the statistics to data which were measured at lower sampling frequency [Singh *et al.*, 2009; Fienberg *et al.*, 2010]. Recently, some studies have shown that it is not obvious that bedload transport rate fluctuations are bounded in natural streams ([Heyman *et al.*, 2013], similarities with granular dynamics). This emphasizes the difficulty of extrapolating data at other scales — shorter or larger, see Fienberg *et al.* [2010] — from data measured at a given sampling frequency. The high sampling frequency and long duration of my data, compared to common studies, permits correct insight in bedload transport dynamics.

4.1.1.3 Bedload transport equations

Although most bedload transport equations are expected not to work well with my data, it is still interesting to make some comparisons, at least with some recent or classical equations. This allows providing of context for my data and inferring specific behaviours. Some hypotheses concerning the differences found between equations and data have already been mentioned.

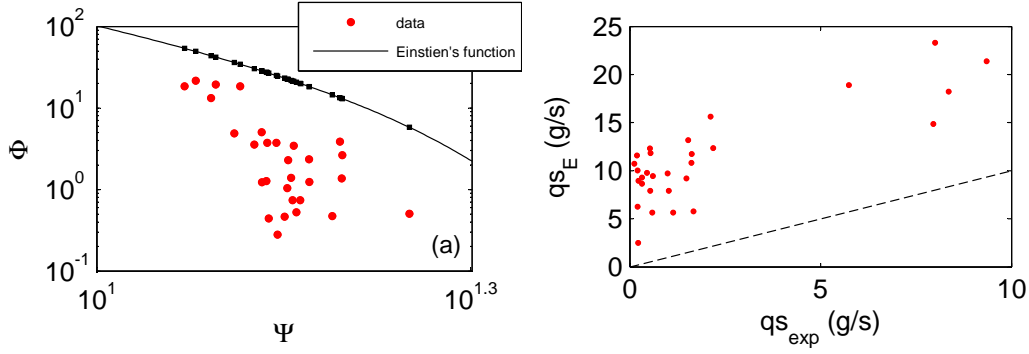


Figure 4.2: (a) Theoretical values given by the Einstein [1950] bedload function and experimental data. (b) Bedload transport rate qs_E deduced from the Einstein [1950] function against the measurements.

Two classic bedload transport equations were tested, a stochastic one from Einstein [1950] and an empirical one from Recking [2010]. These equations — written in section 2.1.3 — should model the data better than most other bedload transport equations for steep flow conditions close to S_{hc} .

In figure 4.2(a), the Einstein's stochastic function $\Phi = f(\Psi)$ is plotted side-by-side with the empirical values (equations 2.5 and 2.7). The data are not well represented by this bedload function. A difference up to two orders of magnitude is observed, especially for low transport rates (figure 4.2).

In the case of the Recking's formula, the data are situated in the partially mobile regime (figure 4.1) and should be better represented by equation 2.9. Figure 4.3 shows relatively good agreement between the measured data and this expression. At least, the order of magnitude is respected for many of the runs, nevertheless, a few data points are still almost two orders of magnitude away from the computed values. This formula seems to overestimate bedload transport for low S_h and underestimate it for higher S_h .

The data do not fit well on the two equations tested. The main reason for this deviance might be due to the sediment supply (section 4.2.2.3). Indeed, several runs with almost the same Shields stress and channel slope produce a wide range of mean bedload transport rates due to different sediment feeding. See, also for instance, the sharp outlier in figure 4.3(a) from the run *3.2deg3v+* where a very low qs_{in} and a moderate S_h were imposed. Thus the sediment supply could be one of the main parameters for sediment transport estimation.

4.1.2 Data statistics and consistency

4.1.2.1 Stationarity

In order to compute correct statistics, the data should be stationary. This means that, at the scale of the experiment, the cumulative bedload transport rate $qs_{out,cum}$ should follow a linear trend. In the case of my data it also implies that, at the time scale of each run, the input solid discharge qs_{in} should be equal to the mean output solid rate qs_m . The stationarity of the data is verified graphically by plotting $qs_{out,cum}$. The trend of the data should follow a straight line with the same slope as the curve representing the cumulative input solid discharge $qs_{in,cum}$. An example of a stationary time series (run *3.2deg6v*) is presented in figure 4.4. The two curves for input and output solid discharges follow the same trend.

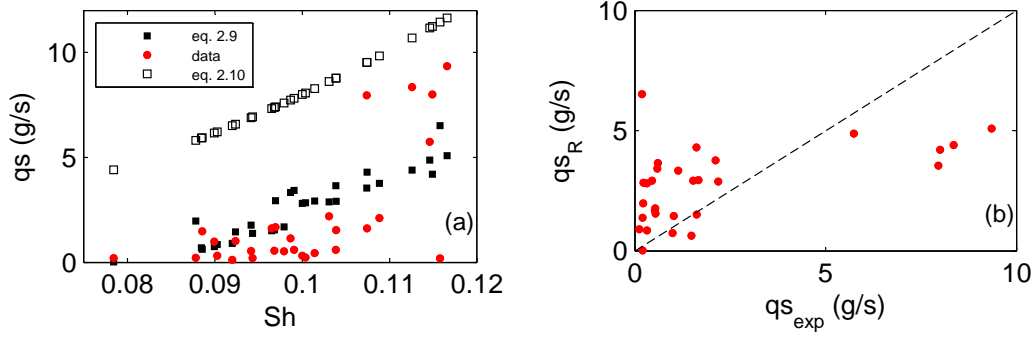


Figure 4.3: (a) Values computed from the Recking [2010] equations 2.9 and 2.10 side by side with experimental data. (b) Comparison between the bedload transport rate qs_R from equation 2.9 and experimental values.

Most of the time, an adjustment of the global channel slope Θ was observed depending on the magnitude of the experimental parameters. The flume was artificially flattened before each run for the same initial conditions and for the verification of the mass balance over the whole experiment. Thus, qs can be significantly larger or lower shortly after the start of the runs. As a certain duration was needed to be sure of obtaining a natural grain packing in the flume. The adjustments last one to five hours — in the worst case with high α and low qs_{in} .

This lag time before reaching the beginning of the stationary state should not be confused with the time taken to observe the stationary state and to record all of the fluctuations of the system as discussed in the following. The main statistical parameters, like the mean qs_m , the standard deviation s and the coefficient of variation Cv (equation 2.12) are computed on the stationary part of the time series. All other statistical parameters, if not otherwise specified, are computed from the stationary part of the data.

4.1.2.2 System size and time scale

To fully characterize the system studied the experiments have to be conducted for long times relative to the system response. The chosen experimental duration is then dependent on the external parameters — Q_l , qs_{in} and α — which drive the processes. If stationary conditions are met, it means that the dynamic stationary equilibrium state of the system is recorded (section 2.3.3), but it does not imply that all of the internal fluctuations of the system evolution are captured. Indeed, a certain recording duration in the stationary state is needed to observe the whole range of fluctuations. One way to verify that all of the fluctuations are recorded is to represent the mean outlet solid discharge as a function of the sampling duration and see when it converges. After convergence, the mean value fluctuates around a unique value, meaning that the largest possible fluctuation time-scale has been recorded. This happens approximately after a duration of 15 hours for the lowest qs_{in} .

Otherwise, the computation of the power spectrum of qs gives a more precise estimate of the largest fluctuation time-scale. The fluctuations, whose their energy is represented for each frequency f on the spectrum (section 4.2.1.3), are bound by the size of the system and the magnitude of the external parameters. For each frequency f , there exists a time scale $t = 1/f$ of the corresponding fluctuations. This leads to the definition of the largest fluctuation time-scale T , which is called the saturation time scale of the system [Jerolmack & Paola, 2010]. On the power spectrum, T corresponds to a change in trend of the spectral density (figure 4.5). For a time scale $t < T$, the spectral density represents the intensity of the fluctuations characterizing the system at the scale

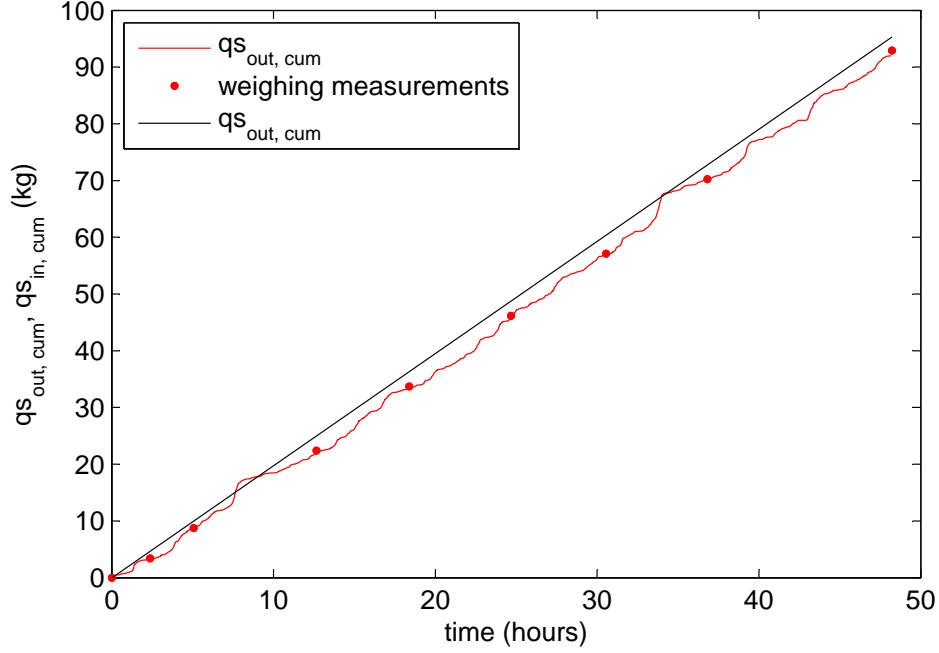


Figure 4.4: Time series of the accumulated sediments over run *3.2deg6v*, the straight line represents the constant feeding, the red curve the continuous outlet measurements and the red dots the outlet discrete measured weight.

t . For $t > T$, the white noise regime is reached. Note also that the spectrum was computed on the stationary part of the time series. Therefore, to be sure of observing the whole range of fluctuations, the time series must last longer than T .

Saturation time scale T of the runs

The saturation time T is greatly dependent on the different parameters. As seen previously, T is dependent on the size of the system, i.e. on the flume width and length, which is not varied here, and also on the external conditions. Jerolmack & Paola [2010] give the following relation,

$$T \sim L^2 / qs_{in}, \quad (4.2)$$

with L the system size. For the main set of runs at constant S_h , the only external parameter to be varied was qs_{in} , and it is also the relevant parameter for higher shear stress experiments — where qs_{in} was also increased. In figures 4.6(a) and 4.6(b), representing T as a function of qs_{in} , T decreases as a power law with imposed transport rates, for all runs. The trend given by equation 4.2 is plotted on the figures, showing a relatively good agreement.

Interestingly, T is also dependent on α , particularly for a weak transport conditions. With increasing α , T increases quasi linearly as shown in figure 4.6(c). It implies that steep channels are subjected to fluctuations at larger time scales than gentle slope channels, requiring longer measurements to study the evolution characteristics of the system. The minimum number of events, i.e. the number of particles flowing out of the flume corresponding to T , was also computed, still in the stationary regime. Its representation as a function of qs_{in} for different Θ (figure 4.6(d)) suggests that a more events have to be recorded for steeper slopes and possibly also for weaker external conditions.

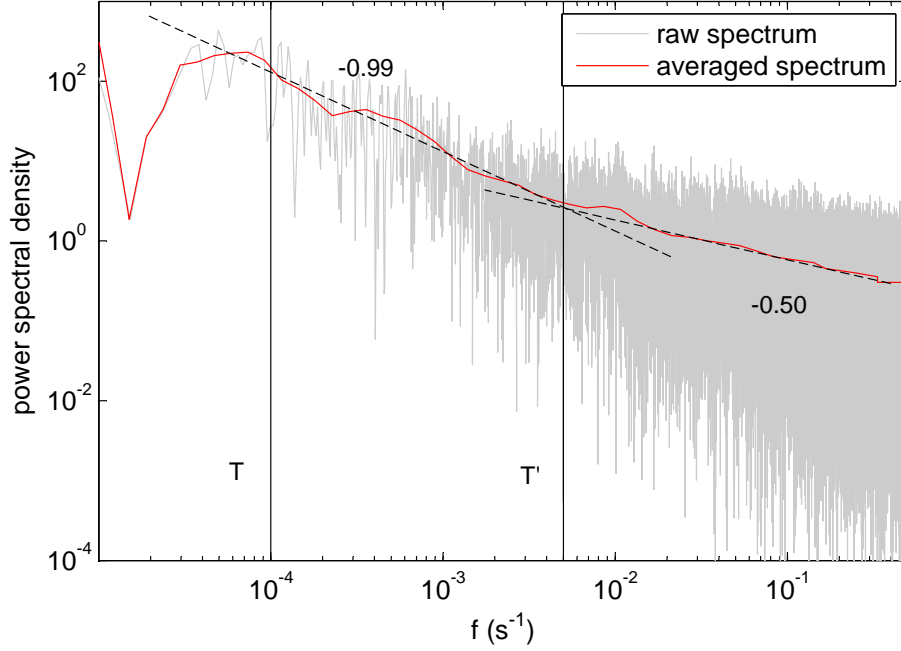


Figure 4.5: Power spectrum of measured outlet solid discharge from run *4deg3v*. The saturation time scale T of the system is estimated around 10000 s ($1/f = 10^{-4}$) and the intermediate time scale T' at 200 s ($1/f = 5 \cdot 10^{-3}$).

In summary, high channel slopes seems to induce an intermittent behaviour. Steep channels require longer experimental runs, especially for low transport conditions, compared to gentle slope rivers. Thus it confirms the initial choice to adapt the run duration according to the experimental parameters (table 3.2).

Natural streams are subject to rapid fluctuations of environmental conditions compared with the time scale to reach a possible bed profile equilibrium. The common interest lies in understand the response of the river to these short-scale events. On the other hand, it is necessary to identify the internal behaviour of the system, i.e. the evolution of the system in a stationary state, by recording the autogenic fluctuations [Jerolmack & Paola, 2010]. That is why most of the runs are conducted in steady conditions — and only a few runs under unsteady conditions.

4.1.2.3 Validation of the experimental methods to solve the problematic

As the main data are from the 2D-flume, which is short and narrow, the question of the influence of the input sediment rate qs_{in} on the outlet measurements arises. Are the bedload transport processes observed independent of the way that qs_{in} is imposed? In other words, I have to verify that I actually observe natural bedload transport behaviours.

First, the probability density function (hereafter pdf) and the coefficients of variation Cv of the time series are compared at different time scales. At all time scales, the fluctuations of qs_{in} are significantly lower than those measured at the outlet. This suggests that the bedload signal measured at the outlet is strongly modified by the processes occurring in the channel.

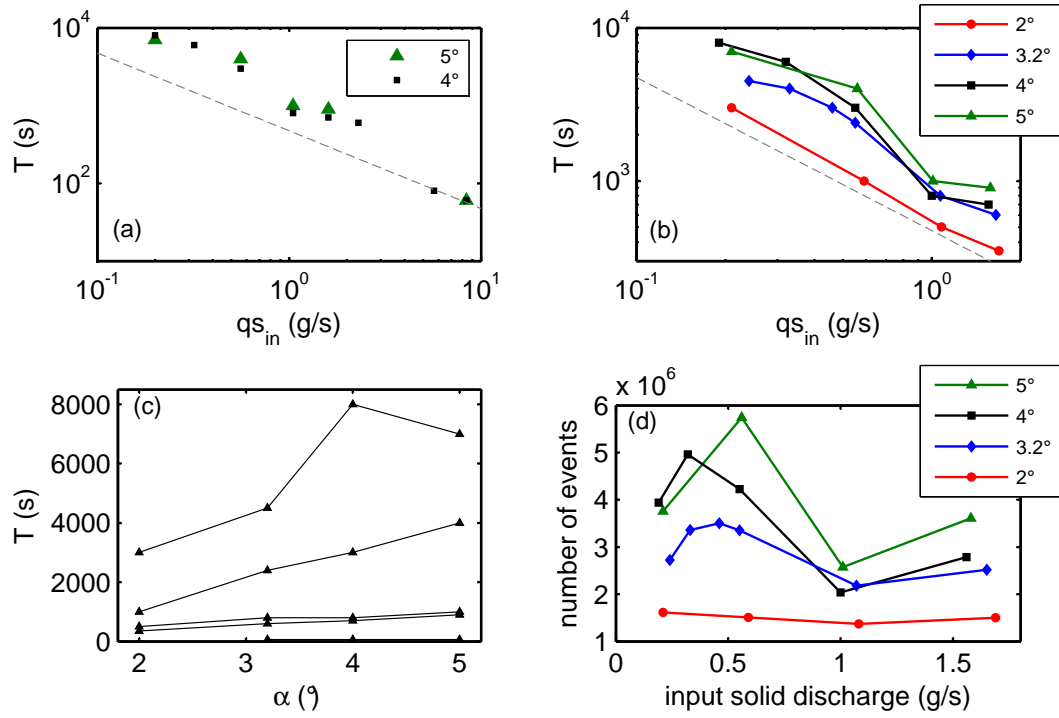


Figure 4.6: Variation of the saturation time-scale T . (a) Dependence on the feeding rate qs_{in} . (b) Zoom on the dependence on qs_{in} for the main measurement campaign at constant S_h . (c) Dependence on the averaged channel slope α for different qs_{in} (low to high rates from top to bottom). (d) Dependence on the number of particles recorded at the flume outlet.

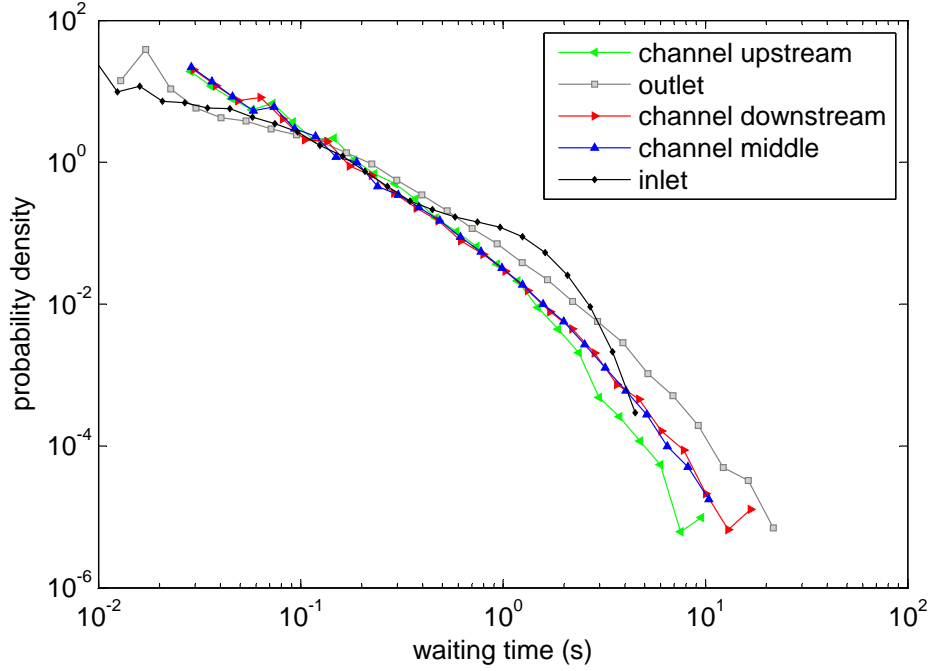


Figure 4.7: Pdfs of waiting time (time between the arrival of two consecutive moving particles) at five different locations along the channel. Data from the accelerometer signal for the two flume ends and from the three cameras for the three locations in the channel.

Second, when comparing pdfs of different statistical variables (waiting time, bedload transport rates at several time scales) at the inlet and outlet, the shapes are significantly different, which implies that natural fluctuations at the different time scales are recorded.

Third, using runs *3.2deg3v+* and *3.2deg6v+*, the bedload transport rate is compared at five locations along the flume, at the inlet, at the outlet and at three different locations along the channel bed (section 3.1.3.4). The pdfs of waiting time, i.e. time between two consecutive moving particles, have the same shape for all locations except for qs_{in} (figure 4.7). The latter do not show large waiting times. Thus the solid discharge seems to adapt quite rapidly in the upstream part of the flume to a natural behaviour due to the interactions with the bed. Note that the tails of the pdfs are larger for downstream locations. This means that for a longer flume, a higher probability of large waiting times, i.e. fluctuations at a larger temporal scale, might be obtained. This is in accordance with equation 4.2 which states that the maximum scale of the fluctuations increases with the system size.

To be sure that the manner in which the system is fed does not significantly influence the bedload transport processes, some experiments were done without sediment input ($qs_{in} = 0$). The pdfs of waiting time recorded at the flume outlet, with and without feeding, are presented in figure 4.8(a) for $\alpha = 3.2^\circ$ and in figure 4.8(b) for $\alpha = 5^\circ$. The shapes are very similar, meaning that the measurements are good representations of bedload transport given that, for no feeding, the behaviour can only be due to the natural bedload transport processes.

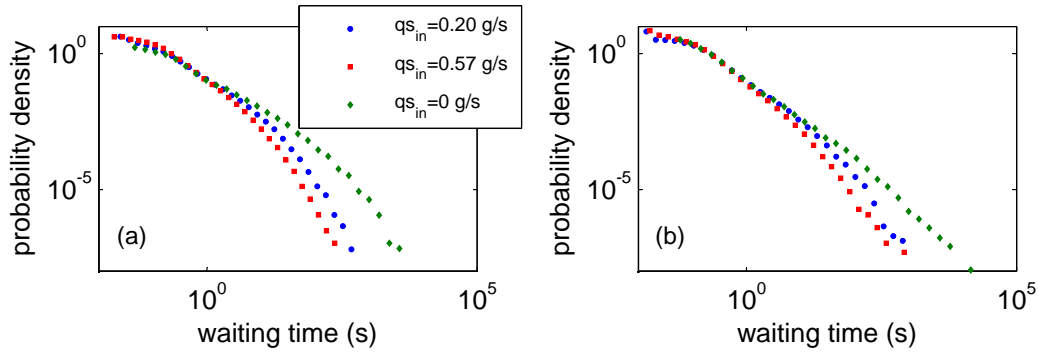


Figure 4.8: Pdfs of waiting time at flume inclinations 3.2° (a) and 5° (b) for three different sediment feeding conditions.

4.2 Bedload transport fluctuations

As previously mentioned, one of the objectives of this thesis is to characterize the fluctuations of bedload transport rates. In this section, several statistical tools are used to define and compare the variability of bedload transport from the bedload data collected on the 2D-flume experiment. First, a general statistical description of the data is presented based mainly on run *4deg3v* which is well representative of low transport and steep channel conditions. Second, I compare the statistics of the different runs to discuss the influence of the experimental parameters on bedload transport variability.

4.2.1 Quantification of the variability

In this section, several tools to study bedload transport time series and describe their fluctuations are used. First, a visually observation of the time series gives preliminary information on the data. For instance, figure 4.9 shows the time series of qs for run *4deg3v*. The signal appears very intermittent with sharp peaks and periods with very low intensities in between. Zooming in on the time series, I observe that most of the time the rate is zero even though a constant non-zero input solid rate was fixed.

4.2.1.1 Mean bedload transport rate and coefficient of variation

Simple statistical numbers, like the mean and the standard deviation computed on several scales, give interesting conclusions that are confirmed and specified using more sophisticated computations. The mean bedload transport rate qs_m and Cv for the different runs are compiled in table 4.1. In figure 4.9, the time series is superimposed on the averaged rates computed for different time scales (for run *4deg3v*). For all these averaged rates, up to around two hours averaging, the fluctuations are still significant which show that bedload transport is subject to strong fluctuations on a wide range of time scales.

To compare the different runs, Cv (equation 2.12) was computed for each run at several time scales, down to one second — see Fienberg *et al.* [2010] for another example. In figure 4.10, Cv decreases through time scales even for relatively large time scales, i.e. for low sampling frequencies. The evolution of Cv is different in shape and magnitude depending on the experimental parameters as detailed in the section 4.2.2. In the following, unless otherwise specified, the value of Cv corresponds to the computation at scale 1 s.

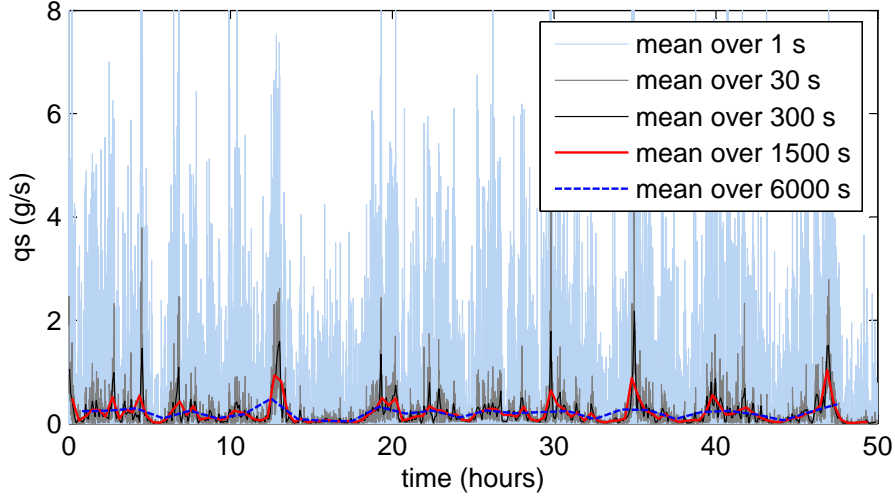


Figure 4.9: Time series of the outlet bedload transport rate for $4deg3v$ and the corresponding averaged rates for different time scales.

At the smallest time scales, the standard deviation s remains well above qs_m , which confirms the high variability of the processes. For especially steep and low transport conditions, s is above qs_m even at large time scales — $Cv > 1$ in figure 4.10(a). This emphasizes the intermittency of bedload transport in such conditions, at all temporal scales shorter than T .

4.2.1.2 Bedload transport rate and waiting time pdfs

The probability density function (pdf) is a common tool to study the probability of occurrence of a given event. In this case, the pdf of bedload transport rates represents the distribution, in term of normalized frequency, of the measured rates (at the scale 1 s). Figure 4.11 gives the pdf for run $4deg3v$. From a high probability of observing a rate close to zero, the function continuously decrease with higher rates. However, the decrease is much slower at the highest rates, suggesting that relatively frequent periods of high rates can occur. For instance, there is a large different in probability between rates of 2 g/s and 4 g/s which is significantly reduced between rates of 10 g/s and 12 g/s.

The intermittency and, particularly, periods with no transport are quantitatively seen in the pdfs of the waiting times (figure 4.12). The waiting times are up to several minutes for a constant input rate of around one particle per second and short waiting time are frequent. This means that grains accumulate during long time in the channel and are temporary evacuated at a much higher rate. The tail of the waiting time pdf is larger than the exponential distribution (figure 4.12), meaning that long periods without transport are relatively frequent, compared to classical precesses well represented by the exponential distribution.

4.2.1.3 Bedload transport rate power spectrum

The power spectrum, via the computation of the power spectral density (PSD) and its average, is an efficient tool to reveal the energy distribution of time series across time-scales. Commonly, the power spectral density is expressed in frequencies, as a good estimate is given using the fast Fourier transform (FFT) [Schmid, 2012]. Generally, scaling regimes — linear trends across certain ranges of frequencies in log-log plot — can be detected on this spectrum underlying the global structure of the data.

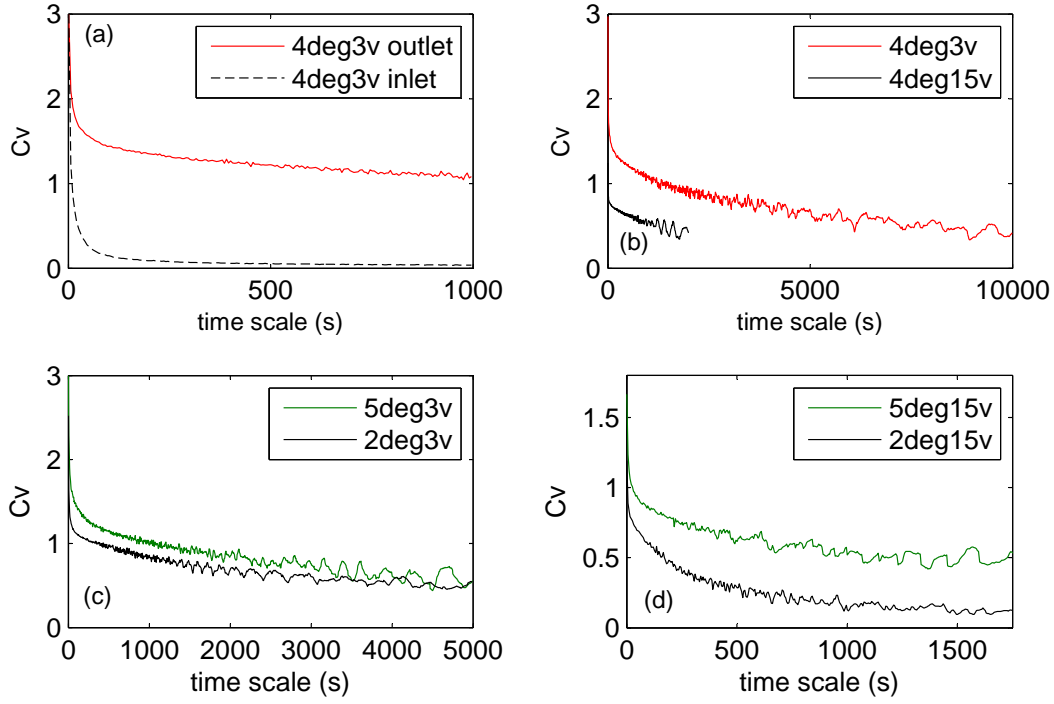


Figure 4.10: Coefficient of variation C_v of bedload transport rates, computed at several time scales (section 2.2.2) for different runs. (a) Comparison with the inlet measurements. (b) Effects of $q_{s_{in}}$. (c) and (d) Effects of α for low and high $q_{s_{in}}$ respectively.

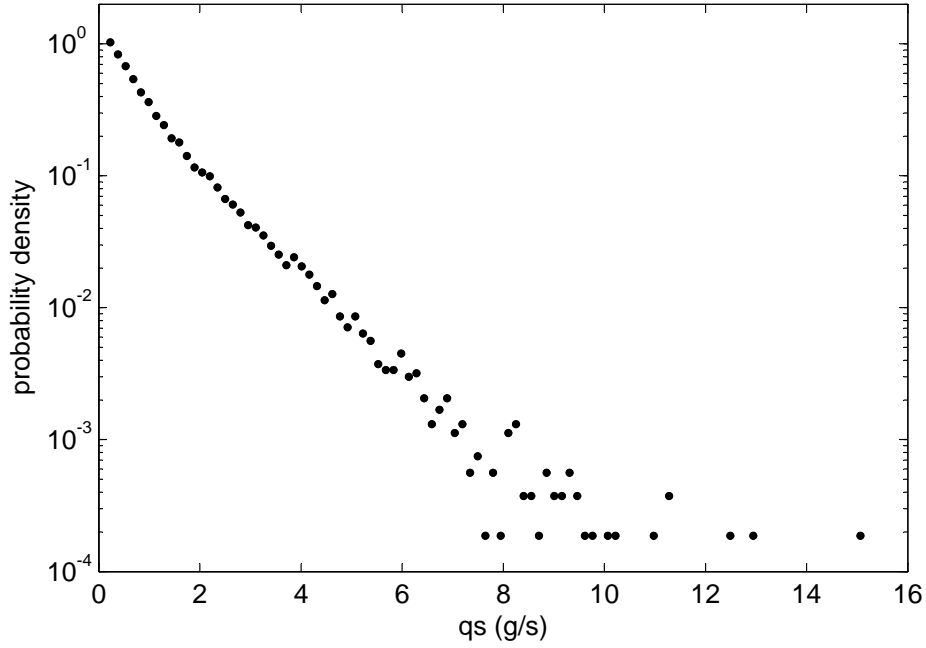


Figure 4.11: Probability density function (pdf) of bedload transport rates for run 4deg3v.

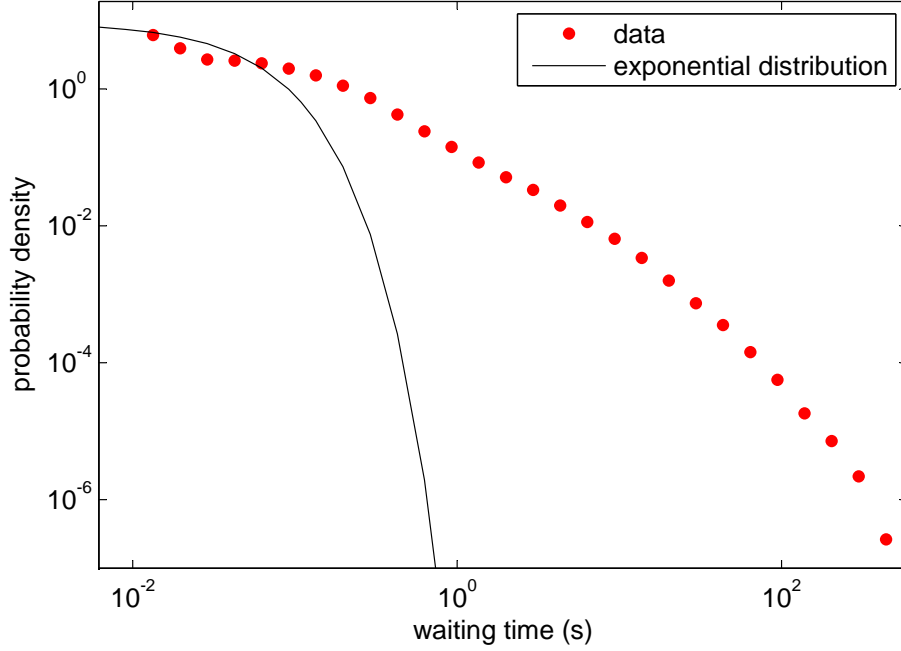


Figure 4.12: Pdf of the waiting times for $4deg3v$ and comparison with an exponential distribution.

In figure 4.5, the power spectrum density of run $4deg3v$ shows an energy distribution over a broad range of frequencies. The continuity of this distribution and the absence of significant humps suggest that bedload transport rates present an erratic variability from seconds to several hours without periodic or quasi-periodic patterns. However, some interesting structures are present, enlightened by the analysis of the spectral slope, i.e. the decreasing trend on the averaged spectrum in log-log plot. The power spectral density decreases from a plateau at low frequency — energy of the largest time-scales — to the high frequencies — short time scales. The spectral slope is larger at intermediate frequencies than at the highest frequencies. In the following, the use of the time-scale $t = 1/f$ is often preferred to the frequency to underline the temporal structure of the data.

Three regimes are identified in the power spectrum. First, a range of constant energy is present at low frequencies. This energy plateau means that above a certain time-scale, defined as the saturation time-scale T (section 4.1.2.2), the energy fluctuations are bounded. This limitation is a characteristic of the studied system under certain external conditions — T depends on the system size and the experimental conditions (equation 4.2). The maximum energy of bedload transport fluctuations is limited by the size of the flume, the flume inclination α , the feeding rate of sediment qs_{in} and the water discharge Q_t .

Second, at intermediate frequencies — time-scale shorter than T and longer than T' , an intermediate characteristic time-scale — a fast linear log-log decrease of the energy is observed across frequencies. It suggests that the release of energy by the system (bedload transport) is made in a wide range of intensity in this regime with a higher intensity for larger time-scales.

Finally, at the highest frequencies — time-scale shorter than T' —, the energy decrease is also present but with a much lower spectral slope. It might indicate the presence of relatively strong energetic fluctuations at the shortest time-scales compared with the intermediate time-scale — still

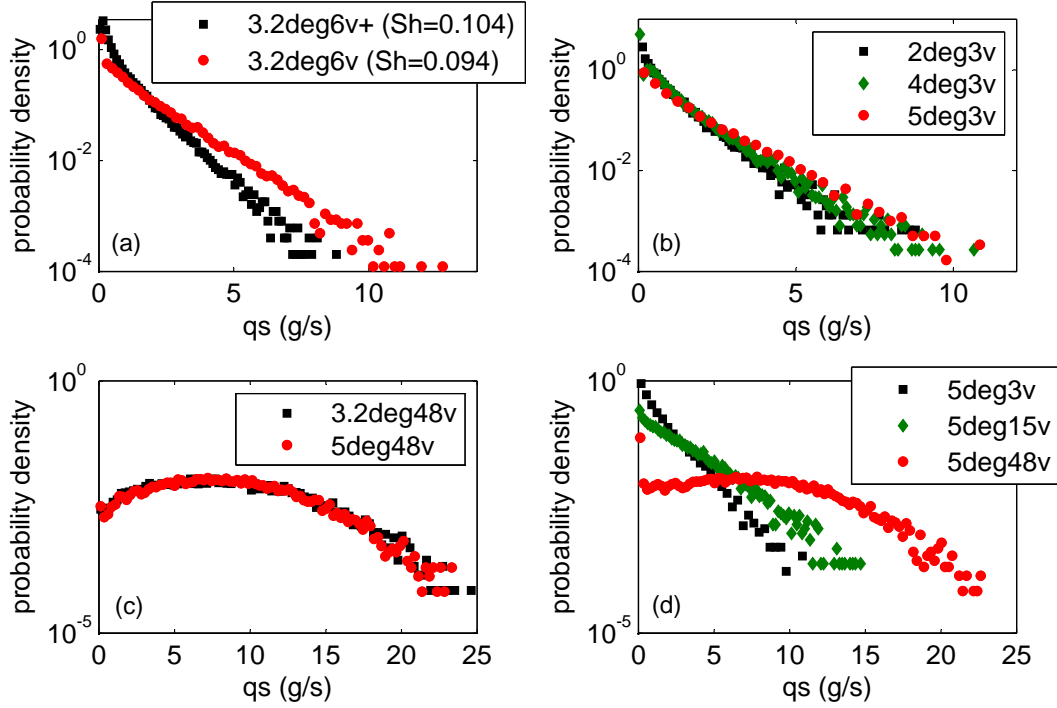


Figure 4.13: Pdfs of bedload transport rates. (a) Comparison with different S_h . (b) Comparison with different α at low qs_{in} . (c) Comparison with different α at high qs_{in} . (d) Comparison with different qs_{in} .

distributed randomly across time-scales. Moreover, noting the shape of the raw spectrum envelope (much wider at high than intermediate frequencies), it seems that an additional phenomenon takes place at small scales compared with the intermediate scale.

The range of these three regimes varies from run to run according to the experimental parameters. The analysis of the spectral slopes, the saturation time scale T and the intermediate time scale T' for each parameter is presented in the following sections.

4.2.2 Effects of experimental parameters

The range of S_h being narrow in the main data set with constant S_{hini} (red dots in figure 4.1), the bulk flow conditions are considered to be the same. These runs are used to precisely study the effects of α and qs_{in} in sections 4.2.2.2 and 4.2.2.3 respectively. Although other runs were conducted at higher S_h , influence of a wide range of bulk flow conditions is difficult to assess independently of qs_{in} .

4.2.2.1 Shields stress

Several runs were conducted at moderate S_h , but the effects of very large S_h cannot be studied with this data set. However, a general increase of S_h — associated with an increase of qs_{in} — leads to a lower Cv . A few runs were performed with moderate S_h and still low qs_{in} , showing also lower Cv — run names with + in table 4.1. This means that increasing the bulk flow conditions reduce the variability. Interestingly, the data show the possibility of increasing bedload transport by imposing a high qs_{in} without significantly changing the flow conditions. This fact is probably only

seen at low flow conditions as the relation between bedload transport rates and the flow strength tends to be more univocal for high S_h .

The comparison between the bedload transport rate pdfs of runs *3.2deg6v* and *3.2deg6v+*, conducted at same α and qs_{in} , shows interesting differences in the distribution of probability. First, the distribution is larger in the case of lower S_h with a much higher maximum rate. Second, at rate close to zero, the probability is higher for high S_h than for low S_h , whereas it is the contrary at high rates. This induces a pdf decrease much slower in the case of lower S_h . It suggests that the relative frequency of high rates — extreme values — is larger for low bulk flow conditions.

4.2.2.2 Flume inclination

The range of α tested, from 2° to 5° , permits to have a precise idea on the effects of the channel steepness on bedload transport variability. Figure 4.14 shows Cv as a function of α for the main data set at low S_h . For the three qs_{in} presented in the figure, the variability increases with α and the relationship is linear.

In figure 4.13, we observe that the increase of α has a similar effect to a low Shields stress on the pdfs. For the highest α tested 5° , the probability density is lower at low rates, and higher at high rates, than the other α . However, this trend seems to be insignificant for strong sediment feeding (figure 4.13). Note that the influence of the channel steepness is also less significant for high qs_{in} from the Cv analysis in figure 4.14. This confirms that steep channels are more subject to fluctuations in bedload transport rates than gentle-slope rivers, especially at low transport conditions.

Looking at Cv for large scales (figure 4.10), Cv remains higher for steeper channels for all qs_{in} . Indeed, for high qs_{in} , variability at larger time-scales is seen to be significantly higher at high slopes than gentle slopes — which was not the case at small time-scales. Therefore the effects of the channel steepness are scale-dependent and are also seen for high transport conditions. This again underlines the important effect of the sampling frequency on the interpretation of the data — and that the use of a sole statistical method to analyse the data is not sufficient.

In the spectral analysis, much higher saturation and intermediate time-scales T and T' are observed for higher than lower α . Thus the bedload transport fluctuations are present on a wider range of time-scales for steeper channels. And the scaling regime of strong energetic fluctuations at low time-scales is more extended towards intermediate time-scales, suggesting that, for steeper channel, the influence of the short-scale fluctuations, like collective motion events, is larger.

4.2.2.3 Sediment supply - input discharge

A wide range of qs_{in} have been tested, thus its influence on the variability of qs can be well interpreted. Figure 4.15 clearly shows a strong dependence of the variability on qs_{in} . The fluctuations are much more pronounced at low transport rates. Cv even decreases as a power law of qs_m , which is also the case for the values of Cv at larger time-scales.

On the pdfs (figure 4.13), the observed influence of qs_{in} on probability distribution is marked. Indeed, from the lowest rate to the highest, the pdfs have a completely different probability repartition and shape. For high qs_{in} , the decrease towards the highest rates is slow at intermediate rates and significantly steepens at high rates. We observe almost the contrary at small qs_{in} , suggesting that extreme pulses of sediment — compared to qs_m — are relatively more frequent at small qs_{in} .

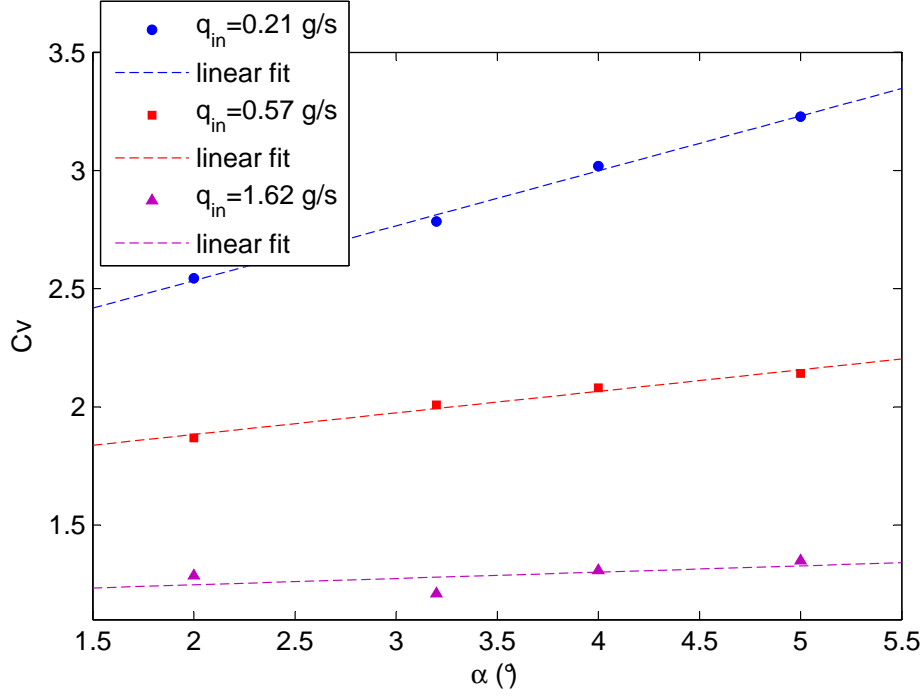


Figure 4.14: Evolution of Cv as a function of the flume inclination for three different solid input discharges.

The spectral analysis shows that T and T' increase with lower qs_{in} , leading to the same effects as an increase of the flume inclination (section 4.2.2.2). The intermittency is also emphasized at low qs_{in} as we saw in figure 4.8, where long waiting times are much more frequent — and long — than at high qs_{in} .

4.3 Discussion

In this section, the variability observed in the 2D-flume is compared with Armfield flume data. The main findings are then summarized and discussed.

4.3.1 Comparison with Armfield flume data

Although a complete data set could not be conducted, the two available long runs are analyzed for comparison with a 3D experiment at a larger spatial scale (the corresponding parameters in table 4.2). Starting from an artificially plane bed, the bed evolves rapidly towards a 3D configuration with the creation of pool-riffle sequences and small subsidiary channels. This new configuration is not fixed, since these bedforms migrate and/or disappear, whereas others develop and grow. A stationary state can still be reached, as shown in figure 4.17 where the cumulative bedload transport rate is represented.

Figure 4.16 shows the time series of run *arm2deg*. The intermittency is well pronounced as expected for such low bulk flow conditions ($S_{hini} = 0.08$). Indeed, the standard deviation is just slightly lower than the mean value and periods with very low transport rates are frequent between intense pulses, similar to what was observed in the 2D-flume experiment.

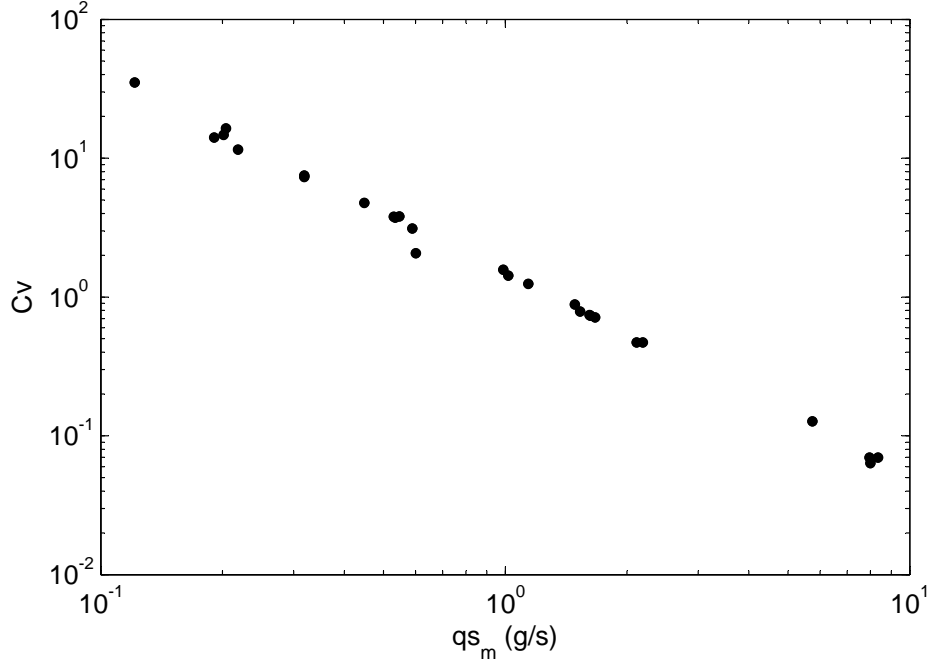


Figure 4.15: Evolution of bedload transport variability, Cv , as a function of the mean solid discharge for all the tested conditions in log-log scales. Note the decreasing power law trend with increasing qs_m .

The value of Cv for the two Armfield runs are plotted side by side with the 2D-flume data in figure 4.18. The two points are very close to the 2D-flume trend. The slightly higher Cv observed can be attributed to the additional variability due to 3D patterns. The lower Cv for the highest flume inclination is explained by the fact that S_h is much higher also. Thus S_h could have a greater influence on variability than the channel steepness at these relative moderate slopes.

4.3.1.1 Lateral variability

The bedload transport rates show strong lateral fluctuations as seen in figure 4.17 where the cumulative rates are plotted for each accelerometer. Clearly, almost all of the bedload at a given time is concentrated on one portion of the channel width [Rickenmann *et al.*, n.d.; Travaglini & Bardou, 2012]. This change from one side of the channel to the other corresponds to the migration of 3D bedforms. Therefore, it is not so surprising that the variability detected from each accelerometer's time series is higher than the variability of the total bedload transport rates at all time scales (figure 4.18). This underlines an important point concerning bedload measurements. The variability is much higher for measurements on a portion of the width and longer sampling are needed for convergence compared to sampling on the whole channel width. Similar issues arise using the other statistical tools. Thus, conclusions from isolated measurements should be drawn carefully as the resulting statistics might not represent the behaviour at the whole channel.

Table 4.2: Experimental parameters of the two long Armfield runs.

name	α (°)	t_{exp}	Q_l	S_{hini}	qs_m	Cv
arm1.4deg	1.43	16	10	0.065	0.0155	0.826
arm2deg	2	32	7.5	0.08	0.0219	0.712

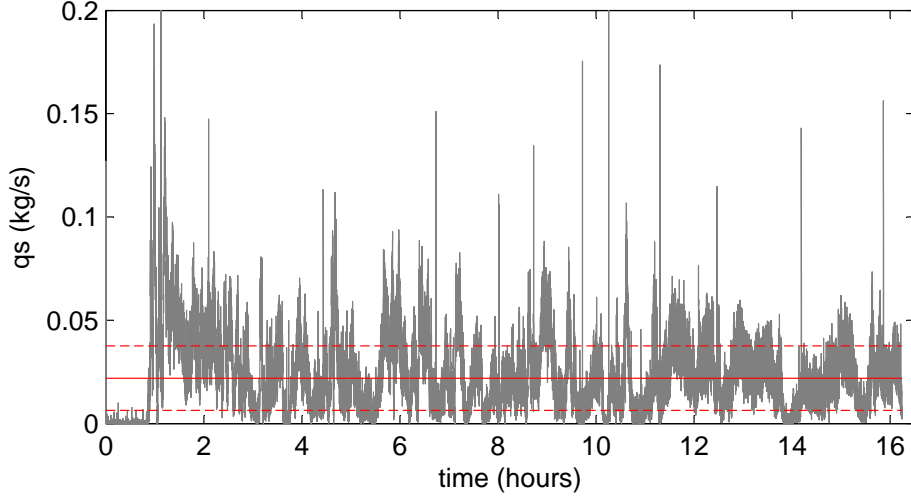


Figure 4.16: Time series of qs in the Armfield flume with an inclination of 2° and $Q_t = 10$ l/s (run *arm2deg*); red lines show the averaged value qs_m and the domain defined by $qs_m \pm s(qs)$ (values computed from the stationary regime).

4.3.2 Conclusion on bedload transport fluctuations

The preliminary analyses of the data show that the particularly extensive collected data in this study is specifically useful to improve our knowledge on the characteristics of bedload transport rate fluctuations, solving classical issues of these type of measurements. The mean stationary bedload transport rates of the runs were first compared with a few existing bedload equations. Although the data were collected from a simple and idealized experiment under steady conditions over many hours in order to obtain stationary state statistics, the equations are not able to represent the data. Many reasons can be given for this disagreement, such as measurement errors, approximate correction of S_h , flow non-uniformity, sediment supply and other phenomena than flow erosion, like granular behaviours in the bed.

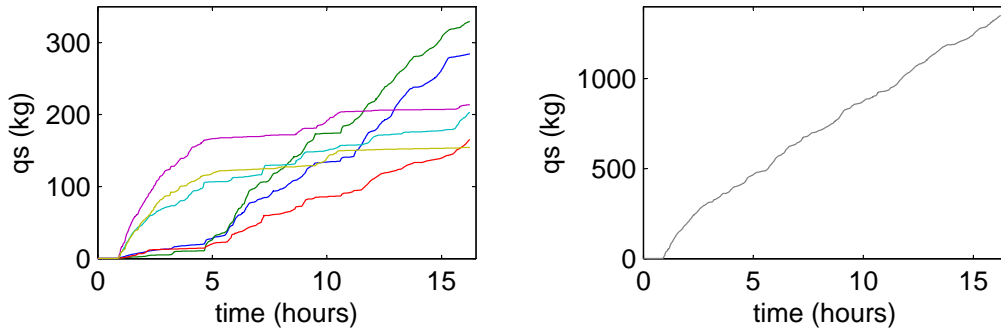


Figure 4.17: Cumulative bedload transport rates measured at the Armfield outlet (same run as figure 4.16), the colors stand for the 6 accelerometers and the black curve for the total bedload transport.

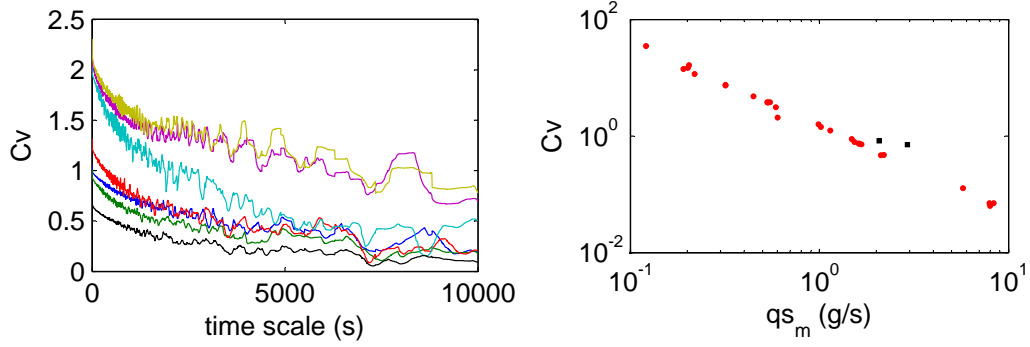


Figure 4.18: C_v of Armfield bedload transport rates (same run as figure 4.16) as a function of the time-scale and comparison with 2D-flume data (red dots), the colors stand for the 6 accelerometers and the black curve for the total bedload transport.

The important question of the sampling time has been discussed. Indeed, the variability should be studied at all time scales for a complete analysis, up to at least one order magnitude larger than the saturation time scale T of the system, corresponding to the largest fluctuation time-scale. It also pinpoints the need to collect data at the correct frequency for long times — depending on the experimental parameters and system size — and to take into account the variability over the width of the channel if the measurement locations are discrete. Moreover, due to the system size and the wide range of environmental conditions, the measurement duration for a natural stream might be even larger than any time series available. This also emphasizes the great interest to conduct flume experiments to understand the natural processes.

The tools to infer the statistical behaviours of bedload transport rates were numerous to cross-checked several interpretations. In addition to simple indicators, like, the mean, the standard deviation and the coefficient of variation, more complex methods and variables were studied, like the pdfs, the waiting times, the evolution of the coefficient of variation across time-scales and the power spectrum.

The analysis of the main experimental campaign (2D-flume) shows that bedload transport rates are subjected to a strong variability on a wide range of scales — from the sampling frequency to several hours. Moreover, it was found that the intermittency significantly increases with increasing channel steepness, decreasing sediment supply and decreasing bulk flow energy. These findings are in accordance with data collected in the Armfield flume. Further, the multitude of runs conducted in the 2D-flume suggests that some variability components seen at high α are significantly lowered — or even suppressed — in strong sediment transport conditions.

In an attempt to account for sediment supply, Recking [2012] determined two equations delimiting the domain of possible bedload transport rates from a large field data set. These two boundaries represent the two extreme cases of no supply and supply limitations. The approach, although not yet permitting the computation of an exact bedload transport rate is in good agreement with the field data tested. The method could not be tested with my data as the equations were deduced from field data where the sediments are poorly sorted. However, this approach suggests that the threshold between partial and full sediment transport for bedload computation (equations 2.9 and 2.10) should depend on the sediment supply. This threshold is lowered when the supply is increased. In my data runs at high feeding rates are better represented by equation for high transport conditions 2.10 than 2.9 (figure 4.3).

Finally, an approach taking account of the sediment supply seems to be a promising way to improved bedload equations, although the fluctuations could not be model except using stochastic formulations. Indeed, at small time scale, the peaks of solid discharge do not depend on the supply variability. Just note that a high supply leads to a more regular conditions, reducing intermittency. Thus, equations developed for high flow conditions should be more adequate in a situation of high supply. This confirms that both qs_{in} , the sediment supply, and flow strength are two input conditions of great importance.

In the following, analysis of the bed evolution shows that the sediment supply implies strong effects on the bed dynamics from small scales (chapter 6) to large scales (chapter 5). This probably leads to the observed dependence of bedload transport rates, and its variability, on the sediment supply. The effects of the granular behaviour of the bed and its relative importance, controlled by the channel steepness and the sediment supply will also be discussed.

Chapter 5

Bed stability at reach scale

In this chapter, the evolution of the global channel variables, i.e. averaged variables at the channel scale, is analyzed in order to investigate the possible causes of the strong observed variability in bedload transport rates. It is found that, in specific circumstances, a stream reach shows strong hysteretic behaviours, similar to metastable systems. The latter depends mainly on the mean bedload transport rate qs and the channel steepness, i.e. the flume inclination in my experiments. Interestingly enough, the fluctuations of local or reach-averaged hydrodynamics variables, e.g. $S_h(t)$, $U(t)$, $Fr(t)$, $h(t)$, have little effect on the variability of qs . First, the evolution of the global space-averaged channel slope Θ is studied. Then, the presence of metastable effects are discussed through the change in flume angle α , feeding rate of sediments qs_{in} and Shields stress S_h . Finally, the results are compared with the Armfield and the Navisence River data to show that similar phenomena occur in natural mountain streams.

5.1 Channel bed hysteresis

The value of the global channel slope and its evolution is a common approach to the assessment of the equilibrium state of a stream reach [Recking, 2006] (section 2.3.3). However, in a natural river, it is relatively difficult to obtain time series of the reach-scale slope Θ , especially during periods of high bedload transport and in mountain environment. Thus, not much is known about the instantaneous equilibrium state of the channel bed relative to its steepness. The bed level data collected here allows for the investigation of the fluctuations in Θ . The latter have great importance in steep-channel morphodynamics. The evolution of Θ shows a hysteresis whose the intensity depends on the experimental parameters α , Q_l and qs_{in} . Particularly, an analogy is proposed between steep channels and metastable systems. A comparison between qs and other instantaneous variables characterizing the flow confirms the relative importance of the gravity — which induces metastable effects, for instance, in grain pile dynamics.

5.1.1 Global channel slope fluctuations

5.1.1.1 Bed slope determination

The instantaneous space-averaged channel slope Θ corresponds to a global parameter that will be used to characterize the stability state of the channel. Indeed, maximum and minimum values of Θ exist for a given set of parameters $\{S_h, \alpha, qs_{in}\}$. In granular systems, for instance a grain pile, where the transport occurs by avalanches, Θ is the criteria for assessing the stability state of the pile profile [Bouchaud *et al.*, 1995; Denisov *et al.*, 2012]. Moreover, the volume of accumulated sediments above the base of the sediment pile, corresponds to the potential energy for granular avalanches [Chevoir, 2008], directly linked to the average profile, i.e. Θ (section 2.3.3).

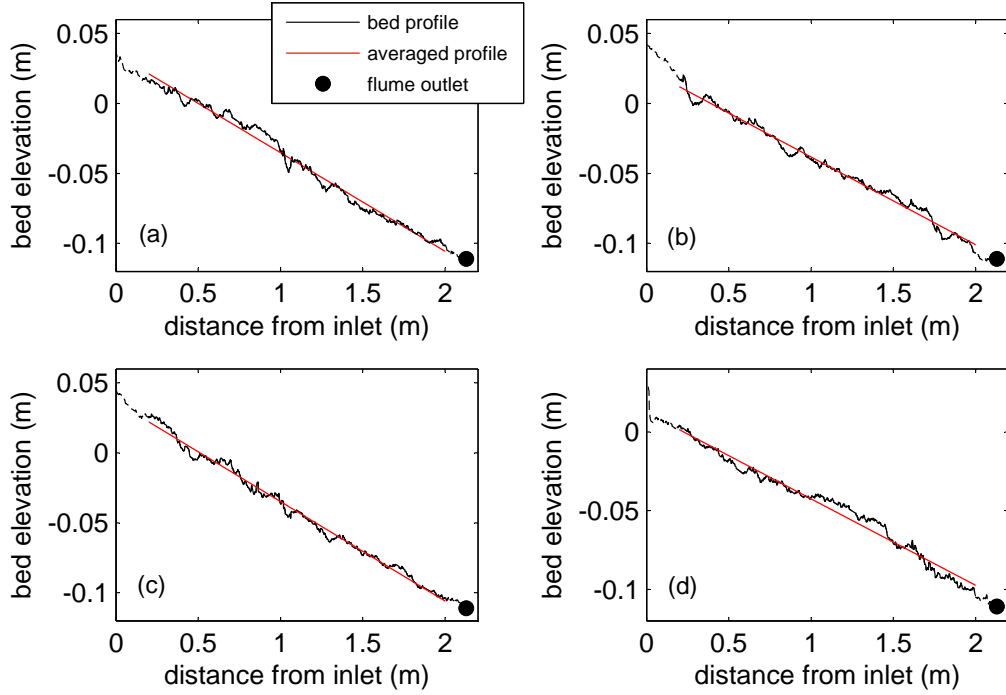


Figure 5.1: Examples of instantaneous bed profiles deduced from camera shots for run *4deg3v*, the linear regression is used to compute the averaged bed profile and determine the global channel slope Θ . (a) $\Theta = 4.03^\circ$ at 4 hours. (b) $\Theta = 3.59^\circ$ at 5 hours. (c) $\Theta = 4.07^\circ$ at 12 hours. (d) $\Theta = 3.14^\circ$ at 15 hours.

Three kinds of morphologies influence the bed elevation and the value of Θ at different scales. They have to be taken into account when computing the bed slope. First, the local position and arrangement of a few grains, i.e. grain clusters, can significantly modify the local bed elevation. The amplitude of the bed elevation fluctuations is on the order of a few centimeters, which has to be compared with the mean grain size $d_{50} = 6.25$ mm. Second, the migration of antidunes strongly modifies the bed elevation as these bedforms scale with the water depth, i.e. a few centimeters deep. Finally, global aggradations and degradations over the whole channel imply slope changes at large temporal and spatial scales but not much larger in magnitude than the other previous contributions.

The computation of Θ is a linear regression of bed elevation data over a 1.8-m-long central portion of 2.2-m-long bed, to reduce the boundary effects. Due to the presence of the three different bedform types mentioned above, the height difference between two channel cross-sections was considered to be an imprecise measure for the computation of Θ . Some examples of bed profiles with the corresponding linear regressions are shown in figure 5.1.

5.1.1.2 Fluctuation behaviour

For the 48-hour-long run *4deg3v*, i.e. $\alpha = 4^\circ$ and low qs_{in} , the evolution of Θ is represented in figure 5.2. Recall that Q_l and qs_{in} were kept constant for the duration of the run. It shows strong fluctuations in Θ , with particularly abrupt decreases and slower increases. The amplitude of the fluctuations, more than 1° , is relatively large compared to the value of $\alpha = 4^\circ$. To clarify, a slope change of one degree corresponds to a 3.8-cm-high elevation change, i.e. around 6 times d_{50} , at the channel scale. Considering these values, it no longer seems appropriate to describe the channel bed as in static equilibrium, although a stationary equilibrium might be reached (section 2.3.3).

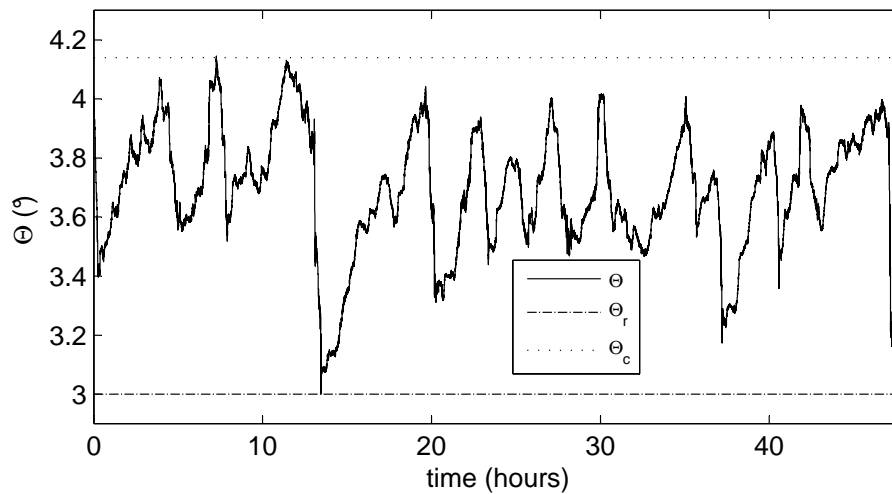


Figure 5.2: Time evolution of the global space-averaged channel slope Θ computed every second for run *4deg3v*: initial slope is 4° , solid input discharge is 0.19 g/s and mean channel slope is 3.7° .

From the observations of Θ evolution (figure 5.2), a typical scenario can be inferred. As the bed shear stress is close to particle entrainment, input particles settle and accumulate in the channel preferentially close to the inlet, slowly increasing Θ . Then, a massive degradation starts and reduces Θ abruptly. The abruptness of the slope decreases suggests the presence of breaks in channel stability, creating strong releases of sediment in a short amount of time. This is confirmed by the comparison between the output sediment rate and the fluctuations in Θ (figure 5.3). Periods of increasing slope correspond to low sediment output rates especially when Θ is low, indicating that sediment accumulates in the channel. Cycles of these successive increasing and decreasing periods occur continuously. However, the amplitude and duration of each cycle change without any periodicity — the cycle duration is not constant. Thus, it could suggest that no unique equilibrium exists. A range of possible slopes is actually observed and can be well-defined in the stationary regime of the system. This fluctuations in global channel slope show then the presence of an hysteresis.

5.1.2 Hysteresis and metastability

5.1.2.1 Analogy with the grain pile case

The large range of possible slopes and the relative high frequency of observed extreme events (section 2.2.2) suggest that the channel bed behaves like a metastable system in the sense of Bouchaud *et al.* [1995] (section 2.3.3). The time series of global slope evolution (figure 5.2), have a similar shape to that reported in the literature for dry granular systems (for instance Denisov *et al.* [2012]). On the scale of several hours, the slope undergoes large fluctuations, indicating that the bed does not converge to its average state. Also, long periods of grain accumulation are followed by the intense and sudden release of grains.

In the present study, although small local avalanches can occur (chapter 6), the relaxation periods are not due to global avalanches, as is the case in granular systems. During these periods, an intense degradation of the bed is observed. These relaxation periods are relatively long (about 15 minutes) compared to an avalanche time scale (several seconds), but are still short compared to the time scale of aggradation periods (up to six hours). Thus, the processes are not the same as in a grain pile, but there is an analogous behaviour of accumulations and failures. Given the wide range of

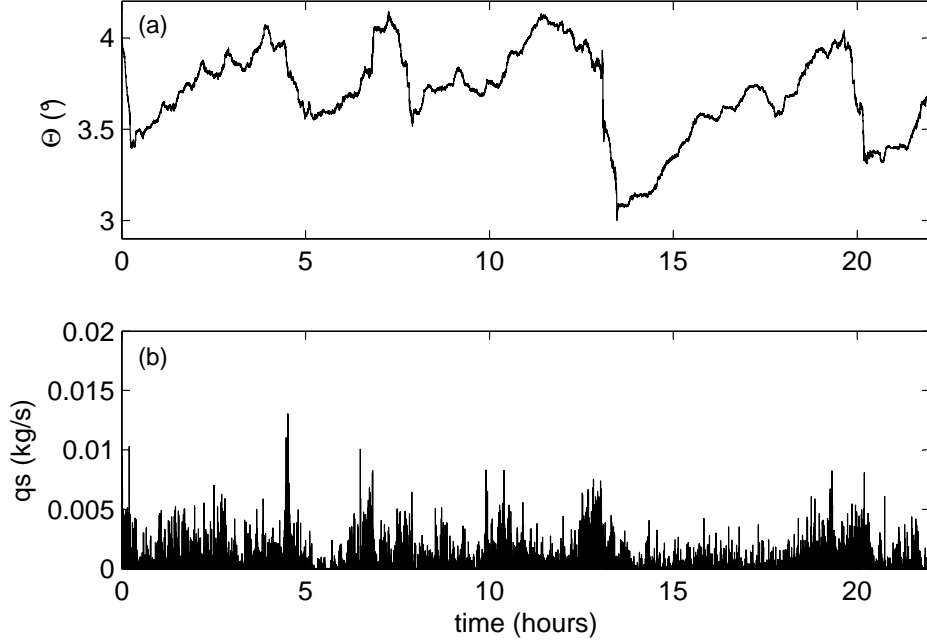


Figure 5.3: Comparison between Θ and qs for the first 22 hours of the time series of run *4deg3v*. (a) Time series of Θ . (b) Time series of qs .

possible slopes and the slow accumulation rate compared with the rapid channel degradation, the system (as in run *4deg3v*) is similar to a metastable system. The conditions under which significant hysteretic effects are seen, depending on qs_{in} , α and S_h , are presented later in section 5.2.

For each run (for instance figure 5.7 and 5.4), the extrema of Θ , Θ_r and Θ_c , correspond to the angle of repose and the critical angle of stability respectively. Their values are reported in table 5.1. At Θ_r , relaxation events are not possible — there is no significant degradation — and the bed is aggrading. At Θ_c , aggradation of the bed is no longer possible and a complete relaxation, i.e. an intense and fast degradation, has a high probability of occurring. Still, significant degradation events can be triggered for any angle $\Theta_r < \Theta < \Theta_c$. An example of a quasi-complete relaxation, from Θ_c to Θ_r , can be seen in figure 5.2 at 13 hours.

5.1.2.2 The slope range: an indicator of the hysteretic behaviours

In the following analysis, the amplitude of the fluctuations in Θ , i.e. the slope range $R = (\Theta_c - \Theta_r)$, is used to characterize the strength of the hysteretic cycles. Denisov *et al.* [2012] used the standard deviation of Θ , i.e. $\sqrt{\sum(\Theta - \Theta_m)^2}$, as an indicator of metastability. However, the latter was not chosen in this analysis because it cannot distinguish the fast and relatively short fluctuations from the rarer large fluctuations. Moreover, the standard deviation is dependent on the sampling time, which compromises comparisons between different studies. Thus, the use of R was preferred. For larger values of R , hysteretic cycles are more pronounced and present on a wider range of scales.

Compared with dry grain piles, the relative amplitude R/Θ_m is around 0.2 for a rice pile profile of one meter long (experiment of [Denisov *et al.*, 2012]). The rice pile being the classic example of a metastable system [Denisov *et al.*, 2012], its relative amplitude $R/\Theta_m = 0.2$ is a high value. In

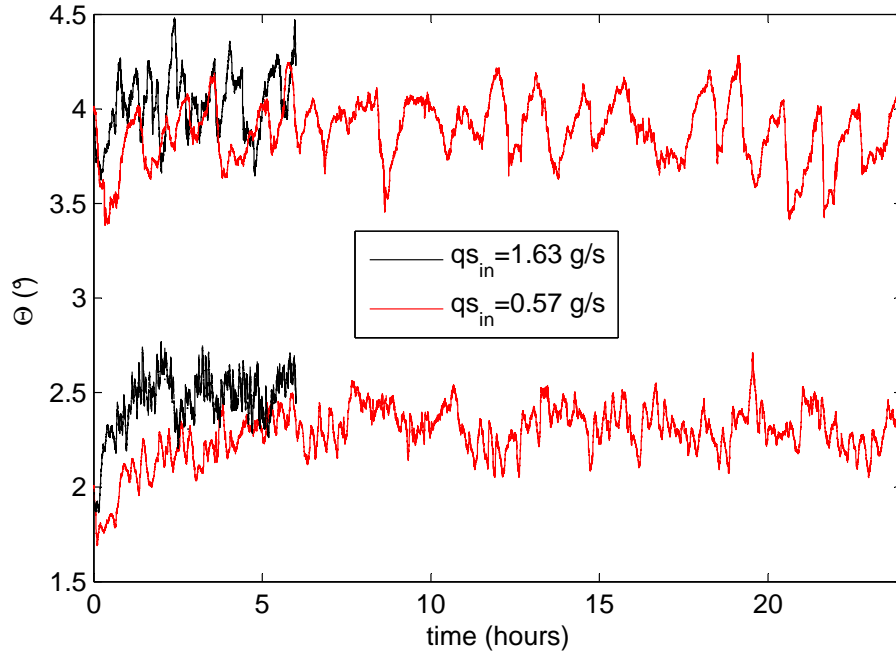


Figure 5.4: Time evolution of Θ for four runs, *4deg6v*, *4deg15v*, *2deg6v* and *2deg15v*. Note that for the highest solid input rate, a six-hour-long run is sufficient to reach the stationary state and record the autogenic fluctuations.

a few runs, the relative amplitude exceeds 0.3, suggesting that metastable or similar effects play a significant role in steep channels.

5.1.3 Comparison with hydrodynamics variables

In the case of supercritical flows with growth and migration of antidunes, the literature reports a quasi in-phase evolution of the bed and water levels (section 2.2.3.2). Although stationary waves are present all along the flume, the mean water depth h is nearly constant. Only during short instants do hydraulic jumps appear.

In the previous sections, the fluctuations in global channel slope Θ were analyzed. Here, the discussion concerns the water surface slope Θ_w which was computed in the same way as Θ . At the scale of the flume, the fluctuations in Θ_w are slightly larger than the ones of Θ . For instance, in run *2deg3v*, the slope range is 0.77° for Θ_w compared to 0.63° for Θ . Second, the comparison between Θ_w and Θ permits an inference of the flow acceleration. And it comes that the periods of high acceleration do not match with peaks of bedload transport rates at reach-scale (not shown here). It underlines the need to study smaller scales.

The hydrodynamic variables were computed over a 40 cm window just upstream of the outlet to try to better explain qs . Figure 5.5 and 5.6, for runs *2deg3v* and *4deg3v* respectively, show the time series of θ_w , θ , S_h and $qs(\Delta t = 60 \text{ s})$ where θ_w , θ and S_h were spatially averaged between the abscissas 1.7 m and 2.1 m (from the inlet).

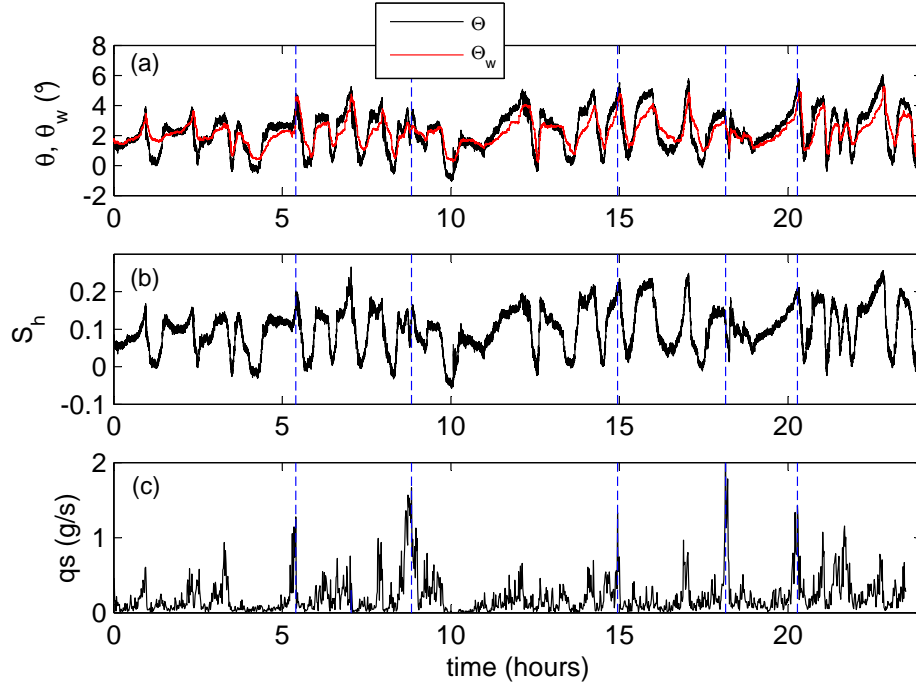


Figure 5.5: Comparison between time series of variables Θ , Θ_w and S_h (averaged over a 40 cm window situated just upstream of the flume outlet) and q_s sampled at one minute for run *2deg3v*. The vertical dashed lines show the main bedload transport peaks.

5.1.3.1 Flow acceleration

In the two figures 5.5(a) and 5.6(a), the evolution of θ_w follows the fluctuations in θ relatively well (at scale 40 cm, right upstream the flume outlet). However, there is sometimes temporal or spatial lag, leading to periods of accelerating or decelerating flow. Most of the time, during an increase of the slope, the flow decelerates in time ($\partial\theta_w/\partial t < \partial\theta/\partial t$) and also in space ($\theta_w < \theta$) which implies an increase of h along the channel. On the contrary, during a decrease in channel slope, the flow accelerates.

Accelerating flows are observed to be more efficient for particle entrainment and transport [Nezu & Onitsuka, 2001]. However, compared with the time series of q_s (figures 5.5(c) and 5.6(c)), periods of high bedload transport do not match with periods of flow acceleration close to the outlet, for both flume inclinations 2° and 4° . It suggests that, here, pulses of q_s are not triggered by high flow acceleration neither at the channel scale or at smaller scales.

5.1.3.2 Shields stress

$S_h(t)$ is observed to be strongly sensitive to θ_w . At the scale of the flume, $S_h(t)$ increases during aggradation phases — periods of low q_s — and decreases during degradation phases — periods of high q_s . Thus no obvious influence of the value of $S_h(t)$ on the variation of q_s is seen at this global scale.

In figure 5.5 and 5.6, the influence of S_h on q_s can be observed at a smaller scale close to the outlet. Generally, large peaks of q_s are not correlated with peaks of high local values of S_h for the run at 4° (see the vertical lines in the figures). However, for the run at 2° , periods of high q_s seems

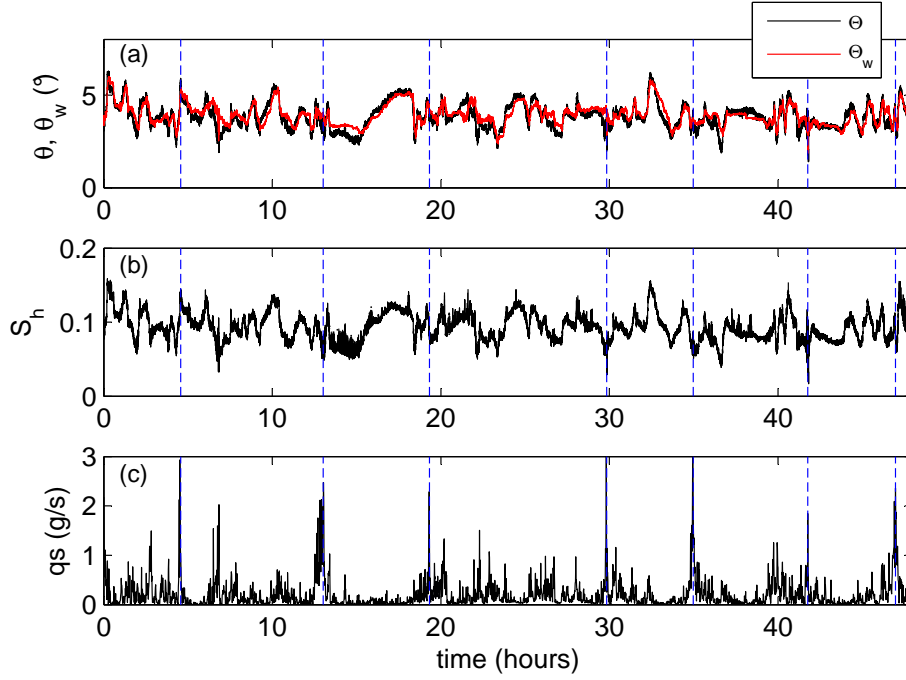


Figure 5.6: Comparison between time series of variables Θ , Θ_w and S_h (averaged over a 40 cm window situated just upstream of the flume outlet) and qs sampled at one minute for run $4deg3v$. The vertical dashed lines show the main bedload transport peaks.

to be related in some way to the fluctuations in S_h — which is not the case at 4° . A significant correlation of 0.40 was found between $S_h(t)$ and $\ln qs$ at 2° and a maximum correlation of only 0.14 between S_h and qs at 4° (negligible correlation between $S_h(t)$ and $\ln qs$ for this last inclination). Thus, although water flow is the main driving phenomenon, the fluctuations in $S_h(t)$ are not the most representative variable of instantaneous changes of qs , at least for steep channels.

The time- and space-averaged value of S_h still remains an essential parameter over the whole experiment, which controls the mean erosion and mean transport rates. Here, other phenomena could have great importance on steep slope, like collective entrainment [Heyman *et al.*, 2013] or granular behaviours [Frey & Church, 2011] at time scales shorter than the saturation time scale T .

5.1.3.3 Discussion

In summary, the data, at high flume inclination, show that there is no direct link between the instantaneous outlet solid discharge $qs(t)$ and the instantaneous Shields stress $S_h(t)$ or between $qs(t)$ and the instantaneous flow acceleration. The instantaneous and local characteristics of the flow, such as $\Theta_w(t)$ and $S_h(t)$, do not fully explain the variability of qs in the case of steep slope. An examination of the local behaviours to try to detect local critical states in the bed is probably essential (chapter 6). The periods of high qs seems to be better correlated with the abrupt changes in channel slope Θ . This confirms the pertinence of studying further the concept of metastability in the case of steep channels.

5.2 Effects of the experimental parameters

In the previous section, an analogy with metastability was presented in steep channels. The range R of the fluctuations in Θ is a good criterion for quantifying the intensity of hysteretic effects. In this section, the specific influence of the experimental parameters S_h , qs_{in} and α for the observation of these hysteretic behaviours are determined. A summary of relevant the parameters is given in table 5.1. In addition, in appendix G, time series of Θ for several runs are plotted.

Table 5.1: Parameters linked with metastability: the time- and space-averaged channel slope Θ_m , the minimum and maximum space-averaged channel slopes Θ_r and Θ_c and the slope range R .

name	α (°)	Θ_m (°)	Θ_r (°)	Θ_c (°)	R (°)	Θ_w (°)	qs (g/s)	Cv	S_h
2deg3v	2.0	2.02	1.70	2.28	0.58	2.02	0.22	2.52	0.088
2deg6v	2.0	2.30	1.96	2.71	0.76	2.33	0.59	1.83	0.099
2deg10v	2.0	2.32	2.01	2.64	0.63	2.33	1.14	1.42	0.099
2deg15v	2.0	2.51	2.20	2.77	0.57	2.41	1.67	1.19	0.097
3.2deg3v	3.2	-	-	-	-	-	0.21	2.84	-
3.2deg3v(b)	3.2	3.01	2.46	3.62	1.16	3.02	0.23	-	0.100
3.2deg4v	3.2	3.07	2.46	3.87	1.41	2.98	0.32	2.33	0.100
3.2deg5v	3.2	3.15	2.30	3.59	1.29	3.11	0.45	2.14	0.101
3.2deg6v	3.2	3.14	2.68	3.58	0.90	3.16	0.54	2.00	0.094
3.2deg10v	3.2	3.22	2.91	3.55	0.63	3.28	1.02	1.45	0.092
3.2deg15v	3.2	3.47	3.00	3.74	0.74	3.55	1.53	1.20	0.104
4deg3v	4.0	3.69	3.00	4.14	1.14	3.76	0.20	2.97	0.094
4deg4v	4.0	3.89	3.50	4.35	0.85	3.96	0.32	2.39	0.090
4deg5v	4.0	3.87	3.32	4.32	0.99	3.94	-	-	0.088
4deg6v	4.0	3.90	3.35	4.50	1.14	3.96	0.55	2.08	0.097
4deg10v	4.0	4.05	3.54	4.41	0.87	4.12	0.99	1.56	0.090
4deg15v	4.0	4.06	3.65	4.48	0.83	4.12	1.49	1.31	0.089
5deg3v	5.0	4.66	3.97	5.17	1.20	4.71	0.20	3.34	0.078
5deg6v	5.0	-	-	-	-	-	0.57	2.15	-
5deg10v	5.0	-	-	-	-	-	0.97	1.67	-
5deg15v	5.0	-	-	-	-	-	1.47	1.36	-
3.2deg6v+	3.2	2.81	2.47	3.10	0.63	2.85	0.60	1.24	0.104
3.2deg3v+	3.2	2.65	2.44	2.93	0.49	2.71	0.19	2.69	0.116
3.2deg15v+	3.2	2.90	2.58	3.17	0.59	2.90	1.62	1.20	0.107
5deg3v+	5.0	4.14	3.65	4.81	1.16	4.18	0.12	4.25	0.092
5deg15v+	5.0	3.96	3.59	4.55	0.96	3.97	1.62	1.19	0.097
5deg6v+	5.0	3.98	3.41	4.45	1.04	3.97	0.53	2.00	0.098
4deg20v	4.0	3.44	3.17	3.69	0.52	3.44	2.19	1.03	0.103
4deg20v(b)	4.0	3.64	3.28	3.90	0.62	3.61	2.11	0.99	0.109
4deg36v	4.0	3.68	3.41	3.88	0.47	3.69	5.74	0.73	0.115
4deg48v	4.0	3.90	3.69	4.16	0.48	3.89	9.35	-	0.117
4deg45v	4.0	3.73	3.40	4.03	0.64	3.72	8.35	0.58	0.113
3.2deg45v	3.2	3.57	3.31	3.80	0.49	3.55	7.95	0.56	0.107
5deg45v	5.0	4.39	4.17	4.60	0.43	4.39	8.00	0.51	0.115

5.2.1 Averaged channel steepness

The effects of the channel steepness on its stability is studied. In the main set of runs, i.e. at constant S_h , the effects of the flume inclination α can be observed independently of the other

parameters. Figure 5.7 shows the time series of Θ for two of these runs at flume inclination of 2° (run *2deg3v*) and 4° (run *4deg3v*). The fluctuations are much stronger for the highest flume inclination. The cycles, i.e. the oscillations from decreasing slope to increasing slope, occur more frequently in the case of 2° , although the decrease is more abrupt in the 4° run. It appears then that degradation events are more intense for steep slopes, whereas at lower channel slopes, the more regular increases and decreases of Θ suggests less intermittency in the processes. These observations are signs that the hysteresis is more pronounced at higher flume inclinations.

In figure 5.8(a), the evolution of R with varying bed steepness for the main set of runs (at constant S_h) is represented. I used the time- and space-averaged channel slope Θ_m as the relevant parameter instead of α because of the adjustment of the mean bed profile at the beginning of each run. Runs conducted with different qs_{in} are plotted in the figure. It shows that for all qs_{in} tested, R increases with Θ_m . Thus for a steeper channel, metastable effects are stronger.

The increasing degree of metastability on grain piles with higher critical angle was deduced by conducting experiments with different types of grains [Denisov *et al.*, 2012]. Indeed, Denisov *et al.* [2012] show that transport on rice piles — rice having one of the highest known critical angles — matches self-organized criticality (SOC) characteristics, i.e. the highest degree of metastability, contrary to other types of grains with lower critical angles. It confirms the analogy with metastability.

The particle shape, characterized by the aspect ratio a , is often shown to influence metastable behaviours and the value of the critical angle. It has been shown, for instance, that the critical angle is linearly dependent on a in grain piles [Denisov *et al.*, 2012]. Here a is around 1.5 for the gravel used, compared to 3.5 for rice. Different critical slopes have been studied by changing the flow discharge but keeping the same Shields stress. In the case of a grain bed sheared by a fluid at fixed S_h , α — or Θ_m — seems to be a key parameter for metastability as a is for grain piles. Moreover, in my experiments, Θ_c and Θ_r are linearly dependent on the channel slope (figure 5.9(a)). Note that Θ_c , the steepest possible angle observed for a given run, shows a much stronger correlation with R than Θ_r (figure 5.9(b)). This underlines the importance of reaching very steep instantaneous bed profile to possibly observe large hysteretic behaviours.

The similarity with the evolution of grain piles, where no shear is imposed by the ambient fluid, suggests that the strong intermittency observed in steep channels, is at least partly due to the emergence of granular behaviour at high steepness where gravity could play a direct role on the evolution of the bed.

5.2.2 Sediment supply

As noted in chapter 4, the variability of sediment transport is more pronounced for cases with low mean transport rates. SOC behaviour and metastability on grain piles are also observed quasi-exclusively under conditions of very low grain feeding rates [Bouchaud *et al.*, 1995]. This behaviour is present in my data and the transition towards higher mean transport rates is also investigated.

First, at least for high Θ_m , R decreases with higher qs_{in} (figure 5.8(b) where all experiments are shown). This suggests that low qs_{in} is a necessary condition for observing the strong hysteretic behaviours. The transition to a more regular system for higher rates may depend on Θ_m (figure 5.8(b)). For instance, at $\alpha = 2^\circ$, R is relatively constant for all qs_{in} . For $\alpha = 3.2^\circ$, a rapid decrease of R with an increase of qs_{in} is seen. Finally, for $\alpha = 4^\circ$, R remains larger than for lower angles. For any flume inclination, at high transport rates, the hysteretic intensity strongly decrease with a limit of $R = 0.5^\circ$ (figure 5.8(b)).

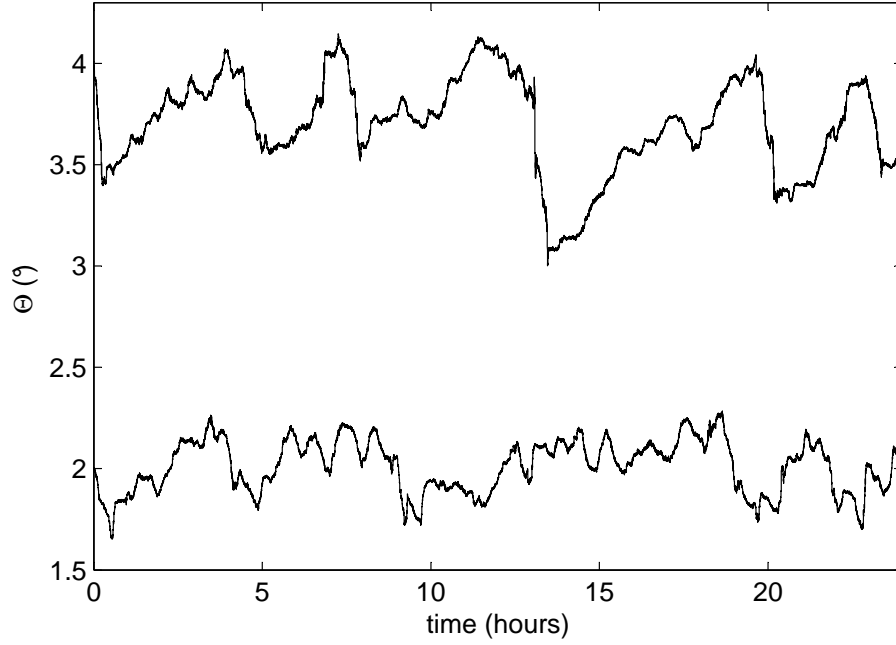


Figure 5.7: Time evolution of Θ for 2 experiments with initial slopes of 2° ($2deg3v$) and 4° ($4deg3v$), low solid input discharge of ~ 0.20 g/s for both runs.

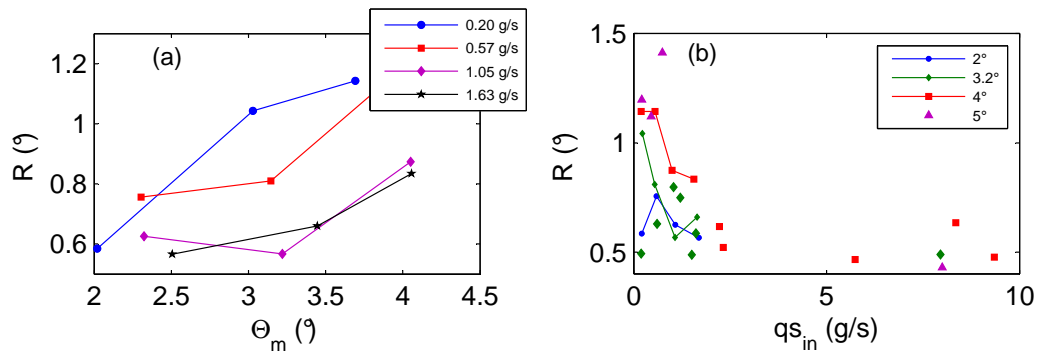


Figure 5.8: (a) $R = \Theta_c - \Theta_r$ as a function of Θ_m for several $q_{s_{in}}$. (b) Θ_m as a function of $q_{s_{in}}$ for different flume angles.

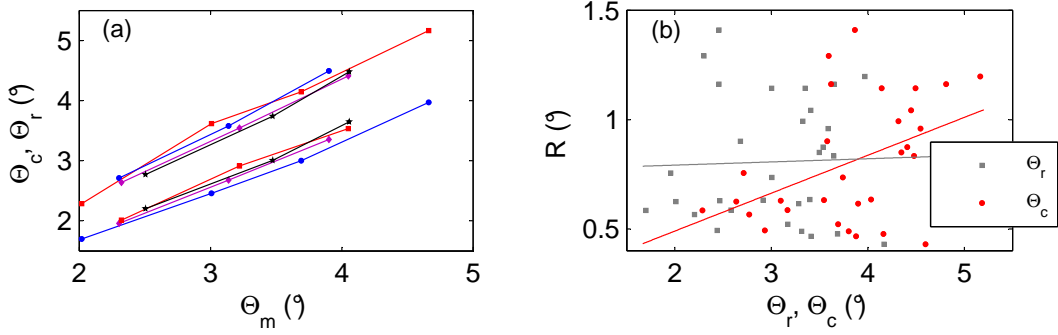


Figure 5.9: (a) Θ_c (above) and Θ_r (below) as a function of Θ_m for several qs_{in} , same legend as the legend in figure 5.8(a). (b) R as a function of Θ_c and Θ_r , the lines represent the linear regressions.

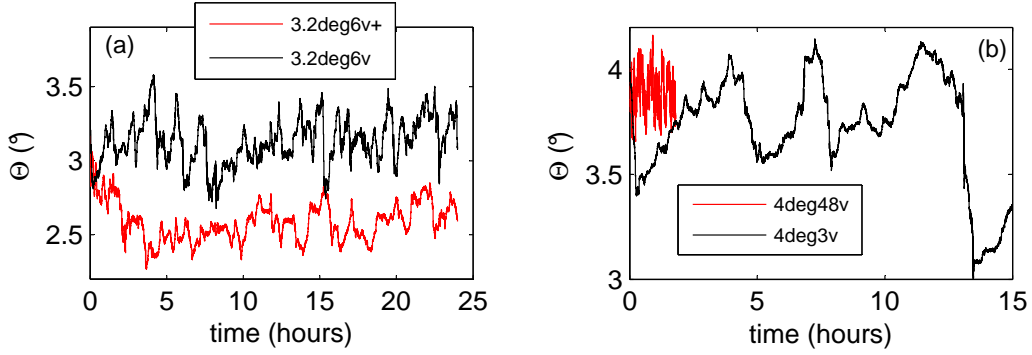


Figure 5.10: Time series of Θ : effects of Shields stress on the fluctuations in Θ . (a) Comparison between runs with same qs_{in} and Θ_{ini} and different S_h . (b) Comparison between runs with strong difference in qs_{in} and S_h .

5.2.3 Shields stress

As noted in chapter 3, a precise study of the effects of S_h , independently of both Θ_m and qs_{in} is difficult. For the same qs_{in} , a change in Ql will induce change in Θ_m . However, some effects of the flow strength on the hysteresis can be hypothesized from data shown in figure 5.10. In figure 5.10(a), runs with the same qs_{in} and Θ_{ini} but different Ql are shown. With a moderate difference in Θ_m of 0.5° and a significant difference in S_h , we can consider that this situation represents the effect of S_h . Indeed, values of S_h are 0.0104 (highest Ql in red) and 0.0094. The change in R is found to be significant: 0.63 for the highest Ql compared to 0.9 for the lowest Ql .

In figure 5.10(b), two runs with approximately the same Θ_m are represented, one with a high S_h (0.117) and also a high qs_m and one with low qs_m and low S_h . For the higher S_h , $R = 0.48$, compared to 1.14 for the lower.

Finally, figure 5.11 which shows R as a function of S_h for all runs, demonstrates that for $S_h \leq 0.1$, high values of R are possible — up to 1.4° — and for $S_h > 0.1$, R remains lower than 0.8. Although the individual effects of qs_{in} and S_h cannot strictly be separated, it is observed that a higher S_h leads to weaker hysteretic effects.

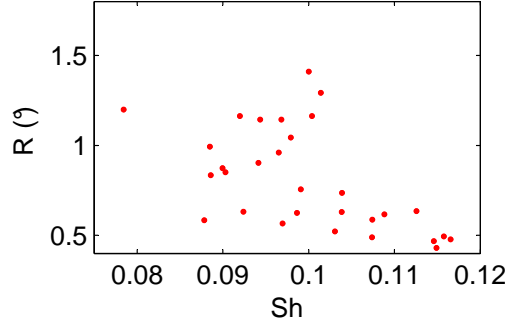


Figure 5.11: R as a function of S_h for all 2D-flume runs.

5.2.4 Discussion

This section showed that low qs_{in} is a necessary condition to observe significant metastable effects, and that the intensity of the hysteresis strongly increases for steeper channels. Interestingly, runs at low transport conditions and constant S_h suggest that the system is able to modify its transport capacity whilst keeping all the time- and space-averaged variables constant (Θ , Θ_w , S_h ...). This is probably achieved by smaller-scale processes in the system.

The higher the external conditions, e.g. higher qs_{in} , the stronger the system response. Moreover, at high qs_{in} , the system shows fewer fluctuations due to strong, constant perturbations at the bed surface. At low sediment transport conditions, the excess of accumulated energy, i.e. large sediment deposition in the system, is released suddenly by through other processes than classical hydrodynamics concepts.

5.3 Hysteresis in mountain streams

In this section, the observations from the 2D-flume experiments are compared to the Armfield data, in order to see whether the hysteretic effects in steep channels are also observed in a large-scale experiment. Could we then generalize this hypothesis to mountain streams? Data from the Navisence River show possible signs of this concept.

5.3.1 Comparison with other data

5.3.1.1 Armfield flume

During experiments in the Armfield flume, the bed elevation and/or the water surface was measured over the whole flume. Thus, the channel slope and/or the free surface slope were computed. As described in chapter 3, the measurements during the experiment were performed with flowing water — without stopping the run. Although the flume inclination is smaller than in the 2D-flume — only up to 2° — the channel slope still shows significant fluctuations.

From the 3D bed profiles, the water level is determined as the minimum elevation for each abscissa — not taking into account the bank elevation. Θ_w is computed from the linear regression of the water level over 12 meters. Both runs with steady conditions and flood cycles are used.

Experiments under steady flow conditions

As seen in chapter 4, the saturation timescale T depends on the magnitude of the external parameters and the size of the system. Thus, the fluctuations should be larger in this flume than

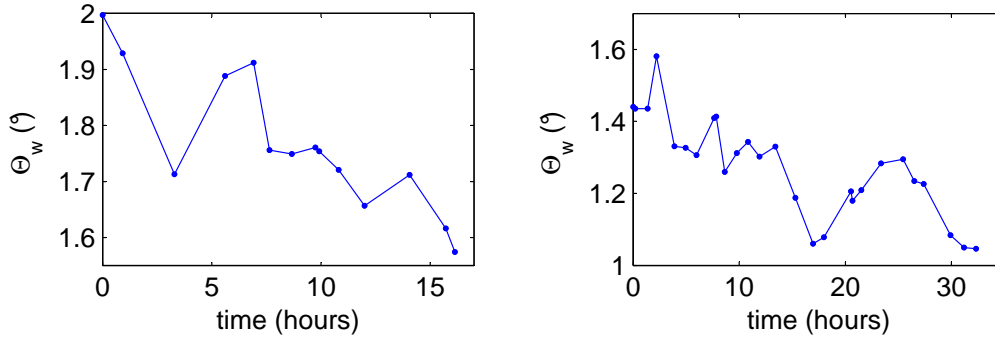


Figure 5.12: Fluctuations of Θ for runs *arm2deg* (left) and *arm1.4deg* (right).

in the 2D-flume due to a larger width and a longer length, for similar transport conditions. To accurately estimate the fluctuations in qs , the saturation time scale T should be reached. This was difficult to obtain as the runs must have a long time length — possibly on the order of a week. However, shorter experiments can still give some information on the channel stability.

Two time series of Θ_w are plotted in figure 5.12. Since qs reached a stationary state (particularly for run *arm1.4deg*, see chapter 4), Θ_w fluctuates around a stationary value. Moreover, the sampling frequency of the measurements being low, the range of fluctuations might be larger than computed as instantaneous extrema may not be captured.

The value of R , which is at least 0.4° and 0.3° for runs *arm2deg* and *arm1.4deg* respectively, is significant which confirms the possible presence of hysteretic effects for a larger system. Note that the Armfield values of S_{hini} cannot be compared with the 2D-flume ones as, in the Armfield flume, the system tends to create narrower channels than the flume width, i.e. with $S_h > S_{hini}$.

Experiment with flood cycles

For the flood cycle experiment, bed elevation was measured after each flood cycle, permitting to compute Θ_w and Θ . As, each cycle has a duration of one hour, the time series is relatively long. Moreover, due to moderate transport during peak discharge, the evolution is faster than for experiments under steady condition. Nevertheless, fluctuations in Θ during floods are significant (figure 5.13).

In this experiment, R is estimated to be at least 0.4° . This significant amplitude shows that the hysteresis is also present when imposing a periodic external conditions. Regarding the relatively gentle slope and moderate transport rates, this value of R is in agreement with the 2D flume experiments.

5.3.1.2 The Navisence River case

For a small stream with nearly constant time-averaged channel slope over years and subject to relatively small and short floods, averaged transport conditions can be considered to be close to the threshold of motion. From the present experimental observations, hysteretic effects could be strong in this type of stream with high slopes. For instance, after several small floods with low bedload transport, a strong bedload transport event may occur for a flood of the same magnitude as the previous ones. Indeed, similarly to small floods in streams, Jerolmack & Paola [2010] show that periodic fluctuations in the experimental parameters do not change the statistics of the transport quantity in geomorphic systems, compared to constant external conditions with same mean rate.

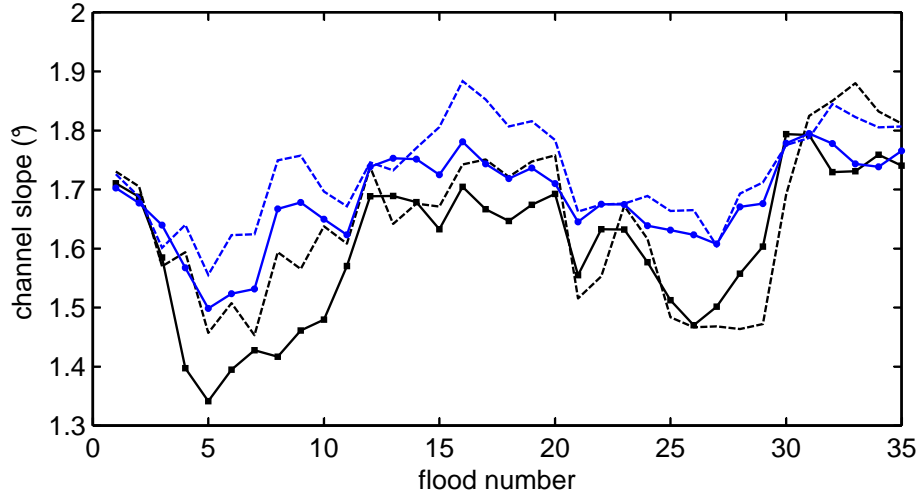


Figure 5.13: Channel (black) and water (blue) slope fluctuations for the experiment of 35 consecutive floods (flume angle 1.7°). The solid line and the dashed line are computed from the linear regression and the height difference of the longitudinal profiles respectively.

This is valid only if the period of the imposed fluctuations is shorter than the saturation time scale T of the system. And, in natural streams, it seems that, in most of the cases, the time-scales of the floods is much shorter than T .

Some evidence from the Navisence River data confirms this hypothesis. For instance, figures 5.14 and 5.15 show two extracts of the time series of the bedload transport rates and the flow rates at the Zinal monitoring station (appendix D). In each figure, relatively regular daily floods are observed, due to glacier and snow melt during daylight hours in spring and summer months. A low flow period in May (figure 5.14) shows small and very intermittent sediment transport. For the first six consecutive days, the bedload transport remains small. However, during the seventh and eighth days, a high bedload transport was recorded, although the flood intensity did not change significantly from the previous days. It could suggest that an aggradation upstream of the monitoring station took place during the first period and a fast degradation occurred after day 6.

This interpretation corresponds well with the hysteretic behaviours of accumulation/failure observed in my experiments. Applying the same reasoning to figure 5.15 for higher flow rates, the same conclusion arises. It shows that these hysteretic effects could be present at different scales, aggradation/degradation locally upstream of the monitoring station for low flow conditions (figure 5.14) or aggradation/degradation on a longer reach at higher flow rates (figure 5.15).

In conclusion, these hysteretic interpretations, similar to metastability, seems to explain at the global scale the intermittency of steep-stream evolution — fluctuations in bed profiles and bedload transport rates. The relation $f(Q_t, qs)$ is certainly not unique. A strong event in terms of water discharge does not necessary mean that bedload transport will be as strong. Conversely, a moderate flood could generate a strong bedload transport event. The only certainty is that the triggering probability of an extreme event is high if the channel slope is close to its critical state. However, the instantaneous stability state of the bed is difficult to assess in real time due the complexity of in-situ measurements.

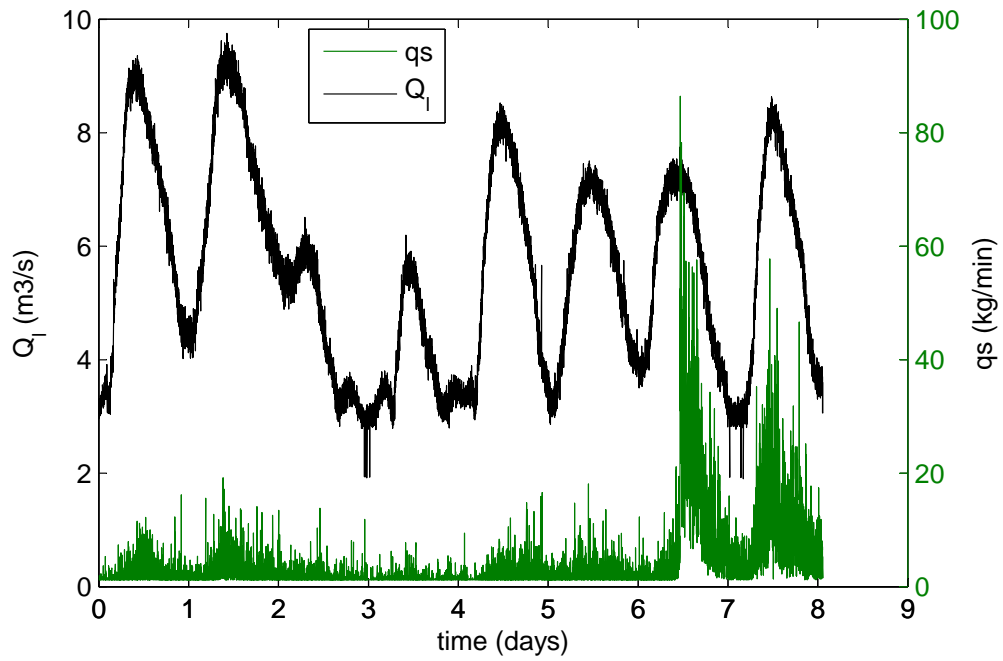


Figure 5.14: Navisence data. Plot of the water discharge Q_l and the sediment transport rate q_s for eight days at the end of May 2012. The hydrogram shows quasi-daily small floods (from snow and glacier melt) of similar magnitudes. The sampling rate is one minute.

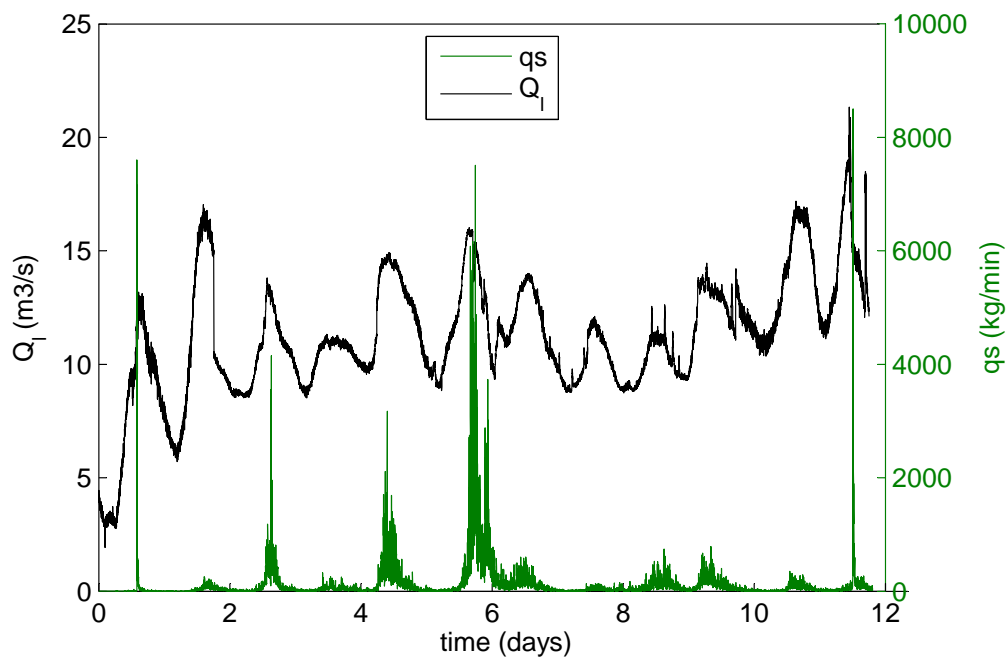


Figure 5.15: Navisence data. Plot of the water discharge Q_l and the sediment transport rate q_s for 12 days at the end of June 2012 during a period of high flow rate with daily peaks. The sampling rate is one minute.

5.3.2 Conclusion

In this chapter, it was proven that strong hysteresis, particularly on the channel profile evolution, are possible in steep streams, similarly to metastability. This behaviour — succession of low increase followed of sharp decrease of the time- and space-averaged channel slope Θ_m at several time-scales — partially explains the strong intermittency of bedload transport. First, the magnitude of the external conditions are highly influential at large temporal scales, i.e. time greater than the saturation time scale T , in describing Θ_m and mean bedload transport qs_m . The figure 5.16(a), representing S_h as a function of qs , shows the dependence of the mean transport on the mean flow intensity, albeit with high scatter for low transport rates.

Second, the instantaneous and local fluctuations in hydrodynamic variables do not entirely explain the variability of bedload transport in steep channels. Even the fluctuations in $S_h(t)$ could be controlled by the large scale aggradations and degradations observed. Moreover, the link between the slope range R — used as the indicator of the hysteretic strength — and Cv is significant (figure 5.16(b)), confirming the influence of the hysteretic effects on the bedload transport intermittency.

The hysteresis strongly increases with the overall steepness of the channel, especially if the maximum angle of stability Θ_c takes a high value. This is particularly the case for low sediment supply. In this case, the bed is subject to only small perturbations, accumulations of sediments in the channel are frequent and larger. And the system evolves to a less stable state where potential strong failure are possible. To summarize, lower sediment supply, higher channel slope and lower Shields stress lead to more intense hysteretic effects.

This hysteresis of the stream profile, in the case of natural streams, has to be validated. The Navisence data show that this concept is an interesting way to explain the morphodynamics variability. However, this should be proven, for instance, by high-temporal-resolution bed surveys. This has not been done yet and would appear to be an arduous task. New technologies using drones might help to achieve this kind of study.

The similarities with granular piles, discussed in this chapter, suggest that granular processes — and gravity — in steep streams have significant impacts on bedload transport. They could partly explain the intermittency of qs and aggradation/degradation events. An analysis of these processes is then conducted at a smaller scale in the next chapter to emphasize the role of local instabilities in steep channels, leading to the observed metastable effects. Note that several other phenomena and concepts show oscillations similar to what is observed here. However, the hysteresis, presented by the analogy with the metastability, permits the development a general mechanism of evolution that is similar to many other geomorphologic issues of accumulations and failures [Jerolmack & Paola, 2010].

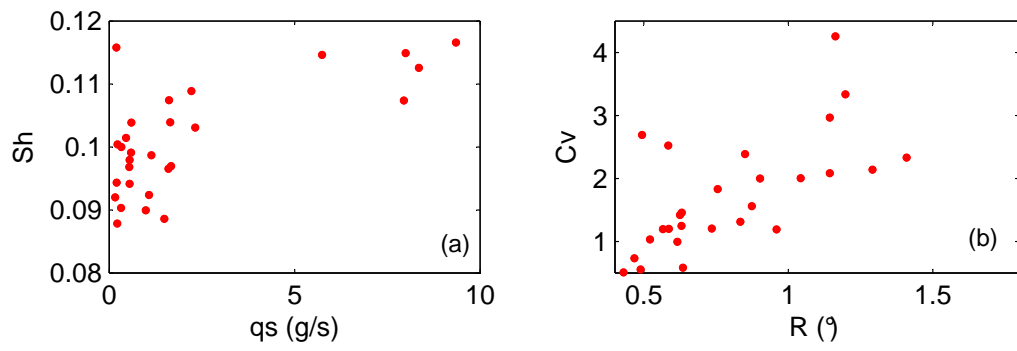


Figure 5.16: (a) Scatter of S_h as a function of qs for all 2D-flume runs. (b) Relation between R and Cv (same data).

Chapter 6

Bedforms and meso-scale instabilities

In this chapter, it is shown that antidunes, the most frequent bedforms present in the 2D-flume, are the main cause of local instabilities. They are fundamental in the global channel evolution. Specifically, antidune migration leads to rapid morphological changes at larger scales, such as global aggradations and degradations. This meso-scale mechanism is then directly related to the hysteresis at reach-scale (chapter 5). The analysis is made from the 2D-flume experiment where extensive and quantitative data are available.

First, the bedforms are characterized. Their presence, their geometry and their activity are quantified. Second, the influence of the experimental parameters is discussed and compared to the literature. Third, local bedload transport rates are predicted using a bedform migration analysis and an avalanche model. The possible occurrence of avalanches/slides on antidune lee sides is shown. Finally, mechanisms of bedform migration from grain-scale processes are summarized.

6.1 Bedforms in steep channels

In this section, the methods for inferring and quantifying the bedform data, and specifically antidune characteristics, are described. The existence of potential local instabilities in the channel is discussed from the analysis of local slopes. The grain pile problem is mentioned again, but addressed from the granular scale. In particular, it is shown that the local critical angle of stability θ_c — to be distinguished from Θ_c at reach-scale — is temporarily reached under specific circumstances.

6.1.1 Antidunes, grain clusters and microforms

6.1.1.1 2D-flume observations

Several types of bedforms, e.g. grain clusters and antidunes, are observed in the different runs. The most distinctive ones are the upstream-migrating antidunes as shown on the spatio-temporal plots of bed elevation in figure 6.1. Indeed, these bedforms move back upstream. Looking at a scour (darker area in figure 6.1) through time, the bedform travels toward the inlet. Also the global aggradations and degradations, addressed in chapter 5, are seen as changes in background brightness. For instance, in figure 6.1(a) at around 10 hours the background is relatively dark (low elevation) whereas between 6 and 8 hours it is brighter before the degradation. Finally, small grain clusters, composed of a few grains (up to 4 or 5 grains) are present. Their signature on the plot is small vertical bars as they do not migrate and as they are created and broke randomly.

The antidunes are observed in all runs (appendix F for spatio-temporal plots of other runs). However, as shown in figure 6.1, their appearance is intermittent and no strict periodicity is detected. Besides, there is no unique migration celerity for any run. Fast migrating antidunes correspond to quasi-horizontal bands on the plots, lower celerity corresponds to more oblique patterns. Generally,

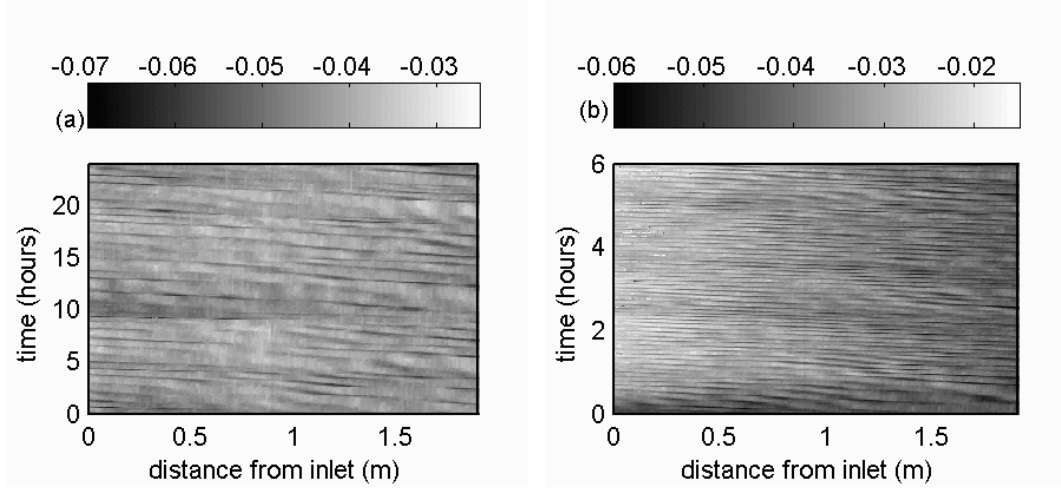


Figure 6.1: Spatio-temporal plots of bed elevation for run *2deg3v* ((a) duration of 24 hours) and run *2deg15v* ((b) duration of 6 hours). The distance is measured from the inlet in the downstream direction.

the water level follows the bed topography. In certain situations, like the presence of a deep scour, a hydraulic jump appears temporarily. This particular interaction between the flow and the bedform is studied in section 6.1.2.3.

Note that, at small temporal scales, the antidunes are not perfectly 2-dimensional although their global evolution is. Collective motion processes, i.e. the simultaneous motion of some grains, are visually observed and occur locally — sometimes not on the whole channel width. However, 3-dimensional effects are not significant as the 2-dimensional shape is re-established by rapid surrounding particle erosion.

6.1.1.2 Other data

On the Armfield flume, the same bedform types are observed but in three dimensions. In addition, riffles and pools have a strong influence at a large scale. Antidunes, grain clusters and reticulate structures appear on riffles with low water depth. On the contrary, no superimposed bedforms are observed in the pools, which are as deep as 15 cm (to be compared to $d_{50} = 6$ mm).

In the Navisence River, no extensive observations were made for the measurement of bed elevation at the bedform scale. However, scours and steps are observed in the stream channel and are associated with significant standing waves at the water surface. For this type of flow close to critical flow, with transition from supercritical to subcritical after the step, these kinds of bedforms should migrate upstream, similarly to observations in the 2D-flume experiment.

Since not enough quantifiable data were collected neither on the Armfield flume nor the Navisence River, bedform dynamics could not be assessed in these cases. However, these visual observations confirm that antidune-like bedforms are present in natural steep streams.

6.1.1.3 Bed elevation processing and quantification

A methodology was developed to characterize antidunes. First, the largest scale component of the longitudinal bed profile, corresponding to the space-averaged channel slope Θ , is removed. The resulting data, for each time step, are filtered to smooth out the micro-roughness, like small particle

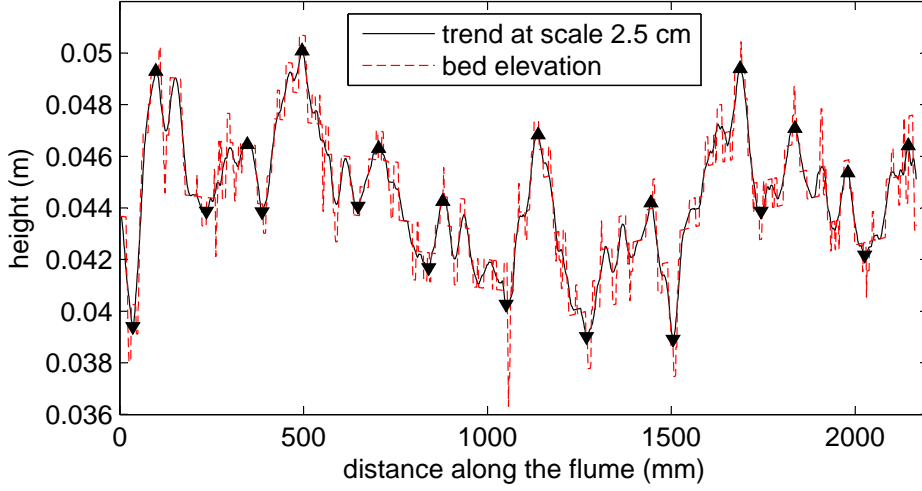


Figure 6.2: Bed elevation profile, its trend at scale 2.5 cm and the computed extrema (triangles) at a given time showing the processing steps for the detection of bedforms.

clusters or single jammed grains. This was performed by applying a moving averaging filter with $2.5 \text{ cm} = 4d_{50}$ window width. Finally, the antidune crests and troughs were detected.

Many authors studying dunes consider antidune crests and troughs as the local maxima and minima, respectively, between zero-crossings [Martin & Jerolmack, 2013]. However, this method does not work when small bedforms superimposed on larger scale bedforms have to be quantified. In the present case, different types of morphologies are present at several spacial scales. As seen in chapter 5, aggradations and degradations occur at the flume scale. Thus, instead of using the zero-crossings method, adjustments are made on thresholds of distances and heights between local maxima and minima in order to extract the relevant bedforms. The method used is similar to the one used by Singh *et al.* [2011]. The different steps are summarized in figure 6.2 where bed elevation, filtered signal and detected extrema are plotted.

The antidune time occurrence, duration and celerity are captured manually on the spatio-temporal plot of bedforms heights. This step is applied for each 0.0025 m range of bedform heights. The visual detection is mainly based on antidune continuity. This manually demanding work was necessary in order to avoid errors due to elevation extrema corresponding to non-migrating bedforms like grain clusters or large scale features — same order of magnitude in height (section 5.1.1.1). The antidune trajectories were drawn on the spatio-temporal plots, since most of the noise due to high grain roughness and isolated protruded grains could not be removed. The antidunes are detected by their troughs, since they are more distinguishable than crests (figure 6.1).

Finally, note that the antidune celerity c , height H , duration and position are computed from this selected processed data. However, the analysis of the shape of the bedforms and other characteristics of the antidunes is performed using the raw extremum data. Also for each antidune, the upstream and downstream height, H_{up} and H_{down} , are defined as the closest upstream and downstream elevation maximum from the considered antidune trough. Similarly, λ_{up} and λ_{down} (with the wavelength $\lambda = \lambda_{up} + \lambda_{down}$) are defined as the streamwise difference between the trough and the position of H_{up} and H_{down} respectively. These antidune characteristics are shown in figure 6.3.

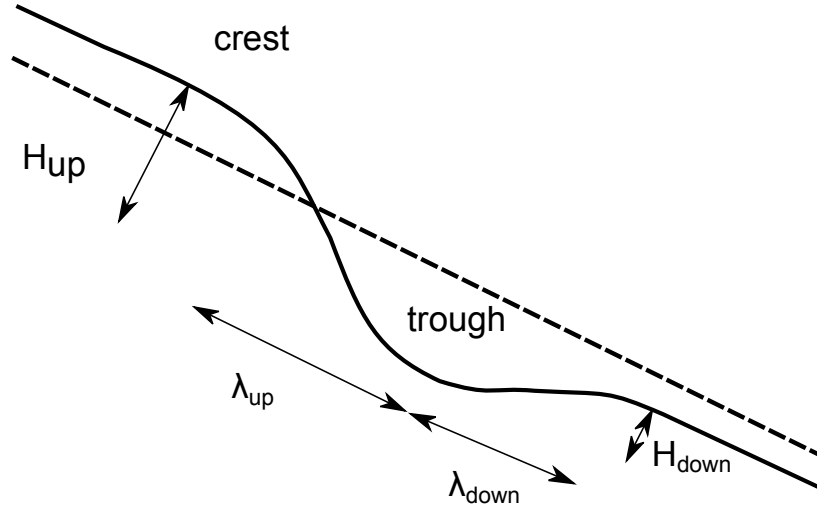


Figure 6.3: Scheme of an asymmetric antidune. Several characteristics are defined. The dashed line represents the instantaneous space-averaged profile of the channel, corresponding to Θ .

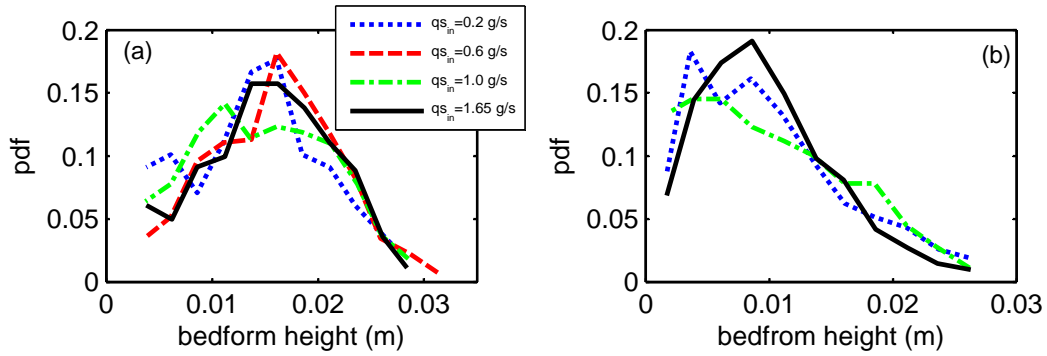


Figure 6.4: Pdfs of antidune heights for runs at flume inclinations 2° (a) and 4° (b).

6.1.2 Antidune characteristics

6.1.2.1 Antidune geometry

Height

The pdfs of antidune height H were computed. For the main set of runs at constant S_h , the pdf shape and the mean antidune height H_m do not depend on the input sediment rate $q_{s_{in}}$ (figure 6.4). $H_m = 0.10$ m and $H_m = 0.015$ m for runs at flume inclination $\alpha = 4^\circ$ and $\alpha = 2^\circ$ respectively. The antidunes are up to almost 3 cm tall, i.e. $4.5d_{50}$. This value is slightly smaller than the bed amplitude corresponding to the amplitude of channel slope fluctuations (more than 5 cm for the experiment with large R , chapter 5). In addition, the highest antidunes are observed for relatively high global instantaneous channel slopes Θ (figure 6.5). However, their presence is less correlated to the quantity of sediment accumulated in the channel, i.e. the total volume of grains in the flume. This suggests a strong interaction between Θ (and its fluctuations) and antidune growth and migration.

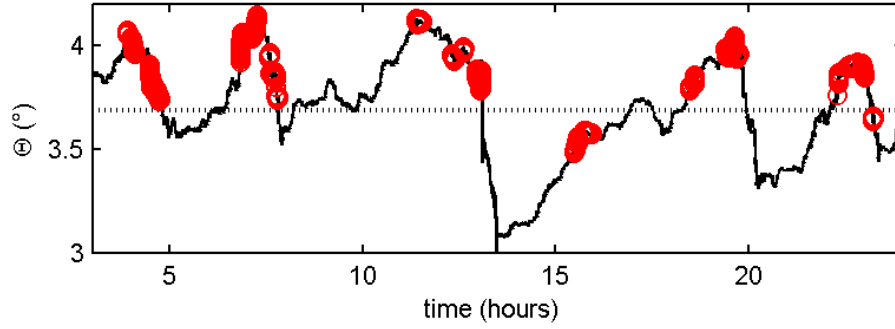


Figure 6.5: Extract of the time series of Θ for experiment *4deg3v* with temporal localizations of the antidune heights superior to 1.6 cm (red circles), the black dashed line represents Θ_m .

Wavelength

The wavelength λ , in addition to H , is an important shape parameter, for instance, for the computation of the slope of the antidune sides. In figure 6.6, λ is represented as a function of $H = (H_{up} + H_{down})/2$ for run *2deg15v*. The bin averaging is used to obtain the mean behaviour. λ increases with increasing H . Note that the slope of the relation gets smaller at higher depth. This means that taller antidunes have steeper sides. Plotting λ as a function of H for all the runs, the relation $\lambda = f(H)$ is approximately the same. However, H_m and λ_m — the corresponding λ for H_m — change.

Asymmetry

The plots of H_{down} versus H_{up} , in figure 6.7, suggest that antidune migration, which is always in the upstream direction here, leads to global degradation or aggradation depending on H . The large scatter seen in figure 6.7 shows that in all runs, whatever the input solid discharge qs_{in} or the flume angle α , H_{up} of the antidune can be higher than H_{down} (case of the scheme in figure 6.3) and inversely for any H . However, computing the bin average, also plotted in figure 6.7, H_{up} is larger than H_{down} except for the smallest migrating antidunes. Thus, a threshold H_{th} is defined to separate aggrading ($H_{up} < H_{down}$) from degrading ($H_{up} > H_{down}$) antidunes.

These observations suggest that the degrading process is associated with antidune migration. The aggradation is a less intermittent process that occurs without strong bed-wave migration (H_{th} very small), except for high α where aggrading antidunes are well present (H_{th} significantly higher). Details about the dependence on α are given in section 6.2.1.1.

6.1.2.2 Migration celerity

Many runs show sporadic occurrence of antidunes. However, their appearance tends to be more periodic for high input sediment rates qs_{in} , similar to the behaviour of the global channel slope fluctuations (chapter 5). If the input of sediments is stopped, the migration of antidunes becomes episodic (figure F.11 in appendix F). In this case, the celerity is low and decreases with the global channel degradation, i.e. for decreasing Θ . It suggests that the migration is strongly dependent on the input sediment feeding and Θ . A closer look at several antidunes confirms that, as they grow, they migrate faster.

Note that, when the initial channel slope is lower or higher than the stationary slope Θ_m , there is a transitional period of slower or faster migration respectively, at the beginning of the run. This

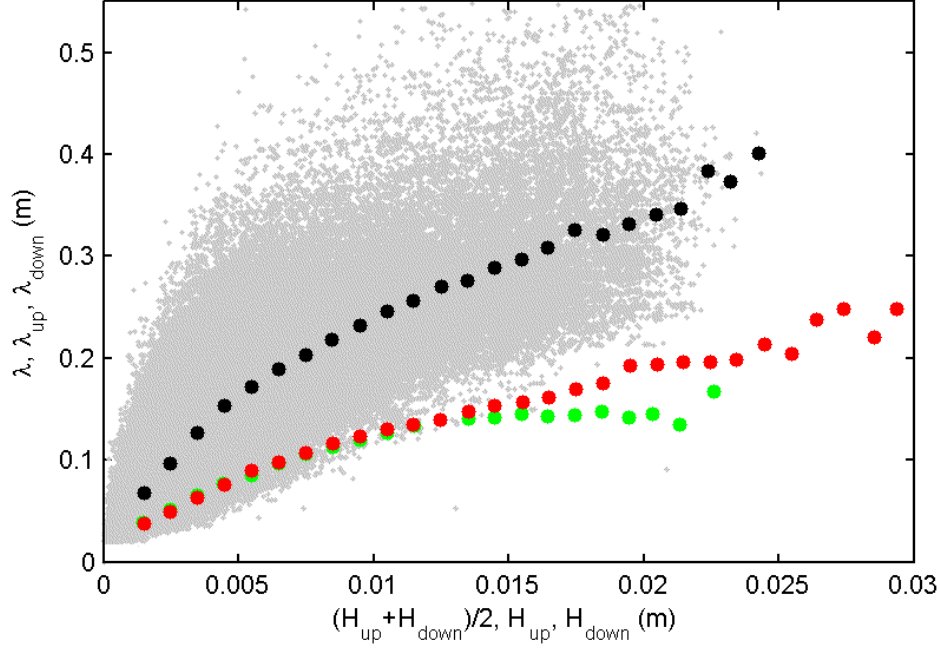


Figure 6.6: λ as a function of $H = (H_{up} + H_{down})/2$ for run *2deg15v*; the black, red and green dots represent the bin averaged values for $\lambda = f(H)$, $\lambda_{up} = f(H_{up})$ and $\lambda_{down} = f(H_{down})$ respectively.

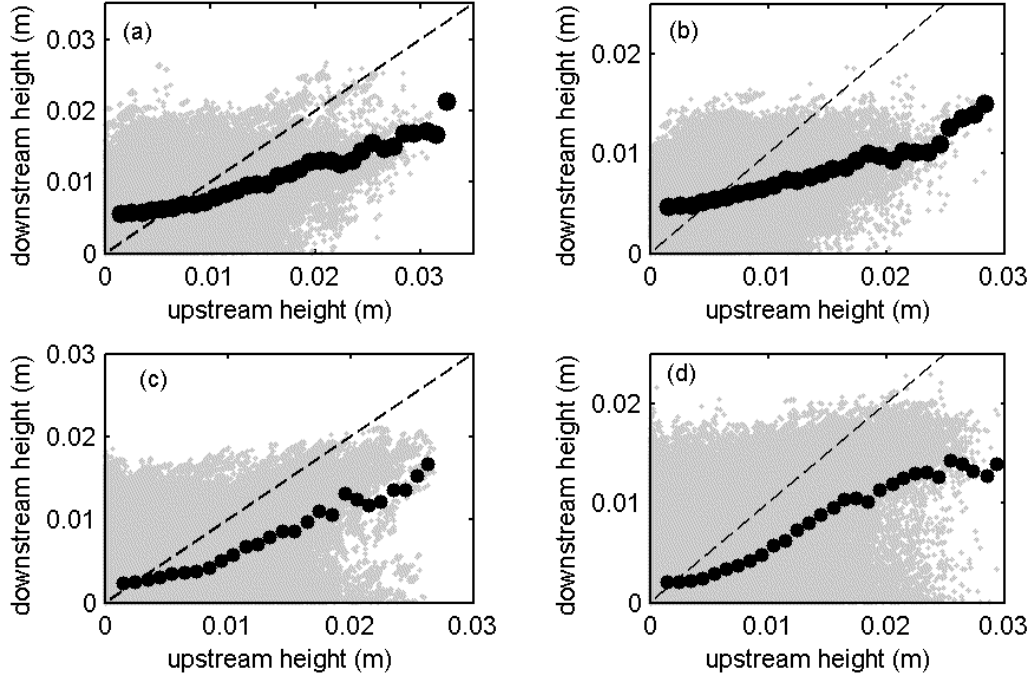


Figure 6.7: H_{down} as function of H_{up} for runs *4deg3v* (a), *4deg15v* (b), *2deg3v* (c) and *2deg15v* (d). Dots are bin averaged values and dashed lines represents $H_{up} = H_{down}$.

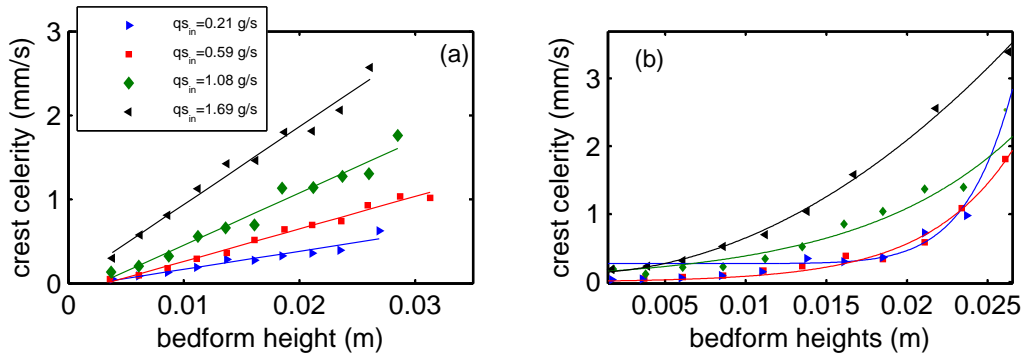


Figure 6.8: Antidune celerity c as a function of antidune height for flume angle 2° (a) and 4° (b).

is, for instance, seen in figure 6.1(b) where antidune migration is slower at the beginning of the run due to an aggradation period.

Antidune celerities c were computed for the stationary regime using the tracking method explained in section 6.1.1.3. Figure 6.8 shows the celerity c as a function of H . In all cases, the higher the antidune the faster the migration. This is an important point because a higher antidune presents a larger lee side surface (potentially erodible) and then a higher migration celerity, which suggests the high potential of strong local bedload transport events. This is discussed and quantified in more detail in section 6.3.

6.1.2.3 Hysteresis in flow over antidunes

Aiming to understand flow characteristics over bedforms in steep channels, a side experiment was designed to produce accurate flow measurements (water depth and local velocities). The installation is a fully transparent flume, similar to the 2D-flume with a smooth sinusoidal-waved bed. In this thesis, only a few interesting points, relative to changes in flow behaviour, are discussed. A description of the experiment is given in appendix C.2.

For growing antidunes, the Froude number Fr decreases on the stoss side and increases on the lee side. At one point, this evolution leads to the appearance of a hydraulic jump on the stoss side at a critical difference between the stoss and lee side Froude number ΔFr [Alexander *et al.*, 2001; Deigaard, 2006]. On the contrary, when the antidune amplitude decreases, due to the changes in flow patterns caused by the hydraulic jump, the hydraulic jump persists for a much lower ΔFr . This hysteretic phenomenon is studied here on a fixed wavy bed by increasing the water discharge to induce the same effect on Fr . The results confirm the presence of a hysteretic behaviour in antidune evolution from growth to breaking [Alexander *et al.*, 2001; Deigaard, 2006]. The corresponding loop of Q_l as a function of h is shown in figure 6.9.

The presence of hysteresis in the flow during antidune migration certainly explains a part of the intermittency observed in the antidune occurrence and migration. The appearance of the hydraulic jump limits the growth of antidunes and often leads to antidune destruction — as the hydraulic jump persists when the antidune is starting to be eroded. Moreover, the high roughness in the 2D-flume experiments adds randomness to the value of ΔFr . Thus, local feedbacks of the flow, i.e. at the antidune scale, have great importance on bed evolution, fixing the antidune amplitude. This verifies that the antidune height is scaled on the mean water depth.

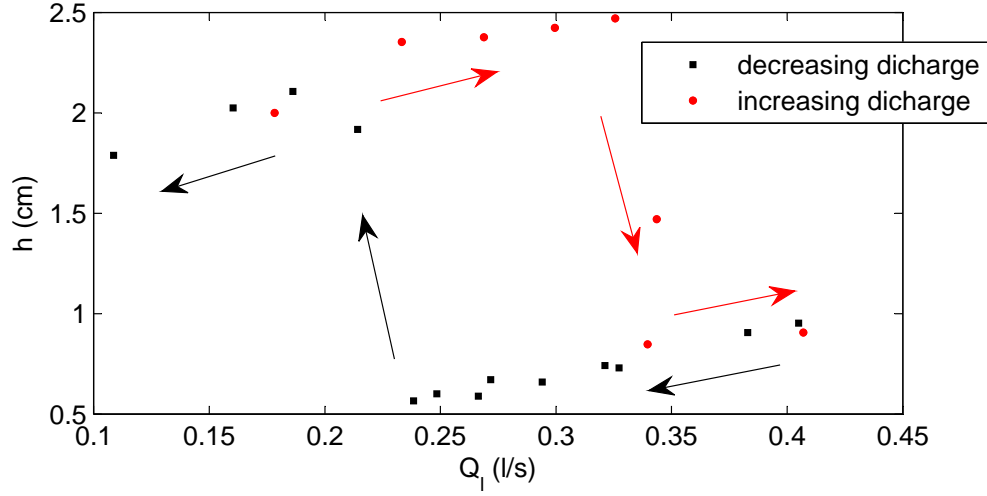


Figure 6.9: Hysteresis in the relation h as a function of Q_l , measurements taken over a fixed wavy bed (appendix C.2), flume inclination is 2° .

6.1.3 Local slope analysis

6.1.3.1 Method of computation

From the present data, the local slope θ is determined at different scales. The largest scale corresponds to the computation of Θ (section 5.1.1.1). At the smallest scales, θ represents the antidune steepness. Thus, the occurrence of active antidunes, i.e. with steep sides, can be deduced. The trended data, moving-averaged at scale $2.5 \text{ cm} = 4d_{50}$ (section 6.1.1.3 and figure 6.2), is used to compute θ . A linear fitting, in the same manner as described in section 5.1.1.1, is made to deduce θ at the desired scale by choosing the appropriate window length. For each window length, the data at each time and each location were used. This means that, for instance, at the scale 2 cm , a set of more than 1000 local slope samples are available at each time — given the channel length of more than 2 m .

6.1.3.2 The grain pile problem and experiments

Two experiments were conducted in order to estimate the angle of repose Γ_r and the critical angle of stability Γ_c of a pile composed of the sediments used in the flume. These values are needed to infer local antidune stability and compare with other grain pile stability experiments. One of the two experiments consists of building a 3D classic conical pile with dry grains. The second consists of a grain pile between two walls under water to reproduce the 2D-flume conditions. θ_c and θ_r might depend on the gap between the walls of the channel, as Γ_c and Γ_r increase with a shorter gap [Courrech du Pont *et al.*, 2003b]. Under water, Γ_c and Γ_r should be lower than in dry conditions [Carrigy, 1970]. The experimental procedures are detailed in appendix C.3.

The results of these experiments show that the avalanche domain of the sediments used extended from 34° to almost 44° (at the scale of the system) between the 8-cm-gap walls under water, with a narrower range in the dry wall-free experiment. As shown later, θ reaches locally similar values, implying that local avalanches or slides might be possible in certain circumstances. Antidune lee sides are, at least locally, within or close to the avalanche slope domain. Moreover, these granular experiments show that local slopes reach extremely high values, up to 64° (local maximum slope γ_c) at the scale 2 cm (table C.1).

Loiseleux *et al.* [2005] observed, in the submerged case, that when the profile slope is close to the avalanche domain, i.e. Γ approaching Γ_r , the particle entrainment by the fluid is easier. Thus, even if Γ_r is not strictly reached, Γ can reach a high value that induces temporary larger particle erosion due to collective motion effects. This behaviour should be similarly present for θ in my case.

6.1.3.3 Local instabilities

The probability density functions of the slope θ at different scales are drawn in figure 6.10. At large scales, the pdfs are spiky (not shown here) but become more continuous and smooth for smaller scales. The high probability of certain angles (spikes) at large scales is a sign of memory effects — for instance stabilization effects due to recent history [Church *et al.*, 1998]. Because of the tight arrangement of grains in the subsurface bed layers, the topography might tend to recover a past shape, until the basal bed layer is destroyed, for instance during an exceptional event.

At a first look, when the scale decreases the pdfs have a nice gaussian shape with an expected value corresponding to Θ_m (figure 6.10(a)). However, representing the same pdf in a log-scale (figure 6.10(b), 6.10(c) and 6.10(d)), the tails of the distributions differ significantly from a gaussian distribution. This difference is larger for positive slopes than for negative ones — counter-flow slopes. The tail of the distribution is larger at smaller scales. This means that the probability of observing very high local slopes is relatively large. Thus locally, the bed profile reaches values close to the maximum angle of stability relatively frequently. Indeed, for some runs, θ at the scale 2 cm, becomes higher than 38° (figure 6.10(d)).

These very steep small-scale surfaces, which correspond to the steepest antidune lee sides, are then prone to small avalanches or slides, or at least to intense collective erosion events. The presence and the activity of these local instabilities in the system, depending on the experimental conditions, are discussed in the next section.

6.2 Effects of the parameters

The influence of the experimental parameters on antidune characteristics and evolution is analyzed in this section. In addition to the flume inclination, the sediment feeding rate qs_{in} and the flow strength, some important points on grain characteristics are discussed. Besides, a brief comparison with the literature on antidunes is presented, underling the particularity of the present data. Finally, the consequences on the observed behaviours of the antidunes are discussed.

6.2.1 Channel parameters

6.2.1.1 Flume inclination

Strong differences are observed when varying the flume inclination α . Here, the antidunes are studied in detail for 2° and 4° runs. Results show different behaviours for both antidune height pdfs (figure 6.4) and for antidune celerities (figure 6.8). In runs at 2° , the relation between antidune height H and celerity c is linear for all ranges of qs_{in} whereas at 4° non-linearity appears — except for strong bedload transport conditions with high S_h and qs_{in} (section 6.2.2.2). At high α , c increases faster with H than a linear relation.

The celerity of the average antidune, i.e. of height H_m , is lower at 4° than 2° , although the converse is true for the largest antidunes. This wider discrepancy of migration celerities in steeper channels is probably related to the large intermittency of bedload transport rates, observed in steep channels.

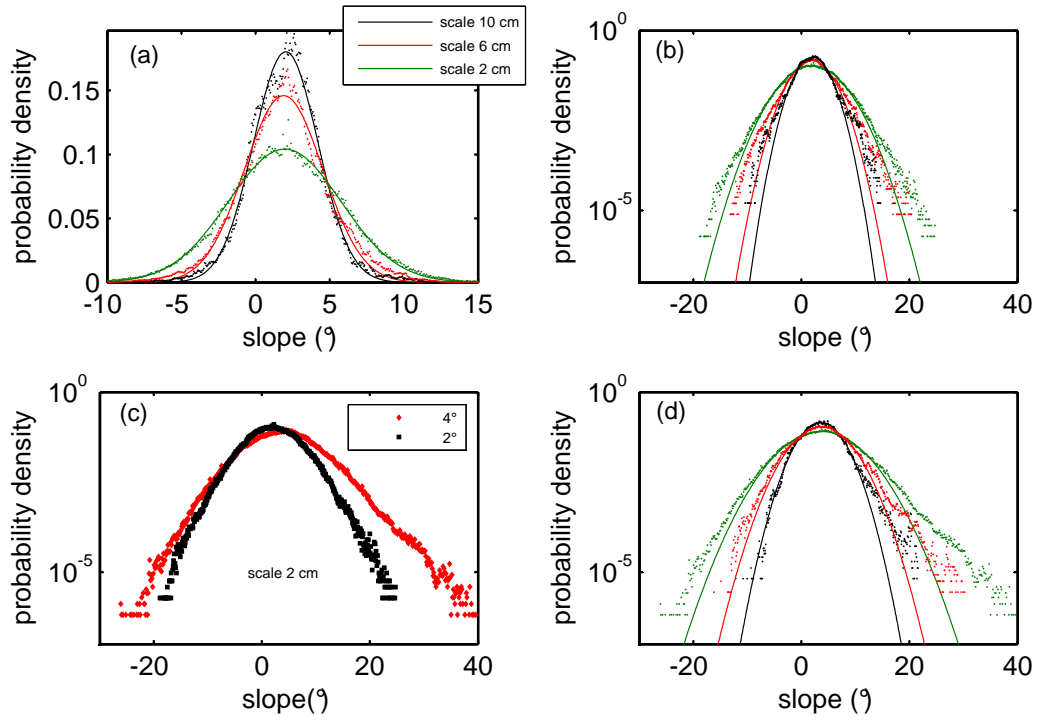


Figure 6.10: Pdfs of local slope for scales 2 cm, 6 cm and 10 cm with gaussian fitting for runs *2deg3v* (b) and *4deg3v* ((a) and (d)). (c) Comparison of pdfs at scale 2 cm for 2° (run *2deg3v*) and 4° (run *4deg3v*).

Although, at 4° , most of the antidune height are small ($H_m \simeq 10$ mm), antidunes taller than H_m are relatively frequent. The corresponding antidune height pdfs (figure 6.4(b)) are significantly skewed, with a large tail towards high value of H . These tall antidunes, in addition to their potential activity due to their surface (large lee side for erosion), migrate faster than the small ones — up to 15 times faster (figure 6.8(b)). These several factors certainly lead to locally strong bedload transport events.

At low α , the presence and the characteristics of antidunes are more regular. The pdf of H for 2° is not significantly skewed. In figure 6.4(a), pdfs of H drop rapidly to zero for increasing H . Note that both the mean and maximum antidune heights are larger for 2° than 4° as the mean antidune characteristics are scaled on the water depth h — for the same S_h , h is higher at lower α .

The migration of a given antidune leads either to a global aggradation or degradation depending on its asymmetry. From figure 6.7, H_{th} is not dependent on qs_{in} and takes the values of 2 and 5 mm for 2° and 4° respectively. Considering the values of H_m , respectively 15 and 10 mm, and the pdfs of H , it is found that aggrading antidunes do not have much influence at 2° as they are small and rather infrequent. In this last case, aggradations take place randomly along the channel from the inlet.

Contrary to low α , at 4° , values of H around H_{th} have a high probability of occurrence. Taking into account the higher value of H_{th} , the presence of significant aggrading waves in steep channel is inferred. These waves, that stop and accumulate most moving particles on their stoss side, during certain stable periods, induce the observed quasi zero outlet solid discharge. Thus, in this case, the migration of these waves is directly dependent on qs_{in} . This mechanism of aggradation might also explain the larger value of the slope range R at higher channel slopes (chapter 5). Indeed, this way of aggradation is efficient, preventing particles from perturbing the bed and permitting larger accumulations of sediment in the system. It confirms that the critical angle of stability Θ_c possibly reaches a higher value in steep channels leading to stronger degradation events.

To summarize, at low α , antidunes degrade the channel bed more constantly, which is then aggraded in a relatively regular way. Whereas, at high α , the periods of aggradation and degradation are well distinct, corresponding respectively to periods of low and high bedload transport rates, underlined in chapter 4.

Concerning the local slope θ (figure 6.10), large differences are observed depending on α . For all scales, the pdfs of θ are larger for 4° than 2° . Both tails, positive and negative, are larger for steeper flume inclinations. At 4° , at the same scale 2 cm, θ can reach more than 38° , although, at 2° , θ remains below 25° . This shows that, in the case of 4° , the system reaches the avalanche domain temporarily and locally, and is sometimes close to the threshold Γ_r , contrary to less steep channels (appendix C.3).

A few points influenced by channel steepness were detailed in this section. Antidune characteristics, such as height, steepness, celerity and shape, seem to explain the high intermittency seen in steep channels. For higher Θ_m , a larger difference between H_m and H_{max} , a wider range of celerity c with low $c(H_m)$ and high $c(H_{max})$, a more efficient aggradation mechanism, more distinct periods of aggradation and degradation, and local slopes close to the avalanche domain were observed. Thus, specific local mechanisms of transport or particle entrainment, like collective erosion and avalanches/slides due to steep local slopes, act in steep channels contrary to gentle-slope channels, probably leading to the additional observed variability.

6.2.1.2 Sediment characteristics

The impact of changing grain characteristics and the grain size distribution is not examined in this thesis. However, some points taken from the literature are important for discussion here in order to specify some conclusions for stream channels. Several studies underline the effects of grain arrangement and compaction on bedload transport [Charru *et al.*, 2004; Zimmermann *et al.*, 2010] which depend on the sediment characteristics.

As mentioned in chapter 3, the use of natural gravel was an important choice. Frette *et al.* [1996] shows that the characteristic details of grains, partly quantified by the aspect ratio, have important implications for grain pile dynamics. Particularly, rough grain surfaces or high angular shapes increase the critical angle of stability Γ_c [Carrigy, 1970].

The gravel type used for this study is round, meaning that they are representative of gravel reaches situated a bit downstream from sediment supply zones. Sediment shows high angular shapes at the top of the watersheds and is rounded by friction and collision while travelling downstream. The present rounded gravel falls into the gravel category found in many mid-mountain streams. In certain steep mountainous streams, like the Navisence River, the grain shapes might be a bit more angular, increasing for instance Θ_c or θ_c — and the corresponding hysteretic and unstable effects.

The grain size distribution is also an essential parameter that characterizes a given stream reach. A wide sediment size distribution adds a significant component for grain arrangement possibilities, which could imply temporary accumulation of sediments. For instance, large stones initiate reticulate structures [Church *et al.*, 1998; Hassan & Church, 2000] and cluster bedforms [Brayshaw, 1985] that increases bed roughness and temporary channel stability, leading to higher Θ_c and θ_c .

Moreover, the rare presence of very large stones induces an intermittent behaviour with the creation of strong force chains and blocking phenomena in the channel. The jammed state hypothesis, defined by Church & Zimmermann [2007], determines the possible presence of steps in step-pool streams (section 2.2.3). One major criteria of this hypothesis is the jamming ratio, defined as the channel width relative to the step keystone size. Thus, a wide grain size distribution leads to additional accumulations of sediment, creating massive amount of temporary stable sediment — that can be easily released by the failure of the step.

To summarize, a larger grain size distribution and rougher angular grains add intermittency and instabilities in stream channels. Although high steep steps appear to be stable at a certain time-scale, they are possibly destroyed by intense floods [Turowski *et al.*, 2009]. Thus, the chance of extreme degradation events is high in this type of stream, and comparable to that observed in the present experiments.

6.2.2 External conditions

6.2.2.1 Sediment supply

Figure 6.8 gives evidence that the relation $c = f(H)$ varies strongly depending on the solid input discharge qs_{in} . At 2° , the relation is linear and its slope increases with qs_{in} . At 4° , the relation is exponential and even greater than exponential for the lowest qs_{in} . This last point confirms the link between intermittency of bedload transport and the temporary presence of fast moving antidunes. At lower qs_{in} , which induces less perturbations on the bed by moving particles, antidunes grow taller, up to their critical state (section 6.1.2.3), relatively frequently, i.e. θ become close to θ_c . These unstable antidunes then propagate rapidly, particularly when the channel bed is in a global critical state, i.e. for Θ close to Θ_c (chapter 5).

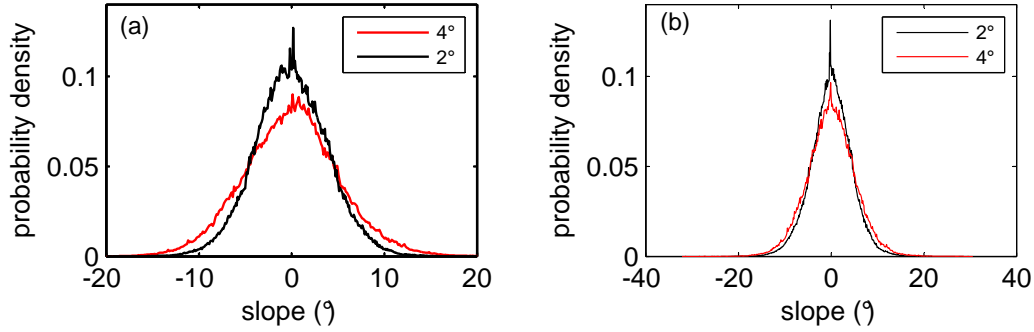


Figure 6.11: Pdfs of the local slope at scale 2 cm for $q_{sin} = 0.2$ g/s (a) and $q_{sin} = 1$ g/s (b) for flume inclinations 2° and 4° .

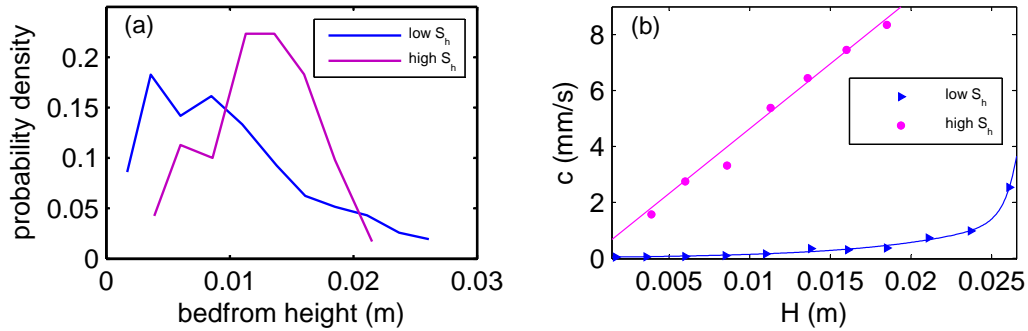


Figure 6.12: Comparison between low and high transport conditions at 4° (respectively runs *4deg3v* and *4deg48v*). (a) Pdfs of bedform heights. (b) Antidune celerity as a function of bedform height.

q_{sin} have some effects on the distribution on local slopes. First, the differences in distribution shape when varying α (previous section) are less pronounced for increased q_{sin} . For instance, the local slope distributions at 2° and 4° are more similar at a rate of 1 g/s than a rate of 0.2 g/s (figure 6.11). Second, at all scales and α , the distribution is narrower when increasing q_{sm} (figure 6.11). Again, this confirms that constant and regular bed perturbations, caused by a high q_{sin} , prevent the development of steep, unstable and local antidunes.

6.2.2.2 Shields stress

It is commonly thought that with higher water discharge, bedforms are larger and more variable in term of shape (Singh *et al.* [2012] for dunes). In the present steep slope experiment, it is verified that the mean antidune height H_m is larger for higher transport conditions, i.e. larger S_h and higher q_{sin} (12.5 cm against 10 cm). This behaviour was expected, as antidune heights scale on h . However, a more variable behaviour is observed for low discharge. For the highest transport conditions, the pdfs of H tend to have a narrower distribution, whereas for decreasing transport conditions, the pdfs are skewed and wider (figure 6.12(a)). At lower S_h , H_m is smaller but very tall and fast-moving antidunes are relatively more frequent. It explains why bedload intermittency decreases with higher flow conditions, as antidune migration occurs for a relative narrow range of antidune heights. A linear trend between c and H at high S_h (compared to an exponential increase at low S_h) emphasizes this behaviour (figure 6.12(b)).

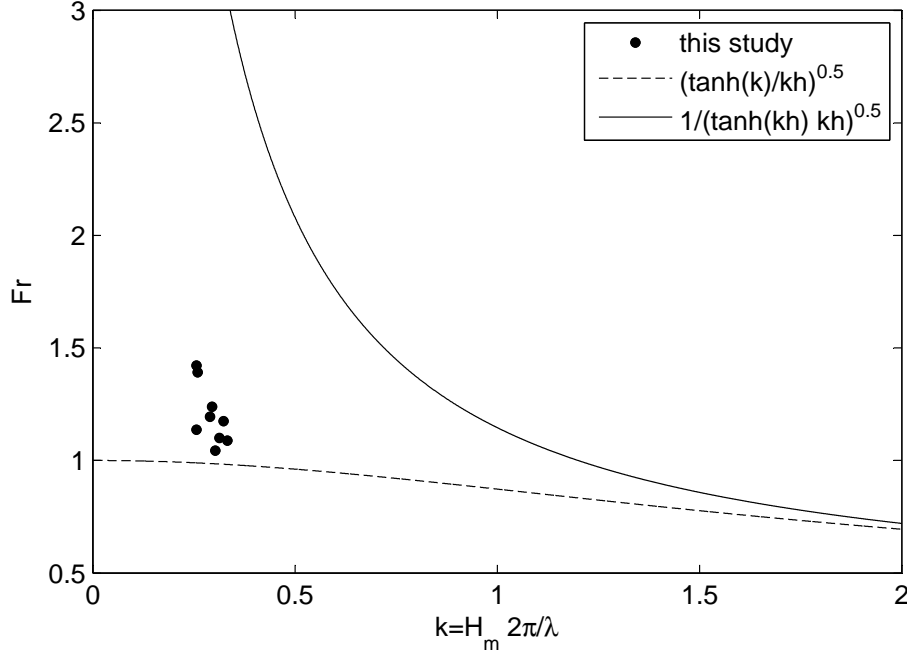


Figure 6.13: Antidune domain defined by the two equations 2.15 and 2.14 (section 2.2.3.1) with the situation of the present data.

6.2.3 Discussion

6.2.3.1 Comparison with existing antidune studies

At first, it is interesting to represent the present data on the classic domain of antidune existence (section 2.2.3.1) to situate the study. This domain was analytically derived [Kennedy, 1961; Reynolds, 1965; Parker, 1975] and confirmed by many experimental data set [Recking *et al.*, 2009a]. All the present runs are found to be in this domain (figure 6.13), confirming the presence of antidunes. The present data set corresponds to lower wave numbers than many other experiments, leading to a particular interest. This situation might be due to the low transport conditions and the high intermittency observed here.

Using equation 2.16, the antidune mobility number Fa was found to be between values of 0.27 and 0.36 for the data set. This confirms the presence of upstream-migrating antidunes ($Fa < 1$). Equation 2.13 has also been tested without a good prediction. In the present case, the range of wavelength is relatively narrow which corresponds to a narrow range of mean velocities (figure 6.13). Thus, the general behaviour of this equation is at least verified.

The mean antidune characteristics of the data set seems to match well with the literature. However, the study of the statistics of their characteristics and the resulting intermittent behaviour is novel, especially for low transport conditions.

6.2.3.2 Bedload intermittency and antidune migration

In summary, antidune dimensions λ and H scale with the water depth, and the migration velocity scales with the solid input discharge and mean channel slope. The wide discrepancy of antidune heights, local slopes and migrating celerities explains the high intermittency in steep channels

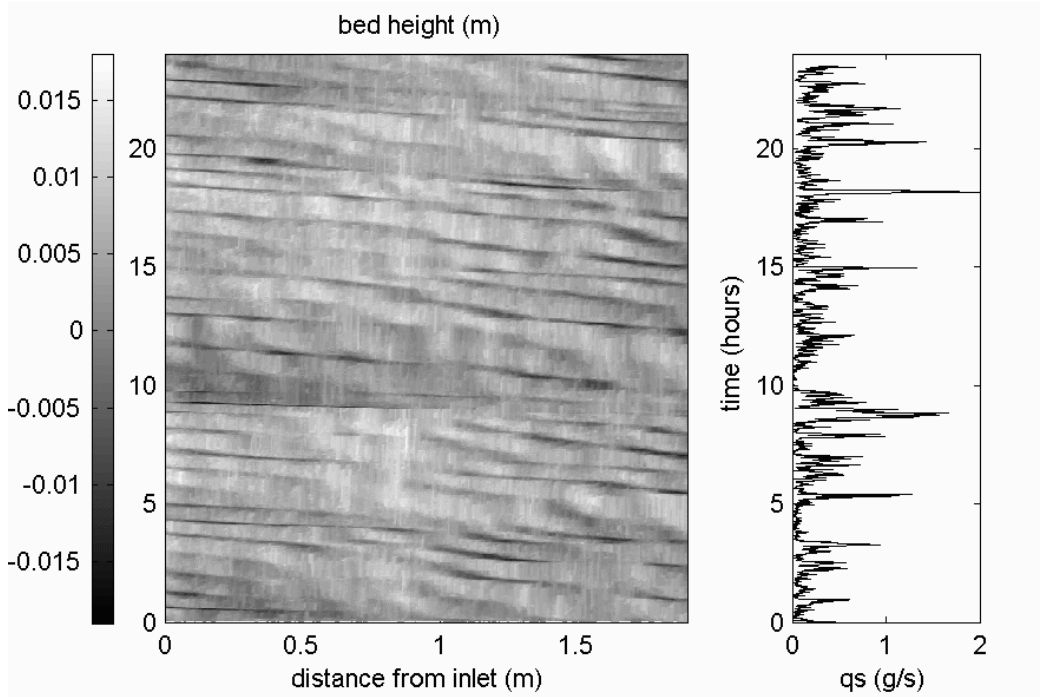


Figure 6.14: Spatio-temporal plot of bed elevation of run *2deg3v* with corresponding outlet bedload transport rates integrated over 1 minute on the right.

subject to low sediment supply and low flow conditions. Aggradation waves allow large sediment accumulations hampering bedload transport for relatively long time periods. When the threshold Θ_c is reached or a sufficiently intense perturbation occurs, a fast degradation starts by propagation of local instabilities, i.e. active antidunes. Their migration seems to be controlled by slides and collective motion events, corresponding to intense pulses of sediment. The comparison between the spatio-temporal plot of bed elevation and qs confirms this conclusion (figure 6.14). The strongest bedload events appear at the same time as fast moving antidunes, especially when they are close to the flume outlet. However, no significant correlation was found between qs and the bed elevation close to the outlet (neither with the bed elevation increment nor taking into account a time lag). It shows the complex behaviour induced by multiple factors, like antidune height, wavelength and celerity or the influence of bedforms far from the outlet. These present behaviours of steep channel evolution should be even more pronounced for natural streams with large grain size distribution and angular gravel.

6.3 Some quantifications of local processes

In this section, two equations are derived to confirm the essential roles of local instabilities, i.e. antidunes, on channel evolution and sediment transport pulses. First, based on the measured antidune characteristics, local bedload transport rates are quantified. Secondly, an avalanche model is developed verifying that the critical angle of stability of the grain arrangement in the channel is reached locally and temporarily in a few experiments. This explains the extremely fast migration of certain antidunes.

6.3.1 Bedload transport rate from bedform migration

An estimate of bedload transport due to antidune migration is difficult, compared to the case of dunes. Since dunes migrate downstream as they grow, a recording at the outlet of the flume gives directly bedload transport pulses linked to dune migration. This is not the case for antidunes, as they grow by migrating upstream, i.e. moving away from the measurement section.

Moreover eroded grains on the antidune lee side only partially deposit on the next stoss side, preventing the exact measurement (at the outlet) of the bedload contribution due to antidune translation. Bedload equations based on bedform translation are more efficient for dunes as the total bedload transport is deposited on the lee side of the dunes due to the flow separation on the dune crest. On the contrary, in the antidune case, similar equations might be approximative. However, ranges of solid discharge are computed and compared, showing that this approach is still valuable.

6.3.1.1 Equation for bedload transport rate due to antidune translation

Local bedload transport due to antidune translation, i.e. the apparent volume of grains that is eroded per unit of time for the displacement of the antidune, is computed theoretically. This definition considers that the mean distance for deposition of one eroded particle is much larger than the wavelength λ , i.e. particles eroded on the lee side are not deposited on the next downstream stoss side. Although the validity of this assumption is discussed later, it seems reasonable knowing that the flow velocity necessary for particle transport is smaller than for particle erosion (the Hjulström curve [Hjulstrom, 1935]). It means that after erosion, the particle travels a relatively long distance before deposition.

The apparent volume of dislodged grains ΔV_g , during one period ΔT , is twice the area A times the flume width W where A is the sectional area of the depression between two crests (figure 6.15). The volumetric bedload transport rate Q_s is then given by

$$Q_s = \frac{\Delta V_g}{\Delta T}. \quad (6.1)$$

The antidune shape is supposed to be sinusoidal which is a common approximation for antidunes [Kennedy, 1969; Recking *et al.*, 2009a] and seems realistic in my case (figure 6.16 for an image of one antidune). Thus, $A = \lambda H/2$ and $\Delta V_g = 2AW = \lambda HW$ with H the antidune height. The bedload transport rate q_{sth} due to antidune migration is then

$$q_{sth} = \rho_{app} H W \frac{\lambda}{\Delta T} = \rho_{app} H W c \quad (6.2)$$

with c the migration celerity of an antidune of height H . As it was shown in section 6.2, c is dependent on H and the global channel slope Θ . From equation 6.2, it is possible to compute the theoretical bedload transport rate produced by a given antidune (the next section). Note that this computation does not account for particles that were eroded upstream of the antidune, passing through the studied window of length λ without deposition.

Equation 6.2 is equivalent to the translation flux derived by Simons *et al.* [1965], McElroy & Mohrig [2009] or Martin & Jerolmack [2013] for dunes, which is proportional to the cross-sectional area of the bedform times the migration speed. It follows that the shape factor β is 0.5 [Simons *et al.*, 1965; Martin & Jerolmack, 2013]. In the antidune case (sinusoidal shape), the shape factor should be also 0.5 if the same assumptions as for dunes are made — particles eroded on the lee side are all deposited on the next downstream stoss side. If we assume that no particle is deposited on the next stoss side, the shape factor is 1, corresponding to q_{th} from equation 6.2. Thus, given my observations, true bedload transport rates due to the antidune migration is somewhere between $q_{sth}/2$ and q_{sth} .

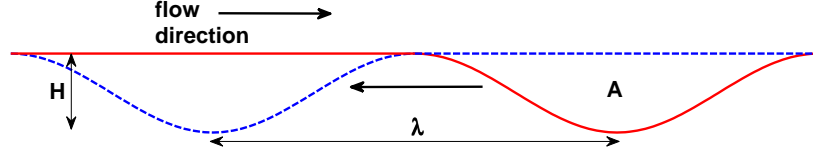


Figure 6.15: Scheme of antidune migrating at celerity c , at time t in blue and at time $t + \Delta T$ in red, A is the cross-sectional area of the scour.



Figure 6.16: Picture showing an antidune in the 2D-flume.

6.3.1.2 Local bedload transport rate

Using equation 6.2, the local bedload transport rate $qs_{loc,m}$, produced by an averaged antidune, and the bedload pulses qs_{loc}^* , produced by the tallest antidunes, are estimated. $qs_{loc,m}$ is computed from the mean antidune height H_m and its corresponding migration velocity $c(H_m)$ is deduced from the fitted curve as shown in figure 6.8. For the estimate of qs_{loc}^* , the measured maximum height H_{max} and velocity c_{max} are used. The two rates read

$$qs_{loc,m} = \rho_{app} H_m W c(H_m), \quad (6.3)$$

$$qs_{loc}^* = \rho_{app} H_{max} W c_{max}. \quad (6.4)$$

Figure 6.17(a) shows $qs_{loc,m}$ and qs_{loc}^* for different input bedload rates qs_{in} and flume inclinations, 2° and 4° . These rates are only locally valid, so that it is possible to have $qs_{loc,m}$ larger than qs_{in} . Moreover, due to aggradation and degradation of the bed at larger scales than the antidune scale, validation by using qs_{out} are difficult.

The local bedload rate increases quasi linearly with qs_{in} except for qs_{loc}^* at 4° . This exception points out the particular case of steep slopes and weak transport conditions which particularly occurs in the *4deg3v* run. Indeed, qs_{loc}^* at 4° is more than four times qs_{loc}^* at 2° for the lowest qs_{in} , and also relatively high compared to values at high qs_{in} . This suggests that the specific high intermittency, seen for steep channels and low mean transport rates, is strongly linked to the transient antidune migration. This is also seen in figure 6.17(c) where pdfs of the local bedload transport rate $qs_{loc} = \rho_{app} H W c(H)$, due to the translation of an antidune of a given height H , are represented normalized with the mean outlet rate. The pdfs decrease quickly with increasing transport rates for most experiments except for the ones with low qs_{in} . Note the large tail for 4° at the lowest qs_m .

When looking at the bedload outlet rates, the above antidune migration effects are present even though no antidune is present in the vicinity of the outlet of the flume, but are well developed on the $2/3$ upstream part of the flume. Thus qs_{loc}^* is expected to be higher than the peaks of qs_{out} if antidunes are effectively responsible for the outlet bedload pulses. This lower value at the outlet is due to the deposition effects between these antidunes and the outlet. To compare the outlet rates

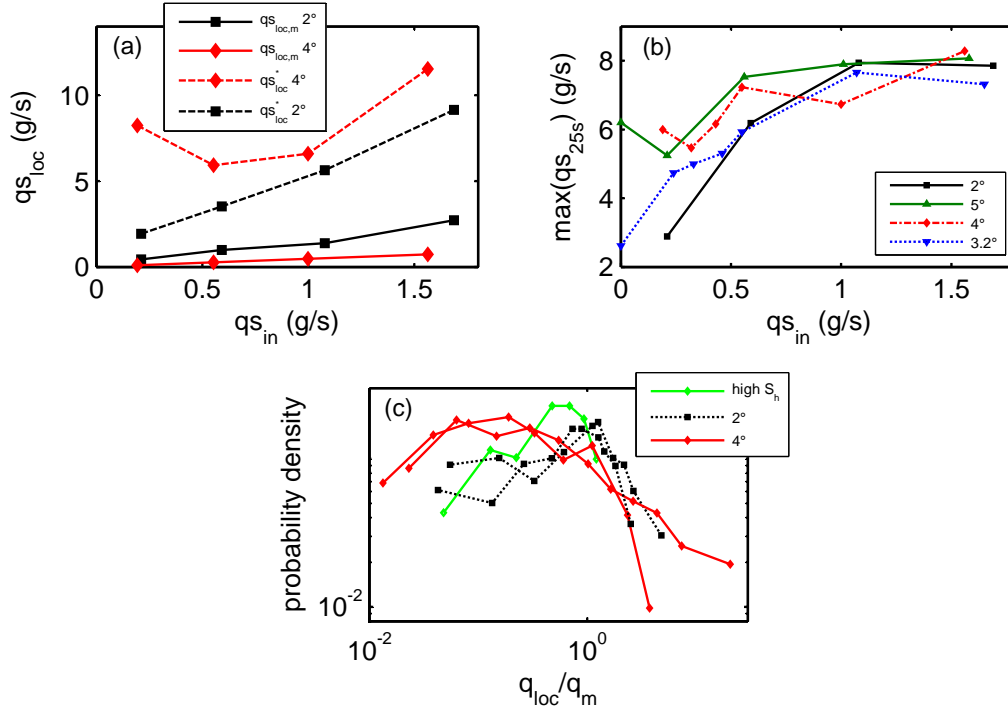


Figure 6.17: (a) plots of $qs_{loc,m}$ and qs_{loc}^* as a function of qs_{in} for flume angle 2° and 4° . (b) Maximum of the outlet bedload rate at the characteristic temporal scale of the highest bedforms (25 s). (c) Pdfs of $qs_{loc}/\overline{qs_{out}}$.

with qs_{loc}^* , it was necessary to determine the characteristic time scale of the highest antidunes, i.e. the fastest ones. From the measurements, the duration of appearance of these antidunes is on the order of 25 s. Thus, this antidune characteristic time scale was chosen to calculate the maximum solid discharge at the flume outlet from the bedload transport time series. The results are plotted in figure 6.17(b). The same behaviour as that deduced from equation 6.4 is observed, suggesting that the antidune migration strongly influences the recorded intermittency at the outlet.

6.3.2 Bedload transport rate from grain slides

6.3.2.1 Avalanche/slide observations

Events assimilable to small avalanches, slides or other kinds of particles reorganization leading to the displacement of a large quantity of particles were observed in the 2D-flume experiment. In figure 6.18, we see one of these events. The time interval between each image is 1 s. Between image b and e, many particles have slid together and have been entrained along the flume. Even if these phenomena occur on a short distance, the particles that were concerned are easily flushed out by the flow. This process effectively induces the intense pulses observed at the flume outlet.

These kinds of events are not driven exclusively by the flow because there is not significant changes in the hydrodynamics before and during the triggering of the event. However, they are potentially triggered by intermittent turbulent events, moving particles from upstream or particles dislodged at the base of the slide.

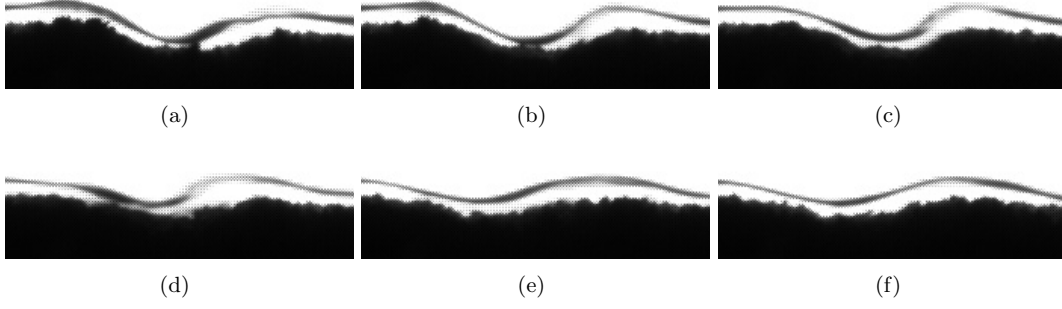


Figure 6.18: Sequence of successive images (sampling time = 1 s) showing a slide event (run *4deg3v* during the sharp failure at time 13 hours). Particularly note the antidune height and the position of the through before and after the event. Flow is left to right.

6.3.2.2 Avalanche model

In this section, the hypothesis that bedload transport pulses are due to local avalanches on the lee side of the steepest antidunes is validated. A simple model, inspired by Loiseleux *et al.* [2005], is developed to investigate the local stability of grain layers at the gravel bed surface. An avalanche is triggered when the local critical angle of stability θ_c is reached. Considering a volume of grains that can potentially move as an avalanche, the force balance at the avalanche onset can be written as in equation 6.5. The apparent weight F_W , the shear fluid force $F_\tau = \tau b L$ and the pressure force $F_p = \Delta P b h$ in the bed, all three acting in the downstream direction, are in equilibrium with the solid friction force $F_f = \mu_e F_W \cos \theta$ between the potentially mobile grains and the motionless bed (figure 6.19). The effective granular friction coefficient can be described as $\mu_e = \tan \theta_0$, with θ_0 the avalanche angle for no flow. This leads to the following equations with h , b and L , being the height, the width and the length of the sliding volume respectively

$$F_W + F_\tau + F_p - F_f = 0, \quad (6.5)$$

$$(1 - \phi)\Delta\rho g b h_{av} L \sin \theta_c + \rho_w g b h_{av} L \sin \theta_c - (1 - \phi)\Delta\rho g b h_{av} L \mu_e \cos \theta_c = 0, \quad (6.6)$$

$$(1 - \phi)\Delta\rho h_{av}(\sin \theta_c - \tan \theta_0 \cos \theta_c) + \rho_w \sin \theta_c(h + h_{av}) = 0, \quad (6.7)$$

$$(1 - \phi)\Delta\rho h_{av}\left(1 - \frac{\tan \theta_0}{\tan \theta_c}\right) + \rho_w(h + h_{av}) = 0, \quad (6.8)$$

$$\tan \theta_c = \frac{\tan \theta_0}{1 + \frac{\rho_w(h + h_{av})}{(1 - \phi)\Delta\rho h_{av}}}. \quad (6.9)$$

The resulting equation 6.9 shows that θ_c is independent on b and L , i.e. the size of the potential area subjected to the instability. θ_c varies only with the water depth h and the avalanche depth h_{av} . Intuitively, θ_c decreases with increasing h , i.e. with increasing fluid force, and increases for increasing h_{av} which corresponds to larger avalanches. This is confirmed in the following where two cases are studied; first, the local case at the scale of the antidunes and second, the global case at the system scale.

6.3.2.3 Local avalanches

The potential length L subjected to an avalanche was estimated visually to be a few centimeters. Moreover, avalanches do not affect the whole width of the flume. This also implies that the avalanche width b is in the same order of magnitude as its length L . The typical depth of an avalanche is estimated to be a few layers of grains [Courrech du Pont *et al.*, 2003a], thus $2 - 3d_{50}$ seems to be a good order of magnitude for the avalanche depth h_{av} .

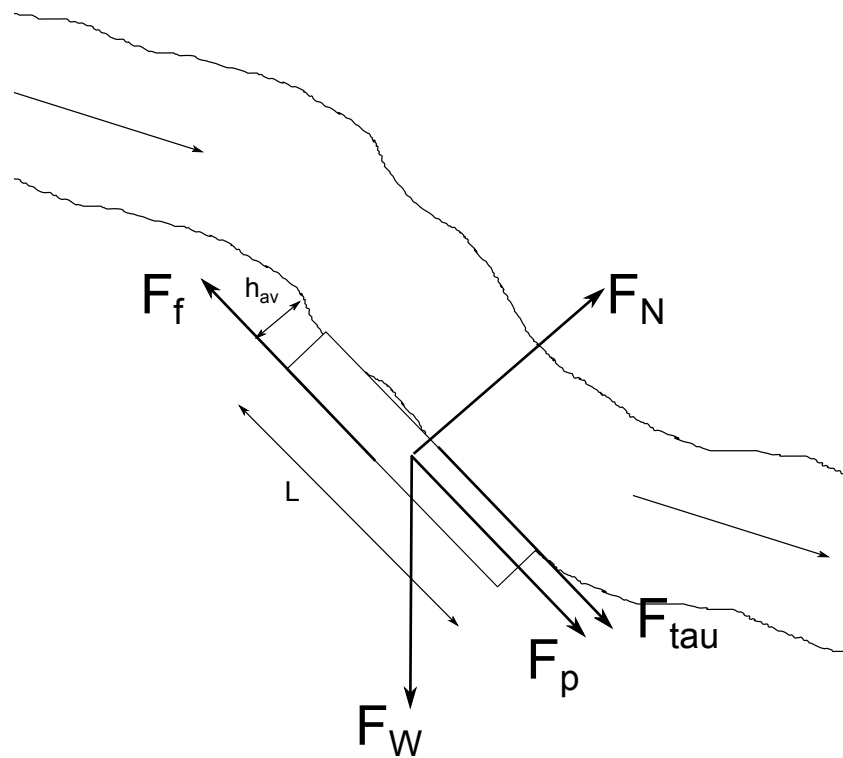


Figure 6.19: Sketch of forces acting on a volume of grains potentially moving as an avalanche.

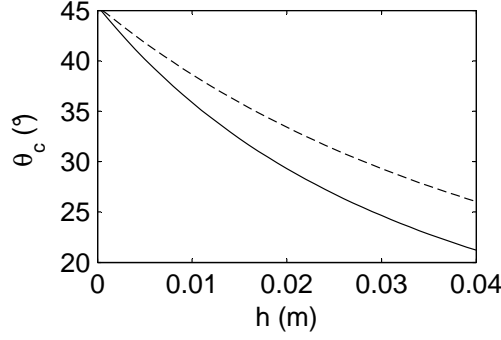


Figure 6.20: Plot showing θ_c as a function of h for $h_{av} = 2d_{50} = 1.25$ cm (line) and $h_{av} = 3d_{50} = 1.875$ cm (dashed line).

The model was tested with $\theta_0 = \gamma_c = 64^\circ$, using the results of the under water grain pile experiment presented in section 6.1.3 and in appendix C.3. This value corresponds to the computational scale 2 cm which is in accordance with the potential avalanche length L . Although, θ_c is not dependent on the avalanche area, nor on b or L , the values of b and L are used to compute the mass of entrained grains m_{av} during a typical avalanche,

$$m_{av} = \rho_{app} b L h_{av}. \quad (6.10)$$

Taking b between 2 and 4 cm, h_{av} between $2d_{50}$ and $3d_{50}$ and $L = 2$ cm, it follows that m_{av} lies in the range 8 to 24 g. These values are in agreement with equation 6.4 and the observed fluxes integrated over one second. For instance figure 6.17 shows a value of qs_{loc}^* around 10 g/s. Moreover, in the steepest experiments, solid discharge peaks of up to 15 g/s were observed.

Model results are presented in figures 6.20 and 6.21. Figure 6.20 represents the decrease in θ_c as a function of the h , i.e. increasing the Shields stress component, for $h_{av} = 2d_{50}$ and $h_{av} = 3d_{50}$. For large h_{av} , the decrease in θ_c is slower, meaning that for higher h , i.e. higher S_h or lower α , avalanches of depth h_{av} are rare. In figure 6.21, θ_c as a function of h_{av} are represented for two runs with very low feeding rates, thus with a minimal sediment transport perturbation. Runs *4deg3v* and *2deg3v* were chosen with $h = h_m/2 = 0.008$ and $h = h_m = 0.029$ m respectively (h_m the mean water depth of the 2D-flume experiment). Indeed, at 4° , the water is much shallower than h_m over the steep bed sections, which is not the case at 2° . The maximum local slopes at the scale of 2 cm are up to 40° and 24° respectively for runs *4deg3v* and *2deg3v* (section 6.1.3), which imply that $h_{av} = 0.02$ and $h_{av} = 0.011$ m respectively. This confirms the presence of local avalanches and their effects on bedload transport pulses in steep channels — larger avalanches exists for higher channel slopes at the same S_h .

6.3.2.4 System relaxation

Although it is not at all an avalanche process at the global channel scale, I try to use this model at that scale. It should permit to confirm the analogy with metastability. In the case of a granular pile, relaxation — return of the system to its lowest energy state — occurs when the pile slope is steep enough for the propagation of local avalanches. In the submerged case, measurements showed that relaxation happens for pile angles up to 44° , corresponding to local instabilities with slope up to 64° at the 2 cm scale (appendix C.3).

In the case of flowing water over a granular bed (e.g. my experiments), the low global bed angle prevents an instantaneous relaxation of the whole system. At these channel slopes, up to 5° in

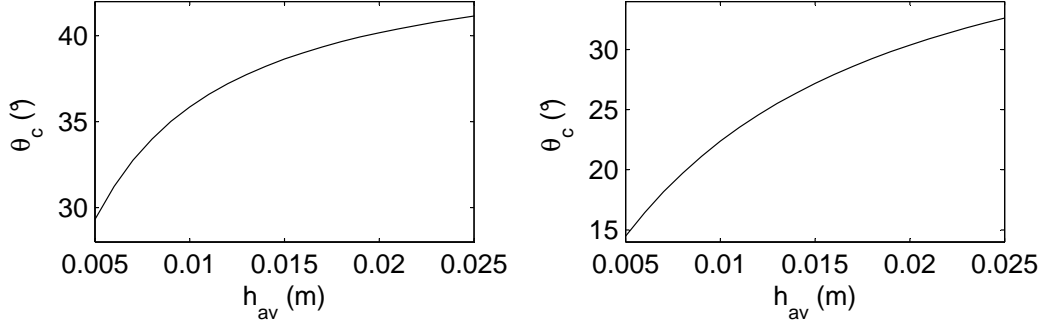


Figure 6.21: Plots showing θ_c as a function of h_{av} for $h = 0.08$ m (case of flume angle 4° , left) and $h = 0.029$ m (case of flume angle 2° , right).

my case, the gravity effects in the granular arrangement are smaller than in the grain pile case. However, the relaxation of the whole channel — at a larger time-scale than the avalanche time-scale — can be studied, supposing that the entire bed may reach a very steep profile. In a natural short reach, this could be due to the deposition of sediments from the stream sides during low flow conditions. Note, that due to the flow shear, the critical angle of stability should be much smaller than in the grain pile case.

The processes are different than in a grain pile relaxation, but from the conclusion of chapter 5, this analogy with avalanche at the global scale might work well. Thus, the following equation, deduced from equation 6.9, is used,

$$\tan \Theta_{c,system} = \frac{\tan \Theta_0}{1 + \frac{\rho_w(h+h_{av})}{(1-\phi)\Delta\rho h_{av}}}, \quad (6.11)$$

with $\Theta_{c,system}$ the critical angle of stability at the scale of the whole system and Θ_0 the same angle under water with no flow.

Figure 6.22 represents equation 6.11, using $\Theta_0 = \Gamma_r = 44^\circ$ (table C.1), for $h_{av} = 2d_{50}$ and $h_{av} = 3d_{50}$. $\Theta_{c,system}$ decreases as a function of h and shows slopes comparable to that which is measured in torrents. For instance, taking $h_{av} = 2d_{50}$, $h = 0.03$ m and $\Theta_{c,system} = 12^\circ$, leading to $S_h = 0.6$ (equation 2.3). This means that a theoretical relaxation of the whole system (i.e. at reach scale), by using this avalanche model, is only possible during an intense flood event, and supposing that the system previously accumulated enough sediments (to reach slope close to 12°). It might be the case in step-pool reaches where the steps accumulate a lot of sediment and are destroyed only during intense floods. Note, that, in this type of streams, the high water depth during large floods reduce the roughness of the bed leading to larger values of S_h .

6.3.3 Summary

The two equations developed, from the migration of antidune and from an avalanche model, validate the hypothesis that local instabilities induce large effects at reach scale, like the strong sediment pulses observed. In particular, the avalanche model confirms the possibility of local avalanches/slides steep channels. The breaking of force chains in the grain arrangement leads to a sudden release of sediment which were accumulated upstream of the local instability. This avalanche mechanism could be present at a fairly large spatial-scale depending on the history of floods and bedload events.

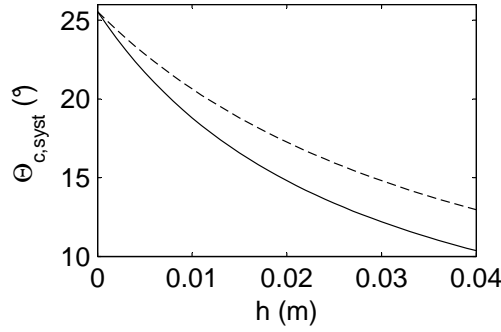


Figure 6.22: Plot showing $\Theta_{c,system}$ as a function of h for $h_{av} = 2d_{50} = 1.25$ cm (line) and $h_{av} = 3d_{50} = 1.875$ cm (dashed line).

6.4 Conclusion: antidunes and channel evolution

This chapter described the local morphodynamic processes, showing the strong influence of antidunes on channel evolution. At the grain- and antidune-scales, important interactions between the flow, the granular arrangement and the moving grains are observed. Feedback of the flow on growing antidunes limits their height. Also the external conditions, such as solid input rate and water discharge, which induce perturbations in the system, set bounds on the development of instabilities. The quantification of local bedload transport from antidune translation shows the presence of collective erosion events leading to intense sediment pulses. Moreover, it is proved that, in low transport conditions at steep slopes, small avalanches or slides occur on antidune lee sides.

From the observations of antidune migration, several interesting behaviours linked to the channel evolution are found. The deeper the antidune trough, the higher the celerity. The steeper the channel, the larger the margin between the mean and maximum value for the antidune celerity and height. At steep slopes, additional morphological mechanisms, to those normally present in low gradient rivers, are present, such as aggradation waves which induce efficient grain accumulation in the channel up to a critical state. The subsequent degradation periods are likely to be very intense due to the high probable presence of tall and fast-migrating antidunes.

The diagram of figure 6.23 summarized these local processes at the antidune scale that lead to the hysteresis and intermittency observed at reach-scale (chapters 4 and 5). The evolution of the controlling parameters is shown for increasing intermittency in the system. Finally, in the last chapter, the mechanisms from grain-grain interactions to reach-scale evolution are summarized and the main conclusions on bedload transport variability and future assessments are given.

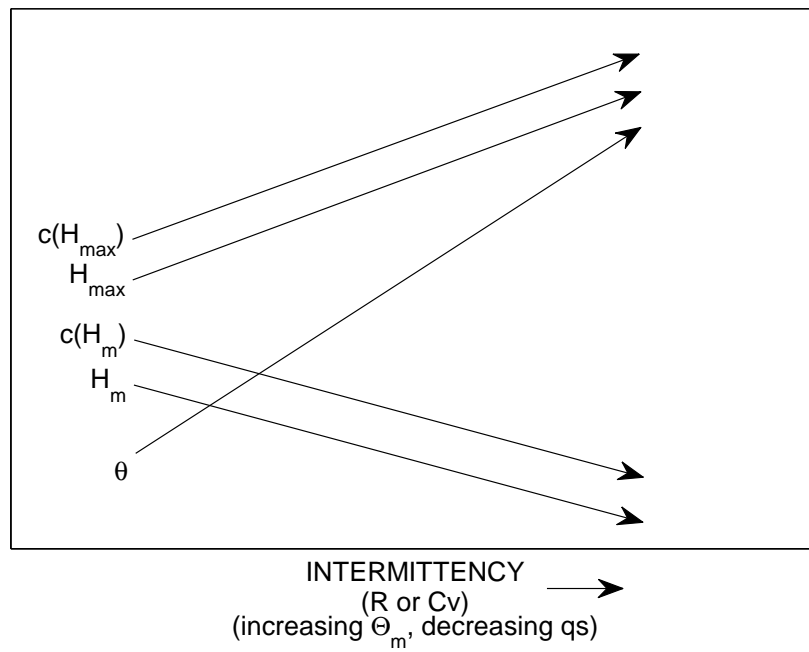


Figure 6.23: Diagram summarizing local bedform behaviours linked with intermittency observed in bedload transport rates.

Chapter 7

Conclusion: from bedform migration to global channel hysteresis

The purpose of this thesis was to experimentally explore the origins of the strong fluctuations in bedload transport rates in steep channels. After a century of research on river morphodynamics, bedload transport intermittency remains quite unpredictable. In addition, the response of mountain streams to environmental conditions (e.g. various flood intensity or debris flows affecting the channel) is an essential issue in hazard mitigation. Several explanations have been proposed to justify the presence of these fluctuations, e.g. bedform growth and migration. However, no extensive data have been collected in steep streams — where measurements are difficult and conducted at discrete locations — for the investigation of bedform evolution and their relation with bedload transport. Here, the aim was to produce such a set of morphodynamic data covering several temporal and spatial scales. This was obtained by carrying out flume experiments using new experimental methods.

The preliminary objective — the design of an idealized prototype experiment (2D-flume) for the study of general morphodynamics processes in steep channels — was fulfilled by building a 3-m-long and 8-cm-wide transparent flume (chapter 3). The installation includes several techniques devised specifically for this study: an accurate sediment feeding system, an innovative system to measure bedload transport rates (at the flume outlet) using accelerometers, 2 cameras with the corresponding acquisition installations to measure the bed evolution, and an ensemble of 3 cameras to measure bedload transport rates spatially along the flume. A bed of well-sorted gravel was chosen to limit the complexity brought by size selective entrainment and sorting. Additionally, an existent flume (Armfield flume), 17-m-long and 60-cm-wide, was used. This installation was upgraded by adding a feeding sediment system, a module to measure bed topography and techniques to measure bedload transport rates (chapter 3).

The second objective of this thesis was to obtain an extensive data set of accurate and long measurements. It was reached by conducting several measurement campaigns in the 2D-flume and the Armfield flume (chapter 3). The resolution of the time series of the bedload transport rates and bed elevation were respectively 0.01 s and 1 s (in the 2D-flume). Particularly, from the accelerometer signal, I was able to compute the arrival time of each particle at the outlet of the flume. At least 50 runs (with duration up to 50 hours), whose 36 are used in this study, and many more tests during the technical development and the calibration of the measurement techniques, were conducted in the 2D-flume. Flume inclinations between 2° and 5° were investigated. The mean bedload transport rates were varied in a range of nearly two orders of magnitude (from 0.2 g/s to 9.35 g/s) with an emphasis at low transport conditions. Very low to moderate flow strengths were studied. Finally, high resolution data of bedload transport rates and bed elevation were obtained in a stationary regime. Two long runs (up to 36 hours), a flood cycle experiment (duration of

25 hours), and several tests, were conducted on the Armfield flume. An important work in signal acquisition techniques, image and signal processing was achieved to obtain the time series of bed and water elevation and bedload transport rates.

The characterization of bedload transport rate fluctuations in steep channel was another objective, completed in chapter 4. Several statistical methods were used to describe the variability of bedload transport rates and its dependence on the experimental parameters — the water discharge, the input sediment rate and the flume inclination. The coefficient of variation was found to be a good indicator to compare the different runs. I paid great attention on the time-scale that had to be taken into account in the analysis. Giving to the method used to measure bedload transport rates, it was possible to study the waiting times between two moving particles, allowing the full characterization of the fluctuations at several time-scales. Other tools, like the probability density function or the power spectral density, were used to affirm the first results and study global behaviours. On the Armfield flume, the same fluctuation trends were verified. Additionally, the variability of bedload transport rates on the width of the channel was observed.

Several mechanisms of channel evolution were proposed at small (chapter 6) and large (chapter 5) scales, which were one of the main objective of this study. An analogy with metastability was investigated at the global scale of the channel by studying the fluctuations of the longitudinal channel profile. This concept was supported by the presence, in the 2D-flume data set, of a hysteresis which was also observed in the Armfield flume experiment and on a mountain stream (data from the Navisence River). From the observation of the bedforms at smaller scales (in the 2D-flume), local mechanisms of migration and of particle rearrangements were proposed. Other experiments (appendix C) were built to come to these findings — in particular, grain pile experiments. Processing methods and statistical tools were also used here to determine and analyse the time-series of the slope at different scales and to obtain bedform geometry and celerity.

Finally, the last objective was to quantify these mechanisms and to infer their influence on the variability of bedload transport rates (chapter 6). In particular, an avalanche model was developed to confirm the importance of granular behaviour, i.e. grain-grain interactions, in steep channel evolution. Also bedform translation equations were determined to confirm the strong influence of bedform migration on bedload transport rate variability. At that stage, interactions between small and large spatial scales were highlighted.

These idealized flume experiments were a valuable approach to understand river processes and establish simple and essential concepts of channel evolution. Comparisons with various other data — large-scale experiments and the Navisence River data — confirmed these findings. In the following, first, the main results are summarized. Second, the evolution mechanism proposed in chapter 6 is underlined. Third, consequences of this mechanism are given in terms of explanations of bedload transport intermittency. Finally, the implications of these results in a natural environment are discussed and further research is proposed.

Summary of the results

The bedload transport analysis of chapter 4 confirmed the strong fluctuations in bedload transport rates over a wide range of temporal scales. This intermittency was observed in the stationary regime without any external perturbations, suggesting that this variability is inherent to the internal dynamics of the system, i.e. due to the transport phenomenon and bedform migration. Two scaling regimes in the power spectral analysis suggests the presence of at least two distinct phenomena. In addition, I found that channel steepness, low flow shear stress and low sediment supply increase the amplitude and the time-correlations of the fluctuations. In these conditions, I observed alternatively

long periods without transport and periods with high bedload transport activity — sometimes very short and intense.

In chapter 5, the study of variations of the channel bed profile — fluctuations in the global channel slope — suggest that the granular bed shows hysteretic behaviours, similar to the metastable effects observed in grain pile dynamics. The analysis of the global channel slope suggests that other precesses (like granular failure) than single particle flow entrainment play a significant role in steep channels. This fact might be one of the reasons why bedload transport formula have particularly weak predictability in mountain streams. Hysteretic cycles of different amplitudes, defined by successive sediment accumulations and failures, were observed (under constant experimental parameters). The data set shows that a steep channel with low sediment supply and low water discharge, are the specific conditions required to observe a strong hysteresis on a wide range of time-scales. This hysteretic behaviour was quantified using the amplitude of the global slope fluctuations — from an angle of repose to a critical angle (an amplitude up to more than 1° was measured). I observed similar hysteretic behaviours in the Armfield flume from stationary data and a flood cycle experiment. Although no bed elevation measurement are available, the flood analysis from the Navisence data is rather in favor of the presence of hysteretic effects — accumulations and failures — at different spatial-scales.

The upstream-migrating antidunes (2D-flume) were characterized in chapter 6. Several important observations are reported here. First, I found that the presence and the migration of antidunes are very intermittent, which means that a large discrepancy of heights, celerity and geometry are observed (especially at high flume angle). Second, the height of an averaged antidune scales with the water depth. Third, antidunes are generally asymmetric, i.e. the bed level changes after the passage of migrating antidune. These bedforms are then either aggrading or degrading waves, depending on the sense of the asymmetry. Fourth, the antidune migration celerity increases with antidune height. In addition, the analysis highlights the dependence on the experimental parameters. The height and celerity of the averaged antidune is lower at higher flume inclinations; however the probability density functions of height and migration celerity are wider, i.e. showing relatively frequent larger values, for steeper slopes. In contrast, aggradation waves are not significantly present at lower flume inclinations. Also, the probability density function of antidune heights do not change with the sediment feeding, contrary to the antidune celerity. At higher flow conditions, the effects on the above variables, seen at high flume inclination and low sediment feeding, are reduced. Finally, equations representing the antidune migration and computing the critical angle of stability (condition for the release of an avalanche) were good to estimate bedload transport pulses.

The following mechanism of channel evolution, from antidune growth and migration to the hysteresis observed at the reach scale, was built on these previous results.

Mechanism of steep channel evolution

This section recalls the mechanism of channel evolution in the case of steep channels and low transport conditions. In these conditions, the channel bed evolves by successive cycles of aggradation and degradation of different durations and intensities.

In the aggrading phase, aggrading waves are present. The deposition in the channel mainly takes place on the stoss side of small asymmetric antidunes characterized by a downstream crest higher than the upstream one. This mechanism of aggradation is efficient and creates a stable channel bed because the particles are easily stopped on the antidune stoss side (local steep counter-flow slopes). In addition, this aggrading process prevents significant perturbations of the bed. This allows a large

accumulation of sediment in the system, where the bed profile might reach a high slope, close to critical angle of stability.

The degrading phase is triggered when the bed profile reaches its critical angle of stability or when sufficient perturbations, e.g. disruption of a grain cluster, turbulent eddies or other collective motion events, occur. The particles, travelling downstream, perturb the bed, destabilizing the grain arrangement and preventing any aggradation. Given the tall, potentially unstable layer of grains accumulated during the previous aggrading phase, tall antidunes develop rapidly. Since the upstream crest of the antidunes is higher than the downstream one, the bed degrades — this is only true for tall antidunes. This degradation is fast as the celerity increases with the antidune height. The high celerity of these tall antidunes is explained by the exceptional steepness of their lee sides (up to almost 40°), which temporarily reach the local critical angle of stability of the local grain arrangement. Thus, the antidune migration, leading to the relaxation of the bed profile, occurs at least partly by small avalanches (or slides) and collective motion events — inducing intense bedload transport pulses.

The mechanisms of these two phases of channel evolution are in agreement with the analog concept of metastability observed at the channel scale. First, aggradation is very efficient relative to the feeding rate, as almost all of the moving particles participate in the process. Second, the fast degradation can occur at any channel state, with a higher intensity for a profile state close to its critical angle of stability. The longer the aggradation, the more intense the successive degradation and the more the system relaxes towards its angle of repose.

Conclusion on bedload transport variability

The concepts and mechanisms summarized in this last chapter explain the observed intermittency of bedload transport rates in steep channels. The long periods with no transport occur during the aggradation phases. Almost all of the particles are caught by the aggrading waves and are accumulated in the channel. The strong bedload transport periods, observed at the channel outlet, correspond to degradation phases in which fast antidune migration mobilized a large amount of easily transportable sediments. In addition, the most intense pulses of bedload transport recorded were probably due to local avalanches occurring on certain steep antidunes during degradation phases.

This explains the bedload transport fluctuations observed in a wide range of temporal and spatial scales. The largest temporal scale of the fluctuations depends on the system size, i.e. the surface available for particle accumulation. In addition to these hysteretic cycles, isolated single particle entrainment and destruction of small grain clusters can occur at any time. This small contribution to bedload transport rates acts as additional random perturbations on the system.

The case of natural mountain streams and outlook

In the case of a steep natural river reach, additional sources of variability must be taken into account. First, the grain size distribution is wide, from suspended load to large boulders. Second, the channel generally presents some sinuities and erodible banks whose the locations change from time to time. Third, the environment conditions are unsteady and also have an intermittent behaviour. These factors might increase the hysteretic behaviours of the given reach and consequently the intermittency in bedload transport rates.

These experimental results are in agreement with bedload transport time series collected in the field (Navisence River), but needs to be confirmed by an extensive bed elevation survey. The study of migrating bedforms and profiles of high temporal resolution in steep channels would be of great

interest. Unfortunately, the quantification of bed elevation fluctuations for a steep stream reach is a arduous task, especially during floods. New technological improvement might help in the future to overcome these field study issues — airborne survey using small drones might be efficient for a relatively low cost.

If the proposed mechanism proves to be present in many mountain stream reaches, the question of how to predict the intense bedload transport events arises. These events should be due to high magnitude flood or bed profile states close to the critical state of the concerned reach. Hydraulic predictions should be used in order to establish the occurrence of the floods, whereas the estimation of the bed profile state might be determined based on a threshold value of the maximum possible accumulation of sediment in the stream reach. For instance, this threshold could be deduced by an estimate of the mass balance in this reach. It underlines that this kind of study has to be conducted reach by reach, and that, afterwards, the interactions between the different reaches has to be assessed. In any cases, it seems important to know the available sediment, i.e. the accumulation above the level corresponding to the minimum possible level (corresponding to the level given by the angle of repose).

Thus, this work has improved the understanding of steep stream evolution and might help to improve bedload transport hazard mitigation. Particularly, it has shed light on the inexplicability of strong bedload transport events caused by relatively small floods, these kinds of flood being relatively frequent.

Appendix A

Shear stress correction

Several different methods for taking into account the smooth wall effects in the calculation of the bed stress τ_b in flume studies were developed. A few of the common ones are tested and compared in this appendix. These methods, that decompose the resistance due to the bed and the walls, are based on Manning roughness coefficient, on Darcy-Weisbach friction factor, or on more or less complicated fitting experimental data. The coefficient related to the roughness of the smooth wall is supposed to be known with a constant value — or in some case adjusted with an empirical formula.

The different tested correction methods are from Einstein [1942], Vanoni & Brooks [1957], Williams [1970] and Cheng & Chua [2005]. In addition, the corrected values were compared with the non-corrected and the hydraulic radius cases. The results are plotted in figure A.1. It shows that, in the 2D-flume, the wall effects do not modify significantly the bed stresses according to Cheng & Chua [2005] and Einstein [1942] corrections. The Vanoni & Brooks [1957] correction slightly changes the stresses, whereas the Williams [1970] formula strongly modifies the stresses.

Depending on the chosen type of correction, the representation of the data are different (figure A.1), affecting actually the relation between the chosen flow intensity variables, e.g. τ_b , and bedload transport rates. This discrepancy in correction might partly explain the poor agreement of some bedload transport equations, particularly for low flow conditions and on steep slopes where a slight change of the bed stresses leads to large changes in bedload transport rates [Recking, 2008]. A brief comparison and review by Cheng & Chua [2005] on the subject argues in this sense. The difficulty to obtain accurate measurements, especially required for flow close to the incipient sediment motion, and the non-normality of the flow over steep-slope channels might be among the other main reasons.

In this thesis, the Vanoni & Brooks [1957] formula was applied in order to correct the empirical bed stresses. This is an arbitrary choice as it seems difficult to know an exact correcting method. However, this method is widely used and was also applied in studies in which some results are taken for comparison in this thesis [Recking, 2006].

Vanoni & Brooks [1957] proposed the following expression using the friction factor f

$$\frac{\tau_b}{\rho g h \sin \Theta} = \frac{W}{W + 2h} \frac{f_b}{f}, \quad (\text{A.1})$$

where $f = 8gR_h \sin \Theta / U_m^2$ and f_b is the bed friction factor that can be expressed in function of f and f_w , the wall friction factor. $f_b = f + 2h(f - f_w)/W$ and f_w was approximated by the function $f_w = (20(Re/f)^{0.1} - 39)^{-1}$ with $Re = 4UR_h/\nu$ [Cheng & Chua, 2005]. In my work, all the calculations have been made using this corrected bed stress τ_b . The corrected bed shear stresses are shown in table 4.1.

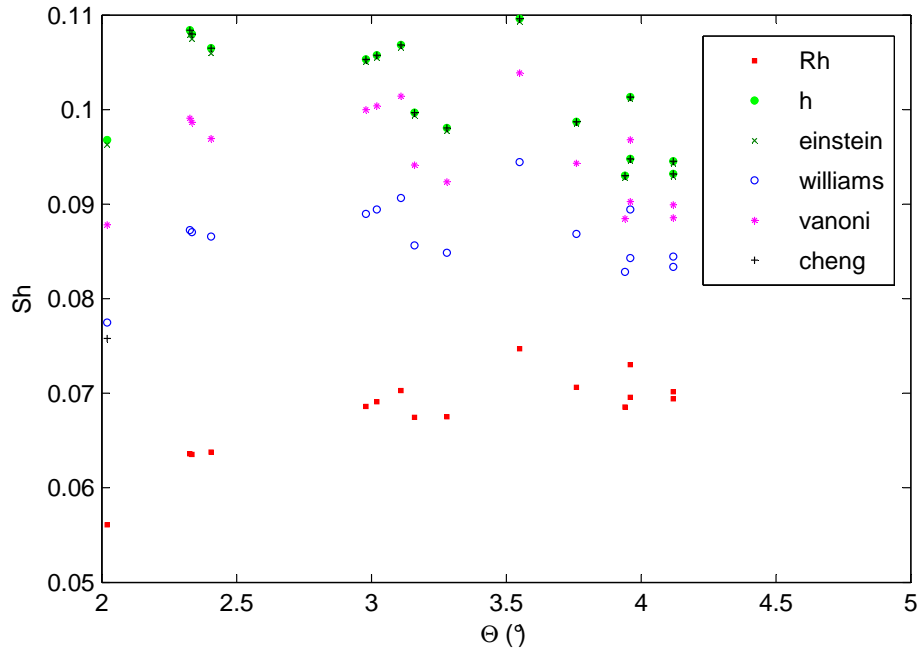


Figure A.1: S_h as a function of Θ_m for the main set of runs (at constant S_h) in the 2D-flume (table 3.2), comparison with the different correction methods. h and Rh represent the assumption of an infinite width and the assumption of walls with the same roughness as the bed, respectively.

Appendix B

Accelerometer constructor characteristics

The whole data sheet of the KIT3376MMA7361LC three axis low-g micromachined accelerometer from Freescale can be found at <http://www.freescale.com>. The main data are given in figures B.1, B.2 and B.3.

$\pm 1.5g$, $\pm 6g$ Three Axis Low-g Micromachined Accelerometer

Features

- 3mm x 5mm x 1.0mm LGA-14 Package
- Low Current Consumption: 400 μA
- Sleep Mode: 3 μA
- Low Voltage Operation: 2.2 V – 3.6 V
- High Sensitivity (800 mV/g @ 1.5g)
- Selectable Sensitivity ($\pm 1.5g$, $\pm 6g$)
- Fast Turn On Time (0.5 ms Enable Response Time)
- Self Test for Freefall Detect Diagnosis
- 0g-Detect for Freefall Protection
- Signal Conditioning with Low Pass Filter
- Robust Design, High Shocks Survivability
- RoHS Compliant
- Environmentally Preferred Product
- Low Cost

Figure B.1: Main features of the accelerometer evaluation board used in the accelerometer measurement system.

Rating	Symbol	Value	Unit
Maximum Acceleration (all axis)	g_{max}	± 5000	g
Supply Voltage	V_{DD}	–0.3 to +3.6	V
Drop Test ⁽¹⁾	D_{drop}	1.8	m
Storage Temperature Range	T_{stg}	–40 to +125	°C

1. Dropped onto concrete surface from any axis.

Figure B.2: Maximum characteristics of operation of the accelerometer evaluation board used in the accelerometer measurement system.

Characteristic	Symbol	Min	Typ	Max	Unit
Operating Range ⁽²⁾					
Supply Voltage ⁽³⁾	V_{DD}	2.2	3.3	3.6	V
Supply Current ⁽⁴⁾	I_{DD}	—	400	600	μA
Supply Current at Sleep Mode ⁽⁴⁾	I_{DD}	—	3	10	μA
Operating Temperature Range	T_A	-40	—	+85	$^{\circ}C$
Acceleration Range, X-Axis, Y-Axis, Z-Axis					
g-Select: 0	g_{FS}	—	± 1.5	—	g
g-Select: 1	g_{FS}	—	± 6.0	—	g
Output Signal					
Zero-g ($T_A = 25^{\circ}C$, $V_{DD} = 3.3 V$) ^{(5), (6)}	V_{OFF}	1.485	1.65	1.815	V
XY		1.32	1.65	1.815	v
Z ⁽⁷⁾		-2.0	± 0.5	+2.0	mg/ $^{\circ}C$
Zero-g ⁽⁴⁾	V_{OFF}, T_A				
Sensitivity ($T_A = 25^{\circ}C$, $V_{DD} = 3.3 V$)					
1.5g	$S_{1.5g}$	740	800	860	mV/g
6g	S_{6g}	190.6	206	221.5	mV/g
Sensitivity ⁽⁴⁾	S, T_A	-0.0075	± 0.002	+0.0075	%/ $^{\circ}C$
Bandwidth Response					
XY	f_{-3dBXY}	—	400	—	Hz
Z	f_{-3dBZ}	—	300	—	Hz
Output Impedance	Z_O	—	32	—	k Ω
0g-Detect	$0g_{detect}$	-0.4	0	+0.4	g
Self Test					
Output Response					
X_{OUT}, Y_{OUT}	Δg_{STXY}	+0.05	-0.1	—	g
Z_{OUT}	Δg_{STZ}	+0.8	+1.0	+1.2	g
Input Low	V_{IL}	V_{SS}	—	0.3 V_{DD}	V
Input High	V_{IH}	0.7 V_{DD}	—	V_{DD}	V
Noise					
Power Spectral Density RMS (0.1 Hz – 1 kHz) ⁽⁴⁾	n_{PSD}	—	350	—	$\mu g/\sqrt{Hz}$
Control Timing					
Power-Up Response Time ⁽⁸⁾	$t_{RESPONSE}$	—	1.0	2.0	ms
Enable Response Time ⁽⁹⁾	t_{ENABLE}	—	0.5	2.0	ms
Self Test Response Time ⁽¹⁰⁾	t_{ST}	—	2.0	5.0	ms
Sensing Element Resonant Frequency					
XY	$f_{GCELLXY}$	—	6.0	—	kHz
Z	f_{GCELLZ}	—	3.4	—	kHz
Internal Sampling Frequency	f_{CLK}	—	11	—	kHz
Output Stage Performance					
Full-Scale Output Range ($I_{OUT} = 3 \mu A$)	V_{FSO}	$V_{SS}+0.1$	—	$V_{DD}-0.1$	V
Nonlinearity, $X_{OUT}, Y_{OUT}, Z_{OUT}$	NL_{OUT}	-1.0	—	+1.0	%FSO
Cross-Axis Sensitivity ⁽¹¹⁾	$V_{XY, XZ, YZ}$	-5.0	—	+5.0	%

Figure B.3: Main technical characteristics of the accelerometer evaluation board used in the accelerometer measurement system.

Appendix C

Complementary experiments

C.1 Tests on fixed bed

Several experimental tests were made on a fixed bed without sediment transport in order to accurately measure the water depth h for the computation of the Shields stress S_h . Thus, the dependence of S_h on the water discharge Q_l and the flume angle α could be determined. These preliminary tests were required to set the initial experimental parameters of each run.

C.1.1 Set-up and runs

As in the experimental campaigns, the bed was filled with the same gravel. This bed was covered with a grid with glued gravel in order to obtain a total bed height of eight cm. This configuration presents the same hyporheic and roughness conditions as during the experimental campaigns, excepted that there is no bedload transport and no bedforms.

For each α , Q_l was varied to have the relation between h and Q_l . Angles 2.3° , 3° , 4° , 5° and 6° were investigated. 30 test runs were conducted. For each couple of parameter $\{\alpha, Q_l\}$, camera shots were taken during 30 s after stabilization of the flow. This allows the determination of the time- and space-averaged water depth h using the image precessing method explained in section 3.2.2.

C.1.2 Shields stress relation

Using the data of the tests, S_h for each run was computed and the empirical relation between S_h and Q_l was derived. The values of S_h were corrected for wall effects using the same method as for the campaign runs (appendix A). Figure C.1 shows the experimental data which are well-represented by a linear regression for each α . The coefficients of the linear regressions for each α are themselves linearly well-fitted as seen in figure C.2. Thus, the relation may be inferred for any α (for instance the two dashed lines in figure C.1). In figure C.1, the deduced initial Shields stress S_{hini} used for the main campaign runs is shown with the corresponding time-averaged Shields stresses. It confirms that the same S_{hini} was set for each run in this campaign.

C.2 Flow observations over a fixed wavy bed

Using a fully transparent 3-m-long and 6-cm-wide flume, an experiment was designed to investigate the flow over a wavy bed. The bed surface with a sinusoidal shape was made of polished, transparent PVC plastic blocs (figure C.3). The chosen wavelength of the sinusoidal wave was 15 cm which corresponds to the order of magnitude of the antidune wavelength observed in the 2D-flume. With a constant α , Q_l was varied to change the flow characteristics and particularly the Froude number Fr . Indeed, the flow fluctuates from fully supercritical to transcritical — with hydraulic

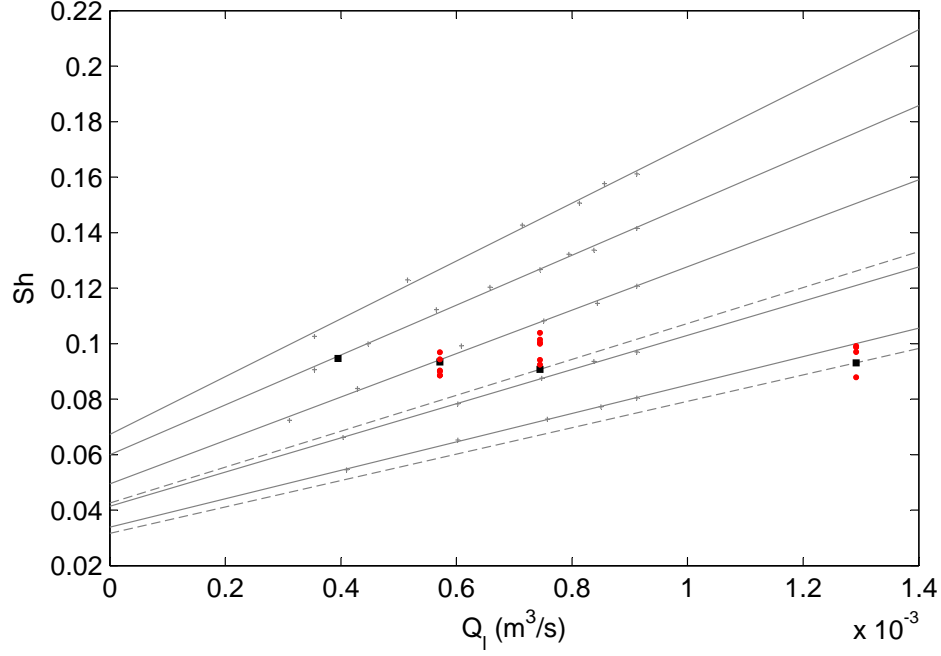


Figure C.1: Shields stress S_h versus water discharge Q_l : experimental measurements (crosses) and linear fitting, for different flume angle α . Black squares represent S_{hini} and red dots the campaign runs.

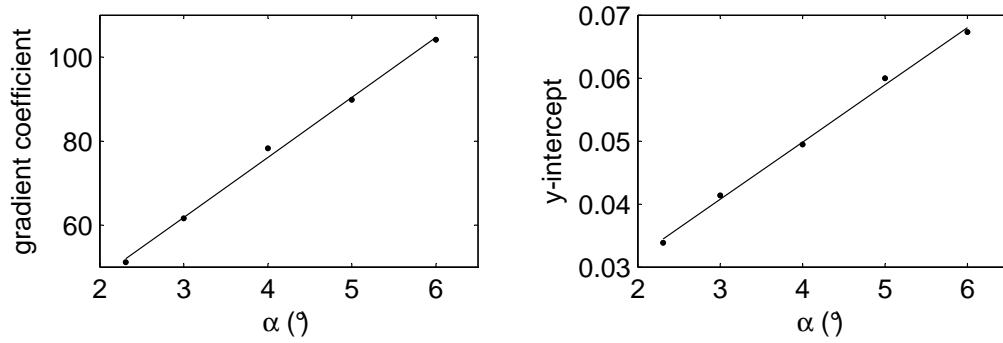


Figure C.2: Linear regression of the coefficients of the linear regression of the relations between S_h and Q_l for different α (figure C.1).

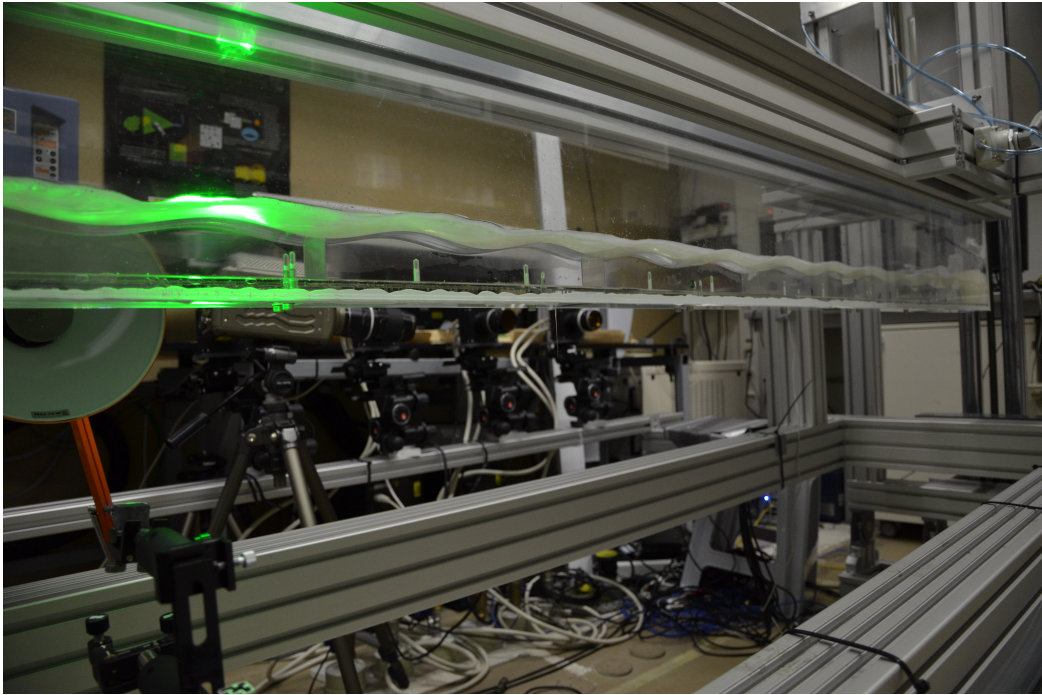


Figure C.3: View of the channel for flow observations over a wavy bed.

jumps. In figure C.4, both cases with and without a hydraulic jump are shown. The appearance and disappearance of the hydraulic jump are due to the variation of Q_l .

During increasing and decreasing Q_l , pictures were taken from the side (figure C.4), which allows to measure the water depth in a specific location for a given Q_l . The results, presented in figure 6.9, prove the existence of the hysteresis in the hydraulic jump existence. Increasing Q_l , the hydraulic jump appears at a much higher value of Q_l than the value of Q_l at which the hydraulic jump disappears during the decrease of Q_l . These conditions of appearance and disappearance can be similarly expressed in terms of Fr at the bedform crest, instead of Q_l (section 6.1.2.3).

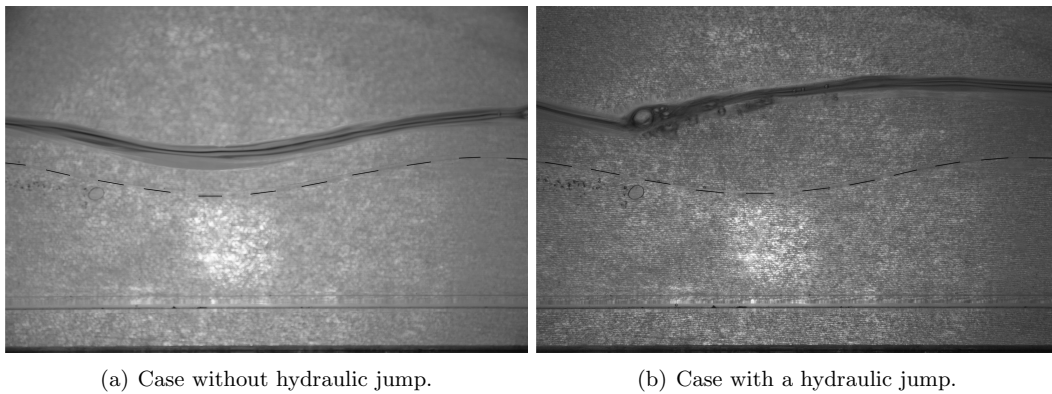


Figure C.4: Side views of the flow over an artificial antidune, flow from left to right.

C.3 Grain pile experiments

A few grain pile experiments were conducted to determine the characteristic angles of the sediments used in my flume experiments. Although grain piles, with different types of grain, have been extensively studied, the angles for particular grains can only be deduced from new experiments due to their specific characteristics like shape and roughness [Carrigy, 1970]. Tests in dry conditions and under water were carried out to be able to compare with the granular literature. In addition, these experiments allow the estimate of θ_0 for the avalanche model developed in section 6.3.2.

C.3.1 Conical dry grain pile

A simple experiment was conducted to obtain an approximation of the maximum angle of stability Γ_c and the angle of repose Γ_r of the sediments used. The gravel was simply poured on a 3D-pile, and the profile of the pile was observed by a camera. The angle of the pile profile was computed from the resulting images. Γ_c was deduced as the mean of the local maxima of the time series of the computed angles and Γ_r as the mean of the local minima. It comes that $\Gamma_c \geq 42^\circ$ and $\Gamma_r \leq 38^\circ$.

The observation of Γ_c is depending on the manner to build the pile and pour the grains. Thus, with a lower and a more constant feeding rate, Γ_c could be slightly higher than this value (section 2.3.3.2). Γ_r has more chance to be observed after a complete relaxation, i.e. right after reaching Γ_c . As Γ_c might be higher than the measured value, Γ_r might also be lower than measured. However, this experiment shows that angles between 38° and 42° are in the avalanche domain in the dry case. Compared with sand and many grain types [Denisov *et al.*, 2012], these angle values are relatively high, situating the gravel used here as potentially subjected to Self Organized Criticality (SOC) behaviour. Indeed, rice piles, being one of the truly SOC system, have a critical angle of stability of 37° (Denisov *et al.* [2012] and see the arguments linking pile steepness and SOC behaviour in section 5.2.1).

C.3.2 Submerged grain pile in a 8-cm-wide gap

To estimate precisely Θ_0 , i.e. the critical angle of stability Γ_c of submerged grains in the 2D-flume, the constraints present in the 2D-flume have to be respected. Thus, the sediment pile have to be confined between walls and studied under water. A 50-cm-long, 8-cm-wide and 30-cm-tall basin was designed to conduct this grain pile experiment (figure C.6). The sediments, the same as used in the 2D-flume, were fed manually on one side from the top. After the grain pile was formed, sediments were manually and slowly fed.

Pictures were taken from the side to compute the fluctuations in the pile profile which was subjected to avalanches. A back light system gave high image quality (figure C.6), similarly to the 2D-flume experiment. The around 40-cm-long profile was detected using the same processing technique as developed for 2D-flume bed measurements (section 3.2.2). The same methods were also used to compute the global and local slopes. Thus, γ , the local slope at the scale 2 cm, and Γ , the global slope at the scale of the system, were determined. Finally, $\Theta_0 = \Gamma_c$ and $\theta_0 = \gamma_c$, with γ_c the critical angle of stability at the scale 2 cm, have been deduced (table C.1).

Table C.1: Characteristic angles computed from the grain pile experiment in a 8-cm-wide gap under water: the critical avalanche angle Γ_c of the profile, the critical avalanche angle γ_c at scale 2 cm and the angle of repose Γ_r of the profile.

Γ_c (°)	γ_c (°)	Γ_r (°)
43.7	64.1	34



Figure C.5: Picture of the conical grain pile experiment.



Figure C.6: Picture of the grain pile experiment in a 8-cm-wide gap under water.

Appendix D

Navisence River site

D.1 Navisence River watershed

The Navisence River is a gravel-bedded mountain river, tributary of the Rhone River in Wallis, South-West of Switzerland (figure D.1). This river is a typical steep high-altitude streams of the Central Alps. At the confluence with the Rhone River, in Sierre (530 m a.s.l), the drainage area reaches 254 km² for a channel length of 26.9 km. The source, at 3000 m a.s.l, is situated at the tong of Weisshorn glacier. The mean slope of the stream to the Rhone River is around 4.5°.

A measurement station was built at 1650 m a.s.l. in Zinal and was operational in May 2011. It drains a basin of 80 km², including vast glacialized terrains and several of the highest Alps peaks, like Weisshorn (4506 m), Zinalrothorn (4221 m) and Dent Blanche (4357 m). In these conditions, a nival and glacial regime is observed, characterized by daily floods during spring and summer. As it is the case in many mountain rivers, the sediment load transport occurs mainly as bedload. The measurement station was designed to infer bedload transport rates using geophones (next section and section 2.2.1.1). The site is managed by CREALP and funded by Canton du Valais.

At the measurement station, the channel slope is around 2°. The mean water discharge measured from May 2011 to August 2013 is around 2 m³·s⁻¹. However, mean water discharge can be much higher during summer months. For instant, it reaches 6.4 m³·s⁻¹ between the 15th of June 2012 and the 15th of August 2012. The highest water discharge peak — averaged on one minute — was measured at 30.5 m³·s⁻¹ the 13th of July 2011. During winter months, the water discharge can drop close to zero.

Extensive morphological measurements were not undertaken on the Navisence close to the station. However, morphological features and behaviours have been visually observed. The channel presents only smooth sinuosities upstream of the station with much of the time lateral — and temporarily central — bars. The locations of the bars often change from flood to flood (figure 1.3). Boulders locally emerge from the water flow. Grain clusters and small steps are observed, the flow oscillating around the critical flow condition.

D.2 Geophone measurements

The approach to measure bedload transport is taken from Rickenmann & McArdell [2008] using piezoelectric sensors, called geophones and settled in the river bed (figure D.2). Indeed, rolling, sliding and saltating particles generate vibrations at the surface of the bed. These vibrations, recorded by the geophones by the intermediate of metallic plates across the stream bed, provide a good measurable variable related to the amount of transported gravel. At the Zinal station, the water flow depth and the number of impulses from the geophones are recorded. The calibration

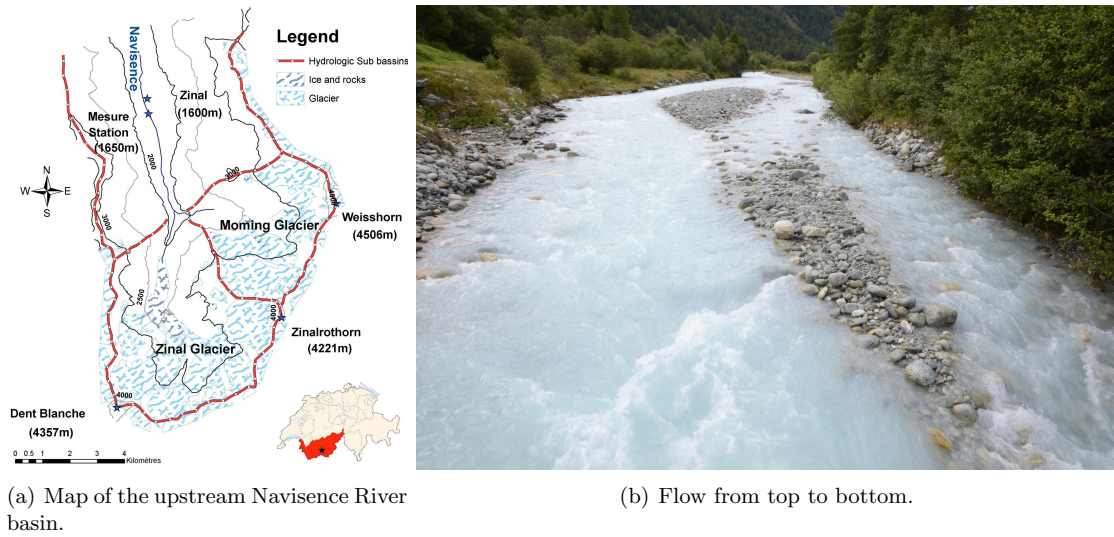


Figure D.1: The Navisence River. (a) Map from Travaglini & Bardou [2012]. (b) The Navisence River just upstream the Zinal measurement station.

(in Travaglini & Bardou [2012]) of the installation, particularly difficult for the bedload transport, gives time series of the water flow and bedload transport rates. Data are available from May 2011 at an acquisition frequency of one minute.



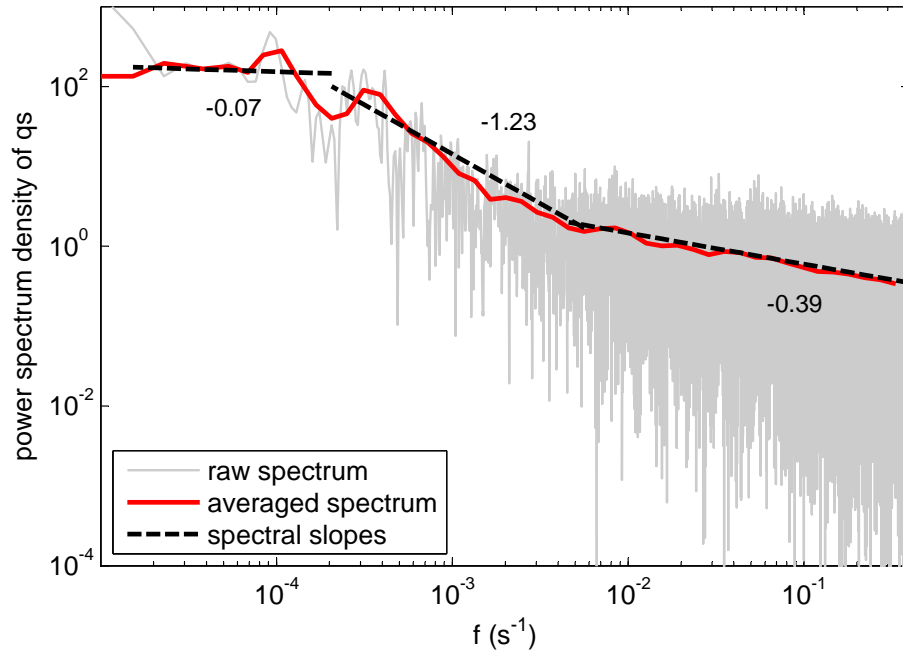
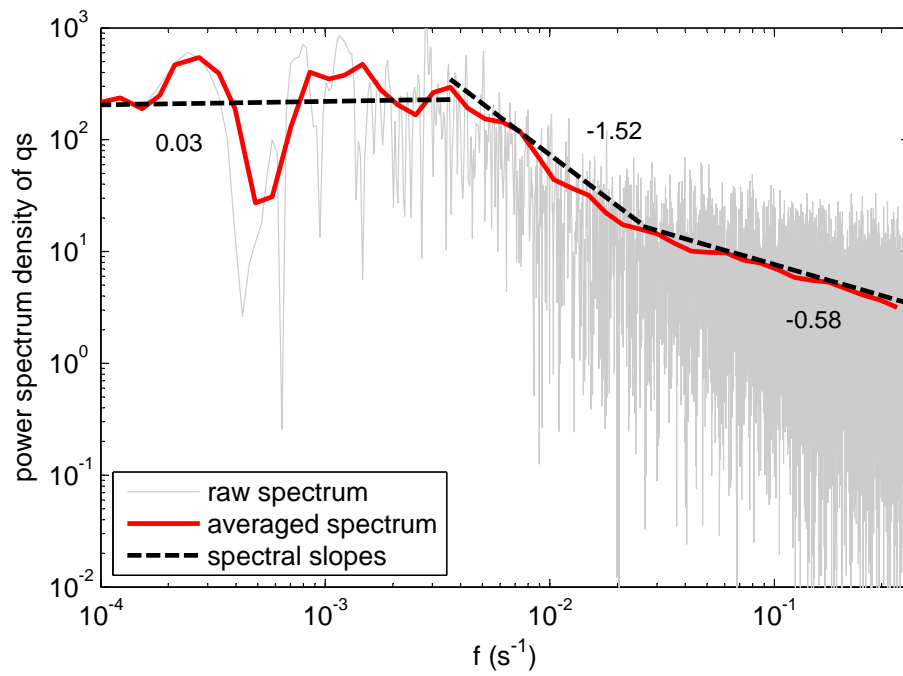
(a) View from upstream.

(b) Geophone plates (grey) under water at the middle cross-section of the station (flow from left to right)

Figure D.2: Zinal measurement station on the Navisence.

Appendix E

Power spectrum of bedload transport rates

Figure E.1: Power spectrum of bedload transport rates: run *2deg3v*.Figure E.2: Power spectrum of bedload transport rates: run *2deg15v*.

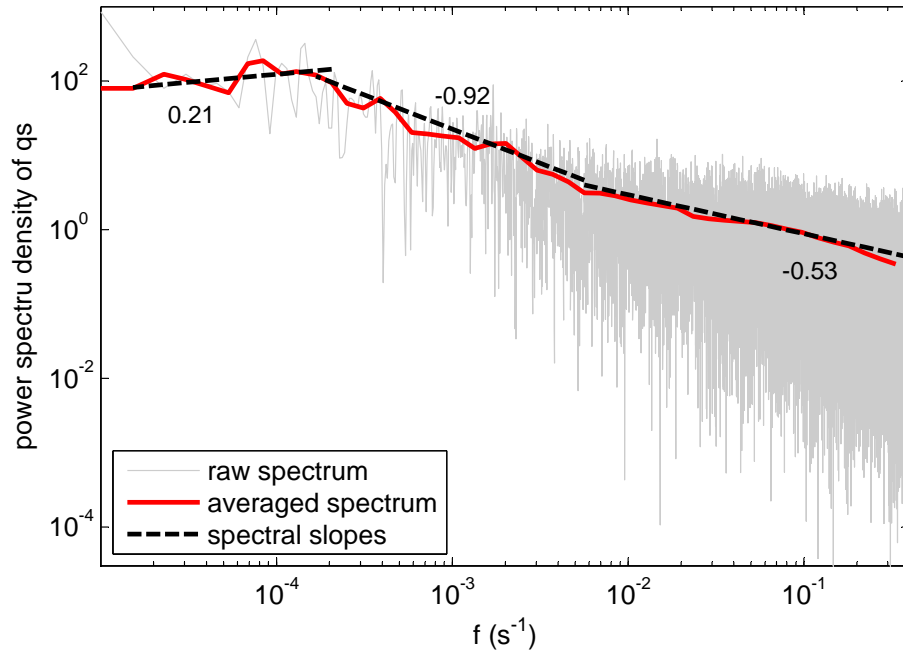


Figure E.3: Power spectrum of bedload transport rates: run *5deg3v*.

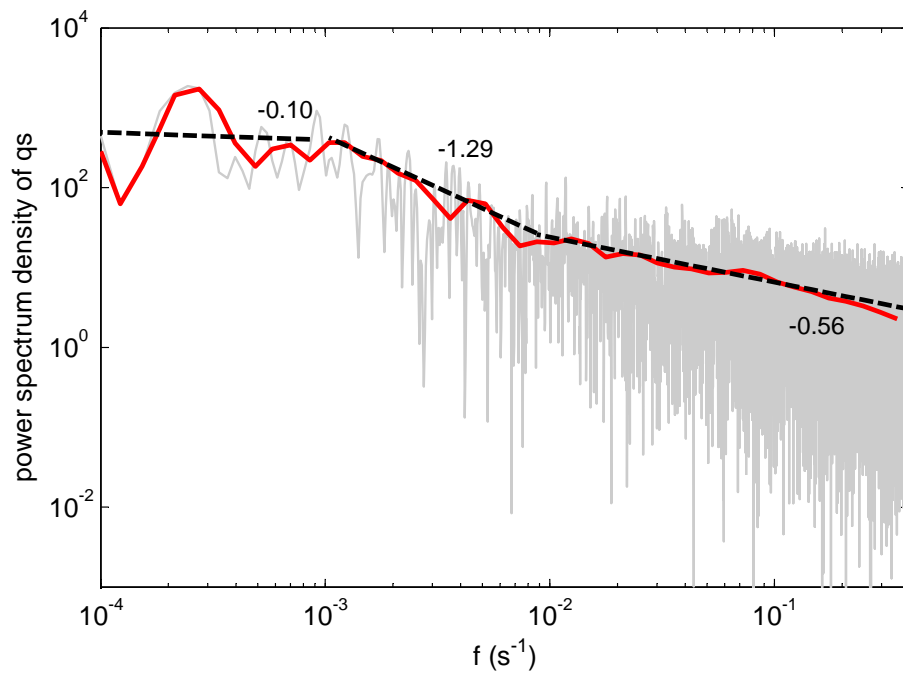
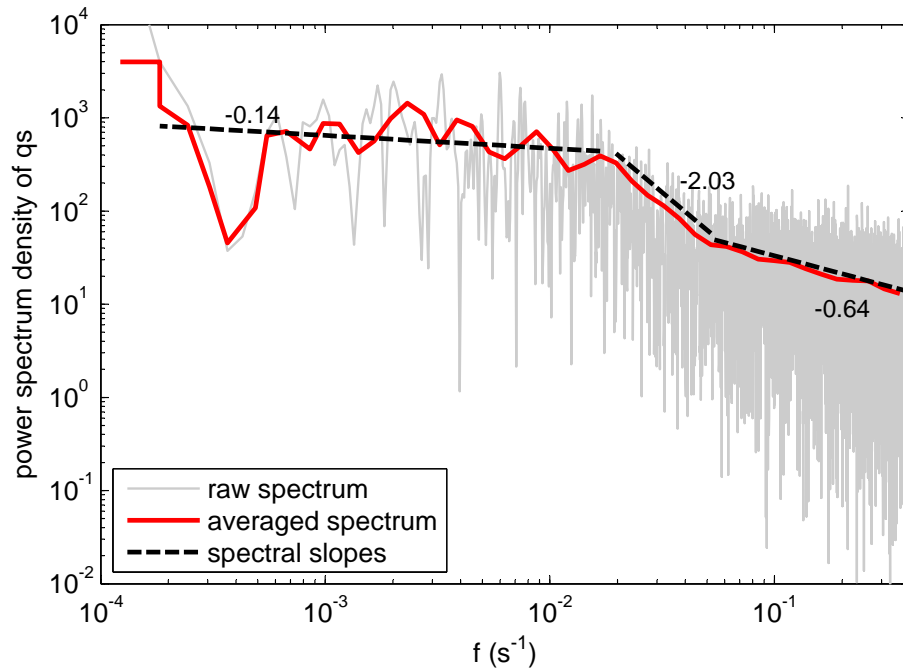
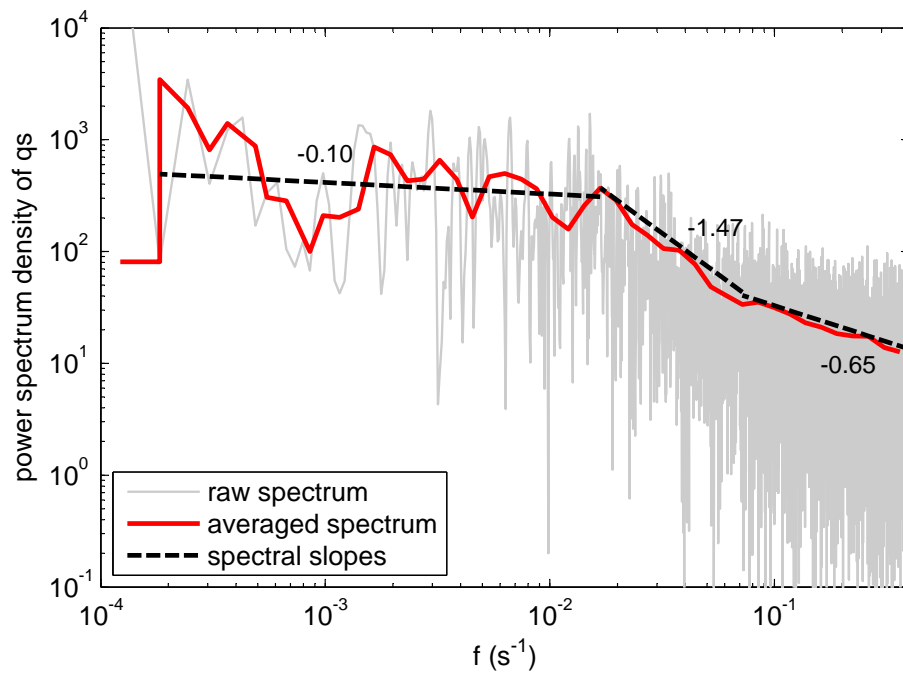


Figure E.4: Power spectrum of bedload transport rates: run *5deg15v*.

Figure E.5: Power spectrum of bedload transport rates: run *3.2deg45v*.Figure E.6: Power spectrum of bedload transport rates: run *5deg45v*.

Appendix F

Spatio-temporal plots of bed elevation

In this appendix, spatio-temporal plots of bed elevation are shown for numerous runs. For comparison between the plots, the viewer has to pay attention to the duration of each run.

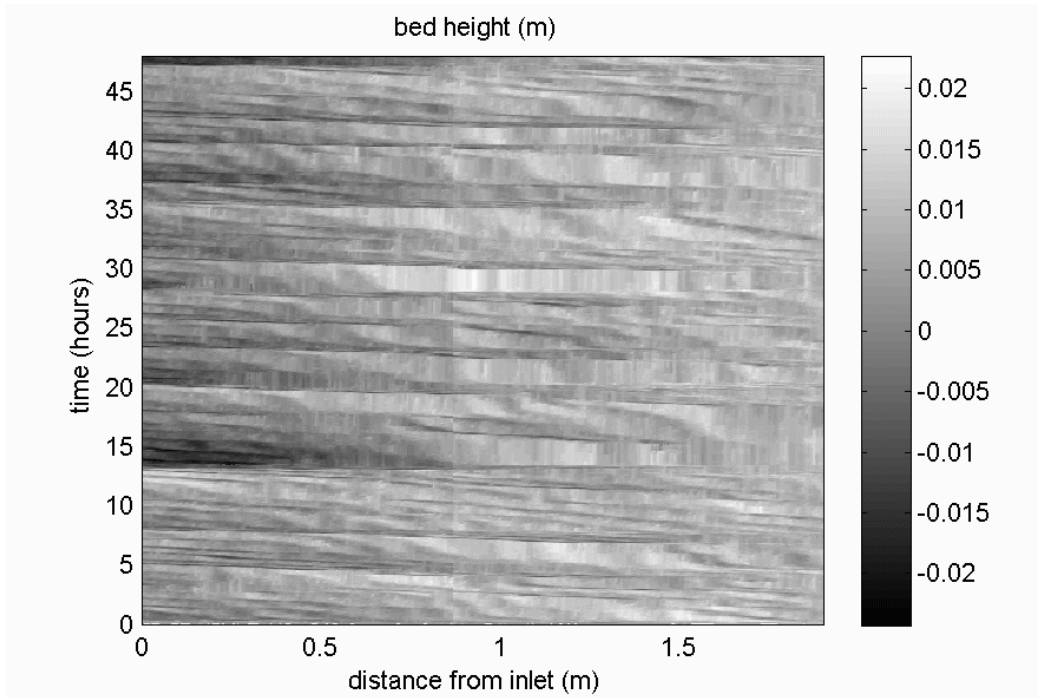


Figure F.1: Spatio-temporal plots of bed elevation: run *4deg3v*.

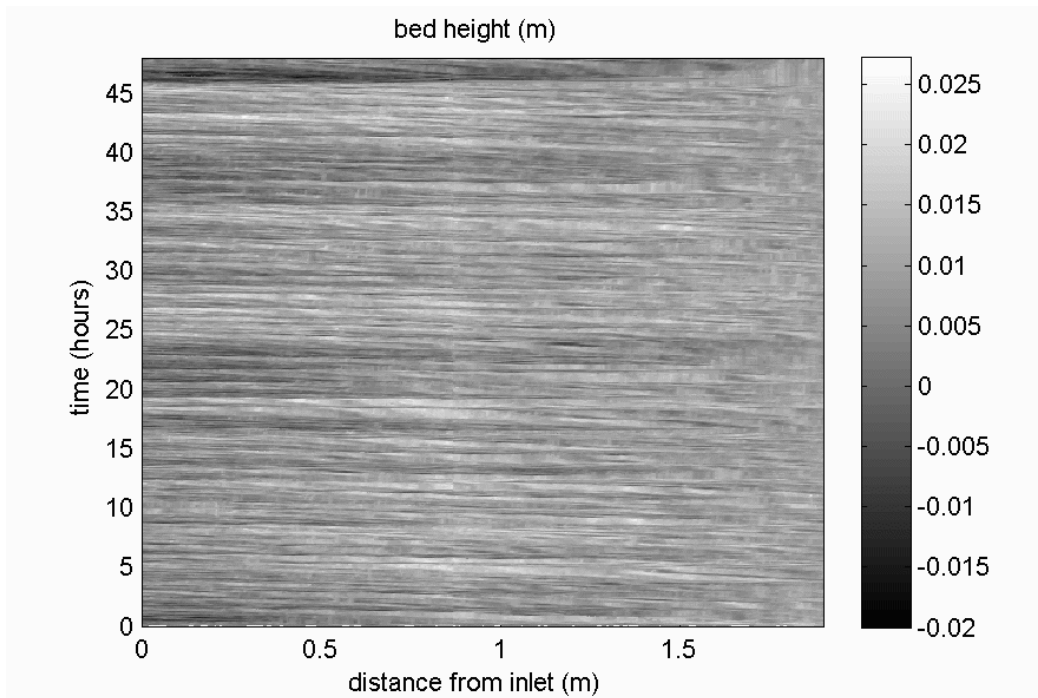


Figure F.2: Spatio-temporal plots of bed elevation: run *4deg6v*.

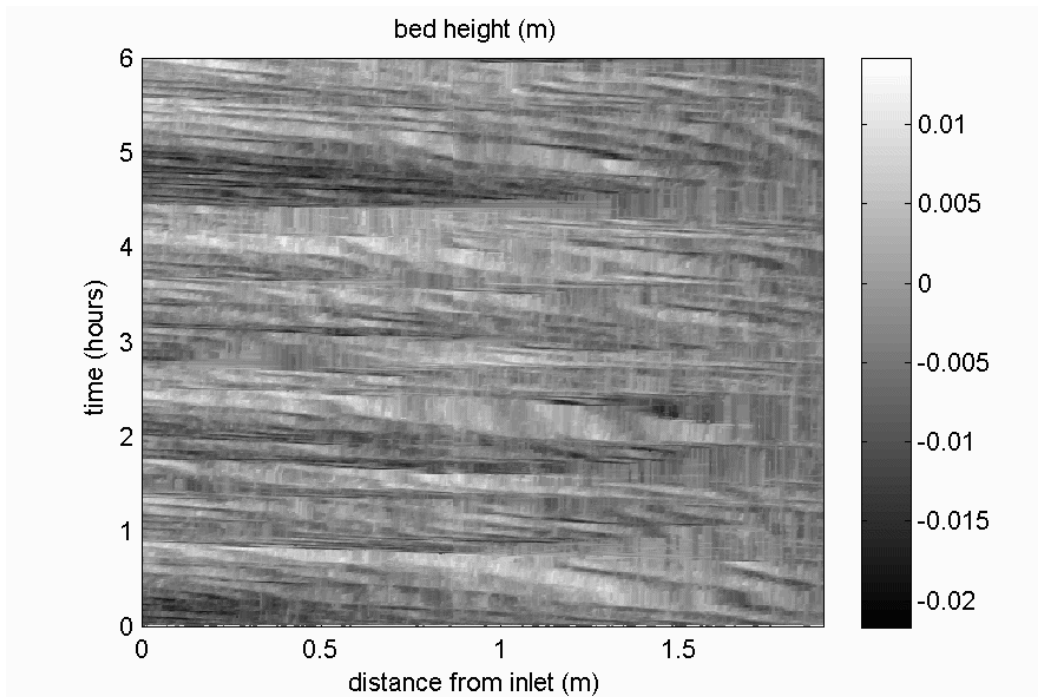


Figure F.3: Spatio-temporal plots of bed elevation: run *4deg15v*.

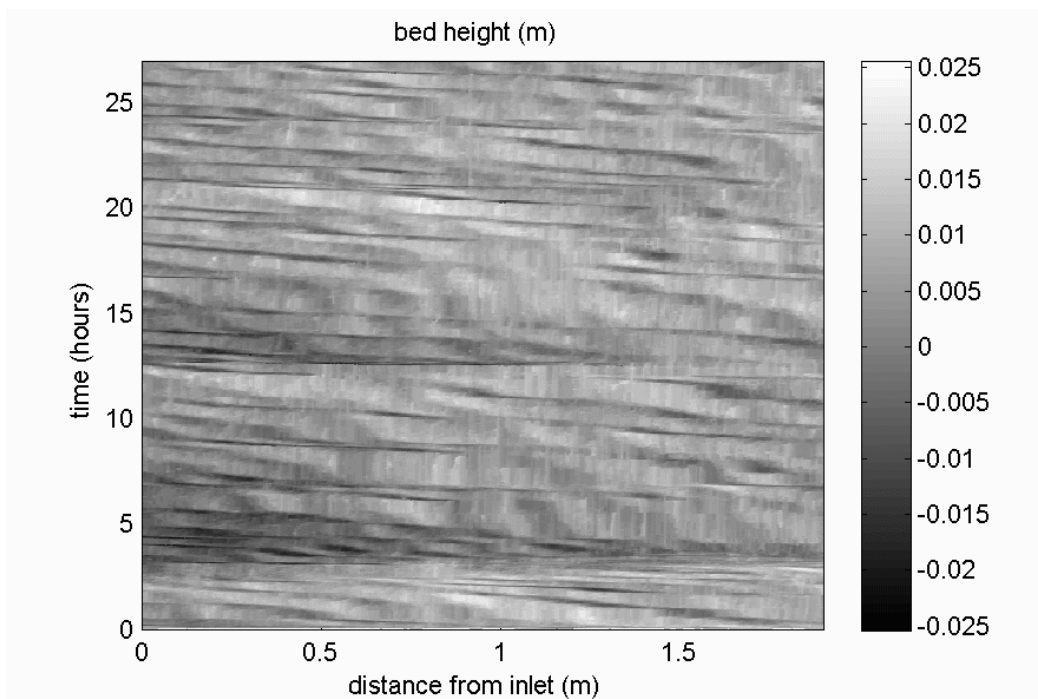


Figure F.4: Spatio-temporal plots of bed elevation: run *3.2deg3v*.

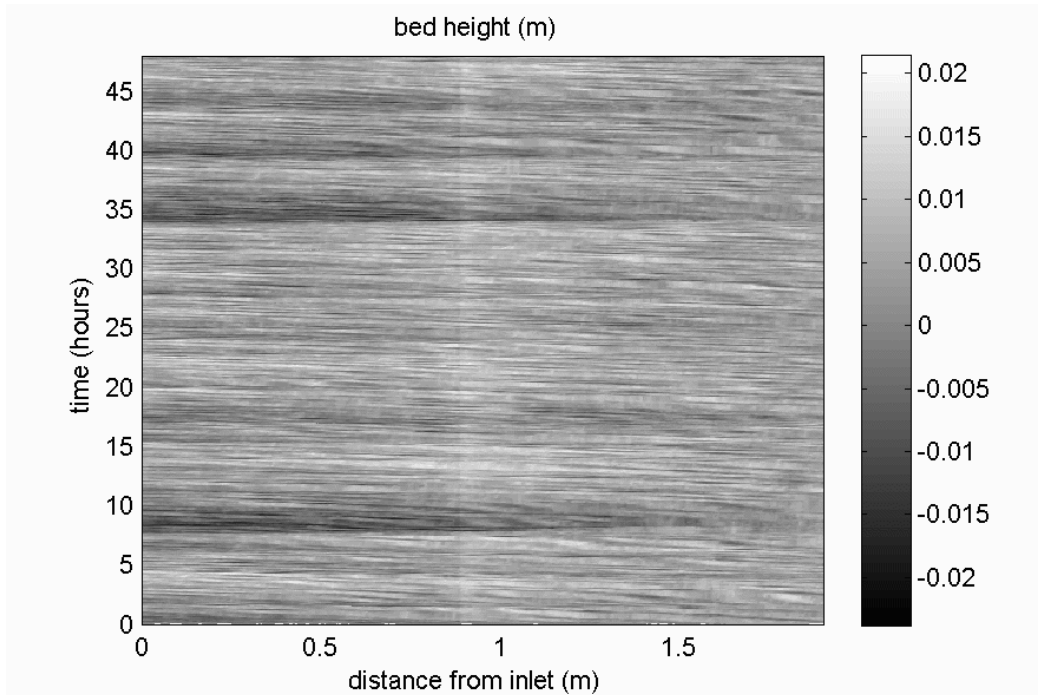


Figure F.5: Spatio-temporal plots of bed elevation: run *3.2deg6v*.

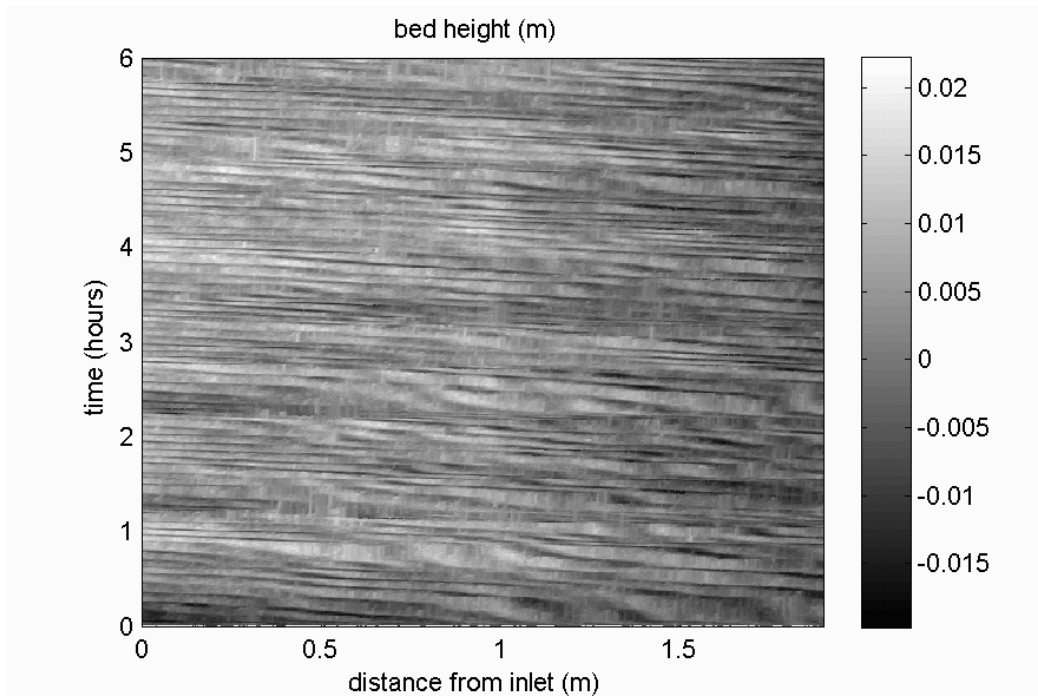


Figure F.6: Spatio-temporal plots of bed elevation: run *3.2deg15v*.

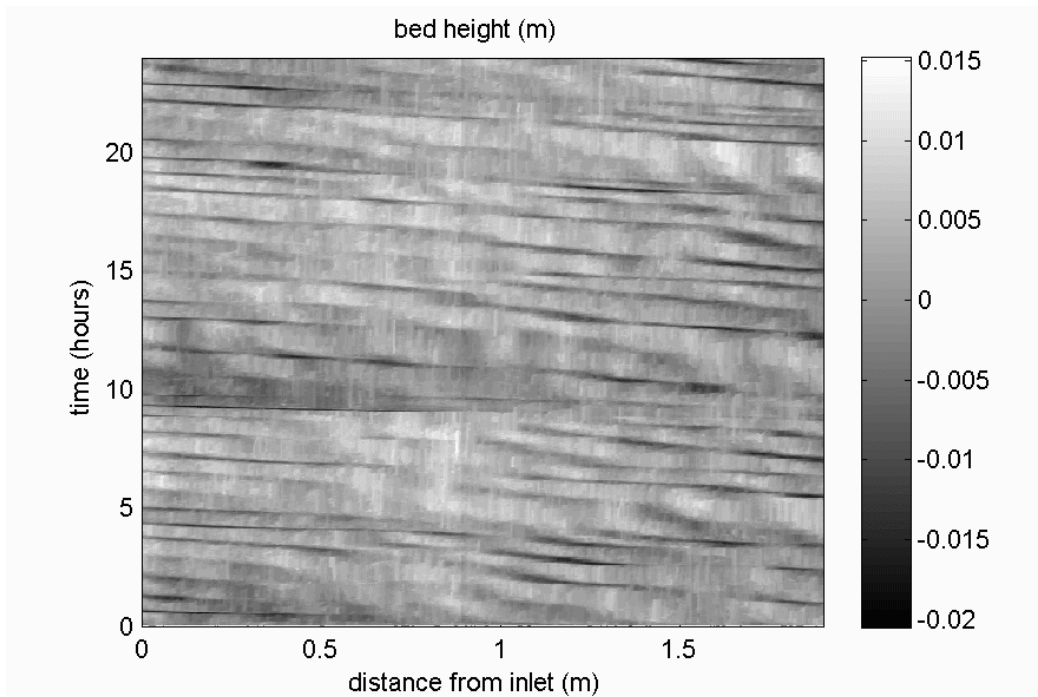


Figure F.7: Spatio-temporal plots of bed elevation: run *2deg3v*.

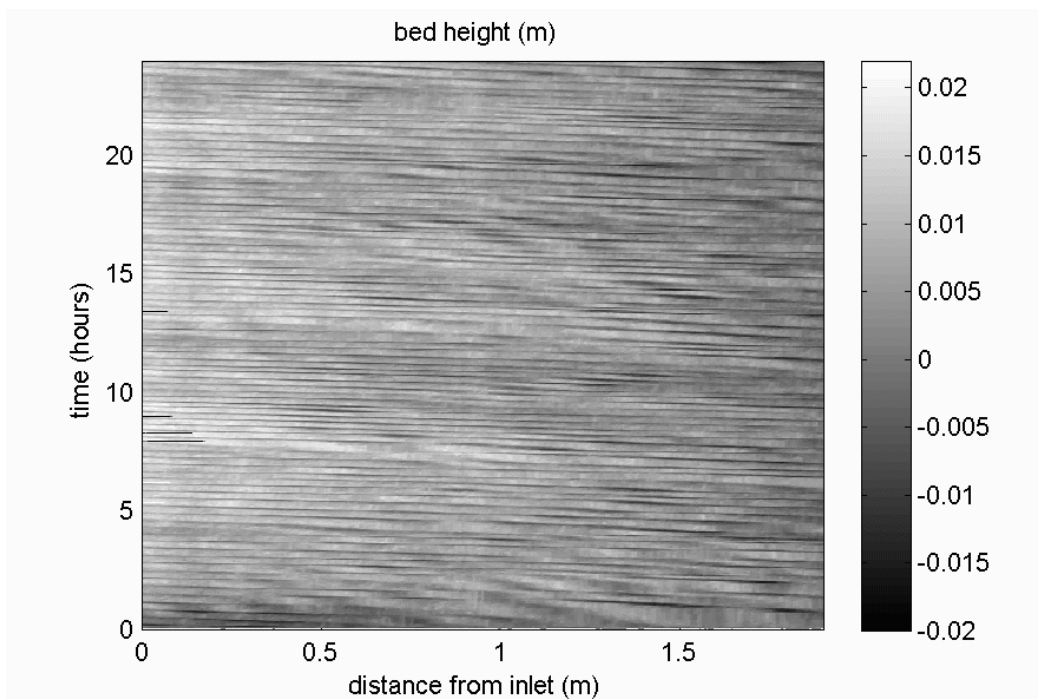
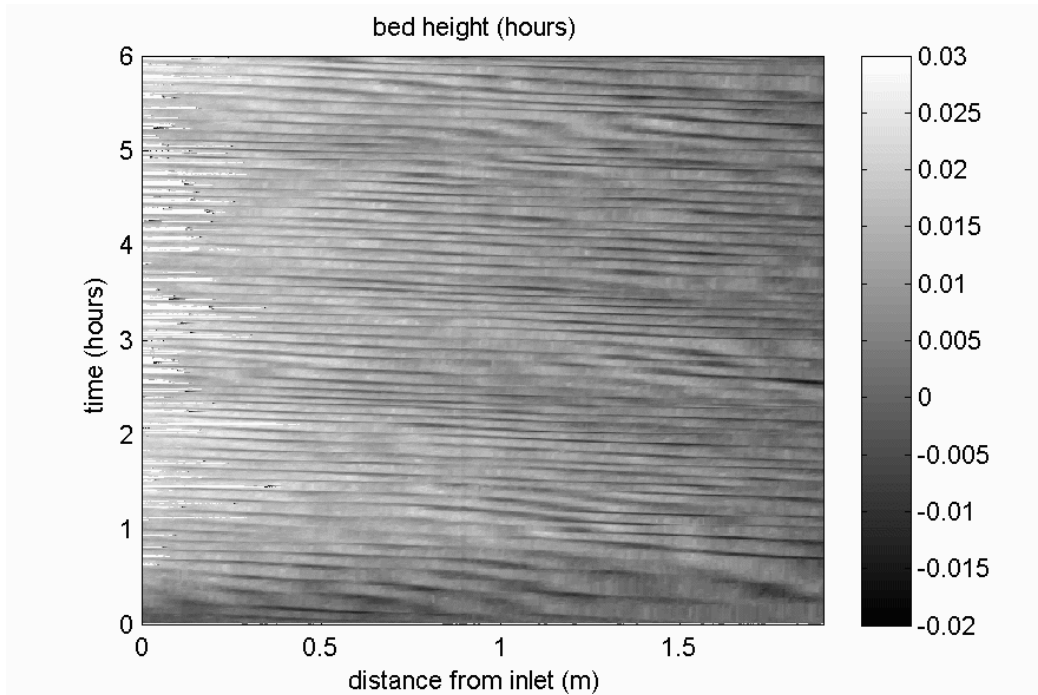
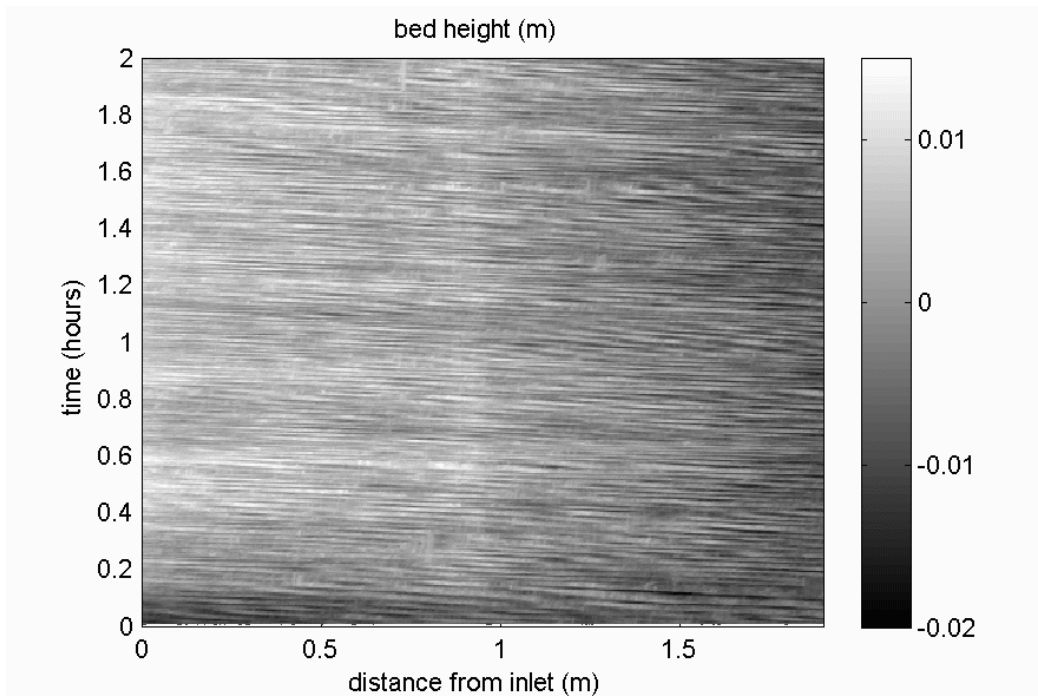


Figure F.8: Spatio-temporal plots of bed elevation: run *2deg6v*.

Figure F.9: Spatio-temporal plots of bed elevation: run *2deg15v*.Figure F.10: Spatio-temporal plots of bed elevation: run *3.2deg45v*.

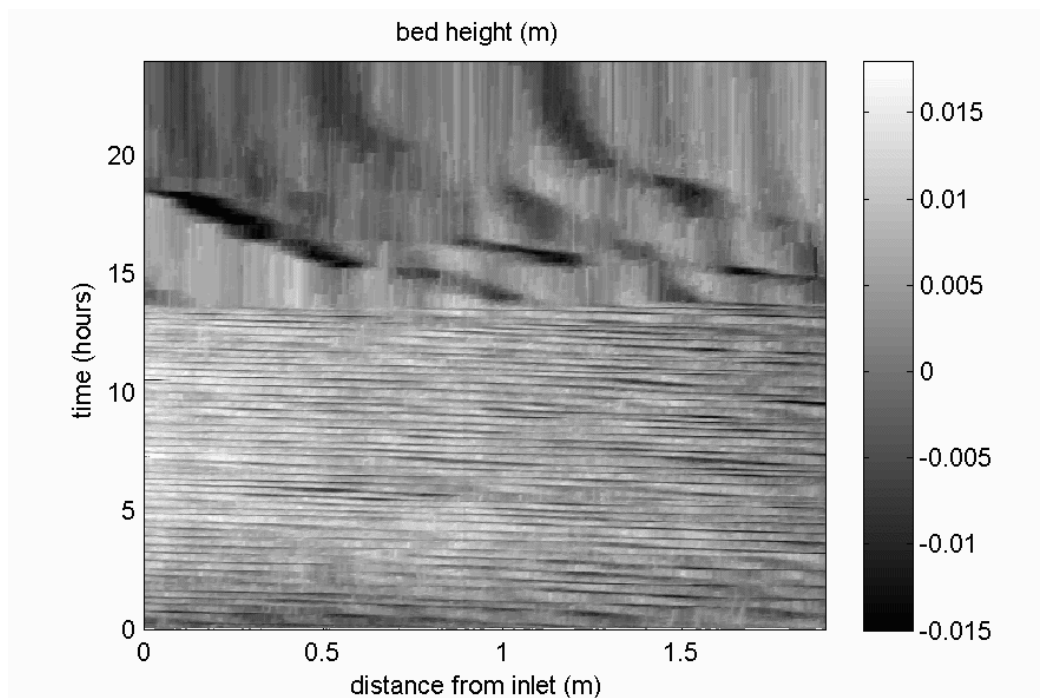


Figure F.11: Spatio-temporal plots of bed elevation: same experimental parameters as for run *2deg6v* with sediment feeding stopped after approximately 14 hours. The system should relax towards a new stationary equilibrium, however, as no feeding rate are set, degradation will continue indefinitely. Thus, the system could not reach an equilibrium.

Appendix G

Global channel slope fluctuations

In this appendix, time series of the temporal fluctuations in the space-averaged channel slope are plotted for several runs, as a complement of figures presented in chapter 5.

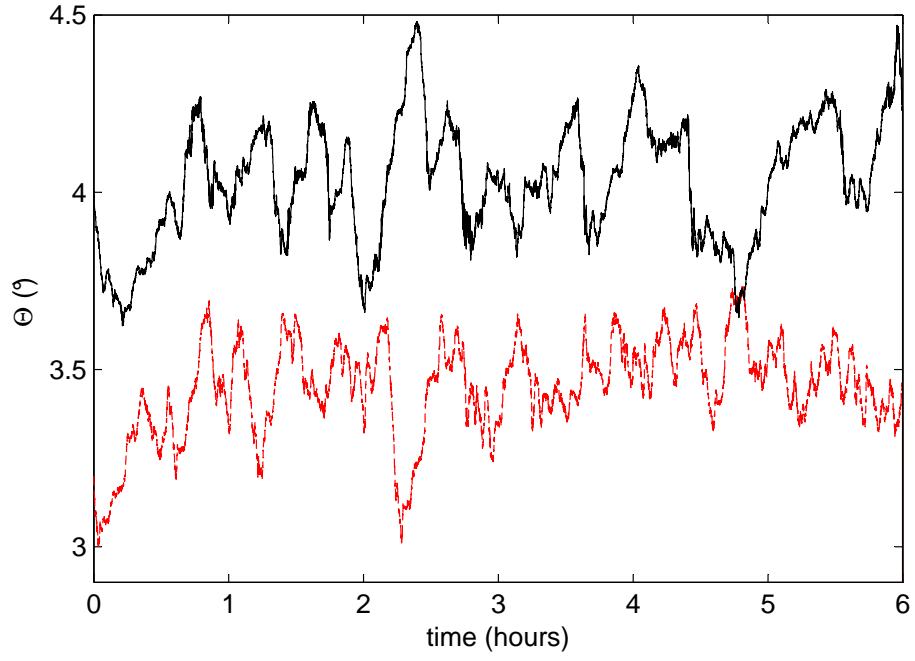


Figure G.1: Θ for run $3.2deg15v$ (red dashed line) and $4deg15v$ (black line).

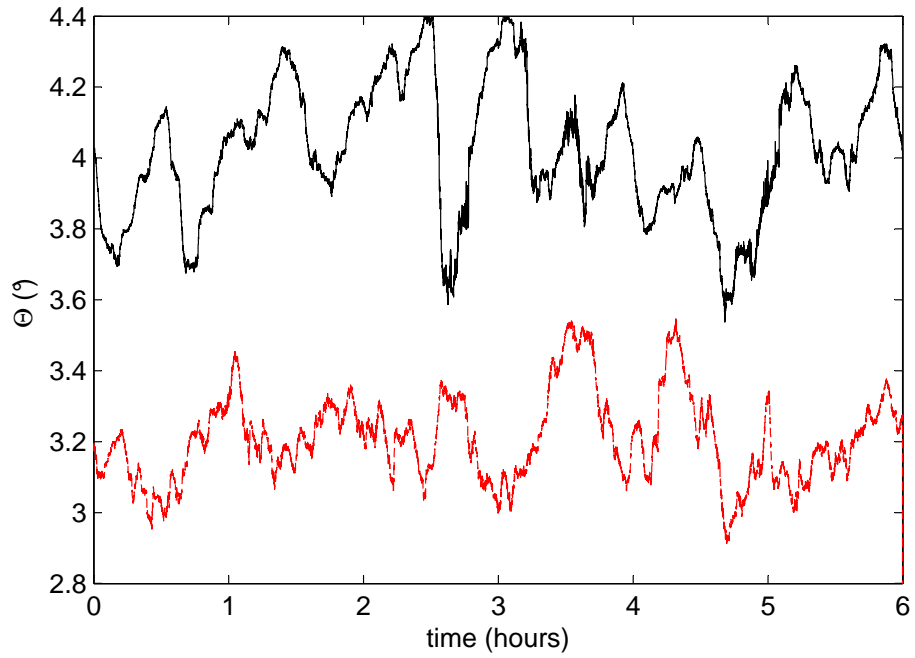


Figure G.2: Θ for run $3.2deg10v$ (red dashed line) and $4deg10v$ (black line).

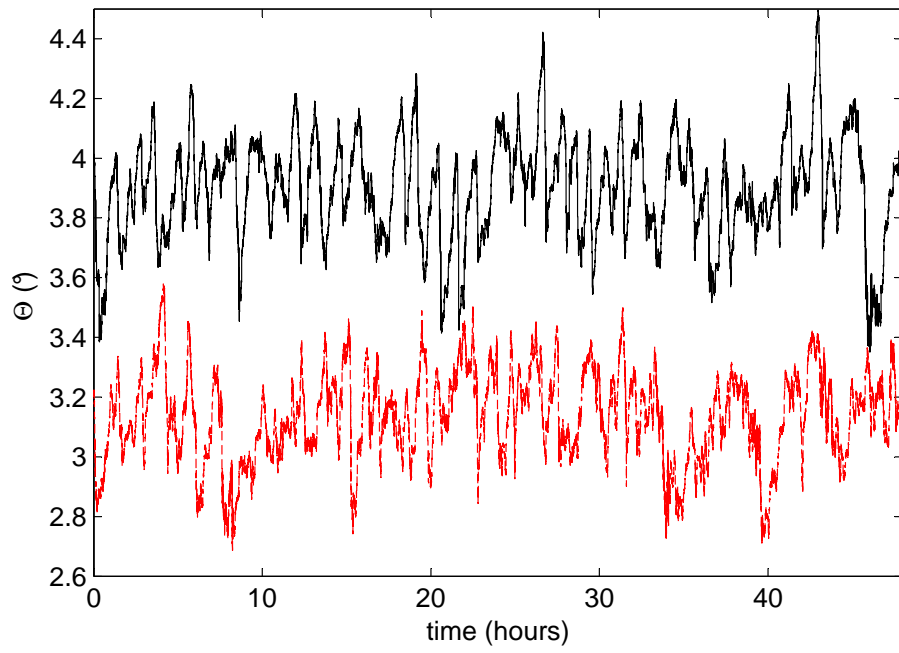


Figure G.3: Θ for run $3.2deg6v$ (red dashed line) and $4deg6v$ (black line).

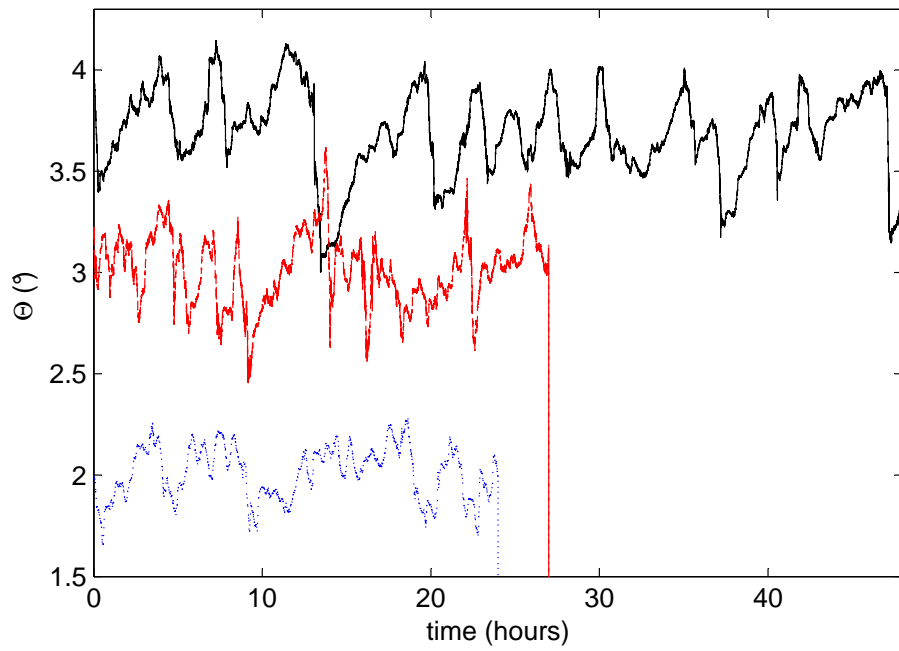


Figure G.4: Θ for run $2deg3v$ (blue dot line), $3.2deg3v$ (red dashed line) and $4deg3v$ (black line).

Bibliography

- Abraham, D., Kuhnle, R. A., & Odgaard, A. J. 2011. Validation of Bed-Load Transport Measurements with Time-Sequenced Bathymetric Data. *Journal of Hydraulic Engineering-Asce*, **137**(7), 723–728.
- Alexander, J. 2008. *Bedforms in Froude-supercritical flow*. Vol. Conference Volume. Leeds University. Pages 1–5.
- Alexander, J., Bridge, J. S., Cheel, R. J., & Leclair, S. F. 2001. Bedforms and associated sedimentary structures formed under supercritical water flows over aggrading sand beds. *Sedimentology*, **48**(1), 133–152.
- Allen, J. R. L. 1984. *Sedimentary structures: their character and physical basis*. Elsevier.
- Ancey, C. 2010. Stochastic modeling in sediment dynamics: Exner equation for planar bed incipient bed load transport conditions. *Journal of Geophysical Research-Earth Surface*, **115**.
- Ancey, C., Bohm, T., Jodeau, M., & Frey, P. 2006. Statistical description of sediment transport experiments. *Physical Review E*, **74**(1).
- Ancey, C., Davison, A. C., Bohm, T., Jodeau, M., & Frey, P. 2008. Entrainment and motion of coarse particles in a shallow water stream down a steep slope. *Journal of Fluid Mechanics*, **595**, 83–114.
- Badoux, Alexandre, & Rickenmann, Dieter. 2008. Berechnungen zum Geschiebetransport whrend der Hochwasser 1993 und 2000 im Wallis. *Wasser Energie Luft*, **100**(3), 217–226.
- Bagnold, R. A. 1966. An approach to the sediment transport problem from general physics. *US Geol. Surv. Prof. Paper*, **422**, 231–291.
- Barry, J. J. 2004. A general power equation for predicting bed load transport rates in gravel bed rivers. *Water Resources Research*, **40**(10).
- Belleudy, P., Valette, A., & Graff, B. 2010. Passive Hydrophone Monitoring of Bedload in River Beds: First Trials of Signal Spectral Analyses. in Gray, J.R., Laronne, J.B., and Marr, J.D.G., *Bedload-surrogate monitoring technologies: U.S. Geological Survey Scientific Investigations Report 2010-5091*, p. 266–282.
- Bohm, Tobias, Ancey, Christophe, Frey, Phillipe, Reboud, Jean-Luc, & Ducottet, Christophe. 2004. Fluctuations of the solid discharge of gravity-driven particle flows in a turbulent stream. *Physical Review E*, **69**(6), 061307.
- Bouchaud, J. P., Cates, M. E., Prakash, J. R., & Edwards, S. F. 1994. A Model for the Dynamics of Sandpile Surfaces. *Journal De Physique I*, **4**(10), 1383–1410.
- Bouchaud, J. P., Cates, M. E., Prakash, J. R., & Edwards, S. F. 1995. Hysteresis and Metastability in a Continuum Sandpile Model. *Physical Review Letters*, **74**(11), 1982–1985.

- Brayshaw, A. C. 1985. Bed Microtopography and Entrainment Thresholds in Gravel-Bed Rivers. *Geological Society of America Bulletin*, **96**(2), 218–223.
- Brierley, Gary J., & Fryirs, Kirstie A. 2005. *Geomorphology and river management: applications of the river styles framework*. Oxford, UK: Blackwell Publishing.
- Buffington, J. M. 1999. The legend of A. F. Shields. *Journal of Hydraulic Engineering-Asce*, **125**(4), 376–387.
- Bunte, K. 2010. Measurements of Gravel Transport Using the Magnetic Tracer Technique: Temporal Variability Over a Highflow Season and Field-Calibration. in **Gray, J.R., Laronne, J.B., and Marr, J.D.G., Bedload-surrogate monitoring technologies: U.S. Geological Survey Scientific Investigations Report 2010-5091**, p. 85–106.
- Bunte, K., & Abt, S. R. 2005. Effect of sampling time on measured gravel bed load transport rates in a coarse-bedded stream. *Water Resources Research*, **41**(11).
- Burtin, A., Bollinger, L., Vergne, J., Cattin, R., & Nabelek, J. L. 2008. Spectral analysis of seismic noise induced by rivers: A new tool to monitor spatiotemporal changes in stream hydrodynamics. *Journal of Geophysical Research-Solid Earth*, **113**(B5).
- Canny, J. 1986. A computational approach to edge detection. *Pattern Analysis and Machine Intelligence, IEEE Transactions on*, 679–698.
- Carey, WP, & Hubbell, DW. Probability distributions for bedload transport. In: *Proceedings of the Fourth Federal Interagency Sedimentation Conference March 24-27, 1986, Las Vegas, Nevada.*, vol. 1.
- Carling, P. A., & Shvidchenko, A. B. 2002. A consideration of the dune : antidune transition in fine gravel. *Sedimentology*, **49**(6), 1269–1282.
- Carling, P. A., Golz, E., Orr, H. G., & Radecki-Pawlik, A. 2000. The morphodynamics of fluvial sand dunes in the River Rhine, near Mainz, Germany. I. Sedimentology and morphology. *Sedimentology*, **47**(1), 227–252.
- Carrigy, M. A. 1970. Experiments on Angles of Repose of Granular Materials. *Sedimentology*, **14**(3-4), 147.
- Cheng, N. S., & Chua, L. H. C. 2005. Comparisons of sidewall correction of bed shear stress in open-channel flows. *Journal of Hydraulic Engineering-Asce*, **131**(7), 605–609.
- Chevoir, F. 2008. *Ecoulements granulaires*. Vol. SI16. Collection Etude et Recherche des Laboratoires des Ponts et Chausses.
- Church, M. 2006. Bed material transport and the morphology of alluvial river channels. *Annual Review of Earth and Planetary Sciences*, **34**, 325–354.
- Church, M., & Zimmermann, A. 2007. Form and stability of step-pool channels: Research progress. *Water Resources Research*, **43**(3).
- Church, M., Hassan, M. A., & Wolcott, J. F. 1998. Stabilizing self-organized structures in gravel-bed stream channels: Field and experimental observations. *Water Resources Research*, **34**(11), 3169–3179.
- Courrech du Pont, S., Gondret, P., Perrin, B., & Rabaud, M. 2003a. Granular avalanches in fluids. *Physical review letters*, **90**(4), 44301.
- Courrech du Pont, S., Gondret, P., Perrin, B., & Rabaud, M. 2003b. Wall effects on granular heap stability. *Europhysics Letters*, **61**(4), 492–498.

- D'Agostino, V., & Lenzi, M. A. 1999. Bedload transport in the instrumented catchment of the Rio Cordon Part II: Analysis of the bedload rate. *Catena*, **36**(3), 191–204.
- Deigaard, R. 2006. Breaking antidunes: Cyclic behavior due to hysteresis. *Journal of Hydraulic Engineering-Asce*, **132**(6), 620–623.
- Denisov, D. V., Villanueva, Y. Y., Lorincz, K. A., May, S., & Wijngaarden, R. J. 2012. Relation between self-organized criticality and grain aspect ratio in granular piles. *Physical Review E*, **85**(5).
- Dinehart, R. L. 1999. Correlative velocity fluctuations over a gravel river bed. *Water Resources Research*, **35**(2), 569–582.
- Drake, T. G., Shreve, R. L., Dietrich, W. E., Whiting, P. J., & Leopold, L. B. 1988. Bedload Transport of Fine Gravel Observed by Motion-Picture Photography. *Journal of Fluid Mechanics*, **192**, 193–217.
- Einstein, H. A. 1942. Formulas for the transportation of bed load. *Transactions. American Society of Civil Engineers*, **107**.
- Einstein, H. A. 1950. The bed-load function for sediment transportation in open channel flows. *U. S. Dept. of Agriculture*.
- Engelund, F., & Fredsoe, J. 1982. Sediment Ripples and Dunes. *Annual Review of Fluid Mechanics*, **14**, 13–37.
- Exner, F. M. 1925. Über die Wechselwirkung zwischen Wasser und Geschiebe in Flüssen. *Sitzber. Akad. Wiss Wien*, **134**(2a), 169–204.
- Ferguson, R. I. 2005. Estimating critical stream power for bedload transport calculations in gravel-bed rivers. *Geomorphology*, **70**(1-2), 33–41.
- Ferro, V., & Baïamonte, G. 1994. Flow Velocity Profiles in Gravel-Bed Rivers. *J. Hydraul. Eng.*, **120**(1), 6080.
- Fienberg, K., Singh, A., Foufoula-Georgiou, E., Jerolmack, D., & Marr, J. 2010. *Theoretical Framework for Interpreting and Quantifying the Sampling Time Dependence of Gravel Bedload Transport Rates*. Pages 171–184.
- Folk, R. L., & Ward, W. C. 1957. Brazos River bar [Texas]; a study in the significance of grain size parameters. *Journal of Sedimentary Research*, **27**(1), 3–26.
- Franca, M. 2005. *A field study of turbulent flows in shallow gravel-bed rivers*. PhD Thesis. Environmental Hydraulics Laboratory, EPFL, Lausanne, n 3393.
- Frette, V., Christensen, K., Malthesorensen, A., Feder, J., Jossang, T., & Meakin, P. 1996. Avalanche dynamics in a pile of rice. *Nature*, **379**(6560), 49–52.
- Frey, P., & Church, M. 2011. Bedload: A granular phenomenon. *Earth Surface Processes and Landforms*, **36**(1), 58–69.
- Frey, P., Ducottet, C., & Jay, J. 2003. Fluctuations of bed load solid discharge and grain size distribution on steep slopes with image analysis. *Experiments in Fluids*, **35**(6), 589–597.
- Furbish, David Jon, Haff, Peter K, Roseberry, John C, & Schmeeckle, Mark W. 2012. A probabilistic description of the bed load sediment flux: 1. Theory. *Journal of Geophysical Research: Earth Surface* (20032012), **117**(F3).

- Garcia, C., Laronne, J. B., & Sala, M. 2000. Continuous monitoring of bedload flux in a mountain gravel-bed river. *Geomorphology*, **34**(1-2), 23–31.
- Ghilardi, T., & Schleiss, A.J. 2012. Steep flume experiments with large immobile boulders and wide grain size distribution as encountered in alpine torrents. *Pages 5–7 of: Proc. of River Flow*.
- Gilbert, G. K. 1914. *The transportation of dbris by running water*. Tech. rept. US Geological Survey Professional Paper, 86.
- Gomez, B. 1991. Bedload Transport. *Earth-Science Reviews*, **31**(2), 89–132.
- Grant, G. E. 1997. Critical flow constrains flow hydraulics in mobile-bed streams: A new hypothesis. *Water Resources Research*, **33**(2), 349–358.
- Griffiths, G. A., & Sutherland, A. J. 1977. Bedload Transport by Translation Waves. *Journal of the Hydraulics Division-Asce*, **103**(11), 1279–1291.
- Hamamori, A., & Laboratorium, W. 1962. *A Theoretical Investigation on the Fluctuation of Bedload Transport*. Hydraulics Laboratorium Delft.
- Hassan, M. A., & Church, M. 2000. Experiments on surface structure and partial sediment transport on a gravel bed. *Water Resources Research*, **36**(7), 1885–1895.
- Hassan, M. A., & Church, M. 2001. Sensitivity of bed load transport in Harris Creek: Seasonal and spatial variation over a cobble-gravel bar. *Water Resources Research*, **37**(3), 813–825.
- Helley, E.J., & Smith, W. 1971. *Development and Calibration of a Pressure-Difference Bed Load Sampler*. Tech. rept. U.S. Geological Survey Open File Report, Washington, USA.
- Heyman, J., Mettra, F., Ma, H. B., & Ancey, C. 2013. Statistics of bedload transport over steep slopes: Separation of time scales and collective motion. *Geophysical Research Letters*, **40**(1), 128–133.
- Hjulstrom, F. 1935. The Morphological Activity of Rivers as Illustrated by River Fyris. *Bulletin of the Geological Institute*, **25**.
- Hsu, L., Finnegan, N. J., & Brodsky, E. E. 2011. A seismic signature of river bedload transport during storm events. *Geophysical Research Letters*, **38**.
- Ikeda, H., & Iseya, F. 1988. *Experimental study of heterogeneous sediment transport*. Tech. rept. Environmental Research Center, University of Tsukuba, Japan, 12.
- Iseya, F., & Ikeda, H. 1987. Pulsations in Bedload Transport Rates Induced by a Longitudinal Sediment Sorting - a Flume Study Using Sand and Gravel Mixtures. *Geografiska Annaler Series a-Physical Geography*, **69**(1), 15–27.
- Jaeger, H. M., Liu, C. H., Nagel, S. R., & Witten, T. A. 1990. Friction in Granular Flows. *Europhysics Letters*, **11**(7), 619–624.
- Jerolmack, D. J., & Paola, C. 2010. Shredding of environmental signals by sediment transport. *Geophysical Research Letters*, **37**.
- Jerolmack, Douglas J. 2011. Causes and effects of noise in landscape dynamics. *Eos, Transactions American Geophysical Union*, **92**(44), 385–386.
- Katul, G., Wiberg, P., Albertson, J., & Hornberger, G. 2002. A mixing layer theory for flow resistance in shallow streams. *Water Resources Research*, **38**(11), 1250.

- Kennedy, F. 1961. *Stationary waves and antidunes in alluvial channels*. Tech. rept. KH-R-2. California Institute of Technology.
- Kennedy, J. F. 1963. The Mechanics of Dunes and Antidunes in Erodible-Bed Channels. *Journal of Fluid Mechanics*, **16**(4), 521.
- Kennedy, J. F. 1969. Formation of Sediment Ripples, Dunes, and Antidunes. *Annual Review of Fluid Mechanics*, **1**, 147.
- Kleinhans, M. G. 2005. Upstream sediment input effects on experimental dune trough scour in sediment mixtures. *Journal of Geophysical Research-Earth Surface*, **110**(F4).
- Kleinhans, M. G., Wilbers, A. W. E., De Swaaf, A., & Van den Berg, J. H. 2002. Sediment supply-limited bedforms in sand-gravel bed rivers. *Journal of Sedimentary Research*, **72**(5), 629–640.
- Kramer, H. 1932. *Modellgeschiebe und schleppkraft*. Ph.D. thesis. Technischen Hochschule, Dresden, Germany.
- Lajeunesse, E., Malverti, L., & Charru, F. 2010. Bed load transport in turbulent flow at the grain scale: Experiments and modeling. *Journal of Geophysical Research-Earth Surface*, **115**.
- Lamarre, H., MacVicar, B., & Roy, A. G. 2005. Using passive integrated transponder (PIT) tags to investigate sediment transport in gravel-bed rivers. *Journal of Sedimentary Research*, **75**(4), 736–741.
- Lane, E. W. 1955. The importance of fluvial geomorphology in hydraulic engineering. *Proceedings of the American Society of Civil Engineers*, **81**, 117.
- Lavelle, J. W., & Mofjeld, H. O. 1987. Do Critical Stresses for Incipient Motion and Erosion Really Exist. *Journal of Hydraulic Engineering-Asce*, **113**(3), 370–+.
- Lee, K. T., Liu, Y. L., & Cheng, K. H. 2004. Experimental investigation of bedload transport processes under unsteady flow conditions. *Hydrological Processes*, **18**(13), 2439–2454.
- Lenzi, M. A. 2001. Steppool evolution in the Rio Cordon, northeastern Italy. *Earth Surface Processes and Landforms*, **26**(9), 991–1008.
- Lenzi, M. A., D’Agostino, V., & Billi, P. 1999. Bedload transport in the instrumented catchment of the Rio Cordon Part I: Analysis of bedload records, conditions and threshold of bedload entrainment. *Catena*, **36**(3), 171–190.
- Leopold, L. B. 1953. Downstream Change of Velocity in Rivers. *American Journal of Science*, **251**(8), 606–624.
- Leopold, Luna Bergere, & Maddock, Thomas. 1953. The hydraulic geometry of stream channels and some physiographic implications.
- LHG, Hydrologische Mitteilungen. 1994. *Die Hochwasser 1993 im Wallis und Tessin - Messdaten und ausgesuchte Auswertungen*. Tech. rept. Bundesamt fur Umwelt, Wald und Landschaft.
- Liebault, F., Bellot, H., Chapuis, M., Klotz, S., & Deschatres, M. 2012. Bedload tracing in a high-sediment-load mountain stream. *Earth Surface Processes and Landforms*, **37**(4), 385–399.
- Loiseleux, T., Gondret, P., Rabaud, M., & Doppler, D. 2005. Onset of erosion and avalanche for an inclined granular bed sheared by a continuous laminar flow. *Physics of Fluids*, **17**(10).
- Mao, L. C. 2012. The effect of hydrographs on bed load transport and bed sediment spatial arrangement. *Journal of Geophysical Research-Earth Surface*, **117**.

- Marquis, G. A., & Roy, A. G. 2012. Using multiple bed load measurements: Toward the identification of bed dilation and contraction in gravel-bed rivers. *Journal of Geophysical Research-Earth Surface*, **117**.
- Martin, R. L., & Jerolmack, D. J. 2013. Origin of hysteresis in bed form response to unsteady flows. *Water Resources Research*, **49**(3), 1314–1333.
- Mazumder, R. 2003. Sediment transport, aqueous bedform stability and morphodynamics under unidirectional current: a brief overview. *Journal of African Earth Sciences*, **36**(1-2), 1–14.
- McElroy, B., & Mohrig, D. 2009. Nature of deformation of sandy bed forms. *Journal of Geophysical Research-Earth Surface*, **114**.
- Meyer-Peter, E., & Muller, R. 1948. Formulas for bed-load transport. *Proceedings of the 2nd Meeting of the International Association for Hydraulic Structures Research*, 3964.
- Mikos, M., & Spazzapan, M. 2006. Laboratory applications of a satellite for measuring dynamics of sediment transport in turbulent flows. *Acta hydrotechnica*, **23**(38), 39–55.
- Milzow, C., Molnar, P., McArdell, B. W., & Burlando, P. 2006. Spatial organization in the step-pool structure of a steep mountain stream (Vogelbach, Switzerland). *Water Resources Research*, **42**(4).
- Molnar, P., & Ramirez, J. A. 1998. Energy dissipation theories and optimal channel characteristics of river networks. *Water Resources Research*, **34**(7), 1809–1818.
- Molnar, P., Densmore, A. L., McArdell, B. W., Turowski, J. M., & Burlando, P. 2010. Analysis of changes in the step-pool morphology and channel profile of a steep mountain stream following a large flood. *Geomorphology*, **124**(1-2), 85–94.
- Montgomery, D. R., & Buffington, J. M. 1997. Channel-reach morphology in mountain drainage basins. *Geological Society of America Bulletin*, **109**(5), 596–611.
- Montgomery, David R., & Buffington, John M. 1998. Channel processes, classification, and response. *River ecology and management*, **112**, 1250–1263.
- Nanson, G. C., & Huang, H. Q. 2008. Least action principle, equilibrium states, iterative adjustment and the stability of alluvial channels. *Earth Surface Processes and Landforms*, **33**(6), 923–942.
- Nanson, G. C., Price, D. M., Jones, B. G., Maroulis, J. C., Coleman, M., Bowman, H., Cohen, T. J., Pietsch, T. J., & Larsen, J. R. 2008. Alluvial evidence for major climate and flow regime changes during the middle and late Quaternary in eastern central Australia. *Geomorphology*, **101**(1-2), 109–129.
- Neill, C. R., & Yalin, M. S. 1969. Quantitative definition of beginning of bed movement. *J. Hydraul. Div. Am. Soc. Civ. Eng.*, **95**, 585–588.
- Nelson, J. M., Mclean, S. R., & Wolfe, S. R. 1993. Mean Flow and Turbulence Fields over 2-Dimensional Bed Forms. *Water Resources Research*, **29**(12), 3935–3953.
- Nezu, I., & Onitsuka, K. 2001. Turbulence measurements of a supercritical unsteady open-channel flow. *Hydraulics of Rivers, Water Works and Machinery, Vol 1, Theme D, Proceedings*, 202–208.
- Nunez-Gonzalez, F., & Martin-Vide, J. P. 2011. Analysis of antidune migration direction. *Journal of Geophysical Research-Earth Surface*, **116**.
- Paiement-Paradis, G., Marquis, G., & Roy, A. 2011. Effects of turbulence on the transport of individual particles as bedload in a gravel-bed river. *Earth Surface Processes and Landforms*, **36**(1), 107–116.

- Paintal, A. S. 1971. Concept Of Critical Shear Stress In Loose Boundary Open Channels. *Journal of Hydraulic Research*, **9**(1), 91–113.
- Papanicolaou, A. N., Diplas, P., Evaggelopoulos, N., & Fotopoulos, S. 2002. Stochastic incipient motion criterion for spheres under various bed packing conditions. *Journal of Hydraulic Engineering-Asce*, **128**(4), 369–380.
- Parker, C., Clifford, N. J., & Thorne, C. R. 2011. Understanding the influence of slope on the threshold of coarse grain motion: Revisiting critical stream power. *Geomorphology*, **126**(1-2), 51–65.
- Parker, G. 1991. Selective Sorting and Abrasion of River Gravel .1. Theory. *Journal of Hydraulic Engineering-Asce*, **117**(2), 131–149.
- Parker, G., & Izumi, N. 2000. Purely erosional cyclic and solitary steps created by flow over a cohesive bed. *Journal of Fluid Mechanics*, **419**, 203–238.
- Parker, Gary. 1975. Sediment inertia as cause of river antidunes. *Journal of the Hydraulics Division*, **101**(2), 211–221.
- Parsons, D. R., Best, J. L., Orfeo, O., Hardy, R. J., Kostaschuk, R., & Lane, S. N. 2005. Morphology and flow fields of three-dimensional dunes, Rio Parana, Argentina: Results from simultaneous multibeam echo sounding and acoustic Doppler current profiling. *Journal of Geophysical Research-Earth Surface*, **110**(F4).
- Petit, F., Gob, F., Houbrechts, G., & Assani, A. A. 2005. Critical specific stream power in gravel-bed rivers. *Geomorphology*, **69**(1-4), 92–101.
- Phillips, J. D. 1995. Self-Organization and Landscape Evolution. *Progress in Physical Geography*, **19**(3), 309–321.
- Powell, D. M. 1998. Patterns and processes of sediment sorting in gravel-bed rivers. *Progress in Physical Geography*, **22**(1), 1–32.
- Radice, A., Ballio, F., & Nikora, V. 2009. On statistical properties of bed load sediment concentration. *Water Resources Research*, **45**.
- Recking, A. 2006. *An experimental Study of Grain Sorting Effects on Bedload*. PhD Thesis. INSA Lyon, 2006-ISAL-00113.
- Recking, A. 2008. Variation of the critical Shields number with slope. *Houille Blanche-Revue Internationale De L Eau*, **5**, 59–63.
- Recking, A. 2010. A comparison between flume and field bed load transport data and consequences for surface-based bed load transport prediction. *Water Resources Research*, **46**, W03518.
- Recking, A. 2012. Influence of sediment supply on mountain streams bedload transport. *Geomorphology*, **175**, 139–150.
- Recking, A. 2013. Simple Method for Calculating Reach-Averaged Bed-Load Transport. *Journal of Hydraulic Engineering-Asce*, **139**(1), 70–75.
- Recking, A., Frey, P., Paquier, A., Belleudy, P., & Champagne, J. Y. 2008. Feedback between bed load transport and flow resistance in gravel and cobble bed rivers. *Water Resources Research*, **44**(5).
- Recking, A., Bacchi, V., Naaim, M., & Frey, P. 2009a. Antidunes on steep slopes. *Journal of Geophysical Research-Earth Surface*, **114**.

- Recking, A., Frey, P., Paquier, A., & Belleudy, P. 2009b. An experimental investigation of mechanisms involved in bed load sheet production and migration. *Journal of Geophysical Research-Earth Surface*, **114**.
- Recking, A., Liebault, F., Peteuil, C., & Jolimet, T. 2012. Testing bedload transport equations with consideration of time scales. *Earth Surface Processes and Landforms*, **37**(7), 774–789.
- Reid, I., Layman, J. T., & Frostick, L. E. 1980. The Continuous Measurement of Bedload Discharge. *Journal of Hydraulic Research*, **18**(3), 243–249.
- Reynolds, A.J. 1965. Waves on the erodible bed of an open channel. *Journal of Fluid Mechanics*, **22**(01), 113–133.
- Rickenmann, D. 1991. Hyperconcentrated Flow and Sediment Transport at Steep Slopes. *Journal of Hydraulic Engineering-Asce*, **117**(11), 1419–1439.
- Rickenmann, D., & McArdell, B. W. 2008. Calibration of piezoelectric bedload impact sensors in the Pitzbach mountain stream. *Geodinamica Acta*, **21**(1-2), 35–51.
- Rickenmann, D, Chiari, M, & Friedl, K. SETRACA sediment routing model for steep torrent channels. *Pages 843–852 of: River flow*, vol. 1. Taylor & Francis London.
- Roseberry, J. C., Schmeeckle, M. W., & Furbish, D. J. 2012. A probabilistic description of the bed load sediment flux: 2. Particle activity and motions. *Journal of Geophysical Research-Earth Surface*, **117**.
- Schmeeckle, M. W., Nelson, J. M., & Shreve, R. L. 2007. Forces on stationary particles in near-bed turbulent flows. *Journal of Geophysical Research-Earth Surface*, **112**(F2).
- Schmid, H. 2012. *How to use the FFT and Matlabs pwelch function for signal and noise simulations and measurements*. Tech. rept. University of Applied Sciences of Northwestern Switzerland.
- Shields, A. 1936. *Anwendung der Aehnlichkeitsmechanik und der Turbulenzforschung auf die Geschiebepbewegung*. Ph.D. thesis. Technischen Hochschule, Berlin.
- Simons, D. B., Richardson, E. V., & Nordin, C. F., Jr. 1965. Bedload equation for ripples and dunes. *USGS Numbered Series, Sediment transport in alluvial channels, 1963-65*, 462–H.
- Singh, A., Fienberg, K., Jerolmack, D. J., Marr, J., & Foufoula-Georgiou, E. 2009. Experimental evidence for statistical scaling and intermittency in sediment transport rates. *Journal of Geophysical Research-Earth Surface*, **114**.
- Singh, A., Lanzoni, S., Wilcock, P. R., & Foufoula-Georgiou, E. 2011. Multiscale statistical characterization of migrating bed forms in gravel and sand bed rivers. *Water Resources Research*, **47**.
- Singh, A., Foufoula-Georgiou, E., Porte-Agel, F., & Wilcock, P. R. 2012. Coupled dynamics of the co-evolution of gravel bed topography, flow turbulence and sediment transport in an experimental channel. *Journal of Geophysical Research-Earth Surface*, **117**.
- Singh, V. P. 2003. On the theories of hydraulic geometry. *International journal of sediment research*, **18**(3), 196–218.
- Smart, G. M., & Habersack, H. M. 2007. Pressure fluctuations and gravel entrainment in rivers. *Journal of Hydraulic Research*, **45**(5), 661–673.
- Smart, Graeme M. 1984. Sediment transport formula for steep channels. *Journal of Hydraulic Engineering*, **110**(3), 267–276.

- Strom, K., Papanicolaou, A. N., Evangelopoulos, N., & Odeh, M. 2004. Microforms in gravel bed rivers: Formation, disintegration, and effects on bedload transport. *Journal of Hydraulic Engineering-Asce*, **130**(6), 554–567.
- Thorn, Colin E, & Welford, Mark R. 1994. The equilibrium concept in geomorphology. *Annals of the Association of American Geographers*, **84**(4), 666–696.
- Travaglini, E., & Bardou, E. 2012. Measuring Bedload with Geophones, Navisence River. CREALP. Poster, CREALP, Sion, Suisse.
- Tsai, V. C., Minchew, B., Lamb, M. P., & Ampuero, J. P. 2012. A physical model for seismic noise generation from sediment transport in rivers. *Geophysical Research Letters*, **39**.
- Turowski, J. M. 2010. Probability distributions of bed load transport rates: A new derivation and comparison with field data. *Water Resources Research*, **46**.
- Turowski, J. M., & Rickenmann, D. 2011. Measuring the Statistics of Bed-Load Transport Using Indirect Sensors. *Journal of Hydraulic Engineering-Asce*, **137**(1), 116–121.
- Turowski, J. M., Yager, E. M., Badoux, A., Rickenmann, D., & Molnar, P. 2009. The impact of exceptional events on erosion, bedload transport and channel stability in a step-pool channel. *Earth Surface Processes and Landforms*, **34**(12), 1661–1673.
- Turowski, J. M., Badoux, A., & Rickenmann, D. 2011. Start and end of bedload transport in gravel-bed streams. *Geophysical Research Letters*, **38**.
- Valyrakis, M., Diplas, P., Dancey, C. L., Greer, K., & Celik, A. O. 2010. Role of instantaneous force magnitude and duration on particle entrainment. *Journal of Geophysical Research-Earth Surface*, **115**.
- Vanoni, V. A., & Brooks, N. H. 1957. *Laboratory studies of the roughness and suspended load of alluvial streams*. California Institute of Technology, Pasadena, CA.
- Weichert, R. 2006. Bed morphology and stability of steep open channels. *Mitteilungen der Versuchsanstalt fr Wasserbau, Hydrologie und Glaziologie an der Eidgenossischen Technischen Hochschule Zurich*.
- Whitehouse, R. J. S., & Hardisty, J. 1988. Experimental Assessment of 2 Theories for the Effect of Bedslope on the Threshold of Bedload Transport. *Marine Geology*, **79**(1-2), 135–139.
- Whittaker, J. G. 1987. Sediment transport in step-pool streams. *Sediment Transport in Gravel-Bed Rivers.*, p 545–579.
- Wilcock, P. R., & Crowe, J. C. 2003. Surface-based transport model for mixed-size sediment. *Journal of Hydraulic Engineering-Asce*, **129**(2), 120–128.
- Williams, G. P. 1970. *Flume width and water depth effects in sediment-transport experiments*. US Government Printing Office.
- Yager, EM, Kirchner, JW, & Dietrich, WE. 2007. Calculating bed load transport in steep boulder bed channels. *Water Resources Research*, **43**(7).

Curriculum Vitae

François METTRA

+ 41 (0) 77 425 58 25

francois.mettra@a3.epfl.ch

SPECIAL SKILLS

- Water management and hydraulics engineering
- Hydrology and natural hazards
- Data processing and statistics
- GIS and mapping

MAIN ACHIEVEMENTS

- Thesis in torrential hydraulics
- Hydrological and bed load transport computations
- Hydraulics modeling

WORK EXPERIENCE

EPFL, Lausanne, Switzerland (2010-2014)

Doctoral assistant at the Environmental Hydraulics Lab (Prof. C. Ancey)

- Experimental thesis on bed load transport in mountainous rivers: conception of the experimental facilities and measurement systems; data acquisition, processing and analysis; description of several morphodynamical mechanisms

Meteo-alpes.org (from 2011)

Meteorological forecaster for western Alps in a 4 person team

University of British Colombia, Vancouver, Canada (2009)

Research assistant (6 months) in Forestry

- Optimization and modeling of water discharge time series
- Snow-hydrology study (field measurements, statistical modeling)

Burgéap consulting firm, Grenoble, France (2008)

Engineer internship (10 weeks)

- Building of a GIS for the diagnosis of a rain water network
- Hydrological computations (rain water network, stormwater basin)

EDF, Grenoble, France (2007)

Engineer internship (1 month) in the Aquatic Environment department

EDUCATION

PhD, EPFL, Lausanne, Switzerland (2014)

Subject: « Morphodynamic mechanisms in steep channels: from local processes to large-scale evolution »

Engineer degree, Engineering School in Hydraulics and Mechanics, Grenoble, France (2009)

Specialties: water resources, hydraulics buildings (<http://ense3.grenoble-inp.fr/>)

Master, University of Joseph Fourier, Grenoble, France (2009)

Subject: « Spatial variability of hydrological processes in a mountainous and partially forested watershed »

LANGUAGES

French	mother tongue
English	fluent (CEFR level: B2.2), talks in international conferences
German	basic skills

SOFTWARE SKILLS

Matlab, R	HEC-RAS
SAGA, Arcgis, Arcview, Mapinfo, Autocad	Word, Excel, Latex

MISCELLANEOUS

Interest in climatology, glaciology, nivology, geology
Sports: skiing, mountaineering, paragliding

François Mettra

+ 41 (0) 77 425 58 25

francois.mettra@a3.epfl.ch

APPENDIX

International conferences

- European Geophysical Union Meeting, Vienna, Austria, 2012, **Characterization of bedload transport in steep slope stream** (talk).
- 8th Symposium on River, Coastal and Estuarine Morphodynamics, Santander, Spain, 2013, **Metastability of steep channels** (talk).
- 8e Conférence Internationale de Géomorphologie, Paris, France, 2013, **From bedform evolution to channel slope fluctuations in steep-slope streams** (talk).
- American Geophysical Union Meeting, San Francisco, USA, 2013, **Bedform migration in steep channels: from local avalanches to large-scale changes** (talk).

Scientific papers

- J. Heyman, F. Mettra, H.B. Ma, C. Ancey, **Statistics of bedload transport over steep slopes: Separation of time scales and collective motion**, Geophysical Research Letters, 40, 128-133, 2013.
- J. Heyman, H.B. Ma, F. Mettra, C. Ancey, **Spatial correlations in bed load transport: Evidence, importance, and modeling**, Journal of Geophysical Research: Earth Surface, accepted (2014).